# Particle-resolved CFD simulations of catalytic flow reactors

vorgelegt von
Dipl.-Ing.
Gregor Dionys Wehinger
geb. in Singen (Hohentwiel)

von der Fakultät III - Prozesswissenschaften
der Technischen Universität Berlin
zur Erlangung des akademischen Grades

Doktor der Ingenieurwissenschaften
- Dr.-Ing. -

genehmigte Dissertation

Promotionsausschuss:

Vorsitzender:     Prof. Dr. Rudibert King
Gutachter:        Prof. Dr. Matthias Kraume
Gutachter:        Prof. Claude Franklin Goldsmith, PhD

Tag der wissenschaftlichen Aussprache: 1. Juli 2016

Berlin 2016

# Acknowledgments

I thank my supervisor Professor Matthias Kraume for his guidance and constant support during all the years. He has been an excellent adviser and I am very thankful that he gave me the opportunity to learn from him. His passion for research and teaching, as well as his precise analyzing always inspired me and will serve as a model for me as I start my professional career.

I want to thank Professor Franklin Goldsmith for making it possible to stay in his research group at Brown University. The three months in the US were very inspiring not only in terms of research. Financial support by the DAAD Doktorandenstipendium for this stay is gratefully acknowledged. In addition, I am very thankful that Prof. Goldsmith referred my thesis and came to Berlin to be part of the scientific defense.

Thanks also go to Professor Horn and his group, especially Dr. Oliver Korup and Viktor Berg, at TU Hamburg. My research was tremendously enriched by the detailed experimental data from their profile reactor and associated discussions.

I thank Professor King for taking the chair of the examination board.

My acknowledgments would not be complete without recognizing the important role that my colleagues at the Fachgebiet Verfahrenstechnik have had. Particular thanks go to Thomas Eppinger for his guidance in the first months of my PhD and the continuous collaboration. Furthermore, I thank my former colleagues sharing the office: Ali, Sherly, Markus, Frauke, and Nico. Thank you for all the memories and all the helpful discussions over coffee, whether about research or life. Also, thank you Ulla for support in all kinds of situations.

I thank my parents and my two brothers for love and support they have provided me with during my years at school and university. Special thanks go to my friend Fred Folke who inspired me for CFD research and reviewed my thesis. Finally, I want to thank Andrea for being the solid ground during the past years.

# Abstract

Dry reforming of methane (DRM) produces syngas from marginal natural gas resources and carbon dioxide. Both are greenhouse gases. Commonly, DRM is carried out in catalytic fixed-bed reactors with a small tube-to-particle-diameter ratio. Backflow, channeling, and strong interactions between local kinetics and local transport phenomena occur. Conventional plug-flow models and pseudo-homogeneous kinetics are questionable in such reactor arrangements. In this thesis a rigorous modeling is presented of catalytic fixed-bed reactors with CFD simulations on the *particle-resolved* scale. This approach takes the actual particle shape into account, which determines the interstitial flow field. Hence, no transport correlations are needed. The particle-resolved modeling includes several aspects, i.e., generation of bed structure, meshing strategies, inclusion of microkinetics, pore processes, and heat transfer mechanisms. In this work these aspects are developed and analyzed critically by comparison with experiments or correlations.

Randomly packed beds were generated artificially with discrete element method (DEM) simulations. Local porosity and velocity profiles were reproduced with high accuracy for beds of spheres and cylinders. Polyhedral meshes can be used for discretization of the complex bed geometry. Boundary layers should be resolved by prism cells close to walls. The boundary layer thickness can be approximated with an equation depending on particle Reynolds number and particle diameter. However, local mesh refinement is strongly advised. Contact regions in packed beds of non-spherical particles can be either points, lines or areas. Local modifications of contact regions are recommended applying either the *caps* method or the *bridges* method. Both showed good results for pressure drop and heat transfer. For higher flow rates the stable caps method overestimated convective heat transfer. The advantage of the bridges method is that the thermal conductivity of the bridges can be used as a tuning factor. DRM on Ni was investigated experimentally and by particle-resolved CFD simulations in a fixed bed of spheres. Heat transfer without chemical reactions was well reproduced with 3D CFD, whereas the 2D model failed. For DRM gas phase species profiles were predicted fairly with a recently published microkinetics. A thermodynamic analysis detected inconsistencies for enthalpy and entropy, especially for high surface coverage. Still, the rigorous modeling of catalytic fixed-bed reactors including radiation and conjugate heat transfer is promising. If pore processes are significant, they can be modeled by the effectiveness-factor approach, since the highly accurate 3D reaction-diffusion model is prohibitively time consuming.

Additionally, an algorithm (*catFM*) is presented, which generates artificially open-cell foam structures ready for CFD simulations on the particle-resolved scale. The algorithm was tested in terms of morphology, pressure drop, and residence time distribution. Finally, the performance of catFM was demonstrated by reproducing partial oxidation of methane in a Rh catalytic foam with high accuracy.

With particle-resolved CFD simulations it is possible to explore and design catalytic flow reactors fundamentally. Gas phase, solid temperature, and species concentrations are predicted without relying on transport correlations.

# Kurzfassung

Mit der Trockenreformierung (DRM) kann Synthesegas aus bedingt abbauwürdigen Erdgasquellen und Kohlendioxid hergestellt werden. Beides sind Treibhausgase. Üblicherweise wird die DRM in Festbettreaktoren mit kleinem Rohr-zu-Partikeldurchmesserverhältnis realisiert. Rückströmungen, Randgängigkeit und starke Wechselwirkungen zwischen lokaler Kinetik und lokalen Transportphänomenen treten auf. Klassische Pfropfenströrmungs- und pseudo-homogene Kinetikmodelle sind für diese Konfigurationen fragwürdig. In dieser Arbeit wird eine rigorose Modellierung katalytischer Festbetten mittels CFD auf der Partikelskala vorgestellt. Die tatsächliche Partikelform wird widergegeben, womit die Strömungsumlenkung bestimmt wird. Folglich sind keine Transportkorrelationen notwendig. Diese detaillierte Modellierung bezieht folgende Aspekte mit ein: Bettstrukturerzeugung, Vernetzungsstrategien, Mikrokinetiken, Porenprozesse und Wärmetransportmechanismen. In dieser Arbeit wurden diese Apekte weiterentwickelt und anhand experimenteller Daten oder Korrelationen kritisch bewertet.

Die zufällig geschütteten Festbetten wurden mit Hilfe von DEM-Simulationen erzeugt. Lokale Porositäts- und Geschwindigkeitsprofile konnten mit guter Übereinstimmung für Kugel- und Zylinderschüttungen reproduziert werden. Polyedernetze können verwendet werden um die komplexe Bettstruktur zu diskretisieren. Grenzschichten sollten mit Prismenzellen in Wändnähe aufgelöst werden. Diese können mit einer Korrelation abgeschätzt werden abhängig von Partikel-Reynoldszahl und -durchmesser. Eine lokale Netzverfeinerung wird jedoch dringend empfohlen. Kontaktbereiche in Festbetten aus nicht-kugelförmigen Partikeln können als Punkte, Linien oder Flächen auftreten. Lokale Modifikationen dieser Bereiche sollten mit der *Kappen-* oder *Brücken*-Methode durchgeführt werden. Beide Methoden zeigten gute Ergebnisse hinsichtlich Druckverlust und Wärmetransport. Für höhere Flussraten jedoch unterschätzte die stabile Kappenmethode den konvektiven Wärmetransport. Der Vorteil der Brückenmethode ist, dass die Wärmeleitfähigkeit der Brücken als Anpassungsparameter dienen kann. DRM an Ni wurde experimentell und mit detaillierten CFD-Simulationen in einer Kugelschüttung untersucht. Wärmetransport ohne chemische Reaktion konnte dabei sehr gut widergegeben werden. Jedoch versagte das 2D-Modell. Für die DRM konnten die Gasphasenkonzentrationen nur bedingt mit einer aktuellen Mikrokinetik reproduziert werden. Eine thermodynamische Analyse stellte die Inkonsistenz hinsichtlich Enthalpie und Entropie fest, vor allem bei hoher Oberflächenbeladung. Trotzdem ist die rigorose Modellierung von katalytischen Festbetten einschliesslich Strahlung und Wärmeleitung vielversprechend. Falls Porenprozesse signifikant sind, können sie mit dem Effektivitätsfaktor-Ansatz modelliert werden, da der genauere 3D-Reaktion-Diffusion-Ansatz lange Rechenzeiten benötigt.

Zudem wurde ein Algorithmus (*catFM*) entwickelt, der künstlich Schwammstrukturen erzeugt, geeignet für detaillierte CFD-Simulationen. Der Algorithmus wurde hinsichtlich Morphologie, Druckverlust und Verweilzeitverteilung geprüft. Die volle Leistungsfähigkeit von catFM wurde durch die Simulation der partiellen Methanoxidation am Rh-Schwamm gezeigt.

Mit diesen detaillierten CFD-Simulationen ist es möglich katalytische Strömungsreaktoren grundlegend zu untersuchen. Gasphasen- und Feststofftemperatur, sowie Spezieskonzentrationen können hervorgesagt werden ohne auf Transportkorrelationen zurückzugreifen.

Kurzfassung

iv

# Contents

# Nomenclature

**Latin letters**

| | | |
|---|---|---|
| $A_k$ | pre-exponential factor | [s$^{-1}$ or m$^2$/mol$\cdot$s] |
| $c$ | species concentration | [mol/m$^3$ or mol/m$^2$] |
| $c_p$ | specific heat capacity | [J/kg$\cdot$K] |
| $C$ | constant in $k - \varepsilon$ turbulence model | [-] |
| $d_{\mathrm{p}}$ | particle diameter | [m] |
| $D$ | catalyst dispersion | [-] |
| $D$ | tube diameter | [m] |
| $D_{ij}$ | binary diffusion coefficient | [m$^2$/s] |
| $Da$ | Damköhler number $Da = k^* \cdot L/D_{ij}$ | [-] |
| $E$ | constant in wall law | [-] |
| $E_{\mathrm{a}}$ | activation energy | [kJ/mol] |
| $f_f$ | friction coefficient | [-] |
| $F$ | probability | [-] |
| $F_{\mathrm{cat/geo}}$ | ratio of catalytic active area to geometric area | [-] |
| $G$ | Gibb's free energy | [kJ/mol] |
| $G_b$ | generation of turbulent kinetic energy due to buoyancy | [m$^2$/s$^3$] |
| $G_k$ | generation of turbulent kinetic energy due to turbulent stress | [m$^2$/s$^3$] |
| $GHSV$ | gas hourly space velocity | [1/s] |
| $h$ | Planck's constant $h = 6.62607004 \cdot 10^{-34}$ | [J$\cdot$s] |
| $h$ | specific enthalpy | [J/kg] |
| $h_{\mathrm{w}}$ | wall heat transfer coefficient | [W/m$^2$$\cdot$K] |
| $H$ | bed height | [m] |
| $j_i$ | diffusion mass flux | [kg/m$^2$$\cdot$s] |
| $j_q$ | diffusion heat transport | [W/m$^2$] |
| $k$ | turbulent kinetic energy | [J/kg$\cdot$s] |
| $k$ | reaction rate constant | [s$^{-1}$ or m$^2$/mol$\cdot$s] |
| $k^*$ | pseudo first-order kinetic constant | [m/s] |
| $k_{\mathrm{B}}$ | Boltzmann constant $k_{\mathrm{B}} = 1.38064852$ | [J/K] |
| $K$ | equilibrium constant | [-] |
| $K$ | spring stiffness | [N] |

**Latin letters**

| | | |
|---|---|---|
| $L$ | characteristic length | [m] |
| $m$ | mass | [kg] |
| $M_i$ | molar weight of species $i$ | [kg/mol] |
| $N$ | tube-to-particle-diameter ratio $N = D/d_\mathrm{p}$ | [-] |
| $N$ | damping | [N·s/m] |
| $N_A$ | Avogadro's number $N_A = 6.02214 \cdot 10^{23}$ | [mol$^{-1}$] |
| $N_\mathrm{g}$ | number of gas phase species | [-] |
| $Nu_\mathrm{w}$ | wall Nusselt number $Nu_\mathrm{w} = h_\mathrm{w}d_\mathrm{p}/\lambda_\mathrm{f}$ | [-] |
| $p$ | pressure | [Pa] |
| $\mathbf{P}$ | reaction matrix | [-] |
| $Pr$ | Prandtl number $Pr = \mu c_p/\lambda$ | [-] |
| $r$ | radial coordinate | [m] |
| $R$ | ideal gas constant $R = 8.31445$ | [J/K·mol] |
| $R_i$ | production rate of species $i$ | [kg/m$^3$·s] |
| $Re_\mathrm{p}$ | particle Reynolds number $Re_\mathrm{p} = v_\mathrm{in}d_\mathrm{p}/v$ | [-] |
| $Re_\mathrm{c}$ | Reynolds number based on averaged cell diameter $Re_\mathrm{c} = v_\mathrm{in}d_\mathrm{c}\rho/(\mu \cdot \varepsilon)$ | [-] |
| $\dot{s}$ | molar net production rate | [mol/m$^3$·s] |
| $S$ | entropy | [kJ/mol] |
| $Sc$ | Schmidt number $Sc = v/D$ | [-] |
| $S_i$ | sticking coefficient | [-] |
| $S_h$ | heat source | [W/m$^3$] |
| $S_V$ | specific particle area | [m$^2$/m$^3$] |
| $t$ | time | [s] |
| $t_\mathrm{W}$ | washcoat thickness | [m] |
| $t^+$ | non-dimensional quantity for turbulent temperature distribution | [-] |
| $T$ | temperature | [K] |
| $T^*$ | reduced temperature for calculating diffusivity | |
| $u^+$ | non-dimensional velocity distribution | [-] |
| $u_\tau$ | friction velocity | [m/s] |
| $v_\mathrm{in}$ | superficial velocity | [m/s] |
| $\bar{v}_i$ | mean velocity components | [m/s] |

**Latin letters**

| | | |
|---|---|---|
| $v'_i$ | fluctuating velocity components | [m/s] |
| $x_i$ | coordinate in $i$ direction | [m] |
| $X_i$ | molar fraction of species $i$ | [-] |
| $y$ | wall distance | [m] |
| $y^+$ | non-dimensional wall distance | [-] |
| $Y_i$ | mass fraction of species $i$ | [-] |
| $z$ | axial coordinate | [m] |

**Greek letters**

| | | |
|---|---|---|
| $\beta$ | thermal expansion coefficient | [-] |
| $\gamma$ | catalyst density $\gamma = F_{\text{cat/geo}}/t_{\text{W}}$ | [1/m] |
| $\Gamma$ | surface site density | [mol/m$^2$] |
| $\delta_{\text{BL}}$ | boundary layer thickness | [m] |
| $\delta_{ij}$ | Kronecker delta | [-] |
| $\varepsilon$ | Lennard-Jones energy | [J] |
| $\varepsilon$ | parameter for modified activation energy | [kJ/mol] |
| $\varepsilon$ | dissipation rate | [] |
| $\varepsilon$ | porosity | [-] |
| $\varepsilon$ | emissivity | [-] |
| $\varepsilon$ | turbulent dissipation rate | [J/kg$\cdot$s] |
| $\zeta$ | arbitrary thermochemical property | [-] |
| $\eta$ | effectiveness factor | [-] |
| $\Theta$ | surface coverage | [-] |
| $\kappa$ | constant in wall law | [-] |
| $\mu$ | dynamic viscosity | [Pa$\cdot$s] |
| $\mu$ | parameter for modified surface rate expression | [-] |
| $\nu$ | kinematic viscosity | [m$^2$/s] |
| $\xi$ | dimensionless wall distance $\xi = (R - r)/d_{\text{p}}$ | [-] |
| $\rho$ | fluid density | [kg/m$^3$] |
| $\sigma$ | coordinate number | [-] |
| $\sigma_{ij}$ | reduced molecule diameter | [m] |
| $\sigma^2$ | variance | [s] |
| $\tau$ | sum of stoichiometric coefficients | [] |

**Greek letters**

| | | |
|---|---|---|
| $\tau$ | stress tensor | [N] |
| $\tau$ | tortuosity | [-] |
| $\tau_w$ | normal stress at the wall | [N] |
| $\bar{\tau}$ | mean residence time | [s] |
| $\tilde{\tau}$ | mode of residence time | [s] |
| $\phi$ | Thiele modulus | [-] |
| $\phi$ | azimuth | [-] |
| $\Psi$ | intermolecular energy | [J] |

**Subscripts**

| | |
|---|---|
| ads | adsorption |
| b | back |
| b | body |
| b | buoyancy |
| c | contact |
| c | cell |
| cat | catalyst |
| catFM | catalytic foam modeler |
| CAE | computer aided engineering |
| eff | effective |
| eq | equilibrium |
| eq | equivalent |
| exp | experimental |
| f | fluid |
| f | forward |
| g | gas |
| g | gravity |
| in | inlet |
| k | kinetic energy |
| Knud | Knudsen |
| L | local |
| M | mixture |
| n | normal |

**Subscripts**

| | |
|---|---|
| out | outlet |
| p | particle |
| r | radial |
| ref | reference |
| rot | rotational |
| rxn | reaction |
| s | surface |
| s | strut |
| t | turbulent |
| t | tangential |
| trans | translational |
| vib | vibrational |
| W | washcoat |
| w | wall |
| w | window |

**Superscripts**

| | |
|---|---|
| ‡ | at the transition state |
| 0 | at standard conditions |
| ads | adsorption |
| gas | gas phase |
| het | heterogeneous |

**Abbreviations**

| | |
|---|---|
| ADPF | axially dispersed plug flow |
| BET | Brunauer-Emmett-Teller |
| BCC | body-centered cubic |
| CAD | computer aided design |
| catFM | catalytic foam modeler |
| CFD | computational fluid dynamics |
| CPOX | catalytic partial oxidation |
| CT | computer tomography |
| DEM | discrete element method |

**Abbreviations**

| | |
|---|---|
| DFT | density functional theory |
| DNS | direct numerial simulation |
| DRM | dry reforming of methane |
| FCC | face-centered cubic |
| FHI | Fritz-Haber-Institut Berlin |
| FHS | front heat shield |
| GTL | gas to liquid fuel |
| IRS | infrared spectrometer |
| KIT | Karlsruhe Institute of Technology |
| LES | Large eddy simulation |
| LNG | liquified natural gas |
| NMR | nuclear magnetic resonance |
| MRI | magnetic resonance imaging |
| LHHW | Langmuir-Hinshelwood-Hougon-Watson |
| LIF | laser-induced fluorescence |
| LNG | liquified natural gas |
| PIV | particle-image velocimetry |
| PPI | pores per inch |
| RANS | Reynolds-averaged Navier-Stokes |
| RTD | residence-time distribution |
| SEM | scanning electron microscope |
| SFR | stagnation-flow reactor |
| SRM | steam reforming of methane |
| SST | shear-stress transport |
| S2S | surface-to-surface |
| TST | transition-state theory |
| WGS | water-gas shift reaction |

# 1 Introduction

A dramatic increase of atmospheric concentration of greenhouse gases has been observed during the last decades. Continued emissions of theses gases lead to further global warming and changes in all aspects of the climate system (Hartmann et al., 2013). The consequence is a global concern over the current technological practices. The field of related research covers greenhouse gas disposal, utilization, and removal. When it comes to chemical engineering and climate change processes are in the focus that combine methane ($CH_4$) and carbon dioxide ($CO_2$), both are highly abundant greenhouse gases. Dry reforming of methane (DRM) is such a process where $CH_4$ and $CO_2$ react heterogeneously to synthesis gas or often called syngas, i.e., a mixture of hydrogen ($H_2$) and carbon monoxide (CO). This highly endothermic reaction is carried out with adequate catalysts, mainly containing cheap nickel particles, at temperatures typically above 1,000 K. Coke formation and hence deactivation of the catalyst is still a major drawback in industrial scale reactors. Commonly, DRM is realized in multi-tubular reactors filled with catalytic particles (spheres, cylinders, one-hole or multi-hole cylinders, etc.). In Fig. 1 a schematic of the core of a DRM reformer unit is given. Open-flame burners provide the huge amount of energy required, which has to be transported from the flame trough the tube wall into the reactor.
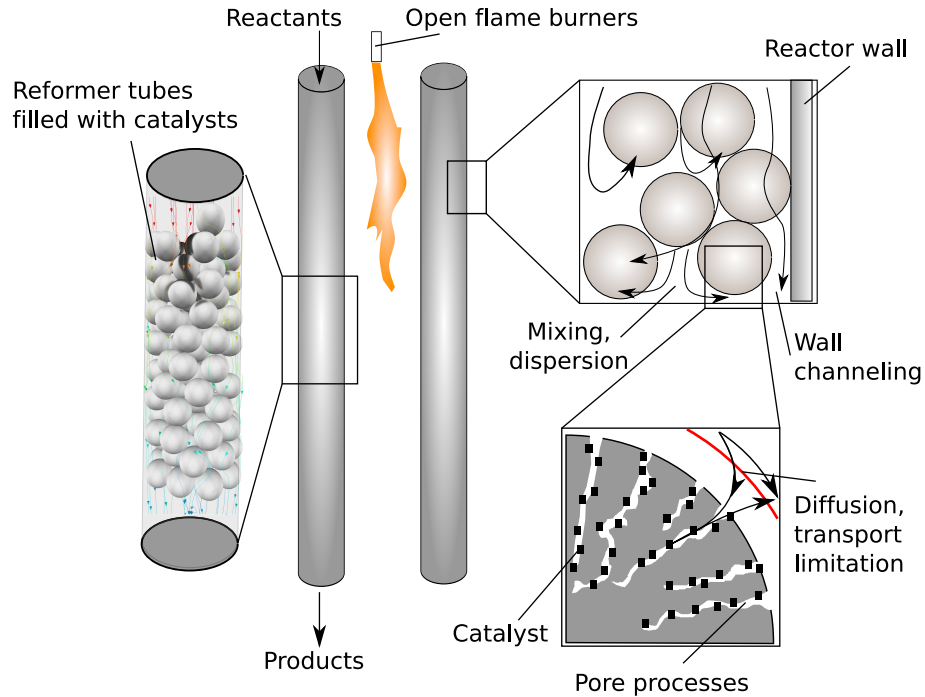


Figure 1: Schematic of reformer tubes filled with catalytic particles.

The choice of tube diameter ($D$) and particle dimensions, i.e., particle diameter $d_P$ and particle length $l_P$, has several constraints. Heat has to be transferred efficiently into the reactor which leads to small tube diameters. A reasonable pressure drop and a high gas throughput constrain the minimum particle diameter. Thus, for highly endothermic reactions a small tube-to-particle-diameter ratio ($N = D/d_P < 10$) is recommended (Dixon, 1997). For these special fixed-bed reactor con-

figurations conventional descriptions based on plug-flow and pseudo-homogeneous models are questionable. Local backflow and stagnation zones occur; channeling in the near-wall region affects the radial heat transfer; radiation plays a significant role at the present temperatures; local kinetics influence local transport phenomena, and vice versa; reaction rates are limited due to film diffusion or pore processes. As a consequence, simplified flow and kinetic models fail to predict severe situations in these multiscale, multi-phenomena reactors. Moreover, the conventional way to investigate catalytic flow reactors, i.e., fixed-bed reactors, foam reactors, monolith reactors, etc., is the examination of inlet and outlet conditions of temperature, velocity and composition of the fluid. The reactor itself is treated, in most cases, as a *black box*. This approach does not shed light on what is happening inside the reactor. Questions remain unanswered like what the formed intermediates look like, what the condition of the catalyst is and which gradients occur.

Over the last decade several researchers have intensively studied heterogeneously catalyzed reactions with in-situ and operando measurement techniques. Theses devices deliver temperature and species profiles or contour plots while the flow reactor is under operation. Horn et al. (2006a) presented a capillary technique with which it is possible to measure temperature and species profiles inside a catalytic foam reactor. The authors investigated the catalytic partial oxidation of methane (CPOX) and were able to determine the transition between the oxidation and reforming zone in their millisecond reactor. Besides capillary techniques, approaches utilizing lasers have been applied more often for catalytic systems.

Besides experimental investigations, numerical models of catalytic flow reactors are becoming more and more popular. This is not only due to the increasing computer power while decreasing costs, but also due to the availability of user friendly commercial and open-access CFD codes. Although numerical models cannot replace well designed experiments, they can enrich the sound understanding, as well as quantify certain phenomena, which are difficult to measure. One of the pioneering works in modeling fixed-bed reactors with CFD was the contribution of Derkx and Dixon (1996). With their short paper on modeling flow between two spheres the idea of resolving the interstitial fluid flow inside a fixed-bed reactor was realized for the first time. The concept is to take into account the actual shape of each individual particle inside the reactor. As a consequence, the fluid flow field is determined by the particles it has to pass by. In the following, this modeling approach is called *particle-resolved CFD simulations* of fixed-bed reactors to emphasis the resolution of the actual bed shape. The advantage is the absence of transport correlations, which are necessary in pseudo-homogeneous or heterogeneous models to describe the transport of momentum, heat and mass. This approach is in line with multiscale modeling, or first-principles approach (Dudukovic, 2009), which pursues to describe entirely the system by theory of the actual phenomena.

The focus of particle-resolved CFD simulations in the past was on pressure drop predictions (Bai et al., 2009) or on describing heat transfer, e.g., Nijemeisland and Dixon (2004) or Dixon (2012). One of the major applications of fixed-bed reactors in chemical engineering is the realization of heterogeneous catalysis. Hence, the logical extension of particle-resolved CFD includes reactions on the particle surface. Several authors used detailed fluid dynamics in combination with pseudo-homogeneous kinetics due to the small number of reaction equations and species (Kuroki et al., 2009; Taskin et al., 2010). However, these kinetics are often limited to a certain range of process

2

parameters and could therefore not be applied to other flow regimes or reactor types (Salciccioli et al., 2011). Especially, the species development inside fixed-bed reactors is often insufficiently reproduced with such kinetics in contrast to the exit concentrations, which was demonstrated by Korup et al. (2011). For a first-principles approach modeling spatially resolved fluid dynamics must be combined with reliable kinetics, i.e., microkinetics. These detailed kinetic models distinguish between adsorption, surface reaction, and desorption.

The aim of this thesis is the rigorous modeling of catalytic fixed-bed reactors on the particle-resolved scale. The modeling consists of several different aspects which can also interact with each other. These aspects, which are shown in Fig. 2, are: morphology of random bed structure, meshing strategies including particle-particle, and wall-particle contact-area modifications, inclusion of appropriate detailed reaction mechanisms (microkinetics), approximation of pore processes, as well as heat transfer mechanisms. In this work these aspects are developed and analyzed critically by comparison with experiments from literature and project partners or correlations.
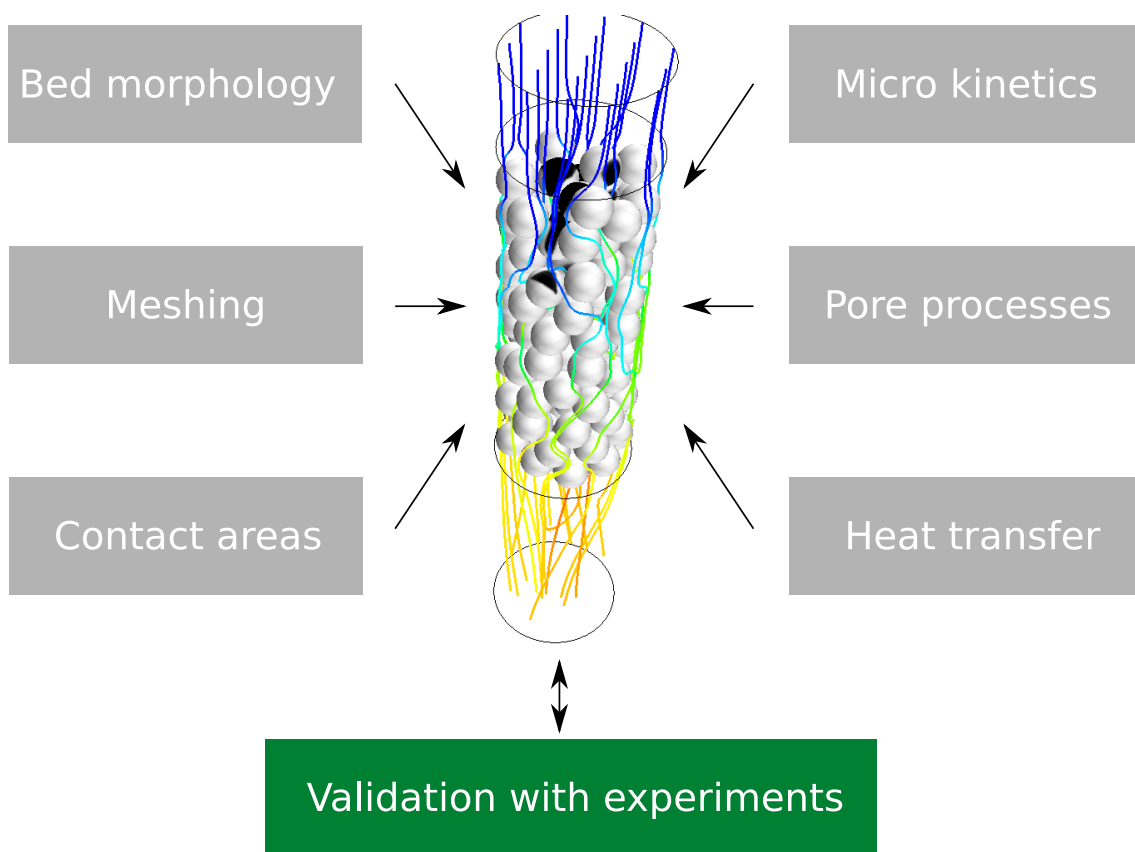


Figure 2: Aspects of particle-resolved CFD simulations of catalytic fixed-bed reactors.

The thesis is incorporated into the cluster of excellence *Unifying concepts of catalysis* (Unicat, EXC 314). In this research cluster scientists have studied catalytic systems on different time and length scales. Mainly methane reforming was on the focus. As a consequence, detailed kinetic data, as well as critical assessments are available. The modeling aspects are investigated by several well designed numerical studies. For each study a brief overview is given of the experimental

setup, as well as of the corresponding CFD setup. For all CFD simulations the commercial CAE software STAR-CCM+ version 9.06 from CD-adapco (CD-adapco, 2014) was used. Three types of flow reactors are studied numerically:

1. Stagnation-flow reactor (SFR) experiments are reproduced to test the feasibility of modeling catalytic flow reactors with adequate kinetics. DRM and oxidation of carbon monoxide is investigated. Transport limitations in washcoat is analyzed by including three pore models into CFD simulations.

2. At the chair of Chemical and Process Engineering at Technische Universität Berlin a work-flow generating automatically representative bed structures was developed by Eppinger et al. (2011). This workflow represents the basis for the rigorous modeling approach of catalytic fixed-bed reactors in this thesis. A short study on morphology and velocity inside fixed-bed reactors is performed. DRM in a small bed of spheres is modeled to get insights into mesh refinement, conjugate heat transfer and inclusion of microkinetics into CFD simulations. Heat transfer without chemical reactions is studied followed by experiments of DRM with Ni catalysts. The influence of contact-area modifications in fixed beds containing non-spherical particles is tested. Finally, a study shows how catalytic fixed-bed reactors of different particle shapes can be explored with particle-resolved CFD simulations.

3. An extension of the particle-resolved approach of packed beds is realized by modeling catalytic foams in a similar manner. A fully automatic workflow (*cat*alytic *F*oam *M*odeler, *catFM*) is developed. With catFM it is possible to model a realistic foam structure ready for CFD simulations without using time consuming image-analysis data. The performance of the modeler is validated against pressure drop data, residence time distribution, and CPOX over rhodium.

Finally, the work presented in this thesis focuses on the question, if CFD is ready to be a design tool for catalytic flow reactors. To answer that question, the different aspects of the modeling approach are analyzed critically. With the help of adequate validation cases strengths and weaknesses of the approach are detected. Recommendations are given regarding meshing strategies, contact-area modifications, as well as including detailed reaction mechanisms. Moreover, an outline is presented for future investigations. Lastly, this investigation highlights that a multi-disciplinary approach combining reactor engineering with reaction engineering is the key for a sound understanding of such complex catalytic systems.

# 2 Literature Review

In this chapter an overview is given over the current status of research in the field of syngas production from marginal gas resources. Among the several reactions suitable dry reforming of methane and catalytic partial oxidation of methane are in the focus of this thesis. Detailed analysis is mandatory for a sound understanding of multiscale reactors in which the above mentioned reactions take place. This can be carried out either with detailed experiments or detailed numerical models. An overview of these two strategies is given with emphasis on particle-resolved CFD simulations of catalytic flow reactors.

## 2.1 Synthesis gas production from marginal gas resources

The global climate change is indisputable and the human contribution is clear. Increased antropogenic greenhouse-gas emissions are the main driver of the observed warming since the mid-20$^{th}$ century (Pachauri et al., 2014). Continued emissions of greenhouse gases will lead to further warming and changes in all aspects of the climate system. Constraining climate change will require serious and sustained reductions of greenhouse-gas emissions (Hartmann et al., 2013). $CO_2$ plays an outstanding role among greenhouse gases. 76% of 2014 greenhouse-gas emissions were $CO_2$ followed by $CH_4$, which had a contribution of 16% (EIA, 2015). Besides consequent $CO_2$ emission reduction, sequestration and storage, and several alternative approaches are available, e.g., algae cultivation with $CO_2$ or biochar, cf. (Hasse, 2013; EASAC, 2013). On the contrary, catalysis and reaction engineering are asked to develop innovative technologies for $CO_2$ utilization, e.g., its conversion to liquid fuels, alcohols, basic chemicals, etc. (Vlachos and Caratzoulas, 2010).
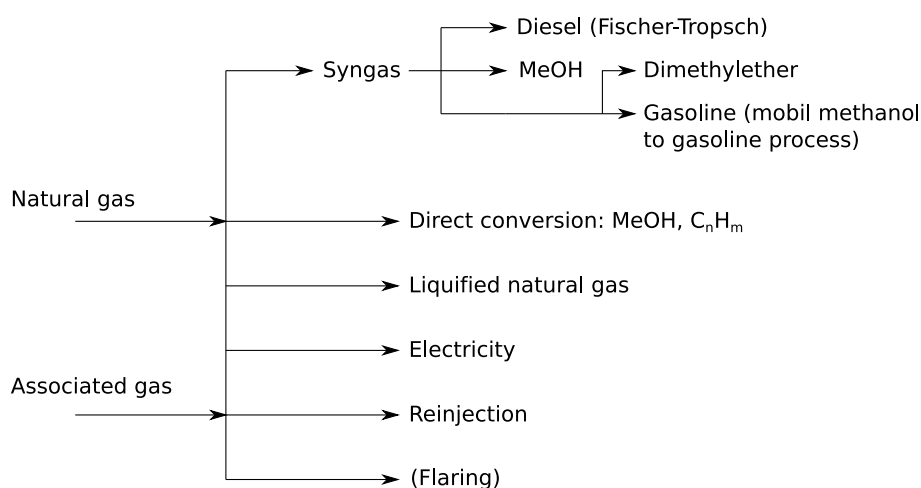


Figure 3: Remote natural gas converion paths. Adapted from Rostrup-Nielsen et al. (2002).

Another important climate gas is natural gas, which is a cheap and widely abundant resource. However, its main components, methane, ethane and propane, are rather chemically inactive. As a consequence, the transformation of natural gas to higher valuable products requires a certain

amount of effort. Over the last thirty years, natural gas has grown in importance, due to a forthcoming oil shortage and climate change issues. Under these circumstances, natural gas is considered as a major feedstock for all kinds of chemical products. Fig. 3 gives an overview over remote natural gas conversion paths. In 2013 the USA was the worldwide largest natural gas producer, see Tab. 1. Natural gas is found mostly far away from areas with high population and present markets for natural gas as fuel. However, recently advanced technologies have provided access to abundant new sources of natural gas. Furthermore, the growth in using unconventional natural gas resources, like shale gas, has amplified this trend. About 3% of produced natural gas is flared, which was approx. 210 billion tons of $CO_2$ in the year 2013 (EIA, 2015). Moreover, much of the produced natural gas is pumped back into the ground (approx. 12%). About 10% of global natural gas is used for the production of chemicals today, including fuel (40%) and feedstock (60%) (EIA, 2015).

Table 1: Natural gas production in 2013 [billion cubic feet] (EIA, 2015)

| Region | Gross production | Vented & flared | Marketed production |
|---|---|---|---|
| North America | 38,101 | 326 | 32,955 |
| Central & South America | 9,345 | 655 | 6,888 |
| Europe | 10,011 | 95 | 10,011 |
| Eurasia | 31,894 | 636 | 30,434 |
| Middle East | 25,802 | 1,156 | 21,727 |
| Africa | 13,106 | 949 | 8,451 |
| Asia & Oceania | 19,222 | 261 | 18,441 |
| Worldwide | 147,481 | 4,078 | 128,907 |

Liquified natural gas (LNG) is the most common form of processing natural gas. However, gas to liquid fuels (GTL) seems to be advantageous over LNG, at least in some cases. The GTL process can be divided into two steps. Firstly, natural gas is converted into syngas, which is a gas mixture of hydrogen and carbon monoxide and a very important intermediate in the chemical industry (Védrine, 2005). Secondly, syngas is converted to synfuel via the Fischer-Tropsch process (Trimm, 2005). Conventional Fischer-Tropsch processing is well established. An overview of kinetics and selectivity of the Fischer-Tropsch synthesis gives van der Laan and Beenackers (1999). An alternative to synfuel is the generation of hydrogen for fuel cells from syngas (Peña et al., 1996). In a typical GTL process approx. 65% of the total cost is associated with syngas production (Trimm, 2005). As a consequence, there is a high interest in improving the syngas process, which can be carried out in different routes. Among these routes several are applied already in industry, and some have not yet been used, see Védrine (2005) for an overview. The three most established routes for syngas production from natural gas are:

1. Steam reforming of methane (SRM)

2. Dry reforming of methane (DRM)

3. Catalytic partial oxidation of methane (CPOX)

SRM is the most common syngas process:

$$CH_4 + H_2O \rightleftharpoons 3H_2 + CO \quad \Delta H^0_{298\,K} = +206\,kJ/mol \tag{2.1}$$
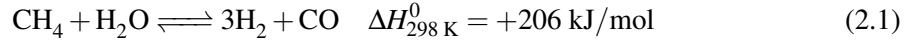
Current industrial catalysts are nickel based. A large amount of heat is required by this highly endothermic reaction, which is generated with open-flame burners pointed at long fixed-bed reactors. Operation temperatures typical for SRM are approx. 1200 K with pressures ranging from 20-40 bar. Although SRM is the most common process path to syngas, it is characterized by three major drawbacks. Superheated steam at high temperature is expensive. The water-gas-shift reaction ($CO+H_2O \rightleftharpoons CO_2+H_2$) produces significant $CO_2$ in the product stream. The $H_2/CO$ ratio is not optimal for downstream processes (Tsang et al., 1995; Rostrup-Nielsen et al., 2002).

In Berlin, the cluster of excellence "Unifying concepts in catalysis" (Unicat) has been studying a wide range of sustainable processes for the conversion of methane and $CO_2$. This thesis was written in the framework of Unicat. Therefore, DRM and CPOX are utilized as test reactions for applying particle-resolved CFD simulations in catalytic flow reactors. In the following DRM and CPOX are presented in more detail. Moreover, appropriate reactors for the two reactions and reactor-modeling strategies are presented.

## 2.2   Dry reforming of methane (DRM)

### 2.2.1   Overview and industrial applications

Dry reforming of methane requires even more energy input than SRM:

$$CH_4 + CO_2 \rightleftharpoons 2H_2 + 2CO \quad \Delta H^0_{298\,K} = +247.3\,kJ/mol \tag{2.2}$$
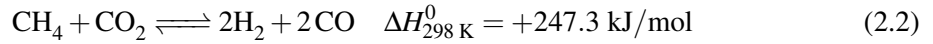
However, the fact that two greenhouse gases, $CH_4$ and $CO_2$, are used as reactants, as well as the advantageously low $H_2/CO$ ratio makes it a promising syngas process. Yet, DRM has some major drawbacks. The endothermic character requires a high energy input. Difficulties of ignition arise at temperatures below 500 °C. In addition, high temperatures are required to reduce coke deposition on the catalyst (Shah and Gardner, 2014). Whereas the first two issues are related to process-operation strategies, the latter one requires a sound understanding of the catalytic system. Hence, the largest obstacles for the industrial use of DRM is to prevent coke formation, which quickly leads to deactivation of the catalyst (Chen et al., 2001; Ginsburg et al., 2005; Guo et al., 2007). Carbon accumulates catalytically on the active sites, which leads to a decline of the reforming reaction rate. In principle, carbon is formed through two reaction pathways during DRM (Shah and Gardner, 2014):

1. $CH_4$ decomposition at temperatures higher than 550 °C

$$CH_4 \longrightarrow C(s) + 2H_2 \quad \Delta H_{1173\,K} = +90\,kJ/mol \tag{2.3}$$
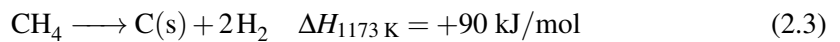
2. CO disproportionation at temperatures lower than 400 °C

$$2CO \longrightarrow C(s) + CO_2 \quad \Delta H_{1173\,K} = -169\,kJ/mol \tag{2.4}$$
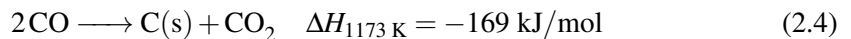
The deposited coke can occur in several forms, which distinguish all in reactivity. Consequently, this prospective process has to be carried out with an appropriate catalyst. In the last decades Nickel-based catalysts and noble metal-supported catalysts (e.g., Rh, Ru, Pd, Pt, Ir) have shown encouraging performances regarding conversion and selectivity (Torniainen et al., 1994; Wang et al., 1996; Guo et al., 2004). Rhodium for example is characterized by its low affinity for carbon formation and its high activity (Rostrup-Nielsen and Hansen, 1993; Bradford and Vannice, 1999). Among the different possible catalysts suitable for DRM nickel dispersed on alumina ($Al_2O_3$) particles represents the most interesting one for the industrial sector. In contrast to noble metal catalysts nickel is dramatically cheaper (27 €/g Pt, 19 €/g Pd, 26 €/g Rh, 0.08 €/g Ni, `http://www.heraeus.com`, 24.11.2015) and still has a relatively high activity. However, the tendency of coking on nickel catalysts is even stronger than for noble metals (Trimm, 1977). On Ni catalysts, there are five different types of carbon from carbon monoxide and hydrocarbons (Bartholomew, 1982):

1. Atomic carbon (dispersed, surface carbide): $C_\alpha$,

2. Polymeric films and filaments (amorphous): $C_\beta$

3. Vermicular whiskers/fibers/filaments (polymeric, amorphous): $C_V$

4. Nickel carbide (bulk): $C_\gamma$

5. graphitic platelets and films (crystalline): $C_C$

Details of coking and coke formation in methane reforming processes can be found in Bartholomew (1982); Rostrup-Nielsen et al. (2002).

To improve the stability of the catalyst and therefore the economical efficiency of DRM, a sound understanding of the reaction mechanism under industrial relevant conditions is necessary. However, this turns out to be difficult with conventional reaction engineering approaches (Olsbye et al., 1997). Solid catalysts are dynamic systems, which adapt to the local temperature, velocity and species surrounding by their geometric, electronic and defect structure. The different aspects of the dynamics of heterogeneous catalysis has been clasified by Ertl (2000) into the following five categories (from microscopic to macroscopic scale):

1. quantum level

2. atomic level

3. nonlinear dynamics

4. continuum description

5. macroscopic kinetics

Due to change of catalyst structure, the kinetics of the catalytic reaction also changes and likewise feed back information to the surrounding temperature and species field. These effects are

almost impossible to cover with conventional Langmuir-Hinshelwood-Hougen-Watson (LHHW) reaction mechanisms. LHHW kinetics lumps the identity and concentration of active centers into pseudo-reaction rates, whereas the surface species concentrations are not accounted for. A rate determining step has to be postulated. However, this determining step can change with position and reaction conditions. In such a case, LHHW kinetics would be valid only for small sections of the reactor. It becomes obvious that LHHW is an insufficient approach for a detailed kinetic investigation of catalytic systems (Salciccioli et al., 2011), and consequently it is not suitable to gain a sound understanding of DRM reactors. An alternative to LHHW kinetics represents the microkinetic modeling of DRM, which distinguishes between adsorption, surface reactions, and desorption.

### 2.2.2   DRM reaction kinetics

Over the last years great effort has been shown to investigate experimentally the reaction mechanism of DRM. Still, kinetics including the dominant reaction path and the rate determining step is discussed controversially and often contradictory. Based on experiments several authors describe methane dissociation and $CH_XOH$ decomposition as rate-determining steps on Ni catalysts (Bradford and Vannice, 1999; Nandini et al., 2006). On the contrary, only the methane dissociation step was determined as rate-determining (Wei and Iglesia, 2004). Furthermore, DRM was analyzed with stationary and transient kinetic methods over a wide range of temperatures on Ni/$\alpha$-Al$_2$O$_3$ catalysts (Cui et al., 2007). The authors claim that at low temperatures the methane dissociation is the rate-determining step, whereas at high temperatures it is the reaction between $CH_X$ and $CO_2$.

Besides experimental investigations microkinetic modeling is a growing tool for detailed examination of heterogeneous catalysts on the molecular level. An overview over the microkinetic approach give Cortright and Dumesic (2001). In the method elementary-like reactions are formulated for adsorption of participating gas phase species, surface reactions, and desorption steps. Its kinetic parameters are based on first-principles, like density functional theory (DFT) or transition state theory (TST) or are gained from detailed experiments. There are several microkinetic models for methane reforming processes available in literature, cf. Mhadeshwar and Vlachos (2007); Maestri et al. (2009); Blaylock et al. (2009); Zhu et al. (2009); Blaylock et al. (2011); Delgado et al. (2015); Fan et al. (2015). The microkinetic model record the identity of the active center, the specific surface concentration of the active center and the energetics of each individual reaction step. Consequently, there is no need for an assumption of the rate determining step. Furthermore, the differential equation of each participating surface and gas phase species is solved. Finally, it is possible to investigate the reaction mechanism in detail under various reaction conditions, e.g., with the help of reaction path analyses. Additionally, a microkinetic simulation delivers the local surface coverage of the catalyst, e.g., atomic surface adsorbed carbon: C*. The asterisk indicates that the species is adsorbed at the catalytic surface. Although atomic carbon is unlikely to be found under real conditions in the reactor the information where C* occurs can gain insights into the interaction between local kinetics and local transport phenomena. Besides all advantages of microkinetic models the determination of the individual kinetic parameters represent a great challenge. Measuring activation energies is a difficult task, especially on surfaces that are close

to real configurations. Often ideal surfaces are investigated neglecting multi-facets and structure defects. Also, for DFT simulations ideal facets are investigated in most of the cases instead of typically occurring multi-faceted surfaces. Still, many studies showed that with DFT-based detailed reaction mechanisms quantitative kinetic insights can be gained.

### 2.2.3   Reactors suitable for DRM

Typical reactor types for endothermic (or exothermic) reactions are catalytic fixed-beds, catalytic foams, catalytic multi-channel reactors, or fluidized-bed reactors. The most common way to carry out heterogeneous catalytic reactions is a fixed-bed reactor. This is mainly due to its simple setup. Randomly distributed catalytic particles are the simplest type of such a reactor, with particle diameters range typically from 2-20 mm (Eigenberger, 2008). Common catalytic particle shapes are spheres, cylinders, one-hole or multi-hole cylinders, or even more sophisticated patterns. The dimension of the pellet is a compromise between a low pressure drop and an optimal heat and mass transfer (Sie and Krishna, 2011). For DRM pellets should be characterized by a high activity, mechanical stability, and guarantee for high gas throughput. This leads to relatively large particles ($\approx$ 20 mm). The endothermic character of DRM demands a high energy input from outside the reactor resulting in a small tube diameter. Large particles in small tubes lead to inhomogenieties of the bed structure and consequently to large gradients in the radial and axial coordinate. In commercially applied SRM the heat input is realized by open-flame burners (Stitt, 2005). Typically, the tube-to-particle-diameter-ratio is small ($N < 7$). Yet, alternative reactor systems have been developed. Najera et al. (2011) for example proposed chemical looping dry reforming of methane as a way to capture and utilize carbon dioxide.

## 2.3   Catalytic partial oxidation of methane (CPOX)

### 2.3.1   Overview and industrial applications

Besides DRM, the catalytic partial oxidation of methane (CPOX) is one of the most recognized alternatives for SRM and DRM. CPOX is slightly exothermic:.

$$CH_4 + \frac{1}{2}O_2 \rightleftharpoons 2H_2 + CO \quad \Delta H^0_{298\,K} = -36\,kJ/mol \tag{2.5}$$
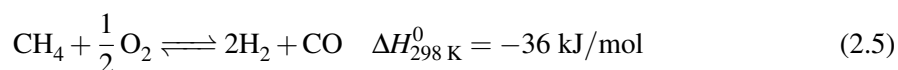
Using an appropriate catalyst even allows autothermal operation, that means no external heat has to be supplied. CPOX also gives lower $H_2$/CO ratios than SRM, which is beneficial for downstream processes. In the 1930s and 1940s CPOX was already investigated (Prettre et al., 1946). However, carbon formation occurred on the metal catalysts, which could not be avoided by increasing the operation temperature, or increasing the $O_2$/$CH_4$ ratio. For that reason, CPOX was nearly banned until the late 1980s. The oil crisis rose the motivation to search for an intensified methane usage. As a consequence, several researchers published their findings since the beginning of the 1990s (Hickman and Schmidt, 1993a,b). An overview from that periode give Tsang et al. (1995). A more recent general review give Zhu et al. (2004). A review emphasising reaction mechanisms over transition metal catalysts give Enger et al. (2008). Many catalysts have been studied, among

which supported Ni and noble metals catalysts showed high activities and $H_2$ and CO yields close to thermodynamic equilibrium (Tsang et al., 1995; Enger et al., 2008). CPOX is already used in industrial applications. Shell for example utilizes CPOX at Bintulu GTL plant in Malaysia and Pearl GTL plant in Qatar. Furthermore, there are several CPOX units in the USA (Shah and Gardner, 2014). Nonetheless, several engineering obstacles have to be overcome. Separation of oxygen from nitrogen and feeding strategies for oxygen are crucial. Additionally, separation technologies for hydrogen ares still under investigation (Enger et al., 2008).

### 2.3.2   CPOX reaction kinetics

The reaction pathway has been discussed intensively over the last decade. There are two main schools of thought about the reaction pathway. The first one claims that the reaction happens in two consecutive zones via primary total oxidation of methane:

$$CH_4 + 2O_2 \longrightarrow CO_2 + 2H_2O \quad \Delta H^0_{298\,K} = -803 \text{ kJ/mol} \tag{2.6}$$
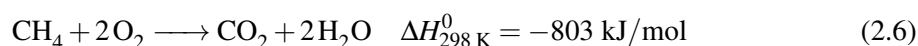
followed by a reforming zone, where SRM (Eq. (2.1)) and DRM (Eq. (2.2)) occur (York et al., 2007). The major argument for this suggestion is the steep temperature gradient observed over the catalyst bed (Schwiedernoch et al., 2003; Horn et al., 2006a; Korup et al., 2013). Furthermore, transient studies showed that there is no direct path from methane to syngas (Buyevskaya et al., 1996). The second school of thought suggests that the reaction mechanism takes place in one direct step from methane to syngas (York et al., 2007).

### 2.3.3   Reactors suitable for CPOX

Many researchers have investigated CPOX in catalytic foams (Hickman and Schmidt, 1993a; Horn et al., 2006a, 2007a; Dalle Nogare et al., 2008; Donazzi et al., 2010; Dalle Nogare et al., 2011), or monolith reactors (Schwiedernoch et al., 2003; Hettel et al., 2013; Diehm et al., 2014; Hettel et al., 2015), rather than fixed-bed reactors (de Smet et al., 2001; Maestri et al., 2005). The reasons can be found in process safety. Hot-spot formation in the exothermic oxidation zone can lead to severe catalyst conditions. Even explosions and runaways at high operation pressures can occur since homogeneous reactions are getting more important at those conditions. As a conclusion, mass and, especially heat transfer characteristics are of paramount importance for the safe operation of a CPOX reactor. Maestri et al. (2005) compared by simulation the performance of three different catalyst supports for the CPOX of methane, i.e., honeycomb, foam and fixed-bed reactor. The authors conclude that the foam catalyst support shows the best performance regarding transport properties, syngas selectivity and pressure drop.

## 2.4   Operando measurement techniques

Over the last two decades many different research groups have investigated catalytic reactors under industrial relevant conditions, i.e., temperature, pressure, feed composition, as well as catalyst shape and reactor setup. These so called *operando* investigations are carried out with special
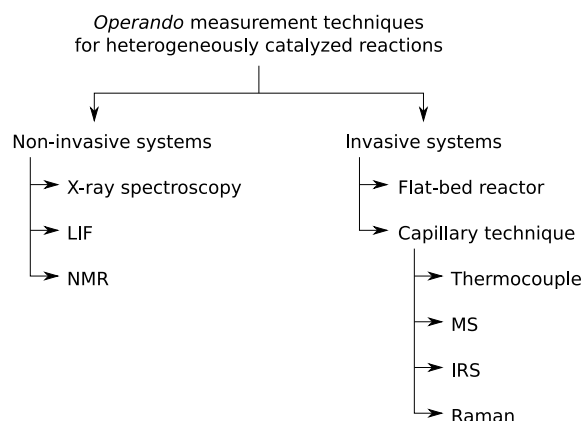
Figure 4: Overview over operando measurement techniques for characterization of heterogeneously catalyzed systems. Laser induced fluorescence (LIF); nuclear magnetic resonance (NMR); mass spectroscopy (MS); infrared spectrometer (IRS).

measurement techniques to gain a better understanding of these complex systems. An overview of current techniques is given in Fig. 4. Recently, Diehm et al. (2014) gave a comprehensive review of the current status of "spatial resolution of species and temperature profiles in catalytic reactors". Operando measurement techniques can be divided into invasive and non-invasive techniques, which are described briefly in the following chapters.

### 2.4.1 Invasive operando measurement techniques

One of the earlier techniques is the so called flat-bed reactor, which mimics catalytic monolith reactors applied in the field of automobile exhaust aftertreament. Single rows are cut out of the multi-channel reactor which are then operated under isothermal conditions (Brinkmeier et al., 2005). Gas samples are taken above the catalytic plate after every four centimeters. With this device it was possible to examine the effect of temperature toward the conversion of lean exhaust gas by conventional three-way catalysts. Lyubovsky et al. (2005) stacked catalytic Microlith screens between which gas samples and thermocouples were placed. In this experimental device the catalytic partial oxidation process was recorded by a resolution of 2 mm. However, for both techniques the catalytic reactor has to be modified from its original form. Hence, other researchers developed systems with which reactions can be studied under more realistic conditions.

One of the most widely used techniques is a capillary that can be moved axially inside the catalytic reactor to measure temperature and species profiles. Horn et al. (2006a,b) developed an in-situ sampling technique for catalytic foams, see Fig. 5 (A). In the center of the foam a hole is drilled in which the capillary (0.65 mm outer diameter) can be moved in axial direction. Gas is sucked at the opening of the capillary and guided to a mass spectrometer. Inside the capillary a thermocouple is inserted with which the axial temperature is recorded. The profiles were measured with a resolution of 0.3175 mm. With this setup mainly syngas production by CPOX over rhodium and platinum was studied (Horn et al., 2006a,b, 2007a,b; Bitsch-Larsen et al., 2008; Dalle Nogare et al., 2008; Michael et al., 2009). Ethane as a reactant was also considered (Michael et al., 2010).
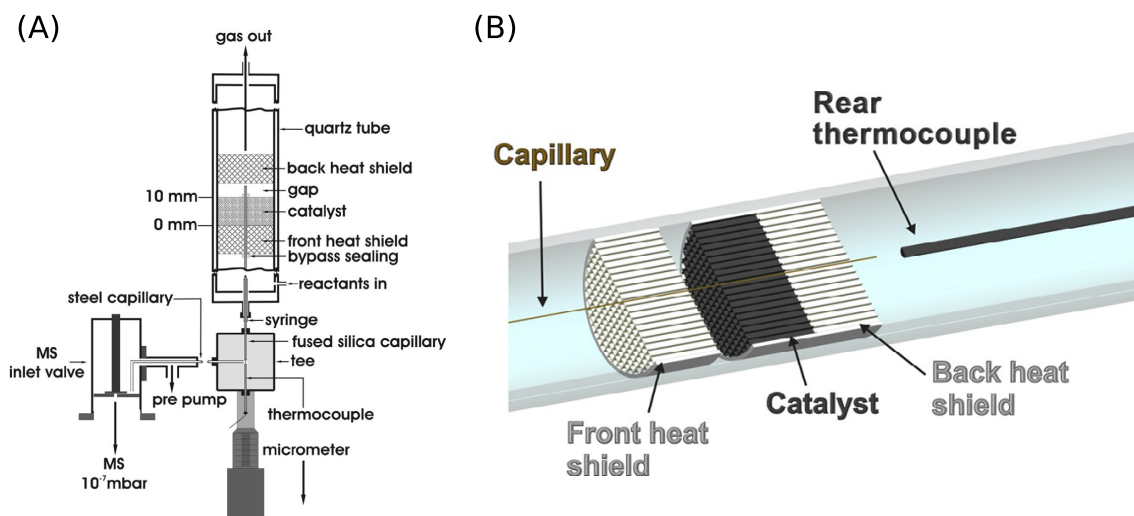
Figure 5: Capillary sampling technique for the investigation of spatial species and temperature profiles inside (A) catalytic foams (taken from Horn et al. (2006b) with permission from Elsevier) and (B) catalytic monoliths (taken from Hettel et al. (2013) with permission from Elsevier).

Horn et al. (2010) improved their reactor which is able to manage industrial relevant conditions, i.e., temperatures up to 1550 K and 45 bar pressure. At the shell of the capillary a sampling orifice was drilled through which gas from the center line of the reactor is transferred to the analysis, i.e., mass spectrometer, gas chromatograph, or high pressure liquid chromatograph. Besides the thermocouple inside the capillary, which measures gas phase temperature, a pyrometer fiber can record the temperature of the solid surface temperature in front of the sampling orifice (Horn et al., 2010). With this improved reactor setup CPOX at elevated pressured (Korup et al., 2011) and high temperature (Korup et al., 2013) was studied. Furthermore, the oxidative dehydrogenation of ethane to ethylene was examined in a fixed-bed reactor by spatial profiles (Geske et al., 2013). A molybdenum trioxide-based ($MoO_3$) catalyst supported on $\gamma$-alumina spheres was used. For the first time the reaction pathway for this process was shown directly. Besides in-situ Raman measurements, ex-situ micro-Raman spectroscopy and X-ray diffraction were applied to gain insights into the mechanistic picture of this reaction.

Honeycomb reactors are used in the aftertreatment of exhaust gases, especially in automobiles. The honeycomb structure is made of alumina on which a washcoat is layered. Into the washcoat the catalyst is dispersed, e.g., Rh, Pt, Ru, which enlarges dramatically the specific surface area. An overview of the current status of exhaust gas aftertreament give Deutschmann and Grunwaldt (2013). In-situ sampling techniques were applied to investigate honeycomb reactors since the work of Donazzi et al. (2011c). A capillary with an inner diameter of 0.34 mm was inserted into one of the catalytic channels (width of 1 mm). The authors measured temperature profiles of the gasphase with a thermocouple and the temperature of the surface with an optical fiber connected with a pyrometer at every 0.3 mm (Donazzi et al., 2011a,b). CPOX of propane, as well as methane, was studied over a Rh/Al$_2$O$_3$ catalyst. With the help of in-situ techniques guidelines were formulated to reduce hotspot formation at the entrance of the honeycomb reactor (Beretta et al., 2011; Livio et al., 2012)

A second group developing the in-situ measurement technique for honeycomb reactors is the Fuels, Engines and Emissions Research Center at Oak Ridge National Laboratory, TN, USA (Choi et al., 2005; Partridge et al., 2006; Choi et al., 2007). The group commercialized their technique *SpaciMS* (`http://hideninc.com/spacims-2/`). Since the probe reduced the cross sectional area inside a single channel, the question arose which influence the capillary has on the measured profiles. Sá et al. (2010) demonstrated with profiles and 3D CFD simulations under different reactor conditions that the SpaciMS technique is minimally invasive.

The Deutschmann group from KIT modified the setup of Donazzi et al. (2011c), see Fig 5 (B). They investigated reaction conditions for the CPOX on methane (Livio et al., 2013; Diehm and Deutschmann, 2014) and CO oxidaton in honycomb reactors (Chan et al., 2014). With the help of detailed 3D CFD simulations the impact of the probe was analyzed critically for CPOX of methane (Hettel et al., 2013, 2015). In contrast to Sá et al. (2010) the authors observed that depending on the position of the probe the impact on gas flux and hence on concentration profiles can be dramatic. In a worst case situation where the capillary is located in central position and is moved throughout the entire monolith the residence time in the channel is modified by a factor of 2. This modification can have a strong influence on conversion (up to 30%), which was demonstrated with CFD simulations (Hettel et al., 2013, 2015). However, these results were criticized and led to a scientific disputation, cf. Goguet et al. (2014) and Hettel et al. (2014). Furthermore, the Harold group from University of Houston recently investigated honeycomb reactors for the complete oxidation of methane on Pt with in-situ measurement techniques but did not identify a noteworthy impact of the probe (Nguyen et al., 2015a,b).

### 2.4.2 Non-invasive operando measurement techniques

Invasive in-situ measurement techniques can have a noticeable impact on the reactor performance itself, as was stated above. As a consequence, researchers have developed non-invasive in-situ measurement techniques.

Besides X-ray absorption spectroscopy methods (Grunwaldt et al., 2006), laser-induced fluorescence (LIF) is an interesting tool to investigate the gasphase concentration near reacting surfaces. However, the reactors have to be optically accessible, which determines substantially its design. Mantzaras (2013) gives an overview of his group's work over the last years. The group developed an optically accessible channel reactor, where LIF and 1D Raman spectroscopy are applied Reinke et al. (2002). Concentrations of trace species and stable gasphase species can be measured. Furthermore, thermocouples quantify temperature profiles along the catalytic channel. Fuel-lean combustion of $CH_4$, $C_3H_8$ and $H_2$ over polycrystalline platinum, and hydrogen combustion over Pt was investigated with this measurement technique (Mantzaras, 2013). At KIT Zellner et al. (2015) developed a 2D LIF spectroscopy to explore the catalytic reduction of NO by hydrogen toward ammonia over a diesel oxidation catalyst, see Fig. 6. With this setup it was possible to detect two-dimensional concentration maps of conversion-relevant species in the gasphase above the $Pt/Al_2O_3$ catalyst. This technique enables the direct comparison with CFD simulations and furthermore, has the potential to investigate experimentally the interactions between chemical kinetics and transport processes on a very detailed basis.
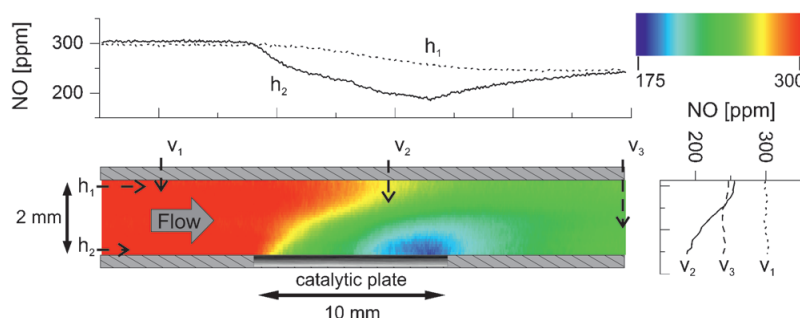
Figure 6: Measured concentration contour over catalytic plate with LIF. Reprinted from Zellner et al. (2015) with permission from John Wiley and Sons.

In contrast to methods that rely on optical access, nuclear magnetic resonance (NMR) techniques, widely used for medical and biomedical applications, can be applied in optically opaque reactors in chemical engineering Stapf and Han (2006). NMR was recently used to study the ethylene hydrogenation reaction over $Pt/Al_2O_3$ (Ulpts et al., 2015). The chemical composition was spatially mapped in an NMR-compatible fixed-bed reactor.

## 2.5   Fixed-bed reactors with low tube-to-particle-diameter ratio

Fixed-bed reactors with small tube-to-particle-diameter ratio ($N$) are widely used for highly exothermic or endothermic reactions. In Fig. 7 four randomly packed beds of small $N$ are shown. Modeling fixed-bed reactors with $N < 16$ with conventional approaches, i.e., pseudo-homogeneous and power-law kinetics, can lead to erroneous predictions of heat and mass transport. This might result in severe situations inside the bed provoking catalyst deactivation or sintering, thermal hot spots, or damage of the reactor tubes (Dixon, 1997; Dixon et al., 2006). The reason for the failure in description is the dominance of local effects caused by bed inhomogeneity. Wall effects, channeling, local backflow, and flow separation result in axial, as well as radial gradients in the local velocity, temperature and concentration fields. The local velocity field is the main driver of the transport phenomena inside fixed-beds since they are mainly operated in the transient or turbulent regime. Local flow was examined experimentally in the interstitial space between particles by using particle image velocimetry (PIV) (Hassan, 2008) or by magnetic resonance imaging (Sains et al., 2005; Yuen et al., 2003). Moreover, numerical simulations of the interstitial flow, which is determined by the actual shape of the particles, can gain important insights.

In the mid 1990s the work by Derkx and Dixon (1996) was the initialization of the *particle-resolved* approach for simulating fixed-bed reactors with CFD. In the Appendix Tab. 25 summarizes in chronological order the most important developments in this field of research. In the table the investigated particle shape, numbers of particles, tube-to-particle-diameter ratio, Reynolds number $Re_p$, bed generation method, as well as modifications of contact areas are given. Since the earliest works, the major difficulty of simulating particle-resolved fixed-bed reactors has been the automatic generation of a realistic bed. Modifications of the contact regions between particles and between particles and the reactor wall is another crucial step. In this section, firstly a
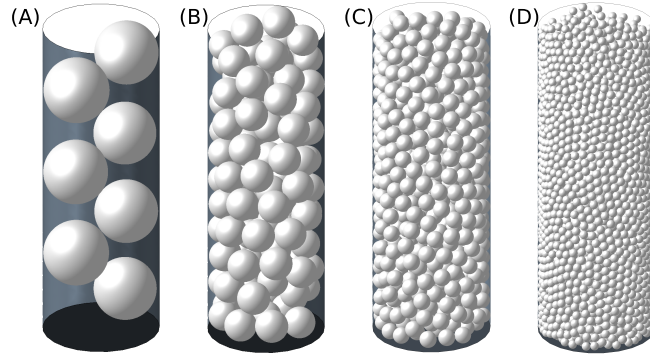
Figure 7: Randomly packed beds of spheres. (A) $N = 1.8$, (B) $N = 4$, (C) $N = 8$, (D) $N = 16$

short survey of randomly packed-bed generation is given. Secondly, the modifications of contact areas will be reviewed, followed by an overview of flow characteristics and turbulence modeling in packed beds. Finally, main findings of detailed CFD simulations including heat transfer and catalytic reactions are summarized.

### 2.5.1 Fixed-bed geometry generation

Direct imaging of real packed beds deliver the most precise geometrical data. By applying methods like X-ray computerized tomography (Caulkin et al., 2009) or magnetic resonance imaging (Sederman et al., 2001; Baker et al., 2011) such direct geometric generation is possible. However, the process is time consuming, considerable complex and limited to the scanned geometry. Consequently, researchers have been developing model-based geometry-generation techniques. In Fig. 8 the main configurations of particle-resolved CFD simulations of packed beds are shown. In the following the main strategies are summarized.
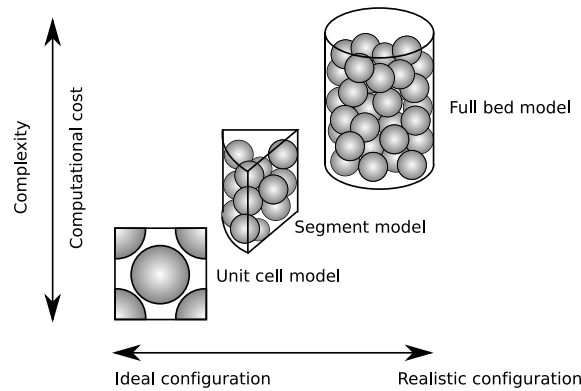


Figure 8: Main configurations for particle-resolved fixed-bed CFD simulations.

CFD simulations of unit cells, i.e., defined cubic crystal arrangements, have been used widely to study flow behavior or to test turbulence models (Gunjal et al., 2005; Shams et al., 2012; Bu et al., 2014). Simple cubic, face-centered cubic (FCC), or body-centered cubic (BCC) geometries were

examined. However, the linkage between these idealized structures and a realistic packed bed is difficult. Still, important studies can be conducted in theses structures like data for validation of different turbulence modeling approaches (Shams et al., 2012).

In the past, structured packed beds with low $N$ have been studied intensively by several authors, like Nijemeisland and Dixon (2001); Calis et al. (2001); Guardo et al. (2004). The position of each particle can be obtained by simple geometrical considerations. Besides very low $N$ beds, these structures are not likely to occur in real configurations. For that reason, strategies resulting in a randomly packed bed are more interesting but also more complex. Monte Carlo methods have been applied in an early stage of particle-resolved fixed-bed simulations (Zeiser et al., 2001; Freund et al., 2003, 2005; Atmakidis and Kenig, 2009; Caulkin et al., 2009; Baker and Tabor, 2010). The basic idea is to place spherical particles randomly into the desired container. Then, the agglomeration is compressed by rearranging the particles with an increased probability into the direction of gravity (Soppe, 1990). A similar approach was presented by Salvat et al. (2005), called *soft sphere algorithm*. Randomly placed particles are allowed to overlap. In a second step force balances are introduced that shift the particles to their final position. This algorithm was applied among others by Dixon et al. (2012b) and Behnam et al. (2013).

The discrete element method (DEM), introduced by Cundall and Strack (1979), was applied by many authors to generate randomly packed beds, e.g., (Ookawara et al., 2007; Bai et al., 2009; Augier et al., 2010; Eppinger et al., 2011; Zobel et al., 2012; Caulkin et al., 2015). DEM is based on the following procedure at every time step: the forces acting on each individual particle are evaluated; Newton's equations of motion are solved; the velocity and position of each particle is updated. Although the early model was formulated for individual spheres, nowadays so called composite particles can be used. The original geometry is approximated by a finite number of spheres, which do not change their position.

Recently, Boccardo et al. (2015) applied the open-source software Blender, that is mainly used for creating animated films, visual effects, etc. (Blender-Foundation, 2015), to mimic the filling of a container with differently shaped particles. The obtained results look promising since any kind of shape can be realized. However, the physics behind Blender are questionable or at least unclear.

### 2.5.2   Contact-area modifications

In reality, randomly packed particles inside a tube touch their neighboring particles or the tube wall. Between spherical particles contact points occur. Contrarily, non-spherical particles stay in contact with other particles or the wall with contact points, lines, or areas. Only few authors stated to apply three-dimensional CFD in particle-resolved fixed-beds without editing the actual particle shape. Magnico (2003) used a fine structured mesh for direct numerical simulations of low $Re_p < 80$, which he claims "avoids contact point problems". However, the interstitial flow between 326-620 particles was discretized only by 9.6-17.7 million cells. According to the author mesh independence was not achieved.

Other authors admitted that contact areas lead to difficulties of numerical convergence. As a consequence, several strategies were established to modify contact areas. The majority of particle-

resolved CFD simulations were carried out in beds of spherical particles. Hence, contact point modifications were investigated. Until now, four distinct contact area modifications have been applied to avoid low quality cells in the proximity of these contact areas: *gaps*, *overlaps*, *bridges*, and *caps*. The wording was introduced by Dixon et al. (2013b). These four methods can be further classified as global methods (gaps and overlaps) and local methods (bridges and caps).
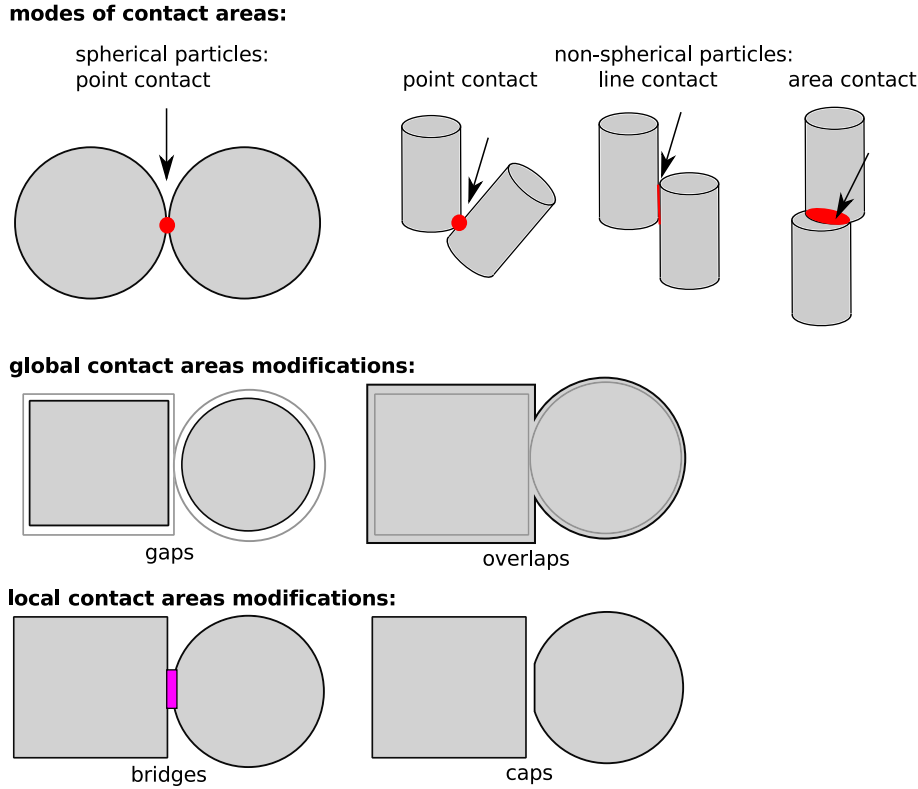


Figure 9: Modes of contact regions in packed beds and modification strategies.

Fig. 9 illustrates the four contact point modifications, with the resulting geometrical modifications enlarged for clarity. The first numerical study of a fixed bed resolving the actual shape of the particles was Derkx and Dixon (1996). The authors studied the fluid flow around three spheres at moderate Reynolds numbers ($Re_\mathrm{p} = 25 - 101$). The three spheres did not touch each other to avoid cells with low quality. A follow-up of this work was the study by Logtenberg and Dixon (1998), where eight spheres were studied. Again, contact point modification was not applied since the spheres did not touch. In contrast, Logtenberg et al. (1999) described for the first time a section of a fixed-bed with touching spheres. In proximity of the touching points the mesh was refined to avoid bad cells. The fixed-bed reactor contained 10 spheres. The first work describing a global contact-point modification was presented by Nijemeisland and Dixon (2001). The authors shrank the size of each of the 44 spheres by 1%. This contact point modification was later called the *gaps method*, see Fig. 9. Until now, this method was used by many authors, where the shrinking value can range between 0.5% (Klöker et al., 2004) and 2% (Augier et al., 2010). The opposite of the global gaps method is enlarging each particle by a certain amount. Guardo et al. (2004) expanded each of the 44 spheres by up to 1%. The spheres were arranged in a structured manner with

$N = 3.9$, and flows with $Re_\mathrm{p}$ up to 912 were studied (Guardo et al., 2005). This global expansion method is called the *overlaps method*, see Fig. 9. Several other authors applied the method, e.g., Boccardo et al. (2015). However, the global methods manipulate the entire bed structure in a drastic way. Concerning overall porosity, global contact point modification lead to an error of approx. 4% for the 99% gaps and 101% overlaps size (Dixon et al., 2013b). But also pressure drop is affected. Dixon et al. (2013b) elaborated a rule of thumb, that 1% change in porosity leads to a 3% deviation of pressure drop.

Under theses circumstances, local modifications have been considered by other researchers. The so called *bridges method* was elaborated by Ookawara et al. (2007) and Kuroki et al. (2009) to calculate pressure drop and heat transfer inside a packed bed, see Fig. 9. The authors connected neighboring spherical particles by placing small cylinders in the contact area. Although the radius of the connecting cylinders was not mentioned, it can be estimated from figures by approx. $d_\mathrm{p}/8$. The authors claimed that this local modification did not influence significantly the macroporous flow properties over the studied range of flow rate ($1 \leq Re_\mathrm{p} \leq 1000$). For heat transfer problems, the thermal conductivity of the bridges can be set independently from the solid and the gas phase. For spherical particles Dixon et al. (2013b) suggest that the thermal conductivity depends on the distance from the particle taking the Smoluchowski effect into account. The counterpart of the bridges method is the so called *caps method*, see Fig. 9. Cheng et al. (2010) was one of the first authors presenting this method. They decreased manually the distance between touching nodes of the surface mesh. Eppinger et al. (2011) used a more elaborated workflow, where the geometry is manipulated dependent on surface proximity. Surfaces close to the touching point are flattened resulting in a gap with a specific width. The authors achieved reasonable agreements between experimental results and predictions of local porosity, and velocity fields, as well as pressure drop.

Only few researchers have compared different contact point modifications and their effect toward pressure drop, velocity, and temperature fields. Dixon et al. (2013b) investigated two touching spheres with CFD regarding drag coefficient and heat flow for the four contact point modifications for a wide range of flow rates ($500 \leq Re_\mathrm{p} \leq 10,000$). They conclude that global methods result in erroneous drag coefficients. Local methods give much better results. The bridges method is to be preferred for heat transfer problems with cylinder radii of $0.05 \leq r/d_\mathrm{p} \leq 0.1$. Moreover, Bu et al. (2014) compared the four modifications in different forms of unit cell configurations, i.e., simple cubic, BCC and FCC. Flow and heat characteristics have been investigated for flow rates up to $Re_\mathrm{p} = 3,000$. The authors suggest to use the bridges method with cylinder radii of $0.08 \leq r/d_\mathrm{p} \leq 0.1$. The results are in line with Dixon et al. (2013b).

Besides finite volume methods for particle-resolved simulations of fixed-beds, Lattice-Boltzmann methods have been developed by Zeiser et al. (2001). This method was further developed by Freund et al. (2003, 2005). Although the method showed encouraging results, it has not been followed up since the work of Freund et al. (2005).

### 2.5.3   Modeling flow regimes in fixed-bed reactors

Knowing the onset of transition from laminar to turbulent flow is of outstanding interest for engineering aspects. In some simple configurations there exists a critical velocity, where the transition occur. In pipe flow with the help of the dimensionless Reynolds number ($Re = v_{in} \cdot D/\nu$, with $D$ being the pipe diameter) this transition happens at $2040 \pm 10$ (Avila et al., 2011). However, in several textbooks this critical Reynolds number can vary from 1700-2300 (Eckhardt, 2009). Whereas in empty pipes the transition can be determined straightforward, the situation in packed beds is much more complex. The transition occurs over a wide range of $Re$, which is furthermore dependent on the type of particle and the distance from the entrance. In packed beds the Reynolds number is mostly related to the superficial velocity $v_{in}$ and the particle diameter $d_p$: $Re_p = v_{in} \cdot d_p/\nu$.

Dixon et al. (2006) give a comprehensive overview of early measurements and findings of flow inside packed beds which reach back to the 1960s using hot-wire anemometry. Different particle shapes and tube-to-particle-diameter ratios have been investigated. Transition was observed at $Re_p \approx 150$. Dybbs and Edwards (1984) summarize results of laser anemometry and flow visualization studies of flow in porous structures. Plexiglas spheres in a hexagonal packing and glass, as well as plexiglas rods aligned in a complex, fixed three-dimensional geometry was chosen as the porous media. Water, and three different oils were tested. A wide range of velocities were studied, i.e., $0.16 \leq Re_p \leq 700$. Four distinct flow regimes were observed (Dybbs and Edwards, 1984):

1. $Re_p \leq 1$: Darcy or creeping flow. Viscous forces are dominant. The velocity distribution is determined by the particle shape. At $Re_p = 1$ boundary layers begin to build up.

2. $1 \leq Re_p \leq 10$: Steady laminar inertial flow regime. The boundary layers become more pronounced and an "inertial core" appears. The pressure drop depends non-linearly on flow rate.

3. $150 \leq Re_p \leq 300$: Unsteady laminar flow regime. Laminar wake oscillations in the interstitial region occur. Traveling waves are the result with distinct periods, amplitudes and growth rates. In this flow regime, these oscillations exhibit preferred frequencies that seem to correspond to specific growth rates.

4. $Re_p > 300$: Highly unsteady and chaotic flow regime. Turbulent flow is qualitatively resembled.

This generalized separation of flow characteristics inside packed beds have been accepted, besides the onset of transition (Dixon et al., 2006). Recently, Patil and Liburdy (2013) studied turbulent flow characteristics in a randomly packed bed with the help of PIV measurements. The transient flow field was examined in different pores throughout the bed. The Reynolds number, which was based on the hydraulic bed diameter, was varied from 418 to 3,964. The authors observed that at a certain Reynolds number ($Re = 2800$) the turbulent measures all collapse. The flow is then independent of the pore shape. However, at lower Reynolds numbers flow characteristics can differ largely from pore to pore, especially when strong recirculation zones or jet-like regions are present.

Under these circumstances, the choice of an appropriate turbulence model in CFD simulations is not explicit. Some early CFD studies included different Reynolds-averaged Navier-Stokes (RANS) turbulence models. For example, Guardo et al. (2005) compared Spalart-Allmaras turbulence model with the $k-\varepsilon$ family and $k-\omega$ turbulence model in terms of pressure drop and heat transfer parameters. The authors conclude that the factors of the two-equation models are probably not suitable to match the flow inside packed beds. As a consequence, the Spalart-Allmaras turbulence model is suggested to be used in fixed-bed CFD. More recently, Dixon et al. (2011) investigated the different RANS turbulence models on a single sphere in terms of drag coefficient and heat transfer Nusselt number for flow rates between $400 < Re_{\mathrm{p}} < 20,000$. As a reference case Large-Eddy simulations (LES) were carried out, which showed good agreement with correlations from literature. However, the small time step and fine mesh required are unpractical for entire bed simulations. The authors suggest using the shear-stress transport (SST) $k-\omega$ turbulence model, that is capable to predict heat transfer accurately (Dixon et al., 2011). In addition, Shams and co-workers have published a series of particle-resolved CFD simulations of pebble-bed reactors (Shams et al., 2012, 2013b,a, 2014). The idea is to provide detailed results of momentum and heat transport inside a packed bed by LES. With this database it will be possible to validate low order (one, and two-equation) turbulence modeling approaches (Shams et al., 2014).

### 2.5.4   Pressure drop

The pressure drop in a fixed-bed reactor is often a crucial parameter, since it designates the necessary energy for pumps and compressors. The dimensionless pressure drop can be written in the form:

$$\frac{\Delta p}{L} = f_f \frac{\rho_{\mathrm{f}} \cdot v_{\mathrm{in}}^2}{d_{\mathrm{p}}} \tag{2.7}$$

with $L$ as the bed height, $f_f$ is the friction factor, $\rho_{\mathrm{f}}$ the fluid density, $v_{\mathrm{in}}$ is superficial velocity, and $d_{\mathrm{p}}$ is the particle diameter. Note that for disperse particles instead of $d_{\mathrm{p}}$ often the Sauter diameter $d_{32}$ is used. The Ergun equation describes the pressure drop adequately for infinite packed beds (Ergun, 1952):

$$f_f = \frac{(1-\bar{\varepsilon})}{\bar{\varepsilon}^3} \left( 150 \frac{(1-\bar{\varepsilon})}{Re_{\mathrm{p}}} + 1.75 \right) \tag{2.8}$$

with $\bar{\varepsilon}$ as the mean bed porosity and the Reynolds number based on the particle diameter $Re_{\mathrm{p}} = v_{\mathrm{in}} \rho d_{\mathrm{p}} / \mu$. The Ergun equation only takes into account frictional losses due to the packing. However, for $N = D/d_{\mathrm{p}} < 50$, frictional losses from the wall of the tube have a significant effect on the pressure drop. Mehta and Hawley (1969) presented a corrected friction factor based on the Ergun equation, which considers both frictional losses from the wall and the packing:

$$f_f = \frac{(1-\bar{\varepsilon})}{\bar{\varepsilon}^3} \left( 1 + \frac{2}{3 \cdot N(1-\bar{\varepsilon})} \right)^2 \left[ 150 \frac{(1-\bar{\varepsilon})}{Re_{\mathrm{p}}} + \frac{1.75}{\left( 1 + \frac{2}{3 \cdot N(1-\bar{\varepsilon})} \right)} \right] \tag{2.9}$$

The equation was derived for tubes filled with beads uniform in size of different diameters resulting in $7 < N < 91$. Eisfeld and Schnitzlein (2001) analyzed pressure data of more than 20 studies in

low $N$ fixed beds of different particle shapes. The authors fitted the coefficients of Reichelt's equation (Reichelt, 1972) to that database, reading:

$$f_f = \frac{K_1 A_w^2}{Re_p} \frac{(1 - \bar{\varepsilon})^2}{\bar{\varepsilon}^3} + \frac{A_w}{B_w} \frac{1 - \bar{\varepsilon}}{\bar{\varepsilon}^3} \tag{2.10}$$

with the coefficients $A_w$ and $B_w$:

$$A_w = 1 + \frac{2}{3 \cdot N \cdot (1 - \bar{\varepsilon})} \tag{2.11}$$

$$B_w = \left[ k_1 \cdot \left( \frac{1}{N} \right)^2 + k_2 \right]^2 \tag{2.12}$$

The fitted coefficients for Eq. (2.10) $K_1, k_1$, and $k_2$ are shown in Tab 2. In Fig. 10 the ratio of friction factor from either Eq. (2.10) or Eq. (2.9) to the friction factor from the Ergun equation is plotted against $Re_p$. Different tube-to-particle-diameter ratios are shown. The equation of Mehta and Hawley predicts friction factor ratios larger unity over the entire $Re_p$ range. On the contrary, the equation of Eisfeld and Schnitzlein shows a transition from ratios above unity to ratios below unity at $Re_p$ that depends on $N$. The Eisfeld equation leads to the conclusion that the Ergun equation underestimates the pressure drop for packed beds of cylinders for $Re_p < 300$. For $N < 4$ and $Re_p > 400$ the Ergun equation overestimates the pressure drop.

Table 2: Coefficients for friction coefficient Eq. (2.10) (Eisfeld and Schnitzlein, 2001)

| Particle shape | Coefficients | | |
|---|---|---|---|
| | $K_1$ | $k_1$ | $k_2$ |
| Spheres | 154 | 1.15 | 0.87 |
| Cylinders | 190 | 2.00 | 0.77 |
| All particles | 155 | 1.42 | 0.83 |

### 2.5.5  Heat transfer and catalytic reactions

Designing a catalytic fixed-bed reactor requires an adequate description of both the reaction kinetics and the transport of heat and mass. In Fig. 11 different mechanisms for heat transfer are illustrated schematically in a fixed bed of spheres. Depending on process factors like flow rate, temperature, and fluid properties certain mechanisms dominate.

The radial transport process of heat is of paramount interest, since it is the direction of heating or cooling the reactor. Especially, for low $N$ fixed beds an accurate description of the transport has caused many problems. Dixon (2012) reviews the state-of-the-art in modeling radial heat transfer in fixed-bed catalytic reactors. The most common formulation is the $k_r - h_w$-model, which is based on the classical pseudo-homogeneous two-dimensional (radial and axial direction) axially dispersed plug flow (ADPF) model. In Europe this model is called "$\alpha_w$" model. The boundary condition at the wall ($r = R$) yields:
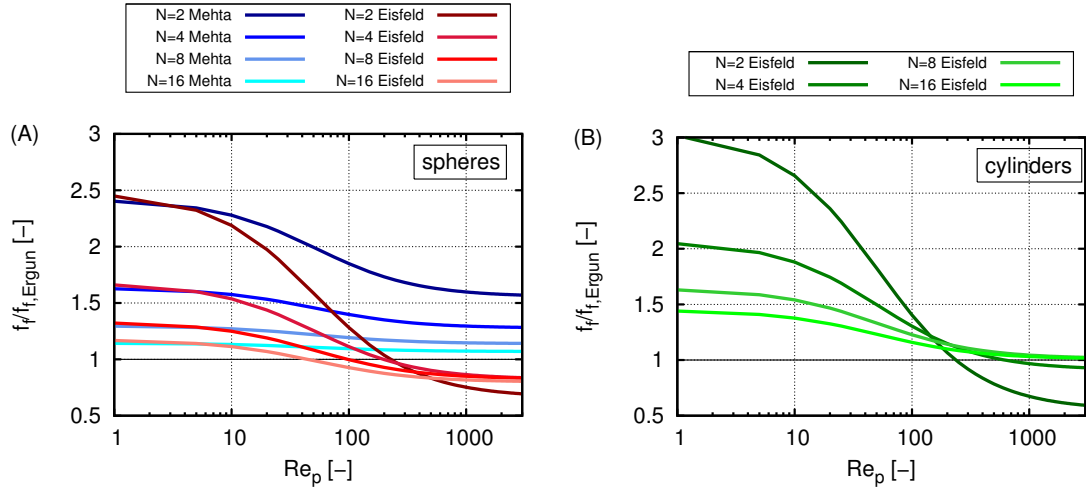
Figure 10: Ratio of friction factor from correlations and Ergun equation over $Re_p$ for (A) spheres and (B) cylinders.

$$-k_r \frac{\partial T}{\partial r} = h_w(T - T_w) \tag{2.13}$$

where $k_r$ is the constant effective radial thermal conductivity, $T$ is temperature, $T_w$ is wall temperature, $r$ is the radial coordinate, and $h_w$ represents the wall heat transfer coefficient. This model shows a temperature 'jump' at the wall, due to $h_w$ (Dixon, 2012). In most cases, $h_w$ is expressed by the wall Nusselt number $Nu_w$:

$$Nu_w = h_w d_p / k_f \tag{2.14}$$

where $k_f$ is the thermal conductivity of the fluid.

At the wall, the global heat-transfer rate can be calculated by:

$$\dot{Q}_w = A_w h_w \Delta T_{\log} \tag{2.15}$$

with $A_w$ as the heat transfer area of the wall and $\Delta T_{\log}$ as the logarithmic temperature difference. For a constant wall temperature it can be written as:

$$\Delta T_{\log} = \frac{(T_w - T_{inlet}) - (T_w - T_{outlet})}{\ln\left(\frac{T_w - T_{inlet}}{T_w - T_{outlet}}\right)} \tag{2.16}$$

Several formulations for $Nu_w$ are available in literature. However, the most recommended form is the mechanistic model. $Nu_w$ represents the sum of the contribution of the decreased solid phase conduction $Nu_{w,0}$ and the contribution of the decreased lateral convective heat transfer near the wall $a \cdot Pr^b Re^c$. Martin and Nilles (1993) formulated $Nu_w$ as:

$$Nu_w = Nu_{w,0} + 0.19 Pr^{1/3} Re_p^{3/4} \tag{2.17}$$
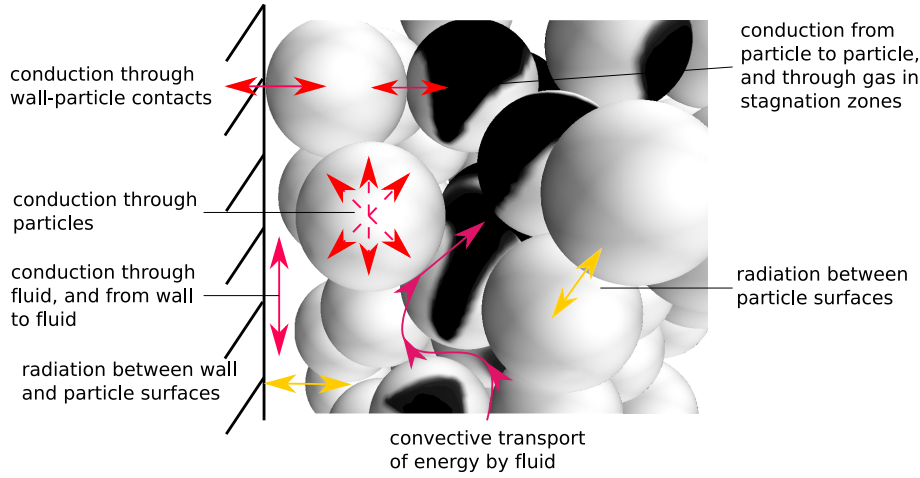
Figure 11: Different mechanisms for heat transfer in a fixed-bed of particles.

where the Prandtl number is defined as $Pr = c_p \mu / k$. Dixon (2012) recommends to calculate $Nu_{w,0}$ with:

$$Nu_{w,0} = \left(1.3 + \frac{5}{N}\right)\left(\frac{k_r^0}{k_f}\right) \tag{2.18}$$

with $N = d_p/D$, and $k_r^0$ is the thermal conductivity of the bed, which can be calculated by the Zehner-Schlünder Eq., see e.g., Dixon et al. (2013a). In literature, there are more formulations found especially for the decreased lateral convective heat transfer near the wall. A critical review on different models and recommendations gives Dixon (2012). The author concludes that the $k_r - h_w$-model shows likely an error range of 20-30%. Under these circumstances, particle-resolved CFD simulations of packed beds can shed light on the radial heat transfer, especially for low $N$ beds. Several authors investigated particle-fluid heat transfer with detailed CFD (Romkes et al., 2003; Guardo et al., 2004; Lee et al., 2007). Magnico (2009) performed transient direct numerical simulation of heat transfer in a bed with 326 and 620 particles, respectively. The author found reasonable agreement for $h_w$ with the correlation of Martin and Nilles (1993). Full-bed CFD simulations with an accompanying experimental measurement are the exception. Dixon et al. (2012b) simulated a full bed of 1,000 and 1,250 spheres including heat transfer through the particles. Radial temperatures were measured at the outlet of the packed bed. The agreement between experiment and simulations is reasonable. Still, the temperature inside the packed bed, where the steepest gradients occur, was not examined.

Only few authors have coupled fluid dynamics of fixed beds with catalytic reactions (Kuroki et al., 2009; Taskin et al., 2010; Dixon et al., 2012a). That means the already complex equation system will be extended by species conservation equations. Several authors used pseudo-homogeneous kinetics in combination with detailed fluid dynamics, due to the small number of additional equations accounting for the chemical kinetics. Nonetheless, these kinetics are often limited to a certain range of process parameters and could therefore not be applied to other flow regimes or reactor types (Salciccioli et al., 2011). Especially the species development inside fixed-bed reactors are often insufficiently reproduced with such kinetics in contrast to the exit concentrations, which was demonstrated by Korup et al. (2011). As a consequence, spatially resolved fluid dynamics must be

combined with reliable kinetics, i.e., detailed reaction mechanisms (also known as microkinetics). As a conclusion, the combination of a first-principle approach at different scales, i.e., detailed reaction mechanism at the catalyst scale and full Navier-Stokes equations at the reactor scale, helps to obtain a fundamental understanding of chemical reactors.

## 2.6   Catalytic open-cell foam reactors

The application of ceramic foams as catalyst carriers represents a promising alternative to fixed beds or structured packings, as the number of scientific publications over the last four decades shows (see Fig. 12). Ceramic foams are characterized by their low specific pressure drop, high
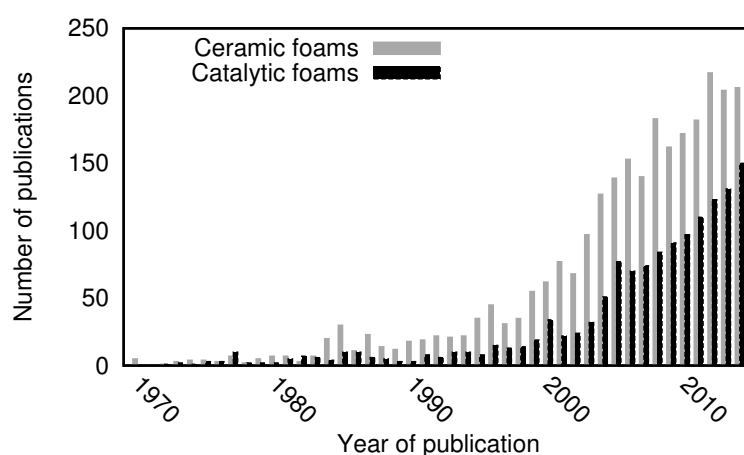


Figure 12: Number of publications per year searching article titles, abstracts and article keywords with "ceramic and foam" and "catalytic foam or catalysis and foam" in the bibliographic database Scopus (Scopus, 2015)

mechanical stability at relatively low specific weight, enhanced radial transport, as well as a high geometric surface area. They can be found in a wide range of technical apparatuses, such as molten metal filters, burner enhancers, soot filters for diesel engine exhausts, and biomedical devices (Twigg and Richardson, 2007). Several catalytic applications have been investigated during the last decades. In catalytic combustion short contact time reactors of ceramic foams were built much smaller than conventional combusters for alkanes (Goralski and Schmidt, 1996). In the field of exhaust gas treatment $NO_X$ was reduced over a zeolite-coated structured catalytic foam (Seijger et al., 2001). CPOX to syngas in foams have been investigated intensively by the Schmidt group and other researchers (Hickman and Schmidt, 1993a; Horn et al., 2006a, 2007a; Dalle Nogare et al., 2008; Donazzi et al., 2010; Dalle Nogare et al., 2011). An overview over additional applications give Twigg and Richardson (2007) and Reitzmann et al. (2006). Several manufacturing techniques of macroporous ceramics have been developed, i.e., replica, sacrificial template, and direct foaming (Studart et al., 2006). The sponge-like structure consists of solid edges and open faces through which fluid can pass. The irregularly shaped strut-network can be expressed by its morphological parameters, i.e., cell and window diameter, strut thickness and porosity (Twigg and Richardson, 2007), see also Fig. 13 (A). However, industrial manufacturers often use pores per

inch (PPI) as a value of characterization, ranging typically between 10-100 and porosity values greater than 75%, see Fig. 13 (B). The replication technique, most commonly used in commercial scale, causes hollow struts, enclosing a certain volume fraction, and a rough surface. In contrary, direct foaming leads to solid struts (Colombo and Hellmann, 2002). Nonetheless, the actual foam shape depends not only on the fabrication process. One of the most import properties of ceramic foams is the specific surface area, which is significant for the transport of momentum, energy and mass (Große et al., 2009; Della Torre et al., 2014). The conventional physisorption measurement of gases (BET-method) would lead to an overestimation of the specific surface area due to surface roughness and the inclusion of internal volumina. Therefore, alternative techniques have been established, e.g., magnetic resonance imaging (MRI) (Garrido et al., 2008) or X-ray computed tomography (CT) (Della Torre et al., 2014; Elmoutaouakkil et al., 2002). In addition, several theoretical approaches determine the specific surface area, e.g., by utilizing the hydraulic diameter (Richardson et al., 2000) or by assuming the tetrakaidecahedron unit cell (Buciuman and Kraushaar-Czarnetzki, 2003; Inayat et al., 2011).
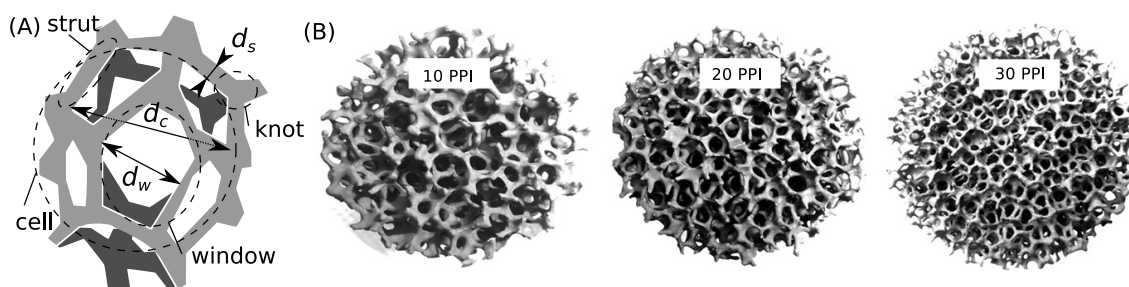


Figure 13: (A) Characteristic dimensions in open-cell foams. (B) Foams of different PPIs (reprinted from Inayat et al. (2011) with permission from Elsevier).

### 2.6.1   Modeling catalytic foams

Many correlations for global parameters for different foam structures, such as the specific surface area or pressure drop, can be found in literature (Richardson et al., 2000). However, as Edouard et al. (2008) report the standard deviation between experimental and theoretical values can be as high as 100%. Predicting the transport of mass between fluid and solid or the transport of energy is even more critical (Reitzmann et al., 2006). Besides black box models, more sophisticated approaches exist. The so called pseudo-heterogeneous models distinguish between gas and solid phase, although the actual foam structure is not taken explicitly into account. As a result axial, and in some cases radial profiles of temperature and species are obtained. Korup et al. (2013) for example compared their "foam" model involving transport phenomena and a detailed reaction mechanism for the catalytic partial oxidation of methane over platinum with spatially resolved experimental data. The model showed accurate results for some species. However, it is based on *a priori* Nusselt and Sherwood correlations.

### 2.6.2   3D CFD simulations of catalytic foams

An alternative to transport correlation-based models are structure-resolved 3D CFD simulations. Eppinger et al. (2011) presented a spatially resolved catalytic fixed-bed reactor simulation with randomly distributed spherical particles. This approach can be coupled with a detailed reaction mechanism on the surface. With such detailed simulations quantitative descriptions can be made of transport phenomena within complex structures without a priori assumptions. Hence, the dependency on empiricism can be reduced. Numerical 3D simulations of foam structures can be divided into model structures of different complexity and real foam models. The latter is carried out by converting the actual geometry by means of 3D CT (Bianchi et al., 2013, 2015) or 3D MRI (Große et al., 2008) into CAD data appropriate for 3D simulations. These procedures are time and cost intensive and include several consecutive steps of preparation (Habisreuther et al., 2009). In contrary, model structures can be separated into deterministic models (unit cells) and stochastic models. The first deterministic model of a foam structure goes back to Lord Kelvin (Thomson, 1887), see Fig. 14 (A). Its cells divide space uniformly and are constructed with tetrakaidecahedrons, i.e., six square and eight hexagonal faces. A newer model consists of eight cells, combining a tetrakaidecahedron with dodekahedrons, the so called Weiare-Phelan structure (Weaire and Phelan, 1994), see Fig. 14. The surface of this cell structure is 0.3% smaller than the Kelvin cell with similar volume. Several authors have investigated Kelvin cell structures in terms of CFD simulations (Boomsma et al., 2003; Krishnan et al., 2006; Kopanidis et al., 2010; Lucci et al., 2014; von Rickenbach et al., 2014; Lucci et al., 2015).
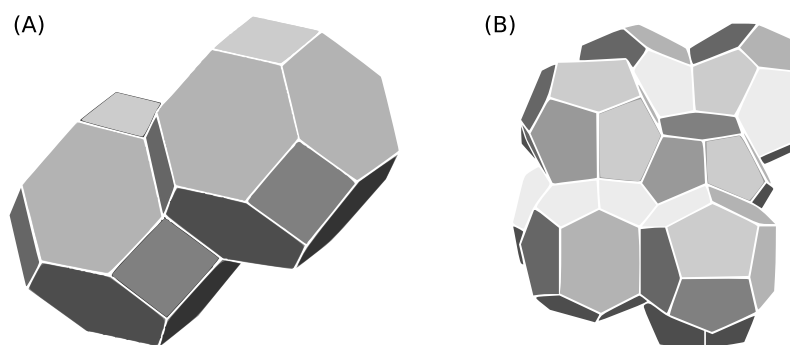


Figure 14: (A) Kelvin cell model. (B) Weiare-Phelan structure.

However, idealized unit-cells do not account for random variations typical for natural foam structures (Zhu et al., 2000). This leads to preferable flow directions in the cell structure. Therefore, the second type of model applies stochastic approaches. Habisreuther et al. (2009) for example randomized a perfectly ordered Kelvin structure by relocating nodes with a stochastic algorithm. Porosity and specific surface were adjusted. The simulated pressure drop and residence time distribution showed good accuracy after closing 40% of the cell windows (Habisreuther et al., 2009). Roberts and Garboczi (2002) investigated different completely stochastic models, i.e., overlapping solid spheres, overlapping spherical pores, overlapping ellipsoidal pores, Voronoi tessellation, node-bond models, as well as Gaussian random fields. They concluded that the open-cell Voronoi tessellations have a microstructure similar to that examined in foams (Roberts and Gar-

boczi, 2002). Nevertheless, their focus was set on mechanical stability investigated with finite element methods rather than fluid simulations.

## 2.7    Stagnation-flow reactors

Stagnation-flow reactors are used in practical applications, such as chemical-vapor-deposition reactors for electronic thin-film growth or in research on heterogeneous chemistry and reactive flow (Warnatz et al., 1994). The reactant gas flow is guided to a catalytic disk which generates a viscous boundary layer, see Fig. 15. In this layer the temperature and species composition depend only on one independent variable, i.e., the axial coordinate. However, the velocity distribution can be two-dimensional or three-dimensional, respectively. Scaling of the primary velocity leads to a simplified 1D stagnation-flow field approximation (Kee et al., 2003; Yuan et al., 2008). Several groups have studied catalytic stagnation flow to identify detailed chemistry (Warnatz et al., 1994; Deutschmann et al., 1996; Taylor et al., 2003; McGuire et al., 2009, 2011; Karakaya and Deutschmann, 2013). Recently, Karadeniz et al. (2015) investigated with numerical methods different washcoat models in SFR. Depending on the conditions of the washcoat diffusion processes inside the pores play a major role toward conversion. However, more sophisticated pore models lead to higher complexity of the model and meanwhile to a higher computational time.
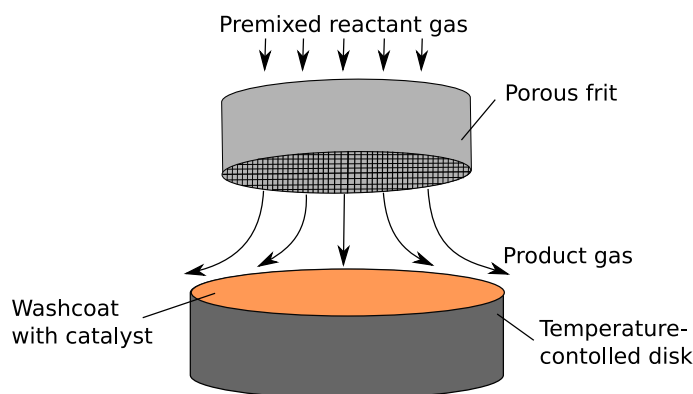


Figure 15: Typical setup of stagnation-flow reactor.

# 3   Fundamentals of modeling heterogeneous catalytic reactors

In Fig. 16 the particle-resolved modeling approach of catalytic fixed-bed reactors is illustrated. The geometry of the packed bed is resolved by the actual shape of each individual particle. Commonly spheres, as well as cylinders with and without holes are used. The transport of momentum, energy and species is described by Navier-Stokes equations. Turbulence is taken into account by Reynolds-Averaged Navier-Stokes (RANS) models depending on the particle Reynolds number. Furthermore, energy exchange between solid particles and the surrounding flow field is considered, i.e., conjugate heat transfer, as well as radiation between surfaces. Adsorption of gas phase species, reactions between surface adsorbed species, and desorption of species is modeled with the mean field approximation. In the following sections fundamentals of modeling heterogeneous catalytic reactors are given.
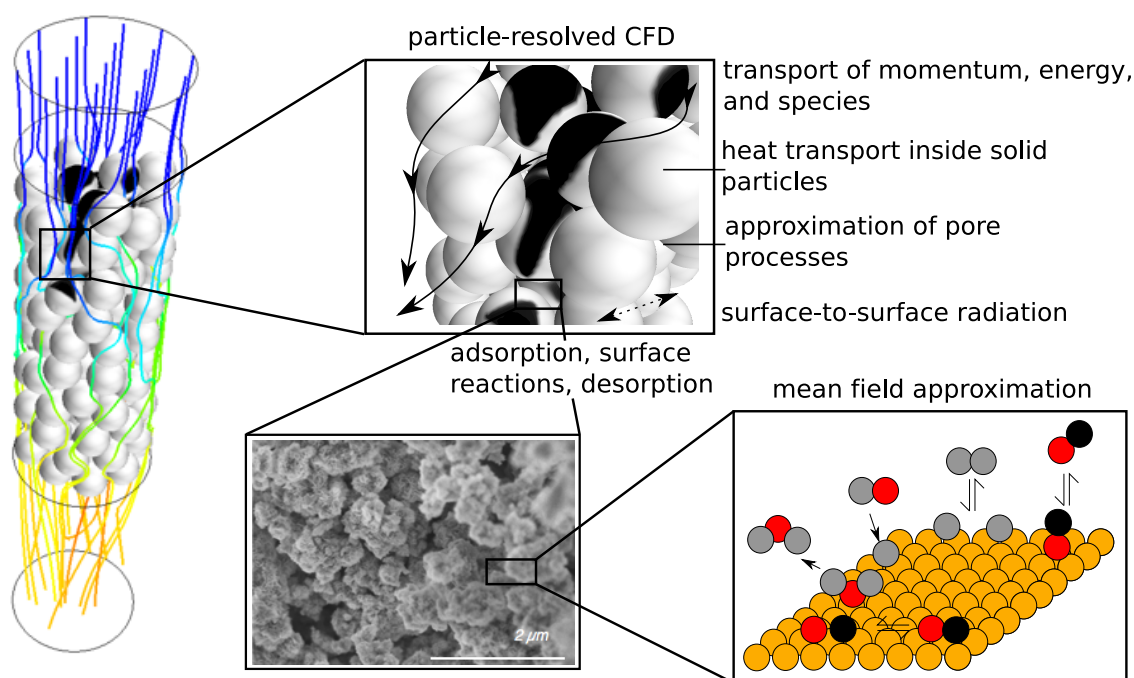


Figure 16: Particle-resolved modeling approach of catalytic fixed-bed reactors including surface reactions described by mean field approximation. Picture taken at FHI Berlin.[1]

## 3.1   Modeling chemically reacting flow

### 3.1.1   Governing equations

The set of governing equations consists of conservation of total mass, conservation of momentum, conservation of mass of each chemical species, and conservation of energy in terms of specific en-

---

[1]At the Department of Inorganic Chemistry at Fritz-Haber Institute Berlin Hitachi a S-4800 semi-in-lens Scanning Electron Microscope (SEM) was used by Gisela Weinberg to take this picture. The Hitachi S-4800 works with a cold field emission gun.

thalpy. The set of equations is formulated in Cartesian coordinates $x, y, z$. A laminar problem with Einstein convention can be written by the following set of equation. For the turbulent formulation see below.

Conservation of mass:

$$\frac{\partial \rho}{\partial t} + \frac{\partial (\rho v_i)}{\partial x_i} = 0 \tag{3.1}$$

where $\rho$ is the mass density, $t$ is the time, $x_i$ are the Cartesian coordinates and $v_i$ are the velocity components.

Conservation of momentum:

$$\frac{\partial (\rho v_i)}{\partial t} + \frac{\partial (\rho v_i v_j)}{\partial x_j} + \frac{\partial p}{\partial x_i} + \frac{\partial \tau_{ij}}{\partial x_j} = \rho g_i \tag{3.2}$$

The stress tensor $\tau_{ij}$ is written as:

$$\tau_{ij} = -\mu \left( \frac{\partial v_i}{\partial x_j} + \frac{\partial v_j}{\partial x_i} \right) + \left( \frac{2}{3}\mu \right) \delta_{ij} \frac{\partial v_k}{\partial x_k} \tag{3.3}$$

where $\mu$ is the mixture viscosity and $\delta_{ij}$ the Kronecker delta, which is unity for $i = j$, else zero.

Conservation of species $i$:

$$\frac{\partial (\rho Y_i)}{\partial t} + \frac{\partial (\rho v_j Y_i)}{\partial x_j} + \frac{\partial (j_{i,j})}{\partial x_j} = 0 \quad \text{for} \quad i = 1, ..., N_g \tag{3.4}$$

with mass fraction $Y_i = m_i/m$ of species $i$ and total mass $m$. $N_g$ is the number of gas phase species. The components $j_{i,j}$ of the diffusion mass flux are described by the mixture-average formulation:

$$j_{i,j} = -\rho \frac{Y_i}{X_i} D_i^M \frac{\partial X_i}{\partial x_j} \tag{3.5}$$

$D_{M,i}$ is the effective diffusivity between species $i$ and the remaining mixture M, which is defined as:

$$D_{M,i} = \frac{1 - Y_i}{\sum_{j \neq i}^{N_G} X_j / D_{ij}} \qquad \text{for } i = 1, ..., N_G \tag{3.6}$$

The binary diffusion coefficients $D_{ij}$ can be obtained through polynomial fits CD-adapco (2014). $M_i$ is the molecular weight of species $i$ and $T$ the temperature. The molar fraction $X_i$ can be written as:

$$X_i = \frac{1}{\sum_{j=1}^{N_g} \frac{Y_j}{M_j}} \frac{Y_i}{M_i} \tag{3.7}$$

Conservation of energy in terms of specific enthalpy $h$:

$$\frac{\partial (\rho h)}{\partial t} + \frac{\partial (\rho v_j h)}{\partial x_j} + \frac{\partial j_{q,j}}{\partial x_j} = \frac{\partial p}{\partial t} + v_j \frac{\partial p}{\partial x_j} - \tau_{jk} \frac{\partial v_j}{\partial x_k} + S_h \tag{3.8}$$

where $S_h$ is the heat source. Diffusive heat transport $j_{q,j}$ is given by:

$$j_{q,j} = -k \frac{\partial T}{\partial x_j} + \sum_{i=1}^{N_g} h_i j_{i,j} \tag{3.9}$$

with thermal conductivity of the mixture $k$ and mixture specific enthalpy $h$:

$$h = \sum_{i=1}^{N_g} Y_i h_i(T) \tag{3.10}$$

as a function of temperature $h_i = h_i(T)$.

Ideal gas was assumed connecting pressure, temperature and density to close the governing equations:

$$p = \frac{\rho R T}{\sum_{i=1}^{N_g} X_i M_i} \tag{3.11}$$

For the calculation of gasphase properties, see section 3.3.

### 3.1.2 Modeling turbulence

With the help of the particle Reynolds number $Re_p$ the flow in fixed-bed reactors can be characterized:

$$Re_p = \frac{v_{in} d_p}{\nu} \tag{3.12}$$

with $v_{in}$ as the superficial velocity. For $Re_p > 300$ the flow behaves highly unsteady, chaotic and qualitatively resembling turbulent (Dybbs and Edwards, 1984; Ziółkowska and Ziółkowski, 1988). Direct numerical simulations (DNS) solves the time-dependent Navier-Stokes-Equations without using an additional model for resolving vortices, etc. However, the calculation time for such DNS are prohibitively intensive. As a consequence, such flow configurations are generally modeled with two different approaches, i.e., Large-Eddy simulations (LES) and Reynolds-Averaged Navier-Stokes simulations (RANS). With these two models the small scale turbulence fluctuations are not accounted for. Both approaches introduce additional terms, which have to be modeled to achieve closure, in the Navier-Stokes equations. LES is always formulated in a transient way, which makes it a time consuming calculation. Consequently, only few authors have applied LES for calculating larger segments of packed beds, e.g., Hassan (2008) and Shams et al. (2014).

With RANS the solution variables are split into mean components $\bar{v}_i$ and fluctuating components $v_i'$. Then, they are integrated over an interval of time much larger than the small-scale fluctuations. The turbulent momentum equation can then be written as (Dixon et al., 2006):

$$\frac{\partial (\rho \bar{v}_i)}{\partial t} + \frac{\partial}{\partial x_j} \left( \rho \overline{v_i v_j} + \rho \overline{v_i' v_j'} \right) + \frac{\partial \bar{p}}{\partial x_i} + \frac{\partial \bar{\tau}_{ij}}{\partial x_j} = \rho g_i \tag{3.13}$$

The Reynolds stresses $\left( \rho \overline{v_i' v_j'} \right)$ have to be put in terms of the averaged flow quantities to close the system of equations. They are modeled applying the Boussinesq hypothesis:

$$\left( -\rho \overline{v_i' v_j'} \right) = \mu_t \left( \frac{\partial v_i}{\partial x_j} + \frac{\partial v_j}{\partial x_i} \right) - \frac{2}{3} \left( \rho k + \mu_t \frac{\partial v_i}{\partial x_i} \right) \delta_{ij} \tag{3.14}$$

The most common used turbulence model in industry is the $k - \varepsilon$ model developed by Launder and Spalding (1972). Here, the turbulent viscosity $\mu_t$ is defined by the turbulent kinetic energy $k$,

and its dissipation rate $\varepsilon$:

$$\mu_t = \rho C_\mu \frac{k^2}{\varepsilon} \tag{3.15}$$

The turbulent kinetic energy and the dissipation rate are governed from the modified transport equations:

$$\frac{\partial(\rho k)}{\partial t} + \frac{\partial(\rho v_i k)}{\partial x_i} = \frac{\partial}{\partial x_i}\left[\left(\mu + \frac{\mu_t}{\sigma_k}\right)\frac{\partial k}{\partial x_i}\right] + G_k + G_b - \rho\varepsilon \tag{3.16}$$

$$\frac{\partial(\rho\varepsilon)}{\partial t} + \frac{\partial(\rho v_i\varepsilon)}{\partial x_i} = \frac{\partial}{\partial x_i}\left[\left(\mu + \frac{\mu_t}{\sigma_\varepsilon}\right)\frac{\partial\varepsilon}{\partial x_i}\right] + C_{1\varepsilon}\frac{\varepsilon}{k}\left[G_k + (1 - C_{3\varepsilon})G_b\right] - C_{2\varepsilon}\rho\frac{\varepsilon^2}{k} \tag{3.17}$$

In the above equations, $G_k$ represents the generation of turbulent kinetic energy $k$, due to turbulent stress:

$$G_k = -\rho\overline{v_i'v_j'}\frac{\partial v_j}{\partial x_i} \tag{3.18}$$

However, $G_b$ is the generation of turbulent kinetic energy $k$, due to buoyancy:

$$G_b = -\beta g_i\frac{\mu_t}{Pr_t}\frac{\partial T}{\partial x_i} \tag{3.19}$$

with $Pr_t$ as the turbulent Prandtl number ($Pr_t = v_t/\alpha_t$) and $\beta$ is the thermal expansion coefficient:

$$\beta = -\frac{1}{\rho}\left(\frac{\partial\rho}{\partial T}\right) \tag{3.20}$$

Values for the constants in the above equations have been established from experiments with air and water by Launder and Spalding (1972): $C_{1\varepsilon} = 1.44, C_{2\varepsilon} = 1.92, C_\mu = 0.09, \sigma_k = 1.0, \sigma_\varepsilon = 1.3$, and $Pr_t = 0.85$.

If heat transfer is considered in the gas phase, the turbulent enthalpy equation reads:

$$\frac{\partial(\rho h)}{\partial t} + \frac{\partial(\rho v_i h)}{\partial x_i} = \frac{\partial}{\partial x_i}(k + k_t)\frac{\partial T}{\partial x_i} - \frac{\partial\sum_j h_j J_j}{\partial x_i} + \frac{Dp}{Dt} + (\tau_{ik})_{\text{eff}}\frac{\partial v_i}{\partial x_k} + S_h \tag{3.21}$$

whereas $k_t$ is the thermal conductivity due to turbulent transport, which is connected to the turbulent Prandtl number via:

$$k_t = \frac{c_p\mu_t}{Pr_t} \tag{3.22}$$

Furthermore, if gradients in the species fields in the gas phase occur, the turbulent convection-diffusion equation looks similar to the equation for enthalpy. Additional terms are the turbulent diffusivity and a turbulent Schmidt number, for more information see CD-adapco (2014). Moreover, Dixon et al. (2006) give an overview of different alternative turbulence models relevant for CFD simulations of packed-beds. Since turbulence modeling is a wide field, the reader is referred to the relevant literature, or CFD software user guides, e.g., CD-adapco (2014).

In this thesis the *realizable k-ε* turbulence model, developed by Shih et al. (1995), was utilized. It shows an improvement of the standard $k - \varepsilon$ turbulence model for many applications (CD-adapco, 2014). In the model a new transport equation has been implemented for the turbulent dissipation rate $\varepsilon$. Furthermore, the critical coefficient of the standard mode, $C_\mu$, is formulated as a function of mean flow and turbulence properties, rather than assuming to be constant. The concept of a variable $C_\mu$ is in line with experimental observations in boundary layers (Shih et al., 1995). For a detailed description of the formulation, see Shih et al. (1995); CD-adapco (2014).

The fluid flow in packed-beds is highly affected by particle surfaces and reactor tube walls, respectively. As a consequence, the turbulence intensity is also changed by the presence of a near wall. Getting closer to a wall, the tangential velocity fluctuations are diminished by viscous damping and the normal fluctuations are damped by kinematic blocking (Dixon et al., 2006). Based on experimental evidence, the region close to the wall, also called inner layer of turbulent flow, can be divided into three layers:

1. The viscous sublayer, where the flow can be assumed to be laminar.

2. The buffer layer or blending layer, where the effects of molecular viscosity and turbulence are equally distributed.

3. The fully turbulent region, logarithmic layer or log-law region.

The resolution of the individual layers inside packed beds is complex, since the flow is highly nonuniform. As a consequence, turbulence models that are based on sublayer resolution, like Spalart-Allmaras and $k - \omega$ model, are termed low-Reynolds number models. On the contrary, the $k - \varepsilon$ model family is originally based on wall functions, so that the sublayer and buffer do not have to be resolved. In the following, the basic concept of the standard wall function, introduced by Launder and Spalding (1972) is explained briefly. The wall laws are set up to provide a value for $u^+$ as a function of the non-dimensional wall distance $y^+$:

$$u^+ = \frac{U}{u_\tau} = f\left(\frac{\rho u_\tau y}{\mu}\right) = f\left(y^+\right) \tag{3.23}$$

with $y$ as the wall distance, $\rho$ the fluid density, $\mu$ the viscosity, $\tau_w$ the normal stress at the wall, and $u_\tau$ as the friction velocity:

$$u_\tau = \sqrt{\tau_w/\rho} \tag{3.24}$$

For temperature and turbulent wall heat flux the variable $t^+$ can defined similarly, which is the non-dimensional quantity for turbulent temperature distribution (CD-adapco, 2014). In the following, only the velocity terms are written for brevity. The wall laws are defined uniformly for the viscous sublayer and the logarithmic layer. The buffer is treated differently for the different wall laws.

(i) Viscous sublayer:

$$u^+_{laminar} = y^+ \tag{3.25}$$

(ii) Logarithmic layer:

$$u^+_{turbulent} = \frac{1}{\kappa} ln\left(Ey^+\right) \tag{3.26}$$

the standard values in this equation are: $\kappa = 0.42$ and $E = 9.0$.

The traditional $k - \varepsilon$ model is not suited for near-wall velocity calculation, since the damping in this region is not accounted for. As a consequence, in all of the simulations, a Two-Layer All-$y^+$ Wall Treatment driven by shear (Wolfshtein, 1969) was utilized. See for example manual of STAR-CCM+ for formulation (CD-adapco, 2014). With this blended wall function, it is possible to use fine meshes with $y^+ \approx 1$ for cells closest to walls. That means, the first calculation-cell centroid is at the edge of the viscous sublayer. With the blended wall function, called All-$y^+$ Wall Treatment, the buffer layer is represented by merging the viscous sublayer and logarithmic region. Commonly, Reichardt's law is applied blending the two region's laws:

$$u^+ = \frac{1}{\kappa} ln \left(1 + \kappa y^+\right) + C \left[1 - \exp\left(\frac{y^+}{D}\right) - \frac{y^+}{D} \exp(1 - by^+)\right] \tag{3.27}$$

with $D = y_m^+$, which is the dimensionless distance of the inner layer, and

$$C = \frac{1}{\kappa} ln \left(\frac{E}{\kappa}\right) \tag{3.28}$$

$$b = \frac{1}{2} \left(\frac{D\kappa}{C} + \frac{1}{D}\right) \tag{3.29}$$

## 3.2 Kinetics

A microkinetic reaction mechanism describes a catalytic reaction in terms of a sequence of adsorption processes, surface reactions and desorption. In the following, the fundamentals of microkinetics for heterogeneous reactions are given. Thermodynamic constraints are summarized briefly followed by the implementation approach of microkinetics for CFD simulations.

### 3.2.1 Description of heterogeneous catalysis

Adsorption processes can be distinguished between physisorption and chemisorption. Physisorption is characterized by week Van-der-Waals forces between adsorbat and surface (8-30 kJ/mol). Chemisorption leads to a chemical bonding between adsorbate and surface, which is characterized by high adsorption enthalpies (40-800 kJ/mol) (Kee et al., 2003). The high bonding energy of the adsorbed molecule can lead to dissociation of the molecule, see Fig. 17.

Besides measuring rate constants for adsorption processes, collision theory can be applied in terms of gas-phase molecules striking the surface per unit area per unit time (Cortright and Dumesic, 2001):

$$F_i = \frac{p_i}{\sqrt{2\pi M k_B T}} \tag{3.30}$$

The rate of adsorption can then be expressed by multiplying $F_i$ with the sticking coefficient $S_i$, i.e., the probability that collision with the surface is accompanied with adsorption:
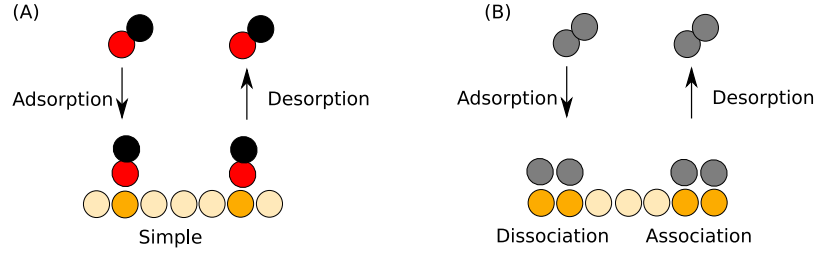
Figure 17: (A) Simple adsorption and desorption. (B) Dissociative adsorption and associative desorption.

$$\dot{s}_i^{\text{ads}} = F_i \cdot S_i \tag{3.31}$$

Since the sticking coefficient depends on surface coverage $\Theta$ and temperature $T$, it can be defined as the product of its initial value $S_i^0$, i.e., on a clean surface, and the surface coverage (Cortright and Dumesic, 2001). The resulting expression for the rate of adsorption is:

$$\dot{s}_i^{\text{ads}} = S_i^0 \sqrt{\frac{RT}{2\pi M_i}} c_i \prod_{j=1}^{N_s} \Theta_j \tag{3.32}$$

Reactions between or with adsorbates can be expressed by two different mechanisms, i.e., Langmuir-Hinshelwood and Eley-Rideal, see Fig. 18. The Langmuir-Hinshelwood mechanism assumes that both reactants are adsorbed at the catalytic surface. On the other hand, the Eley-Rideal mechanism describes the reaction between one gas phase molecule and a surfaced adsorbed species.
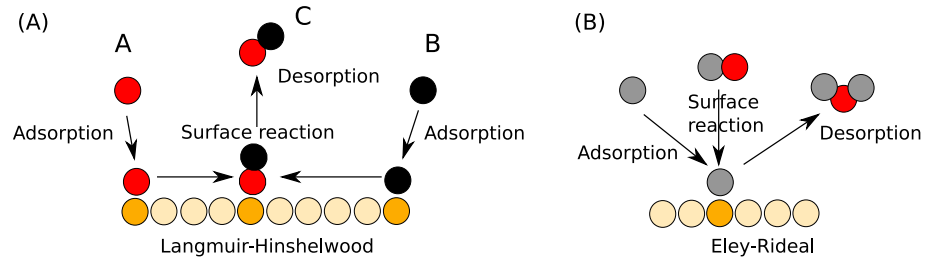


Figure 18: (A) Langmuir-Hinshelwood and (B) Eley-Rideal mechanism.

A first approximation of the pre-exponential factor of any elementary reaction can be assumed to be $10^{13} \, N_A / \Gamma$ [cm$^2$/(mol s)], with $N_A$ being the Avogadro's number, and $\Gamma$ is the site density of the catalyst. $10^{13}$ [1/s] is the order of magnitude of $k_B T / h$, with $k_B$ as the Boltzmann constant, and $h$ being Planck's constant. In Fig. 19 (A) a schematic of thermodynamic property as function of reaction coordinate is illustrated. Pre-exponential factors can be calculated from Transition State Theory (TST) as a function of temperature. The transition state separates the phase space (the space of atomic coordinates and momenta) into a reactants region and a products region with a "dividing surface" orthogonal to the reaction coordinate (Fernández-Ramos et al., 2006). TST expresses rate constants with the Gibbs free energy $G$ of reactants, products and transition states (Salciccioli et al., 2011):

$$k_i = \frac{k_B T}{h} \exp\left(\frac{-\Delta G_i^{\ddagger}}{k_B T}\right) = \frac{k_B T}{h} \exp\left(\frac{-\Delta S_i^{\ddagger}}{k_B}\right) \exp\left(\frac{-\Delta H_i^{\ddagger}}{k_B T}\right) \tag{3.33}$$

$$K_i = \exp\left(\frac{-\Delta G_{i,\text{rxn}}}{k_B T}\right) = \exp\left(\frac{-\Delta S_{i,\text{rxn}}}{k_B}\right) \exp\left(\frac{-\Delta H_{i,\text{rxn}}}{k_B T}\right) \tag{3.34}$$

In the two equations above, $k_i$ describes the irreversible elementary reaction rate constant of reaction $i$ in dependency of the change in Gibbs free energy to transition state $\Delta G_i^{\ddagger}$, the change in entropy $\Delta S_i^{\ddagger}$, as well as the change in enthalpy $\Delta H_i^{\ddagger}$ from reactant to transition state. Eq. (3.34) relates the equilibrium constant $K_i$ of reaction $i$ to the change in free energy of reaction, and entropy and enthalpy of reaction.
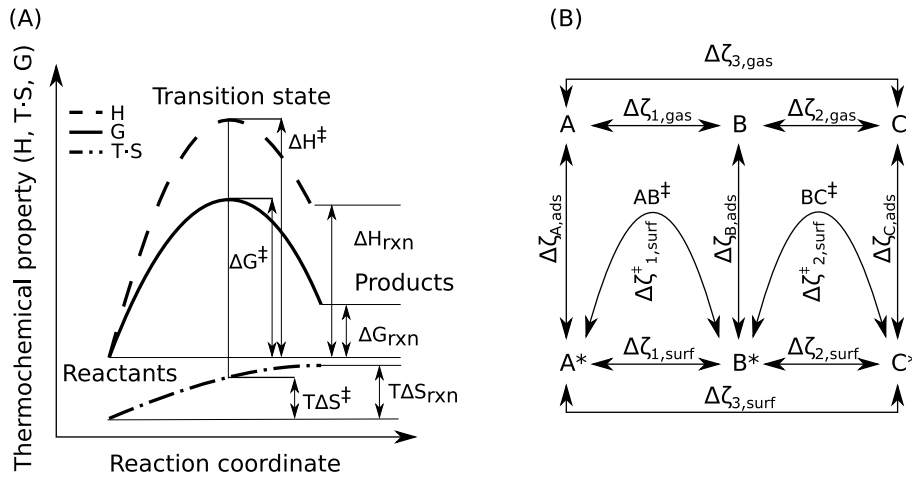


Figure 19: Scheme of thermodynamic property as function of reaction coordinate (A). Diagram of thermochemical property changes $\Delta\zeta$ in model A$\rightleftharpoons$B$\rightleftharpoons$C surface reaction mechanism (B). Partly adopted from Salciccioli et al. (2011).

### 3.2.2   Thermodynamic consistency of microkinetics

Thermodynamic consistency of microkinetics is a very important aspect. However, many mechanisms in literature do not proof explicitly its consistency. Thermodynamic constraints of microkinetics can be formulated by four equations (Cortright and Dumesic, 2001) proofing firstly individual elementary reactions, and secondly the overall net reaction. For individual elementary reactions, the following constraints have to be fulfilled:

$$\Delta E_{i,\text{b}} = \Delta E_{i,\text{f}} - \Delta H_i \tag{3.35}$$

$$A_{i,\text{b}} = A_{i,\text{f}} \exp\left(\frac{\Delta G_i - \Delta H_i}{RT}\right) = A_{i,\text{f}} \exp\left(\frac{\Delta S_i}{R}\right) \tag{3.36}$$

where $\Delta E_{i,\text{b}}$ is the backward activation energy, $\Delta E_{i,\text{f}}$ is the forward activation energy, and $\Delta H_i$ is the standard enthalpy change of the individual reaction step. $A_{i,\text{b}}$ is the reverse pre-exponential factor, and $A_{i,\text{f}}$ the forward pre-exponential factor, respectively. $\Delta G_i$ is the change in standard Gibbs free energy of reaction $i$, and $\Delta S_i$ the change in entropy.

Applying Hess's Law, each reaction step can be formulated with a gas phase reaction having the same stoichiometry. A net reaction, that begins with gaseous reactants and ends with gaseous products, can be described as a linear combination of several reactions. Thermodynamic constraints for the net reactions can be defined by:

$$\sum_i \sigma_i(\Delta E_{i,\text{f}}) - \sum_i \sigma_i(\Delta E_{i,\text{b}}) = \Delta H_{\text{net}} \tag{3.37}$$

and

$$\prod_i \left( \frac{A_{i,\text{f}}}{A_{i,\text{b}}} \right)^{\sigma_i} = \exp\left( \frac{\Delta G_{\text{net}} - \Delta H_{\text{net}}}{RT} \right) \tag{3.38}$$

whereas the subscript "net" denotes the change in thermodynamic state properties from net reactants to net products (Salciccioli et al., 2011). Alternatively, the thermodynamic consistency is defined via the equilibrium constants of each elementary step, as well as the net reaction (Cortright and Dumesic, 2001):

$$\prod_i K_{i,\text{eq}}^{\sigma_i} = \prod_i \left( \frac{k_{i,\text{for}}}{k_{i,\text{rev}}} \right)^{\sigma_i} = K_{\text{net}} \tag{3.39}$$

where $K_{\text{net}}$ is the equilibrium constant of the overall stoichiometric reaction.

In Fig. 19 (B) the relationship is illustrated between gas phase and surface-phase thermochemical properties of gas and surface intermediates and transition states, denoted as $^\ddagger$ for the simple $A \rightleftharpoons B \rightleftharpoons C$ surface reaction mechanism. $\zeta$ represents any of the thermochemical properties, i.e., free Gibbs energy $G$, entropy $S$, and enthalpy $H$. In the figure, $\Delta\zeta_{i,\text{gas}}$ represents the property change connected with the elementary gas phase reactions, in this situation $\Delta\zeta_{3,\text{gas}} = \Delta\zeta_{1,\text{gas}} + \Delta\zeta_{2,\text{gas}}$. Thermochemistry for gas phase species can be obtained from a large group of databases, see chapter 3.3.4 below.

Violation of thermodynamic consistency can lead to erroneous predictions of heat and mass. Enthalpic inconsistency leads to incorrect solution of the energy balance. As a consequence, in a non-isothermal simulation wrong temperatures are predicted and likewise wrong conversion. In an isothermal simulation, the temperatures are fixed, however, the enthalpic inconsistency leads to errors in the mass balance. On the other hand, inconsistency in terms of entropy is characteristic for a fundamental inconsistency of pre-exponential factors. By defining both the forward and reverse reaction steps an incorrect equilibrium constant can be the result of thermodynamic inconsistency. This results in an incorrect prediction of the equilibrium state (Mhadeshwar et al., 2003). As a conclusion, guaranteeing consistency of enthalpy and entropy of microkinetics is of fundamental importance.

### 3.2.3 Mean-field approximation

The catalytic processes at the reacting surface occur at much smaller time and length scales as the surrounding flow field. An efficient model coupling CFD and surface reactions is the mean-field approximation. This model assumes uniformly distributed adsorbates and catalytic sites over a computational cell. Spatially localized effects, i.e., surface facets, surface defects, and coverage effects, as well as interactions between adsorbates are neglected by using averaged values. The condition of the catalyst in a computational cell is determined by temperature $T$ and a set of surface coverages $\Theta_i$, which is defined as the fraction of surface covered by species $i$. Chemical reactions occurring at the catalytic surface are coupled via boundary conditions with the species concentration distribution. Under steady-state conditions gas-phase molecules of species $i$, which are produced/consumed at the catalytic surface by desorption/adsorption, have to diffuse from/to the catalyst (Deutschmann, 2008):

$$\vec{n}\left(\vec{j}_i\right) = R_i^{\text{het}} \tag{3.40}$$

with the outward-pointing unit vector normal to the surface $\vec{n}$ and the diffusion mass flux $\vec{j}_i$. The heterogeneous reaction term $R_i^{\text{het}}$ can be formulated as:

$$R_i^{\text{het}} = F_{\text{cat/geo}} M_i \dot{s}_i \tag{3.41}$$

with $M_i$ as the molar weight, $\dot{s}_i$ as the molar net production rate of gas-phase species $i$ and $F_{\text{cat/geo}}$ as the ratio of catalytic active area $A_{\text{catalytic}}$ to geometric area $A_{\text{geometric}}$.

$$F_{\text{cat/geo}} = A_{\text{catalytic}}/A_{\text{geometric}} \tag{3.42}$$

In this study the mean-field approximation was applied to model the surface reactions. It assumes that adsorbates are randomly distributed on the surface, which is interpreted as being uniform (Kee et al., 2003). The molar net production $\dot{s}_i$ results in:

$$\dot{s}_i = \sum_{k=1}^{K_s} v_{ik} k_{f_k} \prod_{j=1}^{N_g+N_s} c_j^{v'_{jk}} \tag{3.43}$$

where $K_s$ is the number of surface reactions, $c_j$ are the species concentrations in [mol/m$^2$] for the adsorbed species $N_s$ and in [mol/m$^3$] for the gas phase species $N_g$, respectively. In addition, the surface coverage $\Theta$ takes into account the surface site density $\Gamma$ [mol/m$^2$], representing the maximum number of species that can adsorb on a unit surface area. Furthermore, a coordinate number $\sigma_i$ expresses the number of surface sites which are covered by this species:

$$\Theta_i = c_i \sigma_i \Gamma^{-1} \tag{3.44}$$

The time dependent variation of $\Theta_i$ can be written as

$$\frac{\partial \Theta_i}{\partial t} = \frac{\dot{s}_i \sigma_i}{\Gamma} \tag{3.45}$$

Under steady state conditions the left side of Eq. (3.45) equals zero. The reaction rate expression can be modified by the concentration, or coverage, of some surface species:

$$k_{f_k} = A_k T^{\beta_k} \exp\left(\frac{-E_{a_k}}{RT}\right) \prod_{i=1}^{N_s} 10^{\eta_{ik} \cdot \Theta_i} \Theta_i^{\mu_{ik}} \exp\left(\frac{-\varepsilon_{i_k} \Theta_i}{RT}\right) \tag{3.46}$$

with three extra coverage parameters, $\eta_{ik}$, $\mu_{ik}$, and $\varepsilon_{ik}$. The term with $\eta_{ik}$ represents a change of magnitude of the pre-exponential factor in dependency of surface coverage. The term including $\mu_{ik}$ indicates the modification of the surface reaction rate expression proportional to any arbitrary power of a surface species concentration. $\varepsilon_{ik}$ represents a modification of the activation energy as a function of coverage.

The occurrence of adsorption reactions results in a modification of the conventional rate coefficient by referencing sticking coefficients $S_i$:

$$k_{f_k}^{\text{ads}} = \frac{S_i^0}{\Gamma^\tau} \sqrt{\frac{RT}{2\pi M_i}} \tag{3.47}$$

with $S_i^0$ as the initial (uncovered surface) sticking coefficient and $\tau = \sum_{j=1}^{N_s} v'_{jk}$ the sum of all the surface reactant's stoichiometric coefficients (Kee et al., 2003; Deutschmann, 2008).

### 3.2.4  The operator-splitting algorithm

It is computationally expensive to solve detailed reaction mechanisms. In STAR-CCM+ the Dars-CFD Reaction model is used to solve the ordinary differential equations (ODEs) which are stiff (CD-adapco, 2014). The operator-splitting algorithm separates flow-field and chemistry time scales.

The generic transport equation of scalar $\phi$ is given by:

$$\frac{\partial(\rho\phi)}{\partial t} + \nabla \cdot (\rho\phi u) - \nabla \cdot (\Gamma\nabla\phi) = S_\phi \tag{3.48}$$

where the first term states the transient change, the second accounts for convection, the third for diffusion, and the right hand side gives the source term. $\Gamma$ is the diffusion coefficient.

The time integration of the chemical state (species mass fractions $Y_k$ and enthalpy $h$) is carried out in two steps:

1. At the beginning of each time-step, the chemical state is integrated from state $(Y_k, h)^n$ to $(Y_k, h)^*$, taken only the chemical source terms into account:

$$\frac{\partial(\rho\phi)}{\partial t} = S_\phi \qquad \begin{aligned} &\text{for species mass fractions}: \phi = Y_k \text{ and } S_\phi = R_i^{\text{het}} \\ &\text{for enthalpy}: \phi = h \text{ and } S_\phi = S_h^{\text{het}} \end{aligned} \tag{3.49}$$

   The system of Eqn. (3.49) is solved applying the stiff ODE solver from the Dars-CFD library.

2. The flow field is then integrated from $(Y_k, h)^*$ to $(Y_k, h)^{n+1}$ without the chemical source term. The following systems of equations are computed:

$$\frac{\partial(\rho\phi)}{\partial t} + \nabla \cdot (\rho\phi u) - \nabla \cdot (\Gamma\nabla\phi) = 0 \qquad \begin{aligned} &\text{for species mass fractions}: \phi = Y_k \\ &\text{for enthalpy}: \phi = h \end{aligned} \tag{3.50}$$

This algorithm is more suitable for transient simulations, although it can also be applied for steady-state simulations. If the problem is steady-state, a pseudo-time-step, which is based on convection and diffusion fluxes in that cell, is introduced to integrate the ODE for the chemistry step. In STAR-CCM+ this time-step can be observed through the Chemistry Time Step field function.

## 3.3 Calculation of gas properties

The proper calculation of gas properties is very important for CFD simulations since they can change dramatically with e.g., temperature or mixture composition. In the following the main ways to obtain gas properties are presented briefly.

### 3.3.1 Diffusion coefficients

Diffusion is the mass transport caused by concentration gradients (Fick diffusion) and temperature differences (thermodiffusion), that finally leads to a uniform distribution of each of the species in a multi-component system. The calculation of the diffusion flux in a two-component system (species $i$ and $j$) can be carried out with the introduction of the so called binary diffusion coefficient $D_{ij}$. At moderate pressure it can be calculated according to the Chapman and Enskog theory (Kee et al., 2003):

$$D_{ij} = \frac{3}{16} \frac{\sqrt{2\pi k_B^3 T^3 / M_{ij}}}{p\pi\sigma_{ij}^2 \Omega_{ij}^{(1,1)}} \qquad (3.51)$$

with $k_B$ being the Boltzmann constant, $T$ is the absolute temperature [K], $M_{ij} = M_i M_j / (M_i + M_j)$, $\sigma_{ij}$ is the reduced molecule diameter, $\Omega_{ij}^{(1,1)}$ is the so-called *collision integral*, which depends on temperature and interaction potential between the molecules.

The intermolecular energy $\Psi$ between two molecules with a distance $r$ can be described by:

$$\Psi = 4\varepsilon \left[ \left(\frac{\sigma}{r}\right)^{12} - \left(\frac{\sigma}{r}\right)^6 \right] \qquad (3.52)$$

with $\varepsilon$ being the characteristic Lennard-Jones energy, and $\sigma$ the characteristic length.

The collision distance can be calculated applying the Lorenz-Berthelot rule:

$$\sigma_{ij} = \frac{\sigma_i + \sigma_j}{2} \qquad (3.53)$$

furthermore, $\varepsilon_{ij}$ can be calculated as:

$$\varepsilon_{ij} = \sqrt{\varepsilon_i \varepsilon_j} \qquad (3.54)$$

The collision integral $\Omega_{ij}^{(1,1)}$ for the 12-6 Lennard-Jones potential can be approximated according to Neufeld et al. (1972) by:

$$\Omega_{ij}^{(1,1)} = \frac{A}{(T^*)^B} + \frac{B}{exp(DT^*)} + \frac{E}{exp(FT^*)} + \frac{G}{exp(HT^*)} \tag{3.55}$$

which is dependent on the reduced temperature $T^*$:

$$T^* = \frac{k_B T}{\varepsilon_{ij}} \tag{3.56}$$

The parameters in Eq. (3.55) are listed in the table below:

Table 3: Parameters for the calculation of the collision integral according to Neufeld et al. (1972).

| Parameter | Value | Parameter | Value | Parameter | Value |
|---|---|---|---|---|---|
| A | 1.06036 | B | 0.15610 | C | 0.19300 |
| D | 0.47635 | E | 1.03587 | F | 1.52996 |
| G | 1.76474 | H | 3.89411 | | |

Since the solution of a mixture diffusion model is complex, the diffusion of species $i$ in a mixture M is approximated by a mean diffusion coefficient $D_{i,M}$ (Kee et al., 2003):

$$D_{i,M} = \frac{1 - Y_i}{\sum_{j \neq i}^{N_G} X_j / D_{ij}} \qquad \text{for } i = 1, ..., N_G \tag{3.57}$$

### 3.3.2 Viscosity

The dynamic viscosity of a single gas species $i$ in a multi-component gas can be calculated with the Chapman-Enskog equation (Kee et al., 2003):

$$\mu_i = \frac{5}{16} \frac{\sqrt{\pi M_i k_B T}}{\pi \sigma_i^2 \Omega_i^{(1,1)}} \tag{3.58}$$

The dynamic viscosity of the mixture $\mu$ is given by the following equation:

$$\mu = \frac{1}{2} \left[ \sum_{i=1}^{n} X_i \mu_i + \left( \sum_{i=1}^{n} \frac{X_i}{\mu_i} \right)^{-1} \right] \tag{3.59}$$

with $X_i$ being the mole fraction of component $i$, and $\mu_i$ as the viscosity of species $i$.

### 3.3.3 Thermal conductivity

The thermal conductivity of a single species $i$ is calculated from kinetic theory, by assuming that the individual species conductivities are composed of translational, rotational, and vibrational contributions (Warnatz, 1982):

$$k_i = \frac{\mu_i}{M_i}\left(f_{\text{trans}}C_{v,\text{trans}} + f_{\text{rot}}C_{v,\text{rot}} + f_{\text{vib}}C_{v,\text{vib}}\right) \tag{3.60}$$

with

$$f_{\text{trans}} = \frac{5}{2}\left[1 - \frac{2}{\pi}\frac{C_{v,\text{rot}}A}{C_{v,\text{trans}}B}\right] \tag{3.61}$$

$$f_{\text{rot}} = \frac{\rho D_{ij}}{\mu_i}\left[1 + \frac{2}{\pi}\frac{A}{B}\right] \tag{3.62}$$

$$f_{\text{vib}} = \frac{\rho D_{ij}}{\mu_i} \tag{3.63}$$

$$A = \frac{5}{2} - \frac{\rho D_{ij}}{\mu_i} \tag{3.64}$$

$$B = z_{\text{rot}} + \frac{2}{\pi}\left(\frac{5}{3}\frac{C_{v,\text{rot}}}{R} + \frac{\rho D_{ij}}{\mu_i}\right) \tag{3.65}$$

$$C_{v,\text{trans}} = \frac{3}{2}\cdot R \tag{3.66}$$

$$z_{\text{rot}} = z_{\text{rot}}(298K)\frac{F(298K)}{F(T)} \tag{3.67}$$

$$F(T) = 1 + \frac{\pi^{3/2}}{2}\left(\frac{\varepsilon/k_B}{T}\right)^{1/2} + \left(\frac{\pi^2}{4} + 2\right)\frac{\varepsilon/k_B}{T} + \pi^{3/2}\left(\frac{\varepsilon/k_B}{T}\right)^{3/2} \tag{3.68}$$

where $z_{\text{rot}}(298K)$ is the value of the rotation collision. Moreover, for a linear molecule $C_{v,\text{rot}} = R$, and $C_{v,\text{vib}} = C_v - \frac{5}{2}R$. With $C_v$ as the molar specific heat at constant volume of the component, and $R$ as the universal gas constant.

The thermal conductivity of the mixture is given with the following equation:

$$k = \frac{1}{2}\left[\sum_{i=1}^{n}X_i k_i + \left(\sum_{i=1}^{n}\frac{X_i}{k_i}\right)^{-1}\right] \tag{3.69}$$

with $X_i$ being the mole fraction of component $i$, and $k_i$ is the conductivity of species $i$.

### 3.3.4   Thermochemical data

Data on thermochemistry of gas-phase species is available from many sources and mostly the format is either a tabulated value or a polynomial expression. Thermodynamic polynomial data is used to provide heat capacity, enthalpy, and entropy of a species for a wide range of temperatures formulated with a seven-coefficient polynomial curve-fit. The polynomial coefficients are read from a database into STAR-CCM+. Several databases are available, e.g., Chemkin thermodynamic data base (Kee et al., 1987), the NIST chemical kinetics database (Mallard et al., 1992) or online via http://kinetics.nist.gov, or http://www.me.berkeley.edu/gri_mech/. Kee et al. (2003) give an overview of different sources of thermochemistry with an emphasis on combustion

chemistry. The formulation follows the NASA chemical equilibrium code (McBride and Gordon, 1971). For the calculation of heat capacity of a species $i$ the first five coefficients are used:

$$\frac{C_{p,i}}{R} = a_1 + a_2 T + a_3 T^2 + a_4 T^3 + a_5 T^4 \tag{3.70}$$

The polynomial fit for enthalpy of a species $i$ is defined as:

$$\frac{H_i}{RT} = a_1 + \frac{a_2}{2}T + \frac{a_3}{3}T^2 + \frac{a_4}{4}T^3 + \frac{a_5}{5}T^4 + \frac{a_6}{T} \tag{3.71}$$

with

$$\frac{H_i}{R} = \int_{T_{\text{ref}}}^{T} \frac{C_p(T)}{R} dT + h_f^0|_{T_{\text{ref}}} \tag{3.72}$$

Finally, entropy of species $i$ can be calculated with:

$$\frac{S}{R} = a_1 \ln T + a_2 T + \frac{a_3}{2}T^2 + \frac{a_4}{3}T^3 + \frac{a_5}{4}T^4 + a_7 \tag{3.73}$$

A polynomial curve-fit is available for many gas-phase species. As a consequence, in kinetic modeling for gas-phase chemistry it is common practice to define the forward (or the backward) reaction and calculate the equilibrium constant from the given thermochemistry in terms of change of free energy of the reactants. Then, the backward (or forward) reaction rate can be calculated, which is by definition in thermodynamic equilibrium (Goldsmith, 2012). However, an equivalent procedure for surface adsorbed species is not that straightforward. The prediction of thermochemistry of adsorbed species is computationally expensive since it requires knowledge of e.g., the vibrational modes. As a consequence, most of the detailed reaction mechanisms define both the forward and reverse reaction rates. However, thermodynamical violations can occur, especially in terms of entropy, cf. Mhadeshwar et al. (2003) and Salciccioli et al. (2011).

## 3.4   Modeling transport limitations in washcoat

Many of today's catalytic converters consists of a substrate, often times it is alumina that is coated with a thin layer of washcoat containing the catalyst. Although this washcoat is in general very thin ($\approx 50 \mu$m), transport limitations can influence the reactor dynamics, light-off, as well as local and global conversion (Koči et al., 2010). Moreover, the size of the catalytic particles, crystal structure and defects, their distribution in the washcoat or on the substrate, as well as the interaction with the supporting material and deactivation in general also determines the activity of the present catalyst (Ertl, 2000). However, this level of detail is not taken into account with the applied mean-field approximation describing the heterogeneous chemical kinetics. If the catalyst is deposited into the washcoat, most of the active centers of the catalyst lie inside the washcoat rather than at the surface. Transport limitation occur when the intrinsic rate of diffusion of the species, i.e., the participating reactants or products, inside the washcoat is slow in comparison to the intrinsic rate

of reaction. This fact can decline the conversion and therefore decrease the observed reaction rate. The local effectiveness factor $\eta_L$ is defined as the ratio of reaction rate inside the washcoat and the reaction rate at the surface of the washcoat (Hayes et al., 2004):

$$\eta_L = \frac{\dot{r}_{active}}{\dot{r}_{surface}} \tag{3.74}$$

whereas the factor is always in the range of $0 < \eta_L \leq 1$. Several models are available approximating pore processes. In the following, models relevant for CFD simulations are presented shortly.

### 3.4.1   Instantaneous diffusion

Assuming a diminishing transport limitation, the influence of washcoat thickness, porosity, pore diameter and particle diameter vanishes. That means, mass transport inside the washcoat is so fast that none of the species is penetrating into the washcoat. In other words, all of the reactions occur at the interface between gasphase and porous washcoat, i.e., $\eta_L = 1$ in Eq. (3.74). No additional term is introduced to Eq. (3.41). The porous washcoat is treated as an impermeable solid material.

### 3.4.2   Threedimensional reaction-diffusion model in porous media

The washcoat can be modeled as a three-dimensional porous medium. The Navier-Stokes equations in porous media can be solved analogously to the equations above, Eq. (3.1 - 3.8). However, source terms have to be added. Since the velocity at the interface between gasphase and washcoat is assumed to be zero, a momentum source term is not added to Eq. (3.2). Three-dimensional mass transfer in porous media is modeled by modifying the mixture diffusion coefficient $D_{M,i}$. It is replaced by an effective diffusion coefficient $D_{eff,i}$, that takes into account mixture diffusion and Knudsen diffusion (Mladenov et al., 2010):

$$\frac{1}{D_{eff,i}} = \frac{\tau}{\varepsilon} \left( \frac{1}{D_{M,i}} + \frac{1}{D_{Knud,i}} \right) \tag{3.75}$$

whereas $\tau$ is the empirically determined tortuosity, which is defined as the deviation of the washcoat pores from an ideal cylinder. The Knudsen diffusion coefficient $D_{Knud,i}$ of species $i$ is defined as:

$$D_{Knud,i} = \frac{d_{pore}}{3} \sqrt{\frac{8RT}{\pi \tilde{M}_i}} \tag{3.76}$$

with $R$ as the gas constant and $T$ the temperature. At atmospheric pressure, Knudsen diffusion occurs if the mean pore diameter is smaller than 100 nm (Baerns et al., 2006).

The heterogeneous reactions are taken into account as a volumetric mass source term $\tilde{M}_i \gamma \dot{s}_i$ given in [kg/m$^3$s] and occurring at the right hand side of Eq. (3.4). $\gamma$ is the catalyst density, whereas $t_W$ is the washcoat thickness:

$$\gamma = \frac{F_{cat/geo}}{t_W} \tag{3.77}$$

### 3.4.3   One-dimensional reaction-diffusion equation

A one-dimensional reaction-diffusion equation takes only the direction normal to the surface into account. It is assumed that concentration gradients in the other directions are much smaller. Hence, the gradients of the species $i$ in normal direction inside the washcoat influences directly the surface reaction rate $\dot{s}_i$ (Hayes et al., 2004). Consequently, the reaction-diffusion equation normal to the washcoat surface can be written as (Mladenov et al., 2010)

$$\frac{\partial \bar{J}_{i,n}^{W}}{\partial n} - \gamma \dot{s}_i = 0 \tag{3.78}$$

$$\bar{J}_{i,n}^{W} = -D_{\text{eff},i} \frac{\partial c_{W,i}}{\partial n} \tag{3.79}$$

with $\bar{J}_{i,n}^{W}$ is the normal diffusion molar flux of species $i$, $c_{W,i}$ the molar concentration and $D_{\text{eff},i}$ the effective Fick coefficient of species $i$ in the washcoat.

Two boundary conditions are necessary to close the equation system in Eq. (3.78):

$$c_{W,i}(n=0) = c_{0,i}; \qquad \frac{\partial c_{W,i}(t_W)}{\partial r} = 0 \tag{3.80}$$

The first boundary condition implies that the concentration at the gasphase/washcoat interface is the given concentration in the gasphase. The second boundary condition states that the washcoat is thick enough to assume a zero gradient in concentration at the washcoat/support interface.

### 3.4.4   Effectiveness factor approach

An analytical solution exists for the reaction-diffusion Eq. (3.78) for a single species if the following two assumptions are made (Mladenov et al., 2010):

1.  The species is consumed and the reaction rate is of first order ($\dot{s} = -k \cdot c$, with $k$ being the rate constant).

2.  The diffusion coefficient is constant.

An effective surface reaction rate $\dot{s}_{\text{eff}}$ can be obtained by:

$$\dot{s}_{\text{eff}} = -D_{\text{eff}} \lambda c_0 \tanh(\lambda t_W), \quad \text{with } \lambda = \sqrt{\frac{\gamma k}{D_{\text{eff}}}} \tag{3.81}$$

A maximum reaction rate $\dot{s}_{\text{max}}$ assuming no diffusion limitation can be written as:

$$\dot{s}_{\text{max}} = -F_{\text{cat/geo}} k c_0 = -\gamma t_W k c_0 \tag{3.82}$$

The effectiveness factor $\eta$ describes the ratio of the effective to the maximum reaction rate:

$$\eta = \frac{\dot{s}_{\text{eff}}}{\dot{s}_{\text{max}}} = \frac{\tanh(\lambda t_{\text{W}})}{\lambda t_{\text{W}}} = \frac{\tanh \phi}{\phi} \qquad (3.83)$$

In the equation above, the dimensionless term $\phi$ is often denoted as *Thiele modulus*. It indicates which process is rate-limiting. When $\phi$ is small, the diffusional resistance is too low to limit the rate of reaction. When $\phi$ is large, a significant diffusional resistance lowers the observed reaction rate. In multi-species systems one species that satisfies the two assumptions above has to be chosen. The effectiveness factor is calculated and then multiplied with the reaction rates of all of the species:

$$\dot{s}_{\text{eff},i} = \eta \dot{s}_i \qquad (3.84)$$

However, it has to be kept in mind that the species defining the effectiveness factor can be varied by location in the reactor. For example, the species with the slowest reaction rate is chosen. The effectiveness factor model is zero-dimensional, since only the boundary condition at the gas-phase/washcoat interface is manipulated. This is a large simplification in comparison to the three-dimensional or even one-dimensional modeling.

## 3.5   Modeling radiation

In some of the performed simulations radiation between surfaces was taken into account (surface-to-surface (S2S) radiation). Consequently, it predicts thermal radiation exchange between diffuse surfaces forming a closed set. This results in a radiant flux in the energy equation source term at the boundaries. The medium between the surfaces is non-participating. The amount of radiation that a surface receives and emits are determined by the radiation properties, i.e., emissivity, reflectivity, transmissivity, and radiation temperature, as well as by thermal boundary conditions. In STAR-CCM+ the S2S radiation model is operated in two steps. Firstly, view factors are calculated using ray tracing. Secondly, these view factors are applied to compute radiosity and irradiation fields on all surfaces (CD-adapco, 2014). For the two steps the boundary surfaces are spatially discretized into so-called *patches*. A view factor quantifies, for each patch, the proportion of surface area that the other patches illuminate. The number of patches per surface mesh cell can be defined. Since the surface mesh resolution is high due to small boundary layers in the packed-bed, this number can be as low as 10%. For a complete radiation formulation, see Holman (2001).

## 3.6   Meshes for the finite-volume code STAR-CCM+

The finite volumes in which the conservation equations are discretized can have several different shapes. The smallest numerical errors can be achieved, if the cells are oriented toward the direction of the flow field. However, the flow in packed beds is highly complex, which makes it difficult to use a directed mesh. An alternative are polyhedral cells, which are characterized by their high flexibility to discretize complex geometries. The internal meshing tool of STAR-CCM+ allows an efficient meshing with many options to adapt the mesh locally, e.g., different surface discretization

sizes, individual growth rates of the mesh, etc. Boundary layer resolution is an import aspect in packed-bed simulations. In STAR-CCM+ it is possible to discretize the near-wall region with so called *prism layers*. These orthogonal prismatic cells are oriented in normal direction to the surface and can be defined in terms of cell height. In Fig. 20 the gas-phase cells of a packed bed of spheres is shown. Two near-wall prism cells at the tube wall (left-hand side of the picture) and at the sphere surfaces are utilized. As can be seen, the surface is discretized with a very fine mesh.
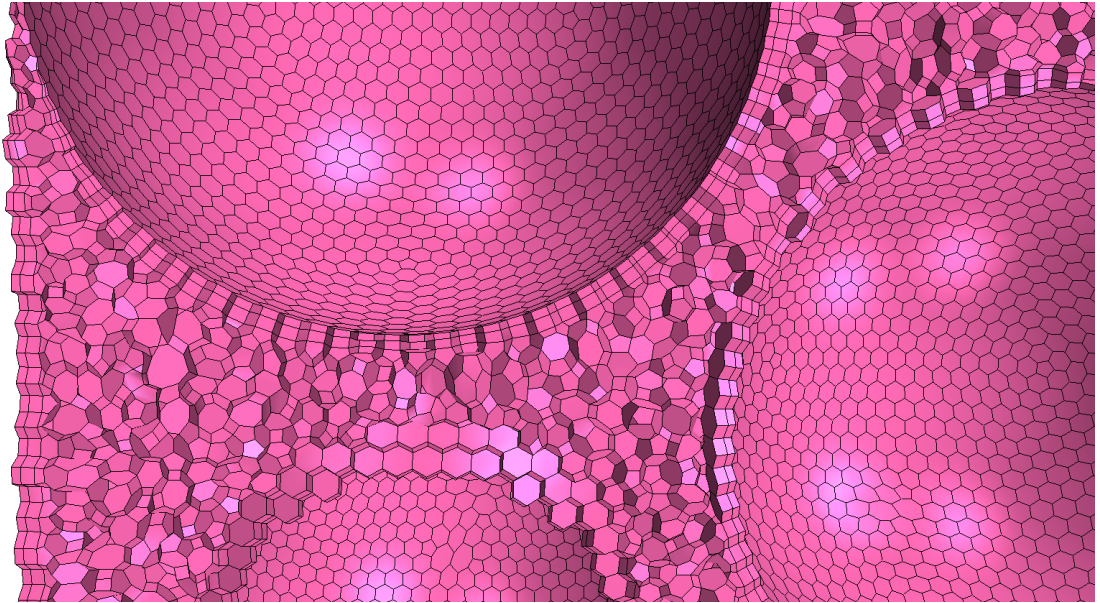


Figure 20: Detail of a typical polyhedral mesh of the interstitial region in a packed-bed of spheres. Close to the walls two layers of prism cells are visible.

# 4 Creating complex geometries for CFD

At the chair of Chemical and Process Engineering at Technische Universität Berlin a workflow generating automatically fixed-bed structures was developed by Eppinger et al. (2011). This workflow represents the basis for the creation of catalytic fixed-bed reactors in this thesis. The following chapter describes the method briefly. Furthermore, a novel algorithm is presented which generates artificially random foam structures. Both approaches are based on the *discrete element method* (DEM), which is shortly described below. Major advantages of an automatically generated geometry is its low time consumption, flexibility in adjusting parameters, like tube and particle dimensions, and its fast convertibility into geometries suitable for CFD simulations.

## 4.1 Automatic creation of fixed-bed reactor geometries for CFD

The creation of randomly packed beds with DEM is described briefly. Several researchers have applied this method to generate fixed beds of spheres (Ookawara et al., 2007; Augier et al., 2010; Zobel et al., 2012) or beds of non-spherical particles (Bai et al., 2009). The basic idea is to obtain the bed geometry by simulating the process of filling of the reactor tube with particles. In the following, first, the discrete element method is introduced shortly. Second, the automatic process of simulating the filling of a tube by DEM-particles is described.

### 4.1.1 Discrete element method

DEM is an engineering approach to simulate many moving discrete particles that interact with each other and the surrounding flow. It is an extension of the Lagrangian modeling approach, which was established by Cundall and Strack (1979). The basic idea of DEM is to include inter-particle contact forces into the equations of motion. In STAR-CCM+ DEM is formulated in a classical mechanic fashion that allows the particles to overlap, which is called the soft-particle formulation (CD-adapco, 2014). The obtained contact force is proportional to the overlap, the particle material and the geometric properties.

In a DEM simulation, DEM particles represent the Lagrangian phase, whereas DEM describes the particle behavior. The interaction between particles and between particles and walls are determined by the momentum balance equation for a material particle:

$$m_p \frac{d\vec{v}_p}{dt} = \vec{F}_s + \vec{F}_b \tag{4.1}$$

where $\vec{F}_s$ are forces acting on the particle's surface, i.e., drag force, and pressure gradient force, and $\vec{F}_b$ are body forces:

$$\vec{F}_b = \vec{F}_g + \vec{F}_c \tag{4.2}$$

with $\vec{F}_{\mathrm{g}}$ as the gravity force, and $\vec{F}_{\mathrm{c}}$ as the contact forces, which are defined as CD-adapco (2014):

$$\vec{F}_c = \sum_{\text{neighbor particles}} \vec{F}_{\text{contact}} + \sum_{\text{neighbor walls}} \vec{F}_{\text{contact}} \tag{4.3}$$

In STAR-CCM+ the contact forces can be specified with several models, e.g., Hertz-Mindlin or Walton-Braun. The basic idea is to formulate the contact force with a spring-dashpot approach. The spring pushes particles apart by repulsive forces, whereas the dashpot dampens collision of particles. At the contact point of particles the forces are formulated as a pair of spring-dashpot oscillators. This pair has a normal direction and a tangential direction force, where the direction is defined in regards of the contact plane normal vector (CD-adapco, 2014).

The Hertz Mindlin model turned out to work fine for most of the investigated cases. It is a variation of the non-linear spring-dashpot contact model, based on the Hertz-Mindlin theory. A comparison of different contact force models and a more detailed description give Di Renzo and Di Maio (2000), as well as Zhu et al. (2007).
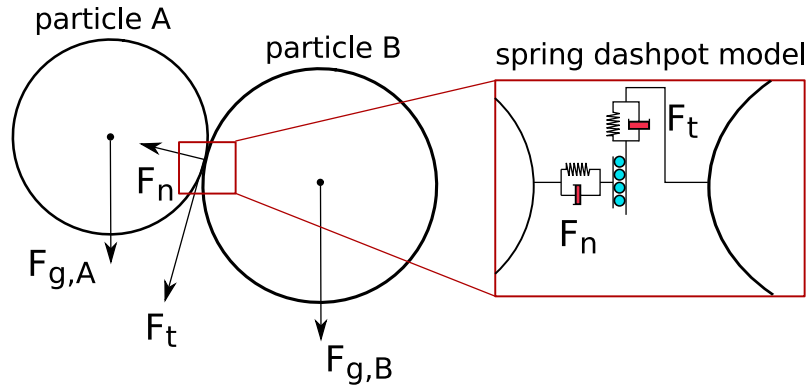


Figure 21: Forces acting on DEM particles with a detail on spring-dashpot contact model at contact point.

In Fig. 21 the forces acting on DEM particles are illustrated with a detail on the spring-dashpot contact model at contact point. The force vector in the contact point between two particles is formulated by:

$$\vec{F}_{\text{contact}} = \vec{F}_n + \vec{F}_t \tag{4.4}$$

with $\vec{F}_n$ being the normal force component and $\vec{F}_t$ the tangential force component, respectively.

The normal component of the force vector can be written as:

$$\vec{F}_n = -K_n d_n - N_n v_n \tag{4.5}$$

with $d_n$ as the overlap in the normal direction at the contact point and $v_n$ as the velocity component in normal direction. The normal spring stiffness is defined by:

$$K_n = \frac{4}{3} E_{\text{eq}} \sqrt{d_n R_{\text{eq}}} \tag{4.6}$$

and the normal damping as:

$$N_n = \sqrt{(5K_n M_{\text{eq}})} N_{n\text{damp}} \tag{4.7}$$

The tangential component can be formulated by:

$$\vec{F}_t = \begin{cases} -K_t d_t - N_t v_t & \text{for} \quad |K_t d_t| < |K_n d_n| C_{fs} \\[2mm] -\dfrac{|K_n d_n| C_{fs} d_t}{|d_t|} & \text{for} \quad |K_t d_t| \geq |K_n d_n| C_{fs} \end{cases} \tag{4.8}$$

In the equations above, $C_{fs}$ is a static friction coefficient, whereas the tangential spring stiffness can be written as:

$$K_t = 8G_{\text{eq}} \sqrt{d_t R_{\text{eq}}} \tag{4.9}$$

the tangential damping is defined as:

$$N_t = \sqrt{(5K_t M_{\text{eq}})} N_{t\text{damp}} \tag{4.10}$$

Furthermore, the damping coefficient $N_{\text{damp}}$ equals one for $C_{\text{rest}} = 0$. Otherwise, it can be calculated by:

$$N_{\text{damp}} = \frac{-\ln(C_{n\text{rest}})}{\sqrt{\pi^2 + \ln(C_{n\text{rest}})^2}} \tag{4.11}$$

The equivalent radius $R_{\text{eq}}$ between particle A and particle B is:

$$R_{\text{eq}} = \frac{1}{\frac{1}{R_A} + \frac{1}{R_B}} \tag{4.12}$$

The equivalent particle mass is defined as:

$$M_{\text{eq}} = \frac{1}{\frac{1}{M_A} + \frac{1}{M_B}} \tag{4.13}$$

In addition, the equivalent Young's modulus $E_{\text{eq}}$ between the two particles can be written as:

$$E_{\text{eq}} = \frac{1}{\frac{1-v_A^2}{E_A} + \frac{1-v_B^2}{E_B}} \tag{4.14}$$

The equivalent shear modulus $G_{\text{eq}}$ is expressed as:

$$G_{\text{eq}} = \frac{1}{\frac{2(2-v_A)(1+v_A)}{E_A} + \frac{2(2-v_B)(1+v_B)}{E_B}} \tag{4.15}$$

with $M_A$ and $M_B$ are the masses of particle A, and particle B, respectively, $R_A$ and $R_B$ are the radii, $E_A$ and $E_B$ are the Young's modulus, $v_A$ and $v_B$ are the Poisson coefficients. Additionally, $d_n$ and $d_t$ are the overlaps in the normal and tangential directions at the contact point, whereas $v_n$ and $v_t$ are the velocity components in the normal and tangential direction.

The equations above are formulated for the particle-particle interaction. For the calculation of particle-wall collision, it is assumed that $R_{wall} = \infty$, and $M_{wall} = \infty$. Hence, the equivalent radius is determined by $R_{eq} = R_{particle}$, and $M_{wall} = M_{particle}$.

Besides spherical particles, non-spherical particles are even more often used in catalytic fixed-bed reactors. Since DEM is formulated for spheres, non-spherical particles are approximated by so called composite particles. The desired shape of the non-spherical particle is approximated by a user-defined amount of spheres which retain their position with each other. The arrangement of the amount of particles is computed automatically. In Fig. 22 (A) the desired cylinder is shown, which is approximated by (B) 20 DEM spheres and (C) 100 DEM spheres. It has to be mentioned that the more DEM spheres are used to approximate the desired shape, the more computational time is required. It turned out that approx. 80-100 DEM spheres represent a good trade-off between accurate shape description and low computational cost. As it can be seen in the figure, the edges of the original particle shape is not represented, since the shape is approximated with spheres. This is a disadvantage of the composite particle approach.
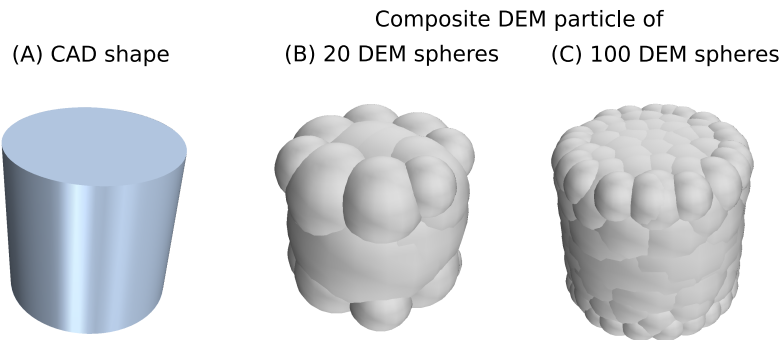


Figure 22: (A) actual CAD particle shape, (B) approximated with 20 DEM spheres, and (C) 100 DEM spheres.

### 4.1.2   DEM simulations for generating random packed beds

The packed-bed structures in this thesis are based on the main ideas of the workflow developed by Eppinger et al. (2011), which has been modified continually over the last years. The procedure of the random packed-bed generation is shown in Fig. 23. In the first step (1) the tube is filled with DEM particles, i.e., spheres or cylinders. When the particles have settled, the local position of each particle can be extracted. With this information a CAD model of the packed bed is built (2) where the cylinders can be replaced by one-hole or multi-hole cylinders with the same outer diameter. Afterward, the surfaces are assigned and the geometry can be meshed (3). Finally, CFD simulations can be performed with desired physical models and boundary conditions (4).

**(1) DEM simulation**
with (a) DEM-spheres or (b) composite particles

settling

data position
extraction

**(2) CAD modeler**
with data position

**(3) Mesing**

**(4) CFD simulation**
with physical models
and boundary conditions
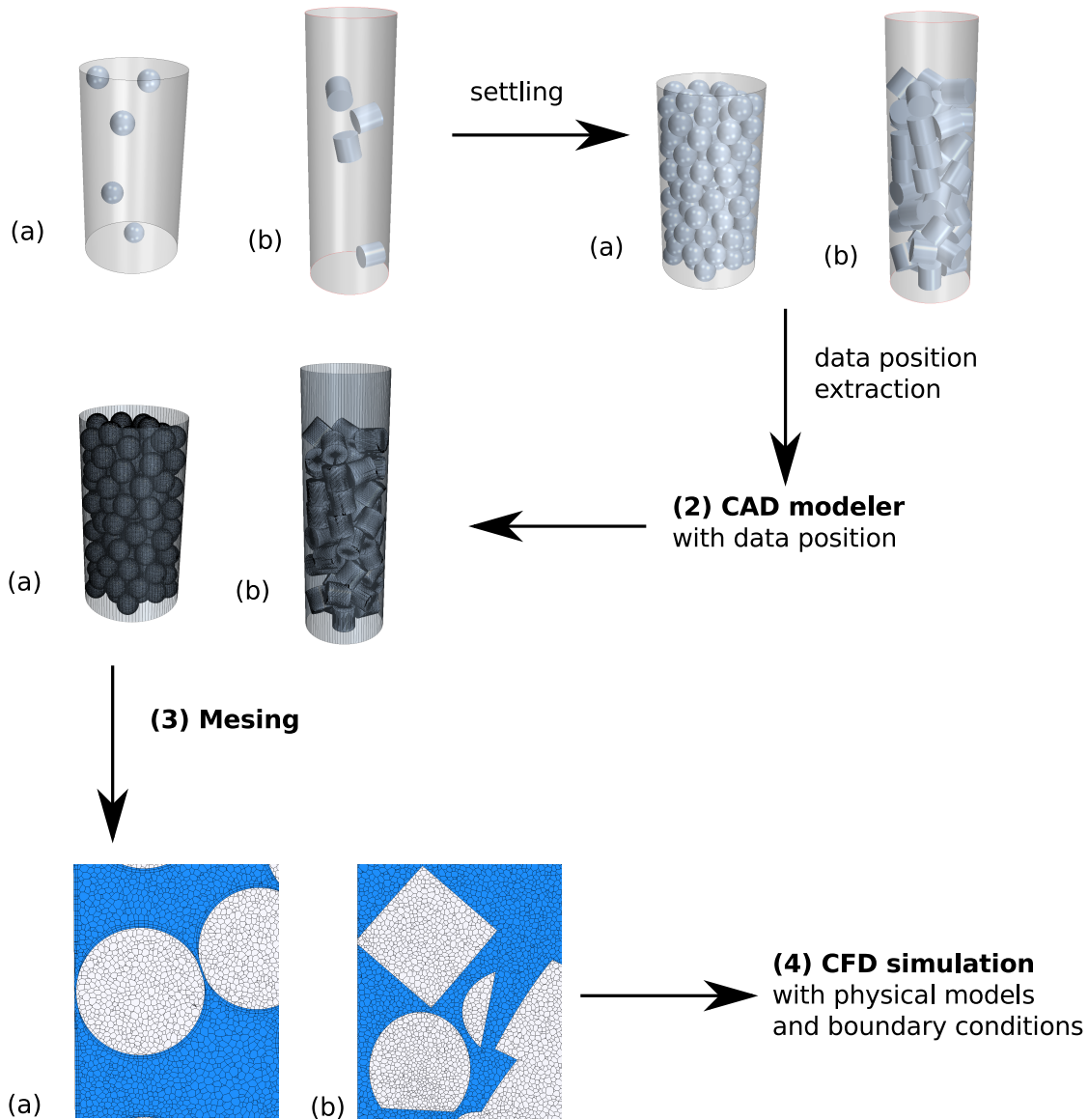
Figure 23: Procedure scheme for random packed-bed generation. (a) with spherical particles and (b) with cylindrical particles.

## 4.2    Contact-area modifications for non-spherical particles

Spherical particles touch neighboring particles or confining walls in points. In contrast, non-spherical particles show point contacts, line contacts, and area contacts, see Fig. 9 for a visualization. As already mentioned earlier, the space close to the contact area tends to be discretized with bad quality cells. To overcome this numerical problem several kinds of contact-area modification methods have been developed. In the following, these methods are described in detail.
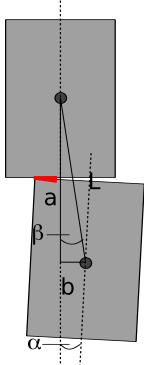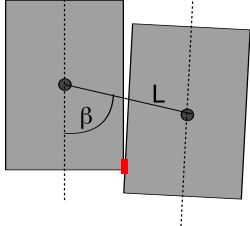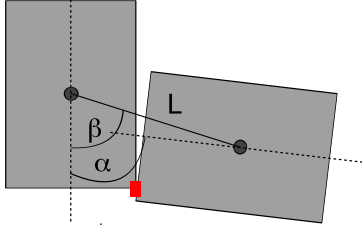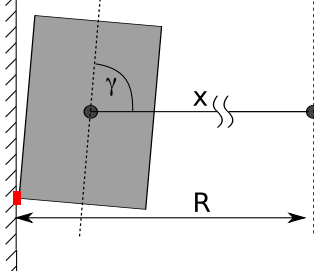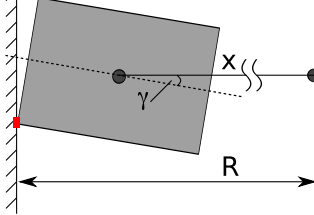
In general two different kinds of contact-area modification methods have been developed, i.e., global (gaps and overlaps) vs. local (bridges and caps) methods. Since the global methods change the bed geometry entirely, local methods are recommended (Dixon et al., 2013b; Bu et al., 2014). In Tab. 4 different contact areas of non-spherical particles with distances between centroids and angles between face normals are listed. This table shows that unlike for spherical particles the contact areas are located in a certain range of distances and angles. Hence, tolerances are introduced defining contact areas, which represent a trade-off between the amount of geometrical modifications. These tolerances are listed in Tab. 4. The position data and face normals are exported from the DEM simulations. The distance $L$ between centroids of particles and angles between face normals $\alpha$ and angles between centroids $\beta$ are subsequently calculated by an Octave code.

Besides the caps method, which flattens touching particles locally, the bridges method is implemented. In Fig. 24 the bridges method is shown schematically. The dimensions of the bridges are enlarged for visualization reasons. In the figure two touching spheres are shown. However, the method can be applied for non-spherical particles in a similar way. Firstly, an object is created (bridge 1), which is larger than the actual bridge but has the same thickness. This object is then subtracted from the two touching particles. The resulting particles represent the solid particle phase. Secondly, bridge 2, which has the same length but a larger thickness than the actual bridge, is merged with the two particles and subsequently subtracted from the entire inner volume of the reactor. As a result, the fluid phase around the particle and the bridge is created. In a last step, the actual bridge shape is inserted into the geometry. The shape of a bridge is a cylinder at area contacts, and a cuboid at line contacts. A similar process is applied for particle-wall contact areas.

In addition to line and area contacts, contact points are critical in packed beds of non-spherical particles. Since the composite DEM particles consist of multiple spheres, sharp edges of cylinders cannot be represented. Consequently, overlaps occur, where DEM cylinders touch each other with edges. In Fig. 25 a schematic of a contact point between two non-spherical particles is shown. The total amount of DEM particles is very low and their dimensions enlarged for visualization purpose. Overlapping regions can be treated generally by two methods. Firstly, the particles can be *united*, which results in several particle clusters, or agglomerations. Secondly, the *caps* method can be applied at contact points. The united method has the disadvantage that heat can be transferred from one particle to another without a resistance. Furthermore, under certain circumstances there are thin regions to be meshed, which provokes bad quality cells. The caps method avoids these difficult regions by introducing gaps between particles. Now heat from one particle to another is transferred only through the gas phase, since there is no direct contact between the particles. As a consequence, the bridges method is applied for contact lines and contact areas in combination with the united method for contact points.

Table 4:  Contact areas of non-spherical particles with distances between centroids and angles between face normals.

| Contact type | Distance | Angle $\alpha$ | Angle $\beta$ |
|---|---|---|---|
| Area contact: end-end | $\dfrac{L}{1.1 \cdot \sqrt{a^2 + b^2}} <$ | $\alpha < 10°$ | $\beta < 10°$ |
| Line contact: side-side | $L < \dfrac{1.02 \cdot r \cdot 2}{\sin\beta}$ | $\alpha < 7°$ | $50° < \beta < 130°$ |
| Line contact: end-side | $L < 1.1 \cdot (L/2 + r)$ | $80° < \alpha < 100°$ | $\beta < 20°$ or $70° < \beta < 110°$ |
| Line contact: wall-side | $x > 0.996 \cdot (R - r)$ | $92° < \gamma < 188°$ | |
| Area contact: wall-end | $x > 0.99 \cdot (R - L/2)$ | $\gamma < 5°$ | |

**1. Creation of solid particles:**



original shape    bridge 1    new solid shapes
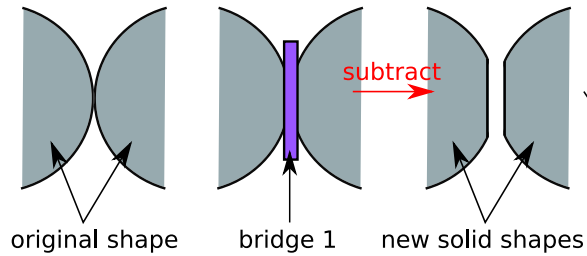
**2. Creation of fluid phase:**

original shape    bridge 2    new fluid phase

**3. Actual shapes**

actual bridge shape

**Bridge shapes:**

bridge 1    bridge 2    actual bridge shape

**Phases:**

solid phase    fluid phase
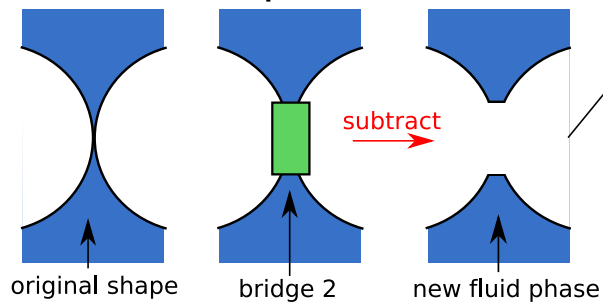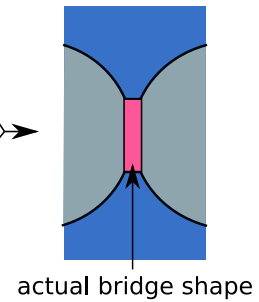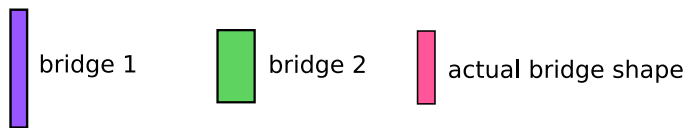
Figure 24: Schematic of the bridges method.



DEM simulation    Extracted geometry    Contact point treatment

contact point

united method

caps method
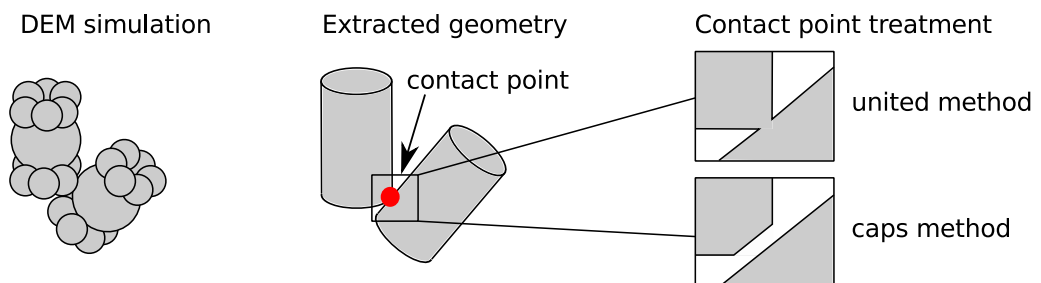
Figure 25: Schematic of contact point modification for non-spherical particles

## 4.3   Automatic creation of foam geometries for CFD

Several authors used scanned foam data for their model algorithms, e.g., Roberts and Garboczi (2002); Lautensack et al. (2008). These models are limited to the scanned structure which is determined by its morphological characteristics. On the contrary, an artificial foam modeler is able to generate structures which can be varied in terms of the most significant morphological characteristics, i.e., porosity, specific surface area and strut dimensions. Furthermore, the modeler does not have to use scanned data but generates the structure automatically, as well as it generates a format that is ready to use for a CFD simulation. In the following section the workflow is denoted as catFM (*cat*alytic *F*oam *M*odeler), which is summarized in Fig. 26. The basic geometric operations are performed with Java-3D 1.5.1 (Sun Microsystems, 2008). The algorithm is vector-based, i.e., no functions are used for evaluating pixel graphics.

| 1.Initial set of points | → | 2. Set of tetrahedrons | → | 3. CAD foam structure |
|---|---|---|---|---|

– Import set of points *S*

– Tetrahedron mesh:
   - convex hull of S
   - meshing

– Triangulation of foam structure

– Parameterizing
   - porosity
   - specific surface area
   - strut dimensions

– Bed of spheres

– Distribution of radii

– Transformation:
   tetrahedron mesh → mosaic

→ **Set of points *S***
   in *.csv* format

→ **Tetrahedron mesh & foam structure**

→ **CAD foam structure**
   in *.step* format

Program: STAR-CCM+

Program: Java

Program: Java

Figure 26: Workflow of catFM

The catFM algorithm applies the Voronoi tessellations, which have a microstructure similar to that observed in foams (Roberts and Garboczi, 2002). Around each point or seed there exists a region of space that is closer to that point than any other. This region designates the cell of a Voronoi tessellation (Chiu et al., 2013). The first part of the workflow is the generation of an initial set of points, or seed of points. It is obtained by a packed bed of spheres, see Fig. 27. A randomly distributed packed bed can be generated with DEM, as described already in section 4.1. Spherical particles with log normally distributed diameters are injected on top of a cylinder. The size distribution of the spheres is chosen close to that of the pore distribution of a 30 pores per inch (PPI) foam. It is assumed that the relative distribution does not change significantly with PPI, which was observed experimentally by Garrido et al. (2008). Consequently, the absolute size of the distribution of the spheres is not significant toward the foam structure. However, the confining walls are influencing the radial porosity in a packed-bed. For mono-sized particles the effect occurs as far as five sphere diameters (van Antwerpen et al., 2010). On the contrary, the effect is much smaller for poly-dispersed particles. Goodling et al. (1983) recognized an influence as far as two sphere diameters for polydisperse particles. For deformed spheres Giese et al. (1998) noticed a wall influence until 2.5-3. Therefore, a tube-to-particle-diameter ratio larger than 10 was

56

chosen for the packed bed. Finally, for the CFD simulations only a inner section of the resulting geometry is considered. Consequently, an irregular foam structure is expected with a certain size distribution of large and small cells with only a small influence of the packed-bed setup. When all the particles are settled, the position of their centroids is extracted and used as the initial set of points. This part is performed with STAR-CCM+ (CD-adapco, 2014).
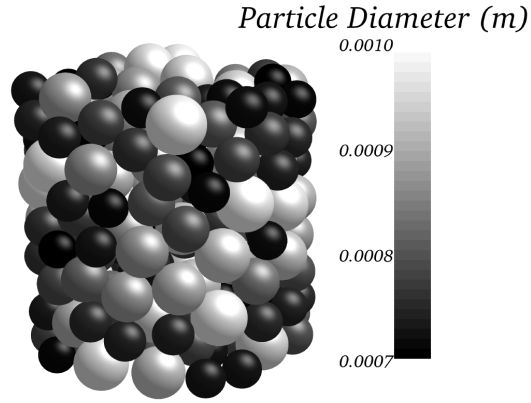


Figure 27: Packed-bed of spheres providing initial set of points

The second part of the algorithm is the generation of tetrahedrons from the initial set of points. Keep in mind that the Delaunay triangulation of a set of points corresponds to the dual graph of the Voronoi diagram for this set of points. In other words, connecting the centers of the circumcircles of the Delaunay triangulation produces the Voronoi diagram (de Berg et al., 2008). Hence, the set of points is triangulated by the Delaunay condition. In Fig. 28 a set of points is triangulated with the Delaunay algorithm (A), whereas in (B) the same set of points is shown with a Voronoi diagram. Three circumcircles are shown. In Fig. 28 (C) both algorithms can be seen.
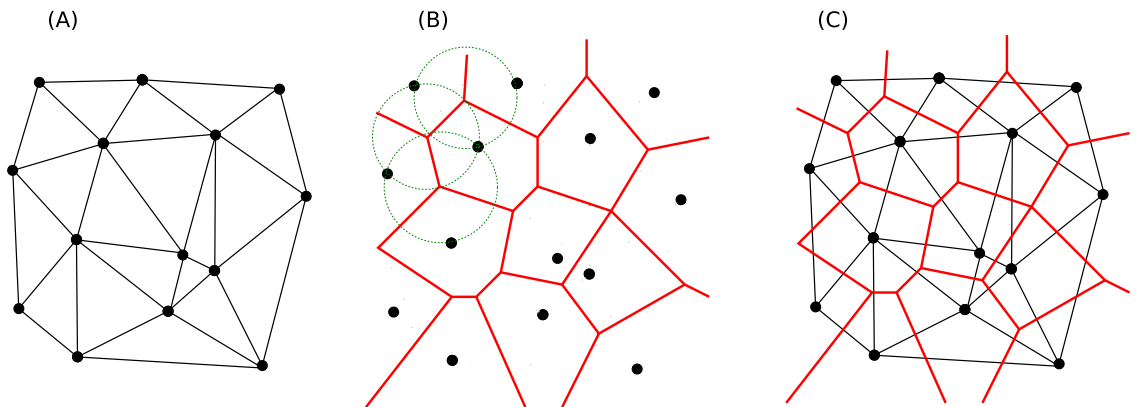


Figure 28: (A) Delaunay triangulation and (B) Voronoi diagram for the same set of points. (C) shows both algorithms.

Additional constraints are formulated to obtain a high quality tetrahedron mesh, i.e., skewness of triangles and tetrahedrons and aspect ratio of tetrahedrons. Furthermore, two nearby triangles are checked whether a smaller skewness is achieved by reordering common edges, also known as

flipping (de Berg et al., 2008). In a first step the points at the edge of the region are identified to limit the meshing in terms of space. Therefore, a convex hull is generated involving these points. Subsequently, the triangles are optimized by the before mentioned constraints. As a second step, points near the hull are identified and enclosed into the hull followed by an optimization. The generation of a tetrahedron mesh starts by applying an initial tetrahedron in the center of the domain resulting in a convex hull. This hull is extended until every point is included in a contiguous set of tetrahedrons, see Fig. 29. In a consecutive step the tetrahedron mesh is transformed in the foam structure. For this purpose, centroids of nearby tetrahedrons are connected resulting in closed curves. These curves form a window and finally the rudimentary foam structure.



(1) Initial tetrahedron        (2) Meshing Process        (3) Tetrahedron volume mesh
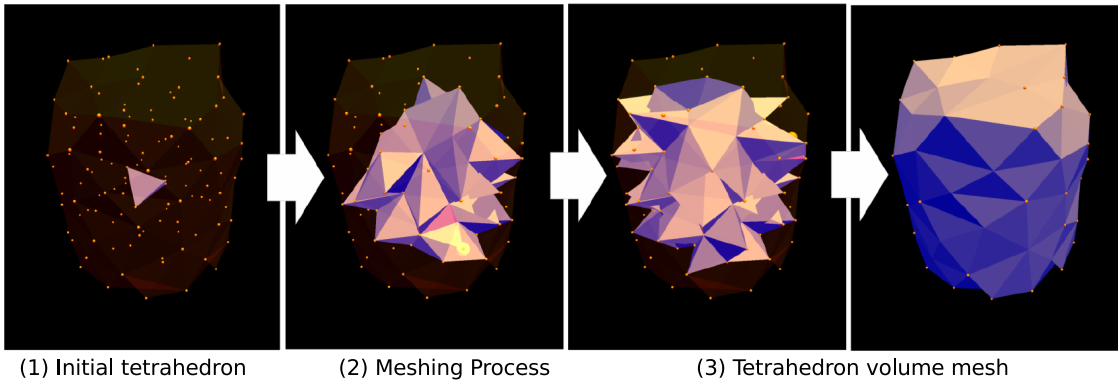
Figure 29: Generating the tetrahedron mesh

In the third part of catFM the CAD foam structure is developed. Two groups of surface vertices are created. In a first step, for each window the dedicated vertices are duplicated and moved toward the center of the window with a minimal extend. After creation of these window surface-vertices, the same procedure is applied for the dedicated cells. Subsequently the created surface vertices are meshed by a simple algorithm that creates a surface triangulation. As a consequence, rudimentary cell windows and struts are created. Finally, the morphological properties, i.e., porosity, specific surface area and strut dimensions can be adjusted, see Fig. 30. The CAD model is written in STEP format which can be imported conveniently into CFD software, where it is meshed appropriately.
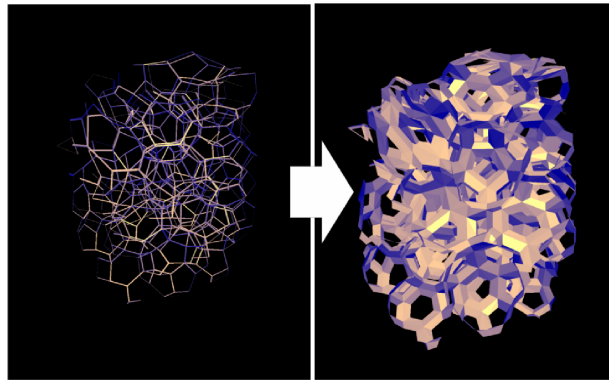


Figure 30: Parametrization of the foam structure

# 5 Simulating catalytic stagnation-flow reactors

A stagnation-flow reactor (SFR) is an example how catalytic reaction kinetics can be investigated in a device with only small influence of fluidic effects. Since several years SFR have been used to study reactions under realistic conditions, i.e., heterogeneous reactions in typical washcoats. The following studies are intended to prove the feasibility to include microkinetics in CFD simulations and to extend the model taking into account pore processes.

## 5.1 Dry reforming of methane on rhodium[2]

The first set of numerical simulations is orientated toward the stagnation-flow reactor experiments of McGuire et al. (2011). A gas flow is guided to a catalytic disk which generates a viscous boundary layer. In this layer the temperature and species compositions depend only on one independent variable, i.e., the axial coordinate. However, the velocity distribution can be two-dimensional or three-dimensional, respectively. Scaling of the primary velocity leads to a simplified 1D stagnation-flow field approximation (Kee et al., 2003).

### 5.1.1 Experimental setup

In Fig. 31 the setup of the stagnation-flow reactor from McGuire et al. (2011) is illustrated. The reactant gas enters the reactor chamber from below through a porous frit to guarantee a uniform flow distribution. The catalyst surface is approx. 5 cm in diameter and has a distance of 1.6 cm from the frit. The temperature of the catalyst is maintained by a heating device. A rhodium catalyst supported on strontium-substituted hexaaluminate ($SrAl_{11}O_8$) was used. Gas phase concentrations were measured by a microprobe made of quartz. The tip of the probe is 0.3 mm in diameter and was placed 10 mm from the center of the catalytic disc. Gas flow was sent to a quadrupole mass spectrometer (SRS RGA 200) for analysis. For more details on the experimental setup, see McGuire et al. (2011).

In addition to the measurements, the gas phase concentration, velocity, as well as temperature profiles were simulated with an idealized 1D model, i.e., an axisymmetric stagnation-flow boundary-layer problem. The independent variable is the normal distance from the catalytic surface. The dependent variables are the axial velocity, the scaled radial velocity, the temperature, and the mass fractions (McGuire et al., 2011). In the result section, the data denoted by *1D* is taken from McGuire et al. (2011).

---

[2]This section is based on the publication: Wehinger, G. D., Eppinger, T., Kraume, M. (2014). Fluidic effects on kinetic parameter estimation in lab-scale catalysis testing – A critical evaluation based on computational fluid dynamics, *Chemical Engineering Science*, 111, 220-230
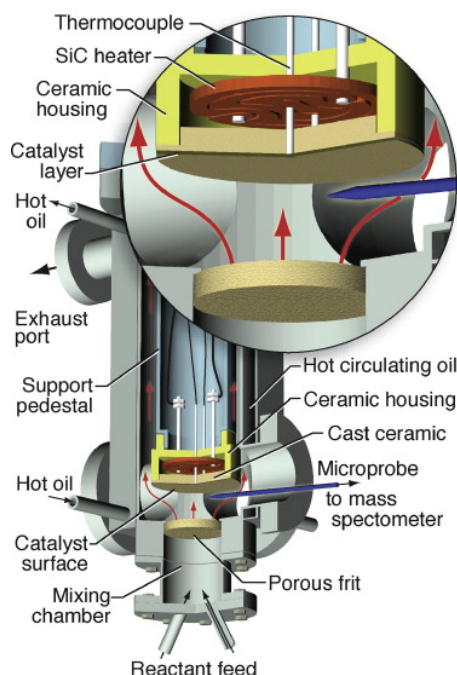
Figure 31: Stagnation-flow reactor setup. Reprinted from McGuire et al. (2011) with permission from Elsevier.

### 5.1.2 CFD setup

The calculation domain of the stagnation-flow reactor was abstracted as a flat cylinder, see Figure 32. The diameter represents the catalytic surface in the experiments, i.e., 5.0 cm. The height of the domain is 1.6 cm, which is in accordance with the separation distance between the reactant inlet and the catalyst in the experiments. A finer mesh is chosen close to the catalytic surface where the steepest gradients of the transport quantities appear. Toward the inlet the mesh size gets larger, see Figure 32 (B). After a mesh independence study, the total number of cells amounts to approx. 800,000. The boundary layer, approx. 3.5 mm in height, is resolved with $\approx 20$ cells in the axial coordinate $z$.

The conditions at the flow inlet are: velocity in axial direction $v_{in} = 0.9$ m/s, pressure $p_{in} = 1$ bar, temperature $T_{in} = 27\,°C$, inlet mole fractions $x_{CO_2}/x_{CH_4}/x_{Ar} = 0.15/0.10/0.75$. The reactor in the experiments operated under steady state conditions at 40 kPa. Therefore, at the outlet the pressure is set to $p_{out} = 40$ kPa. At the catalytic surface the temperature is constant at $T_{cat} = 800\,°C$. Only heterogeneous reactions are taken into account. Consequently, at the catalytic wall surface reactions occur described by the DRM microkinetics, see Appendix Tab. 22. The catalyst is dispersed in the porous support. Therefore, the catalytic surface is much larger than the geometric surface. The $F_{cat/geo}$ value in Eq. (3.42) is set to 90 in line with McGuire et al. (2011). The total available surface site density $\Gamma$ is $2.72 \cdot 10^{-9}$ mol/cm$^2$. The catalyst layer amounts to approx. 20 $\mu$m in the experiment, which leads to negligible intraporal diffusion (Seyed-Reihani and Jackson, 2004). Consequently, no additional pore model is used.
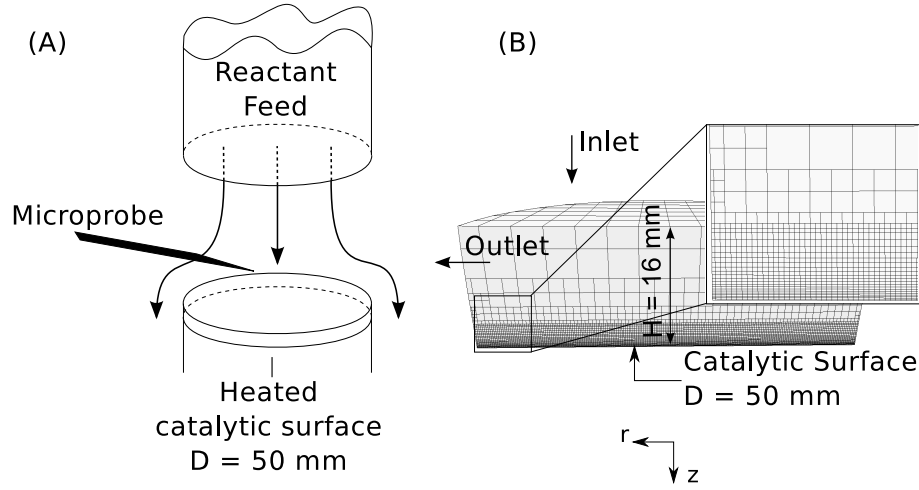
Figure 32: (A) Scheme of stagnation-flow reactor. (B) Calculation grid for the 3D stagnation-flow reactor with closer view of local mesh refinement.

### 5.1.3   Results and discussion

Figure 33 shows the temperature and axial velocity profiles as a function of the axial distance from the surface. The one-dimensional simulations are based on an axisymmetric stagnation-flow boundary-layer problem. It can be clearly seen, that the one-dimensional prediction of McGuire et al. (2011) and the three-dimensional simulation are in excellent agreement.
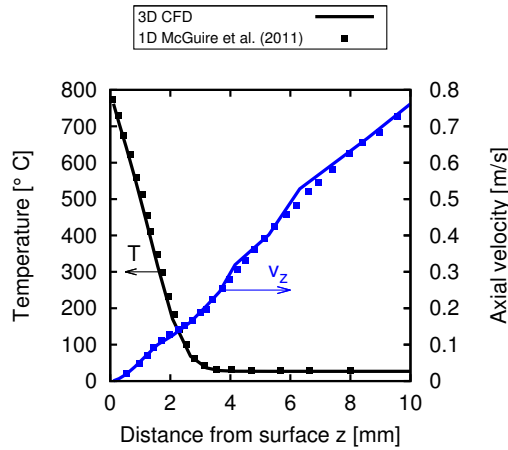


Figure 33: Temperature and velocity profile of the stagnation-flow simulation. One-dimensional (from (McGuire et al., 2011)) and three-dimensional results.

In Figure 34 (A) and (B) mole fractions over distance from surface are illustrated. Only the near-surface boundary layer is shown ($z = 0 - 3$ mm). The dots indicate the experimentally measured mole fractions from McGuire et al. (2011). The lines represent the simulations. Again, the one-dimensional and three-dimensional profiles are in excellent agreement. The microkinetic 1D and 3D models predict the experiments accurately, except for the measurement of $CO_2$ and CO closest

to the surface. McGuire et al. (2011) suggests influence of the microprobe as the reason for this discrepancy.
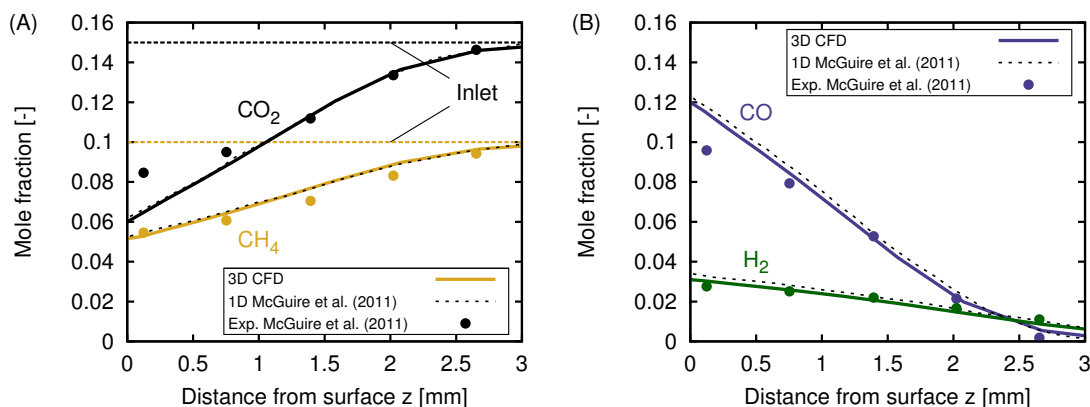


Figure 34: Mole fractions of (A) $CH_4$ and $CO_2$ and (B) $H_2$ and CO over distance from surface. Comparison between experiments, 1D simulations from (McGuire et al., 2011) and 3D simulations.

Figure 34 (B) shows the mole fractions over distance for the DRM products, i.e., CO and $H_2$. As a result of excess $CO_2$, the reverse water-gas-shift process ($H_2 + CO_2 \rightleftharpoons CO + H_2O$) causes an increased CO:$H_2$ ratio. The boundary layer of $H_2$ is larger than the boundary layer of CO, due to the higher mass diffusivity of $H_2$ at these temperatures. The simulations predict the product concentration profiles in good accuracy to the experiments. And again, one-dimensional and three-dimensional simulations fit very well.

Comparing the concentration profiles between one-dimensional and three-dimensional simulations, it is evident that a higher spatial resolution of the domain does not lead to more information. Fig. 35 and Fig. 36 illustrate this behavior. The temperature and concentration profiles show a one-dimensional orientation toward the catalytic surface except for the edges of the domain. It can be concluded that the stagnation-flow reactor can be simulated adequately by a one-dimensional model. It has to be kept in mind that a measure device, e.g., a microprobe, has always an influence on the flow and concentration field. In the case of the stagnation-flow reactor measurements close to the surface are affected. In other cases, e.g., honeycomb channels, the in-situ measurement devices have a stronger influence of the flow field, as (Hettel et al., 2013) showed with CFD simulations. Nonetheless, the stagnation-flow configuration is well suited to investigate reaction kinetics with a low influence of fluidic effects. In addition, modeling the pore diffusion would enrich such calculations.
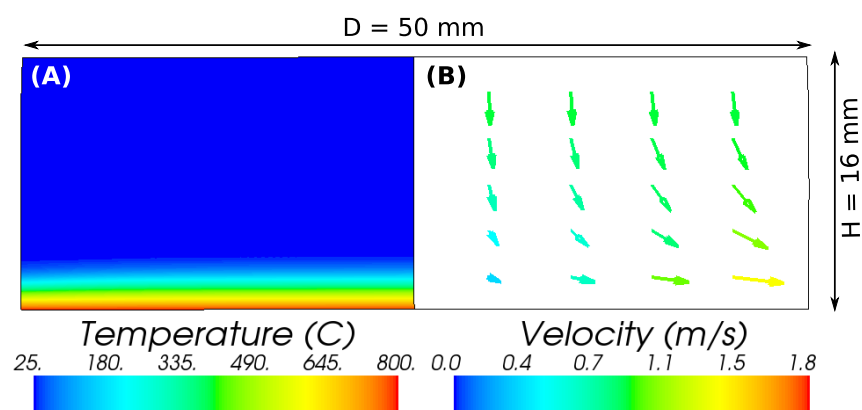
Figure 35: (A) Temperature distribution and (B) velocity vectors of the stagnation-flow reactor.
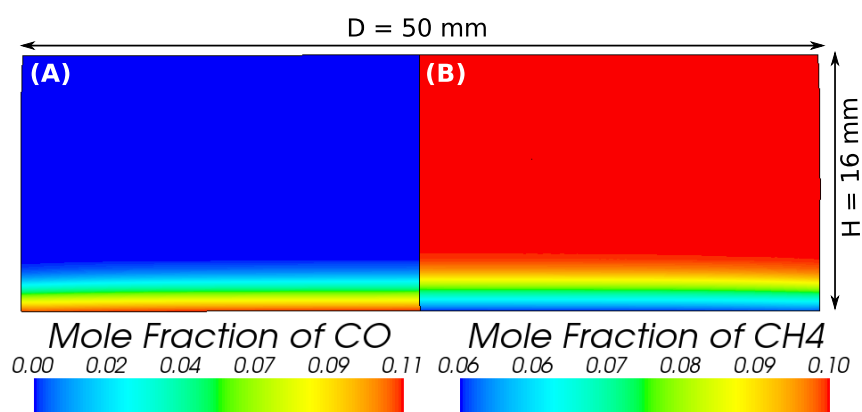


Figure 36: (A) CO mole fraction and (B) CH$_4$ molar fraction of the stagnation-flow reactor.

## 5.2   CO oxidation on rhodium

The second example is oriented toward the publication of Karadeniz et al. (2013), who investigated oxidation of carbon monoxide on a $Rh/Al_2O_3$ catalyst in a stagnation-flow reactor. Although this reaction is not as complex as DRM, mass transport inside the porous washcoat is significant. Three different approaches for taking these limitations into account are implemented in the CFD simulations and are compared with the detailed experiments. Furthermore, the CFD results, which are 2D and 3D, respectively, are compared with 1D simulations from (Karadeniz et al., 2013).

### 5.2.1   Experimental setup

The reactant gas, which consists of CO and $O_2$, is guided toward a catalyst layer, which can be heated up to a specific temperature. The catalyst layer, outer diameter of 5.5 cm, consists of a aluminum disc onto which a washcoat is coated. The rhodium catalyst was dispersed into the washcoat, which had a thickness of 100 $\mu$m, a mean pore size of 10 nm, and a porosity of 60%, as well as a tortuosity of 3. For more information about the catalyst preparation, see (Karadeniz et al., 2013). The SFR was operated at a pressure of 0.5 bar, and at temperatures of the catalytic disk between 500 and 900 K. Fig. 37 shows the setup used by Karadeniz et al. (2013).
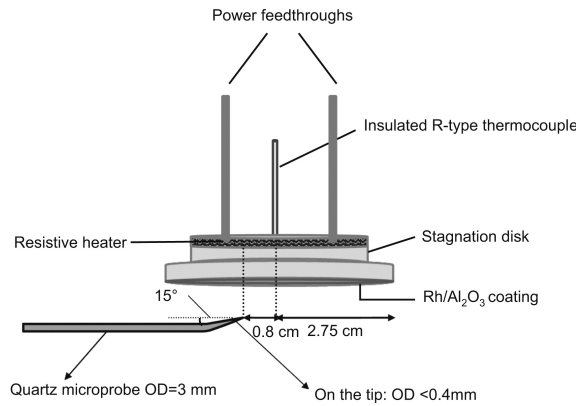


Figure 37: Stagnation-flow reactor setup used by Karadeniz et al. (2013). Reprinted from Karakaya and Deutschmann (2013) with permission from Elsevier.

The authors measured an active specific surface area of 0.21 $m^2$/g based on temperature-programmed desorption of CO. With this value the ratio can be calculated of catalytic active area to geometric area of the disc ($F_{cat/geo} = 30$). Firstly, the density and the porosity of $Al_2O_3$ can be related to the density of the catalyst: $\rho_{cat} = (1 - \varepsilon)\rho_{Al_2O_3}$. Secondly, the mass of the catalyst can be calculated: $m_{cat} = \rho_{cat}L\pi r^2$, with $L$ being the washcoat thickness. Utilizing the measured active specific surface are of CO, $F_{cat/geo}$ can be obtained. A microprobe was place above the catalytic surface in a radial distance of 0.8 mm. With the microprobe the gasphase concentration above the catalytic surface was measured as a function of distance from the surface. A resolution of 0.5 mm was achieved.

### 5.2.2   CFD setup

A subset of a detailed reaction mechanism of the water-gas shift reaction was utilized to describe the oxidation of carbon monoxide on Rh. It was published by Karakaya and Deutschmann (2013) and can be found in the Appendix Tab. 21. The microkinetics was implemented into STAR-CCM+ via the add-on program DARS-CFD. The mechanism is written in the Chemkin format. DARS-CFD compiles the microkinetics formulation to Fortran files, which can be edited by the user. $F_{cat/geo}$ for example has to be added in these Fortran files. The thermodynamic polynomials of the gasphase species CO, $CO_2$, and $O_2$ were taken from the Chemkin thermochemistry database (Kee et al., 1987). In the following two tables, Tab. 5 and 6, the parameters of the simulation and the boundary conditions are listed. Three different sets of experiments were reproduced with CFD simulations, i.e., case 1-3, whereas mainly the temperature of the catalytic disc is changed in the range of 521-873 K. For every experimental case three different washcoat models, i.e., *instantaneous diffusion, effectiveness factor* and *3D reaction-diffusion approach*, were applied.

Table 5: Parameters for simulating CO oxidation on Rh/Al$_2$O$_3$, from Karadeniz et al. (2013).

| | |
|---|---|
| Distance inlet to catalytic disk | 8 cm |
| Diameter of catalytic disk | 5.5 cm |
| Mean pore diameter | 10 nm |
| Washcoat thickness | 100 $\mu$m |
| Washcoat porosity | 0.6 |
| Tortuosity | 3 |
| Surface site density of Rh | $2.72 \cdot 10^{-9}$ mol/cm$^2$ |
| $F_{cat/geo}$ | 30 |

Table 6: Boundary conditions for simulating CO oxidation on Rh/Al$_2$O$_3$, from Karadeniz et al. (2013).

| Case | $T_{cat}$ [K] | $T_{in}$ [K] | $v_{in}$ [m/s] | $p$ [bar] | $x_{CO}$ [%] | $x_{O_2}$ [%] | $x_{Ar}$ [%] |
|---|---|---|---|---|---|---|---|
| 1 | 521 | 313 | 0.51 | 0.5 | 2.67 | 2.23 | 95.10 |
| 2 | 673 | 313 | 0.51 | 0.5 | 5.67 | 2.89 | 91.44 |
| 3 | 873 | 313 | 0.51 | 0.5 | 5.66 | 2.83 | 91.51 |

The first model, *instantaneous diffusion* or $\infty$–approach, assumes an infinitesimal fast mass transport inside the washcoat. As a consequence, the region where carbon monoxide reaction occur is limited to the interface between the washcoat and the gasphase, i.e., $\eta_L = 1$ in Eq. 3.74. No additional term is introduced to Eq. 3.41, i.e., $\dot{R}_i^{het} = F_{cat/geo}\tilde{M}_i\dot{s}_i$, with $F_{cat/geo} = 30$. The porous washcoat is treated as an impermeable solid isothermal material, which is not resolved by computational cells. The simulation is stationary and 2D axisymmetric. The applied calculation mesh accounts for approx. 3,000 cells, see Fig. 38. The trimmed cell model was used in STAR-CCM+, which produces hexahedral cells in 3D. The closer the catalytic wall, the finer the mesh. Inlet temperature and velocity, as well as feed composition are listed in Tab. 6. At the outlet a pressure

of 0.5 bar is taken into account to reflect the operation condition as reported in Karadeniz et al. (2013). At the catalytic surface, the experimental temperature of the catalyst was set as the thermal boundary condition and a no-slip velocity condition. In addition, the detailed reaction mechanism was implemented as a species boundary condition.
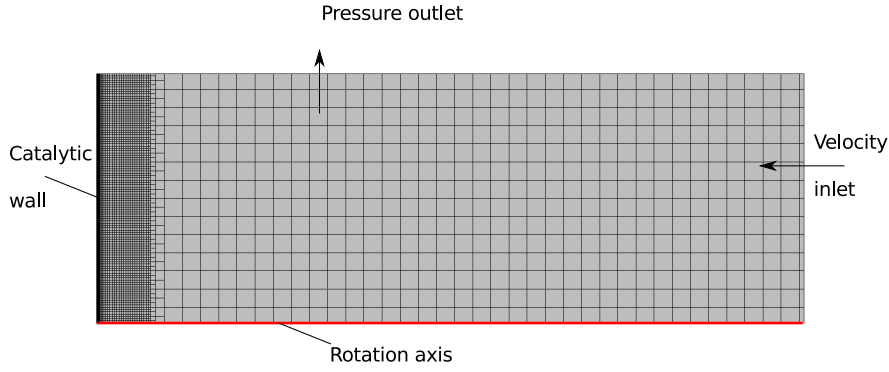


Figure 38: 2D mesh for the simulation of carbon monoxide oxidation on rhodium.

The second model accounts for transport limitations inside the washcoat, *effectiveness factor approach* or $\eta$–approach. It assumes that all of the species source terms are declined by the same value $\eta$, i.e., $\dot{R}_i^{\text{het}} = \eta F_{\text{cat/geo}} \tilde{M}_i \dot{s}_i$, with $\eta$ being the effectiveness factor, which is $\leq 1$. CO is chosen to be the limiting species, since it is consumed prior to oxygen. The same mesh as for the $\infty$–approach was used. Furthermore, all of the boundary conditions from the $\infty$–approach simulations were used, except for the species source term at the catalytic wall. The $\eta$–approach model was implemented in the Fortran files compiled by DARS-CFD. $\eta$, and consequently, the Thiele modulus $\phi = t_{\text{W}} \sqrt{(\gamma \dot{s}_{\text{CO}})/(D_{\text{eff}} c_{\text{CO},0})}$, is calculated in every substep of the simulation. Since the effective diffusion coefficient $D_{\text{eff}}$ is not implemented in DARS, it is also calculated in the subroutine with Eq. 3.75.

The three-dimensional reaction-diffusion model accounts for three-dimensional mass transport inside the washcoat. Consequently, the washcoat is discretized with computational cells. A common obstacle in simulating porous particles or layers is the fact that the velocity at the interface between gasphase and porous media is zero due to low permeability (Hayes et al., 2004). However, the conventional porous media model allows a momentum transport throughout this interface. The intention of this model is to simulate larger scale porous media, e.g., foams, packed beds or rock formation, where convective flow occurs. Consequently, the conventional porous media model would lead to velocity gradients inside the porous washcoat, which is physically not meaningful on this scale. To overcome this obstacle, gasphase and washcoat are treated as two separate computational regions, which are linked through a defined flux of energy and species mass. However, momentum is not transferred between the two regions. With this modeling approach convective flow is guaranteed to be neglected in the washcoat region. Inside these regions the conservation equations are solved separately. In this way mass transport by diffusion can be defined by the effective diffusion coefficient, see Eq. 3.75, in a convenient way. In STAR-CCM+ so called *Co-simulations* can be defined with one simulation being the leading simulation and the other

being the lagging simulation, respectively (CD-adapco, 2014). In the following, the steps of the Co-simulation approach are summarized:

1. The leading simulation, i.e., gasphase, iterates for a certain amount of steps. No reactions are taken into account, since they only occur in the washcoat. The interface to the washcoat is defined as an impermeable wall with a constant temperature and constant mass flux of each species.

2. By reaching the stopping criterion for the leading simulation, the mass fractions of all of the species at the wall are read out. This data is than mapped to the wall of the lagging simulation. These values are set constant.

3. The lagging simulation, i.e., the porous washcoat region, iterates until the stopping criteria, e.g., a certain amount of steps, is reached.

4. Mass fluxes at the catalytic wall are calculated from concentration gradients normal to the wall $\dot{m}_i = -D_{\text{eff},i}\rho\,\partial Y_i/\partial n$. Theses values are read out and mapped into the leading simulation. The loop begins again with step one.

Each simulation iterates for 50 steps until fluxes are exchanged between the two regions. To reduce the calculation time only a small section of the catalytic disk is simulated, i.e., a $4°$ slice. In the gasphase diffusion coefficients are calculated by kinetic gas theory. In the washcoat Knudsen diffusion is accounted for. Again, hexahedral cells are used with mesh refinement close to the wall, see Fig. 39. The gasphase accounts for 10,400 cells. The porous washcoat is discretized with 2,200 cells. Boundary conditions can be found in Tab 6. Since the actual surface is not resolved in the porous washcoat a source term accounts for the heterogeneous reactions. The ratio between catalytic surface to reaction volume is required in the model, which can be calculated by $F_{\text{cat/geo}}/L_{\text{W}} = 300,000$ 1/m.

### 5.2.3  Results and discussion

In Fig. 40 and Fig. 41 mole fractions of CO, $CO_2$, and $O_2$ are compared between the experiments from (Karadeniz et al., 2013) and CFD simulations for three different temperatures. The CFD simulations differ by pore model, i.e., instantaneous diffusion, effectiveness factor approach, and 3D reaction-diffusion inside the washcoat. As can be seen, the gradient at the catalytic wall is steeper for CO than for $O_2$. Furthermore, the larger the temperature, the higher the conversion of reactants.

Generally, the instantaneous diffusion approach overestimates the consumption of reactants. For all three temperatures the concentration of carbon monoxide is predicted to be zero at the catalytic wall. Expect for the lowest temperature, also oxygen is predicted to be totally consumed by the $\infty$–approach. However, the experimental values for CO at the catalytic disk are none-zero, which indicates an influence of mass transport limitations inside the porous washcoat. The $\infty$–approach does not capture this limitation.
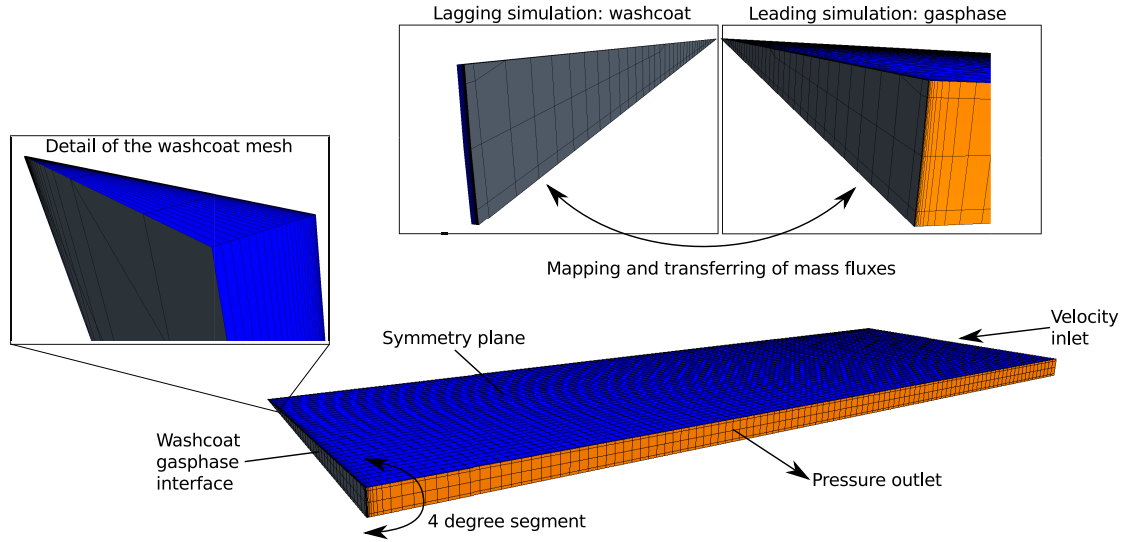
Figure 39: 3D mesh for the simulation of carbon monoxide oxidation on rhodium. With details of the washcoat mesh, and procedure scheme of Co-simulation approach.
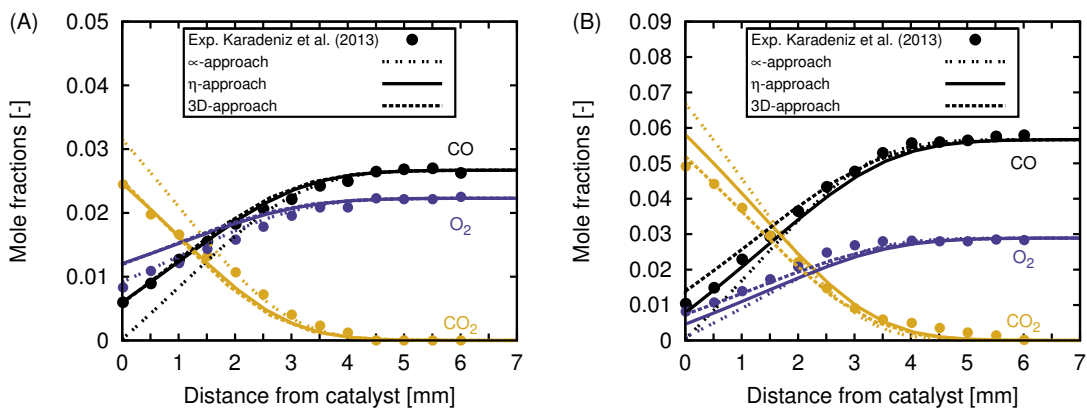


Figure 40: Mole fractions of the CO oxidation. Comparison between experiments from Karadeniz et al. (2013) and CFD simulations with different pore models. (A) $T_w = 521$ K, (B) $T_w = 673$ K.
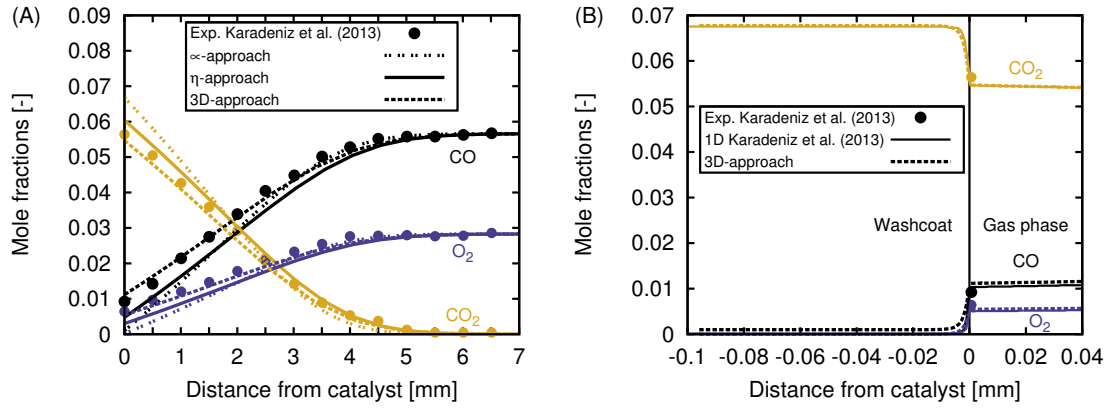
Figure 41: Mole fractions of the CO oxidation. (A) Comparison between experiments from Karadeniz et al. (2013) and CFD simulations with different pore models at 873 K. (B) Mole fractions inside the washcoat at 873 K.

For the lowest temperature, i.e., $T_{cat} = 521$ K, the concentration profiles of the $\eta$–approach and the 3D reaction-diffusion approach coincide. The experimental results are well predicted for CO and $CO_2$, however they differ by some extant for $O_2$. Karadeniz et al. (2013) assumes an error in measurement precision, since the molar balances for species are not violated in the simulations.

For higher temperatures, i.e., $T_{cat} = 673$ K, and 873 K, the $\eta$–approach and the 3D reaction-diffusion approach predicts slightly different species profiles. In both cases the more sophisticated reaction-diffusion model shows a better agreement with the experimental profiles than the effectiveness factor approach. The 3D model predicts a larger limitation of consumption of reactants. The effectiveness factors depend on the local reaction rates, as well as on the gas and washcoat parameters. The values are $\eta = 0.036$ for a temperature of 521 K, $\eta = 0.0186$ for $T_{cat} = 673$ K, and $\eta = 0.011$ for $T_{cat} = 873$ K. Theses values highlight that mass transport is highly limited inside the porous washcoat. Furthermore, the larger the temperature, the larger the influence of mass transport limitations.

A great advantage of the sophisticated 3D diffusion model are the species profiles inside the washcoat, as illustrated in Fig. 41 (B). With the help of these profiles a detailed idea of the penetration depth of each species is given. This is especially helpful for designing the height of the washcoat and hence the amount of dispersed catalyst. As can be seen in the figure, the reaction takes place only in the first 15 $\mu$m of the washcoat. After that distance oxygen is totally consumed and the reaction is stopped. However, the entire washcoat is 100 $\mu$m in depth, which makes approx. 85% of the washcoat unused. In general, the 3D reaction-diffusion model is in great agreement with the 1D reaction-diffusion model of Karadeniz et al. (2013).

In Fig. 42 a comparison between the one-dimensional species profiles of Karadeniz et al. (2013) and the CFD simulations are illustrated. The deviations between the different simulation approaches are very small. Furthermore, the effectiveness factors for the 1D and 3D model are in close agreement (not shown). Although the 1D model is a great simplification for the description of stagnation-flow reactor, it captures all the features of the symmetrical boundary layer flow.
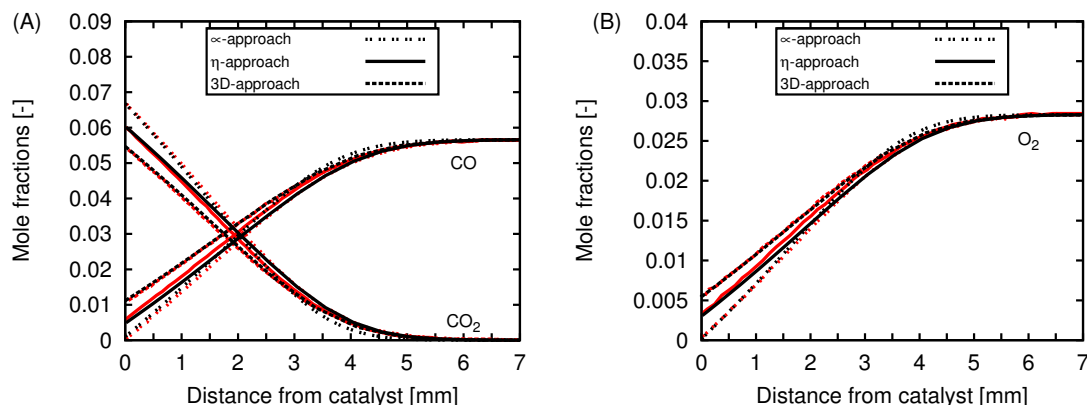
Figure 42: Comparison between 1D simulations from Karadeniz et al. (2013) (*red*) and CFD simulations (*black*) with different pore models at 873 K. (A) Mole fractions of CO and $CO_2$, (B) mole fractions of $O_2$.

Consequently, 2D or 3D models are not necessary, since the 1D model predicts the characteristics of catalytic stagnation-flow reactors in much more computationally economic way.

## 5.3   Conclusions

In the first study dry reforming of methane on rhodium in a stagnation-flow reactor was simulated fully three-dimensional with a detailed surface reaction mechanism. Instantaneous diffusion was assumed. The measured concentration profiles were reproduced with good accuracy. Moreover, the three-dimensional formulation gives no more information than the stagnation-flow boundary-layer problem from McGuire et al. (2011), which is one-dimensional. The temperature and axial velocity of 3D and 1D simulation coincide. In catalytic stagnation-flow reactors a boundary layer of temperature and concentration is formed at the heated catalytic surface. Consequently, gas phase concentration profiles can be measured promptly for estimating kinetic data. Furthermore, the boundary-layer problem describes the reactor in an adequate manner. No time-consuming three-dimensional CFD simulations have to be carried out. This reactor setting is a valuable example how fluidic effects on kinetic parameter estimation can be suppressed.

In the second study CO oxidation on Rh was studied numerically. Three different pore models were compared, i.e., instantaneous diffusion ($\infty$–approach), effectiveness factor ($\eta$–approach), and 3D reaction-diffusion model. In general, the most sophisticated pore model, i.e., the 3D reaction-diffusion model, predicts the experimental profiles with the highest accuracy. However, the time consumption is high due to the Co-simulation approach. Whereas the 2D $\eta$–approach takes about 30% more calculation time than the 2D $\infty$–approach, the 3D reaction-diffusion model consumes up to a factor of 200 more time than the instantaneous diffusion model. These ratios can obviously vary from case to case. Still, it has to be kept in mind that one should first analyze the present washcoat before deciding on another model than the "cheap" instantaneous-diffusion model. For such an analysis, a detailed description of the washcoat is necessary, i.e., pore size

distribution, washcoat porosity, washcoat thickness, catalyst loading, etc. But also the reaction regime should be known, i.e., diffusive vs. kinetic regime, which can vary locally. Although the two studies showed the advantage of 1D models for SFRs, such simplified model cannot be applied for complex geometries found in fixed-bed reactors.

# 6 Simulating catalytic fixed-bed reactors

In the following chapter, different aspects of modeling particle-resolved CFD simulations of fixed-bed reactors are analyzed critically. The investigated aspects are: automatic generation of packed beds consisting of spherical and non-spherical particles, conjugate heat transfer, surface reactions described by microkinetics, meshing strategies, as well as contact-area modifications. In the last chapter, fixed-bed reactors of different particle shapes are explored with particle-resolved CFD simulations. With this approach a quantitative understanding can be gained of their effect toward reactor performance.

## 6.1 Morphology and fluid dynamics

In this chapter, the morphology and resulting fluid dynamics are studies by particle-resolved CFD simulations. The ability of reproducing realistic packed-beds with DEM is tested, and the local velocity fields governed from CFD simulations of these geometries are compared with adequate experiments. It has to be mentioned that in literature there is only little data available for both, local porosity distribution and local velocity data for the same geometries. With the first data set it is possible to validate the automatic generated packing. With the latter, one can use the validated geometry of the packed bed and compare the velocity field inside the bed.

### 6.1.1 Experimental setup

One of the most comprehensive studies in the field of experimental investigation of fluid dynamics in packed beds is the contribution from Giese et al. (1998). The authors measured the local interstitial velocity fields inside packed beds with Laser-Doppler velocimetry in a refraction-index matched system. Different kinds of particle shapes, i.e., spheres, deformed spheres, cylinders, and Raschig rings, were studied at different flow rates. The particles were made of glass components, ranging from 8-8.6 mm in diameter. The reactor tube was 80 mm in diameter. The fluid was chosen as a mixture of 95% dibutylphalat and 5% ethyl-aclcohol to match the refraction index. The density of the fluid was $\rho = 1006.9$ kg/m$^3$, and the viscosity was $\mu = 8.5 \cdot 10^{-3}$ N$\cdot$s/m$^2$. The system was operated at 24 °C and ambient pressure. With a resolution of approx. 1 mm the interstitial velocity was measured for several cross sections of the bed. Then the velocities were averaged in terms of circumference and height. Superficial velocities were obtained by using these averaged velocities inside the bed and the corresponding local porosity $(\bar{v}(r) \cdot \varepsilon(r))$. Instead of using local porosity profiles from literature, the authors measured the local porosity by rotating the packed tube at high speed around its axis. At a certain sequence, ink is inserted in the rotating tube of a defined volume. Then the averaged ink level inside the packed bed is compared with the height of ink without particles, which results in the porosity as a function of distance from the outer wall. For a more detailed description of the experiments, see Giese (1997). Yet, it can be questioned if the exact particle structure was existent for both of the experiments, i.e., the stationary velocity measurements and the rotating porosity measurement setup.

### 6.1.2   CFD setup

For the validation of the packing generation and interstitial CFD simulations, two different kinds of packed beds were studied numerically. One consists of spheres of 8.6 mm in diameter, the other consists of cylinders of 8 mm in diameter, and 8 mm in length. The tube has a diameter of 80 mm, which results in a tube-to-diameter ratio $N = 9.3$ and 10, respectively. The tube height is 130 mm. All the dimensions are in line with the experiments from Giese et al. (1998). The generation of the packed bed was realized with the DEM approach, as it is described in chapter 4.1. In Fig. 43 the two computer generated packed-beds are illustrated.

Two different particle Reynolds numbers were compared: $Re_\mathrm{p} = 532$ for the spherical particles and $Re_\mathrm{p} = 136$ for the cylindrical particles. For both cases, the realizable $k - \varepsilon$ turbulence model with the All $y^+$ Wall Treatment was chosen, cf. chapter 3.1.2. The fluid phase was discretized with polyhedral cells and prism cells close to the wall to ensure an appropriate resolution of the near-wall gradients. The caps method developed by Eppinger et al. (2011) was applied, which results in flattening of the particles at contact areas. The total amount of cells accounts for 23 million for the bed of spheres and 20 million for the bed of cylinders, respectively. An incompressible fluid with the same properties as described by Giese et al. (1998) was used.
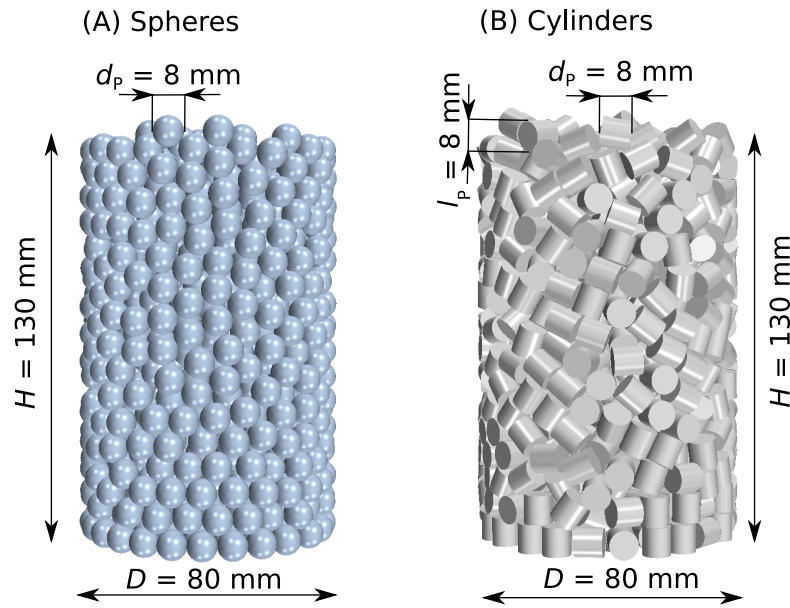


Figure 43: Computer generated packed bed of spheres (A) and packed-bed of cylinders (B) with dimensions as described in Giese et al. (1998).

### 6.1.3   Results and discussion

In Fig. 44 the local porosity (A) and the local velocity (B) for the two beds from Giese et al. (1998) are compared with the CFD simulation results. The CFD results are obtained by averaging the velocity component in axial direction, i.e., the $z$ coordinate, in terms of circumference and height. As can be seen, the DEM packing generation method captures the local porosity profile very well.

Also, the minima and the maxima of the porosity profiles are reproduced by the simulation. The bed of spheres shows the closer agreement in comparison with the experiments. The porosity profile of the simulated bed of cylinders does not show the same maxima that can be seen in the experiments. However, the characteristic shape is well reproduced. As the authors mention, the experimental values closer to the axis of the bed are unreasonable, starting form $(R-r)/d_\mathrm{p} = 3.5$ for both, porosity and velocity (Giese, 1997). This is due to difficulties of precise measurement, since the cross section close to the axis is getting smaller. Consequently, also the CFD simulations are only shown in this range.

The velocity field is more complex to measure than the porosity, since fluctuations can also occur and the measurement resolution plays an important role. The simulated velocity fields capture the essential characteristics of the measured data. However, the maxima are underpredicted by some extent by the simulations. This might be due to the averaging process of the simulation results, since the resolution of data points in the CFD simulation is higher than the resolution of the experiments. A typical CFD cell size is 0.3 mm in diameter, whereby the experimental resolution is 1 mm.



(a) Spherical particles          (b) Cylindrical particles
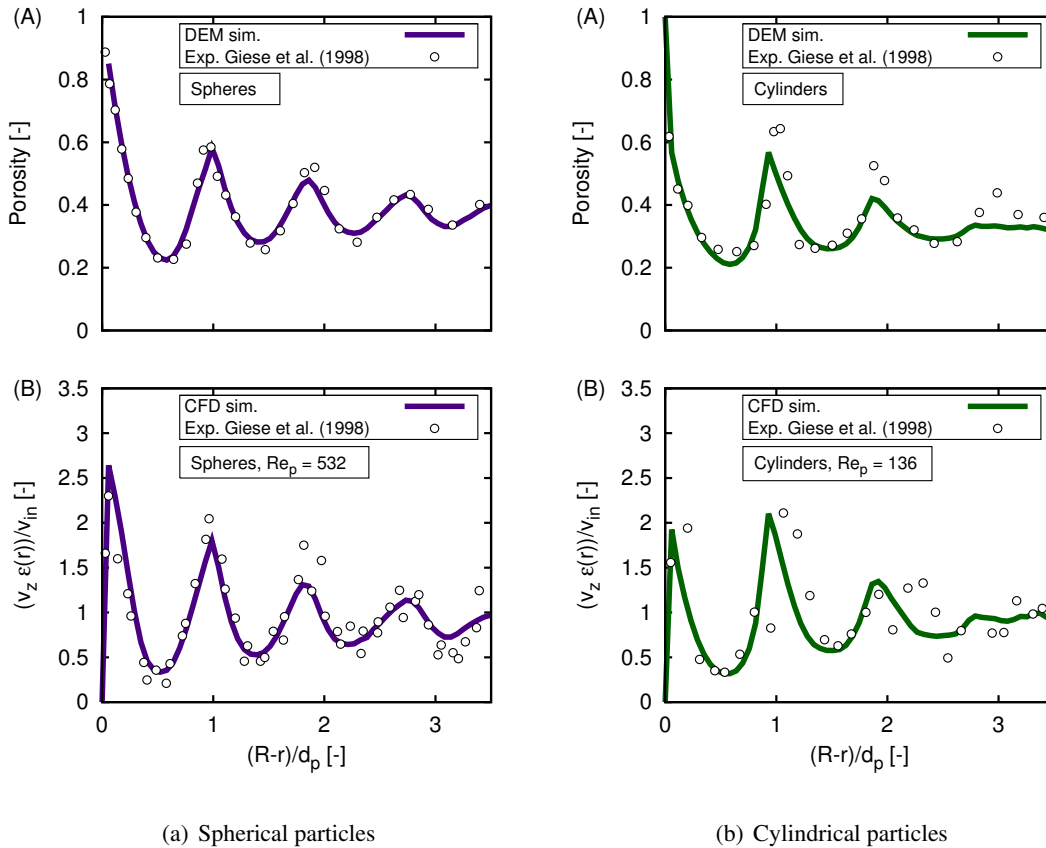
Figure 44: (A) local porosity and (B) specific velocity $(v_z \cdot \varepsilon(r))/v_\mathrm{in}$ for experiments from Giese et al. (1998) and CFD simulations for packed bed of spheres and cylinders.

## 6.2   Preliminary study of dry reforming on rhodium[3]

This is a numerical study with no equivalent experiment. In this study an entire bed of catalytic spherical particles is simulated. On the particle surface a detailed reaction mechanism is implemented. Furthermore, conjugate heat transfer between the solid particles and the gas phase is taken into account.

### 6.2.1   CFD setup

The scheme of the spherical fixed-bed reactor is shown in Fig. 45. In addition to the fixed bed an upstream and downstream region was generated to minimize the influence of the boundary conditions. The geometric quantities of the reactor are: catalytic bed height $H = 40$ mm, reactor diameter $D = 16.2$ mm, sphere diameter $d_p = 4.09$ mm, which leads to a tube-to-particle-diameter ratio $N = D/d_P = 3.96$. The reactor contains 113 spheres, which were packed randomly. This leads to a specific particle area $a = A_{P,\text{total}}/V_{\text{Reactor}}$ of 784 $m^2/m^3$. The geometric generation of the randomly packed bed was carried out with a DEM simulation, see chapter 4.1. In the DEM simulation the tube was filled with particles. When all particles were settled, the geometric information of the particle centroids was extracted. This information was then used to build up the desired packed bed.

A polyhedral grid was chosen to mesh the solid particles and the gas phase. Additionally, prism layers were introduced at the interface between fluid and solid phase. In the meshing process the particles were flattened locally at particle-wall contact-points and particle-particle contact-points, respectively, to avoid bad cell qualities, see Fig. 46. In all the simulations the boundary layer thickness $\delta_{\text{BL}}$ was resolved with two prism layers. $\delta_{\text{BL}}$ can be approximated with a correlation for the stagnation point of a sphere (Dhole et al., 2006):

$$\frac{\delta_{\text{BL}}}{d_p} = 1.13 \cdot Re_p^{-0.5} \tag{6.1}$$

In addition, as recommended by Dixon et al. (2013b), the dimensionless cell-wall distance $y^+$ was kept at approx. 0.5-2.0. For the investigated cases the velocity boundary layer (BL) thickness was smaller than the temperature BL and the concentration BL, respectively. The Prandtl number $Pr$ was of the same order of magnitude as the Schmidt number $Sc$. The influence of the mesh size was investigated by means of mesh refinement, see Tab.. 7. The base size is a characteristic dimension of the mesh model, to which all other mesh dimensions refer. It can be interpreted as a scaling factor of the mesh resulting in the total number of cells (CD-adapco, 2014).

The conditions at the inlet were: feed gas composition $x_{CO_2}/x_{CH_4}/x_{N_2} = 0.20/0.10/0.70$, inlet velocity $v_{\text{in},1} = 0.886$ m/s or $v_{\text{in},2} = 17.72$ m/s. The corresponding particle Reynolds numbers were: $Re_p = 35,700$ calculated with a mean dynamic viscosity $v_{\text{gas},973K} = 9.504 \cdot 10^{-5}$ m$^2$/s and the particle diameter $d_p = 4.09$ mm. On the catalytic surface the detailed reaction mechanism of

---

[3]This section is based on the publication: Wehinger, G. D., Eppinger, T., Kraume, M. (2015). Detailed numerical simulations of catalytic fixed-bed reactors: Heterogeneous dry reforming of methane, *Chemical Engineering Science*, 122, 197-209
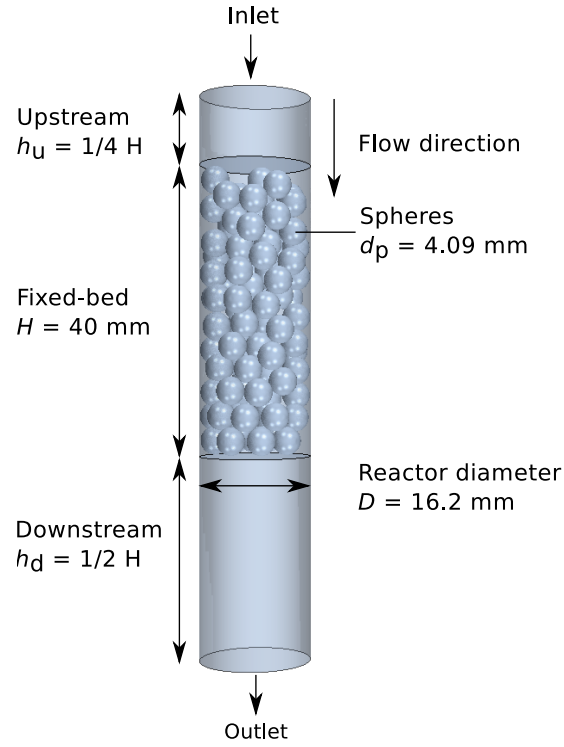
Figure 45: Scheme of the spherical fixed-bed reactor.

Table 7: Characteristics for the investigated meshes

| Mesh | Prism layer thickness [mm] | No. of layers | Base size [mm] | Total No. of cells $[10^6]$ | No. solid cells $[10^6]$ |
|------|------|------|------|------|------|
| Laminar Re $= 35$ | | | | | |
| M1 | 0.19 | 2 | 8 | 0.6 | 0.11 |
| M2 | 0.19 | 2 | 4 | 2.6 | 0.65 |
| M3 | 0.19 | 2 | 3 | 3.2 | 0.67 |
| Turbulent Re $= 700$ | | | | | |
| M4 | 0.0427 | 2 | 4 | 2.8 | 0.66 |
| M5 | 0.0427 | 2 | 3 | 3.5 | 0.67 |
| M6 | 0.0427 | 2 | 2 | 10.5 | 3.38 |
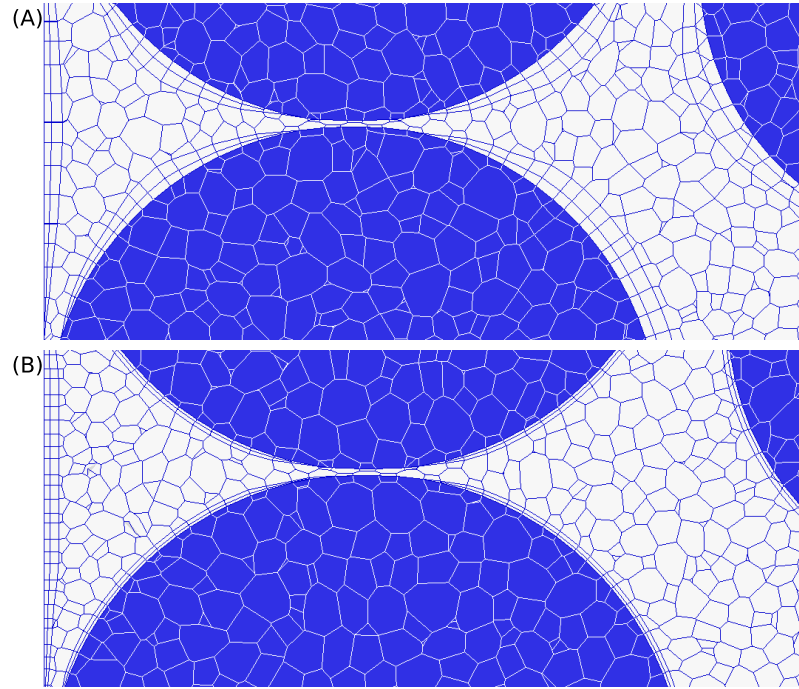
Figure 46: Section of fixed-bed reactor meshing. (A) mesh M3 for $Re_p = 35$ and (B) mesh M5 for $Re_p = 700$. Gas phase polyhedral mesh in gray and solid sphere polyhedral mesh in dark. Flattening is visible between the particles.

DRM on Rh was implemented, see Tab. 22. In line with the experiments by McGuire et al. (2011) processes in the pores were treated as instantaneous diffusion with an enlarged catalytic active area $F_{cat/geo} = 90$ in Eq. (3.41). Furthermore, a constant reactor-wall temperature and inlet temperature $T_{wall} = T_{in} = 973\,K$ was chosen. The reactor was under steady-state operation at ambient pressure, which is indicated by the pressure outlet $p_{out} = 1$ bar. The spheres were treated as solid particles with conjugate heat transfer, that means the temperature of the solid was not constant. The solid density $\rho_{cat}$ was set to 2,214 kg/m$^3$, specific heat $c_{p,cat} = 850$ J/(kg K) and thermal conductivity $k_{cat} = 12.6$ W/(m K), as reported in Schwiedernoch et al. (2003) for alumina monolith including porosity.

### 6.2.2  Results and discussion

#### 6.2.2.1  Porosity

The local porosity $\varepsilon$ as a function of dimensionless wall distance $\xi$ was obtained by averaging the local porosity distribution in terms of height and circumference over 40 cylindrical planes of different radii inside the fixed bed. The first and last layer of particles were not taken into account to avoid edge effects. In Fig. 47 the porosity of the computer-generated bed is compared with
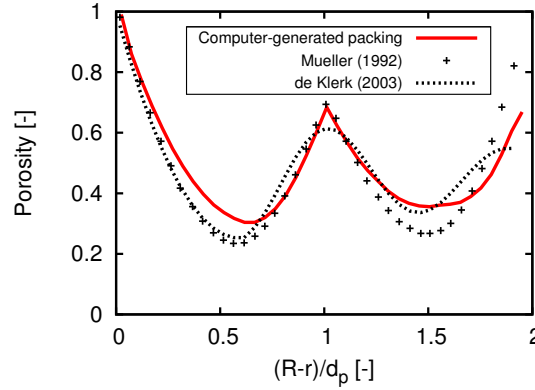
Figure 47: Comparison of porosity $\varepsilon$ as a function of dimensionless wall distance $(R-r)/d_p$ between computer-generated packing and experimental measurements from Mueller (1992) averaged over the reactor height and a general equation from de Klerk (2003).

experimental data from Mueller (1992) and a more general equation from de Klerk (2003):

$$
\begin{aligned}
\varepsilon(r) &= 2.14r^2 - 2.53r + 1 && \text{if } \xi \leq 0.637 \\
\varepsilon(r) &= \bar{\varepsilon} + 0.29\exp(-0.6r) \cdot [\cos(2.3\pi(r-0.16))] && \\
&\quad + 0.15\exp(-0.9r) && \text{if } \xi > 0.637
\end{aligned}
\tag{6.2}
$$

with $\xi = (R-r)/d_p$ as the dimensionless wall distance.

The first peak of the porosity $\varepsilon \approx 1$ occurs at the wall $\xi = 0$, where spheres touch the wall in contact points. The second peak at $\xi = 1$ can be reproduced by the simulation. In the center of the bed, $\xi = 2$, experimental values are higher than for the virtual bed. The minimum values of the experiments are lower than the computer-generated packing and they occur at smaller wall distances. The more general equation from de Klerk (2003) is valid for a wide range of $N$ and therefore not too accurate to compare with the simulated case with $N \approx 4$. However, the trend is comparable. The reason for the discrepancy between simulation and experiments is the loose packing structure, as it can be seen in Fig. 45, and the low height-to-radius ratio of the computer-generated bed $H/D \approx 2.47$ in comparison with the experiments from Mueller (1992) $H/D \approx 7.84$. Consequently, inhomogeneities are more dominant toward the averaged results. For loose packings the porosity is generally higher than for more dense packings, except for the center of the bed. That means in the simulation the channeling in the center is not as severe as in the experiments. Such packing effects have a great influence on the local porosity and, therefore, on the fluid behavior, e.g., pressure drop and velocity distribution. The overall porosity in the computer-generated bed accounts to 0.5, whereas in Mueller's experiments a global porosity of 0.47 was measured. That highlights the loose packing structure of the simulated bed. Surface roughness and filling speed influence the packing density. Mueller (1992) for example used plexiglas polished spheres to obtain radial porosity distributions. In contrary, porous spheres, which have a rougher surface, would be expected to have a looser packing density. However, filling speed and surface roughness should be aligned with an industrial relevant case. Since the focus of this study is on transport phenomena and kinetics, the bed structure is satisfactory.

### 6.2.2.2   Pressure Drop

In Fig. 48, and Tab. 8 pressure drop as a function of $Re_p$ is given for the CFD simulations with and without catalytic reactions for $T = 973$ K and calculated with the Ergun Eq. (2.8) and Eisfeld Eq. (2.10). The temperature decreases due to endothermic reactions when DRM takes place, hence gas properties change. Therefore, the definition of the Reynolds number is not explicit. The Eisfeld Eq. as well as the Ergun Eq. were calculated for two different reference temperatures, i.e., 873 K and 973 K, with feed gas mixture composition, resulting in different viscosities and densities. For low $N$, the Ergun Eq. underestimates the pressure drop for low $Re_p$ and overestimates the pressure drop for turbulent regimes, which was demonstrated by Reichelt (1972). As can be seen, the simulated pressure drop is between the Ergun and Eisfeld Eq. for 873 K, i.e., lower pressure for equivalent $Re_p$. It has to be kept in mind that the simulated bed has a low $H/D$ ratio. Eisfeld's equation was developed for much larger fixed-beds. The low pressure drop in the simulated bed might result from the loose packing and the low $H/D$ ratio leading to wall channeling and strong effects of the edge zones of the bed, respectively. Concerning pressure drop grid independence is reached with mesh refinement M2 in the laminar case, see Tab. 8. For the turbulent case, the pressure drop increases with mesh refinement. Though, the deviation between smallest and largest mesh is less than 5%. As can be concluded, the simulated pressure drop is in reasonable accuracy with predictions from the literature even in the turbulent regime. However, local quantities provide more information about mesh dependence. Therefore, in the Appendix in Fig. 105 and 106 velocity, temperature and species profiles are compared at three different positions for the investigated meshes and discussed in the following chapters. The three lines, i.e., in the stagnation zone above one of the first spheres, in a channel between a sphere and the wall, and in the interstitial area between two spheres, are highlighted in Fig. 104.
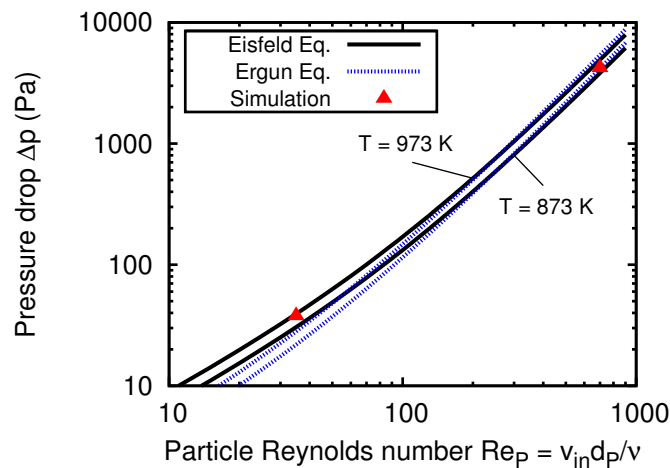


Figure 48: Pressure drop over particle Reynolds number. Comparison between simulation (meshes M3 and M5) and Equation 2.8 and 2.10, respectively.

Table 8: Results of investigated meshes for laminar and turbulent case.

| Mesh No. | $\Delta p$ w/o,chem. [Pa] | $\Delta p$ w,chem. [Pa] | $\bar{y}^+$ [-] | $X_{CH_4}$ [%] | $X_{CO_2}$ [%] | $Y_{CO}$ [%] | $Y_{H_2}$ [%] | $Y_{H_2O}$ [%] | $\bar{\Theta}_{CO^*}$ [-] | $\bar{\Theta}_{C^*}$ [-] |
|---|---|---|---|---|---|---|---|---|---|---|
| Laminar Re $= 35$ | | | | | | | | | | |
| M1 | 34.7 | 33.2 | - | 32.7 | 19.8 | 28.1 | 27.5 | 1.5 | 0.512 | 0.098 |
| M2 | 37.9 | 36.5 | - | 35.2 | 21.9 | 29.7 | 28.7 | 2.2 | 0.534 | 0.058 |
| M3 | 37.9 | 36.5 | - | 35.4 | 22.1 | 29.9 | 28.8 | 2.2 | 0.535 | 0.056 |
| Turbulent Re $= 700$ | | | | | | | | | | |
| M4 | 4218 | 4120 | 0.59 | 11.1 | 8.4 | 5.0 | 5.7 | 0.3 | 0.346 | 0.009 |
| M5 | 4220 | 4124 | 0.59 | 10.9 | 8.2 | 5.0 | 5.7 | 0.3 | 0.346 | 0.009 |
| M6 | 4400 | 4300 | 0.65 | 11.6 | 8.9 | 5.0 | 5.7 | 0.3 | 0.343 | 0.008 |

### 6.2.2.3  Velocity distribution

Fig. 49 shows the specific velocity distribution $|\vec{v}|/v_{in}$ on a plane cut through the fixed bed for $Re_p = 35$ (M3) and $Re_p = 700$ (M5). The flow direction is from top to bottom. In both cases the flow field around the particles is highly three-dimensional. Axial, as well as radial differences occur. Several different kinds of characteristic zones can be noticed: stagnation zones in front of particles, wake and eddying behind particles, acceleration in void regions, deceleration and channeling, especially in the near wall region. The highest specific velocities $|\vec{v}|/v_{in} \approx 7$ are found for the flow field of $Re_p = 35$, see Fig. 49 (A). Thus, in the turbulent flow regime Fig. 49 (B) the non-axial velocity components must be larger than for the quasi-laminar flow. In Fig. 50 besides spheres, cells with zero or negative velocities are illustrated. For $Re_p = 700$ these regions are larger than for the laminar case. The flow is highly characterized by back flow regions and non-axial velocity components.

The local specific axial velocity $v_z \varepsilon(\xi)/v_{in}$ as a function of dimensionless wall distance for different $Re_p$ is presented in Fig. 51. It follows the local porosity in Fig. 47. High velocities are found in regions with high void fraction. Close to the reactor wall the velocity decreases due to the boundary layer and no-slip condition at the wall, respectively. The highest local specific axial velocities are in the range of 2.0-2.5, which was also observed in experiments (Giese et al., 1998). The largest differences are found in the region close to the wall and in regions with high void fractions. The different thicknesses of boundary layers for laminar and turbulent regimes can be clearly seen. Additionally, the diagram highlights that in the turbulent regime radial and circumferential velocity components contribute to a more leveled velocity distribution. It should be noted that back-flow regions are not detected, due to averaging of the axial velocities. Consequently, taking into consideration only two dimensional velocity distributions can be misleading.

In Fig. 105 and 106 (A), (E) and (I) the specific velocity profiles are shown for the different meshes at three positions, respectively. The boundary layer in the stagnation zone (A) is well resolved by all meshes. However, the flow field differs from single sphere profiles due to disturbance by other spheres, cf. Fig. 104. The channeling between the wall and a sphere is shown in the Fig. 105
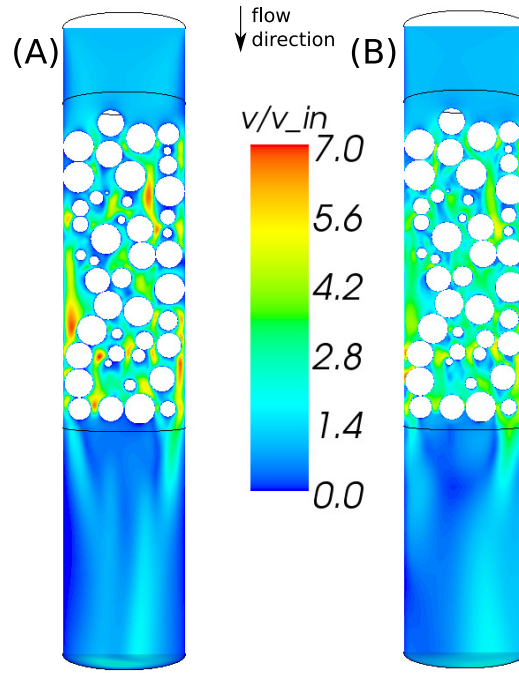
Figure 49: Specific velocity distribution $|\vec{v}|/v_{in}$ on a plane cut through the fixed bed. (A) for $Re_{\mathrm{p}} = 35$ M3, (B) for $Re_{\mathrm{p}} = 700$ M5.
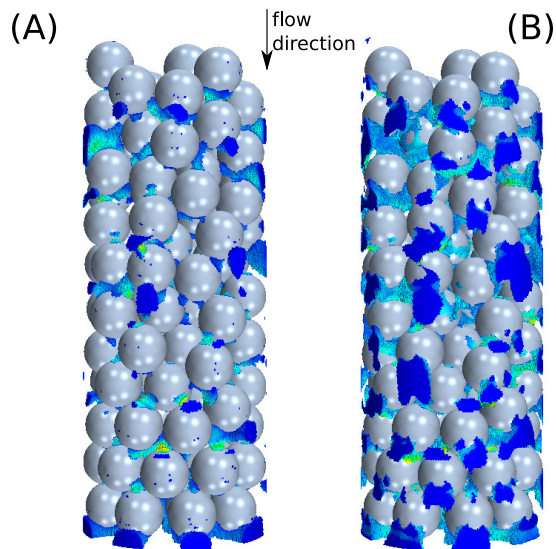


Figure 50: Backflow regions, i.e., cells with negative velocities. (A) for $Re_{\mathrm{p}} = 35$, (B) for $Re_{\mathrm{p}} = 700$.
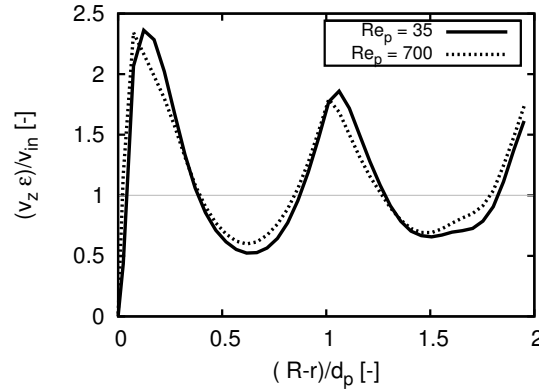
Figure 51: Specific axial velocity $v_z \varepsilon(\xi)/v_{in}$ as a function of dimensionless wall distance for different Reynolds numbers.

and Fig. 106 (E), i.e., position 2. For the laminar case a parabolic velocity profile occurs with a specific velocity of approx. 6. The peak is moved to the sphere's side. For the turbulent case a typical profile is shown with a steep gradient near the surfaces and a flattened center with approx. $v/v_{in} = 4.5$. Position 3 (I) represents the area between two spheres, which is highly influenced by the surrounding flow field. Two velocity peaks can be recognized located near the surfaces. The flow decelerates in the center due to a recirculation zone further upstream. In the laminar case the velocity increases smoothly, whereas it shows a steep rise for the turbulent case. In Fig. 105 (A) the calculated velocities from mesh 1 are slightly different than for mesh M2 and M3. On the contrary, the meshes M2 and M3 show almost identical results in the laminar case. For higher Reynolds numbers, only at position 3 the meshes show different velocities while mesh refinement. Here, the minimum velocity decrease in the center with a finer mesh.

Finally, Fig. 52 shows the frequency of $y^+$ values for meshes M4-M6. As can be seen, most of the cells are small enough that $y^+ < 1.5$. Hence, velocity boundary layers are well resolved.
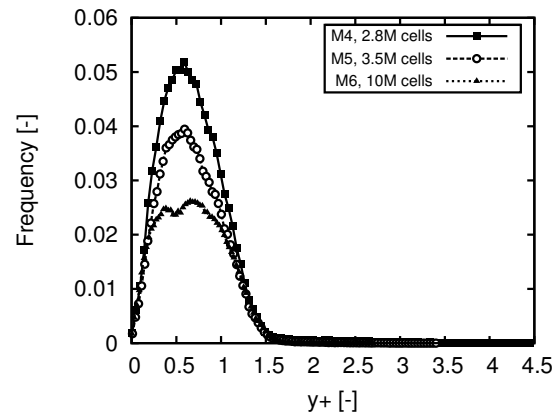


Figure 52: Frequency distribution over dimensionless wall distance $y^+$ for different meshes.

#### 6.2.2.4    Temperature distribution

The temperature distribution in the fixed bed, i.e., gas phase and solid particles, is shown in Fig. 53. The inlet temperature and wall temperature is set constant to 973 K. Due to the endothermic reactions the temperature inside the bed decreases. Again, strong axial and radial temperature differences up to approx. 80 K occur. Low Reynolds numbers result in large residence times and hence higher conversion. Consequently, in Fig. 53 (A) the overall temperature is lower than in Fig. 53 (B). In (A) a cold spot appears after approx. half of the reactor length, whereas in (B) the temperature in the center decreases constantly. This is due to the shorter residence time which moves the cold spot out of the bed. In Fig. 53 (B) the hot flow reaches deep inside the fixed bed, whereas for $Re_p = 35$ the flow cools down immediately. The solid particles can be detected easily due to their almost constant temperature, which is caused by the higher thermal conductivity. As a result of channeling in the near wall region, the thermal penetration into the bed is declined. Again, the transport property energy shows highly three-dimensional behavior.
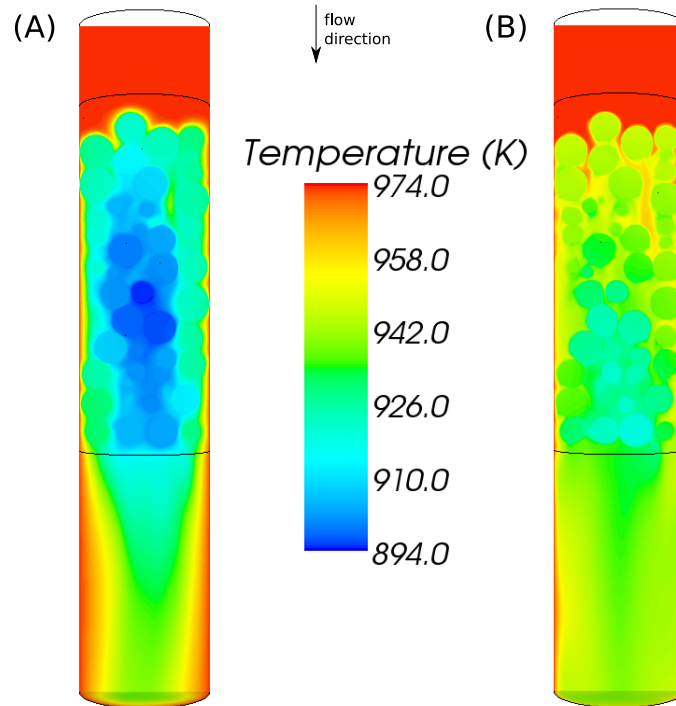


Figure 53: Temperature distribution on a plane cut through the fixed bed. (A) for $Re_p = 35$ mesh M3, (B) for $Re_p = 700$ mesh M5.

In Fig. 105 and 106 (B), (F) and (J) temperature profiles are shown for the different meshes at the three positions, respectively. At position 1 the temperature decreases from the inlet to the sphere's surface due to endothermic reactions. However, for $Re_p = 35$ it is lower than for the turbulent case. At position 2, i.e., between wall and sphere, the temperature decreases from the constant wall temperature $T = 973$ K to the specific surface temperature, which is influenced firstly by the surrounding flow and secondly by the surface reactions. In the laminar case the temperature decreases almost linearly from the wall to the surface. For the higher Reynolds number boundary

layers can be noticed near both surfaces, which are of the order of magnitude of the velocity boundary layers. Finally, between the spheres at position 3 (jJ) the temperature field is highly influenced by the flow field. In the laminar case the temperature decreases from the outside to the center. Therefore, the left surface in (J) is cooler than the right side. Again, an almost linear profile is shown although the recirculation zone delivers cooler gas. For $Re_p = 700$ the endothermic reaction cools down the surface, whereas hot gas passes by. The recirculation zone is larger than for lower Reynolds. Hence, temperature decreases stronger in the center.

### 6.2.2.5   Surface adsorbed species

As mentioned before, catalyst deactivation through carbon deposition is one of the major drawbacks of DRM. It has to be noticed that in reality coke formation takes place including many carbonaceous atomic layers. However, the present reaction mechanism only accounts for mono-layer carbon (C*) on the surface. Consequently, the model determines the regions where coking takes place rather than the amount of coke. In Fig. 54 surface site fractions of adsorbed carbon and some streamlines are illustrated for the different Reynolds numbers. As can be seen, the carbon deposition is not only dependent on $Re_p$ but is due to the interactions between velocity, temperature and gas composition. In Fig. 54 (A) several regions of spheres are totally blocked by carbon mainly in the center of the inlet region of the bed. Hence, the catalyst is deactivated resulting in declined or stopped production of syngas. In Fig. 54 (B) almost no carbon is adsorbed. Catalyst deactivation by carbon deposition for DRM especially in the inlet regions of fixed beds was observed experimentally and numerically by Kahle et al. (2013). Fig. 54 highlights the advantage of this type of reaction mechanism for DRM. It can contribute to identify conditions and regions where deactivation of the catalyst is likely to occur. In addition, Fig. 55 (A) shows radially and
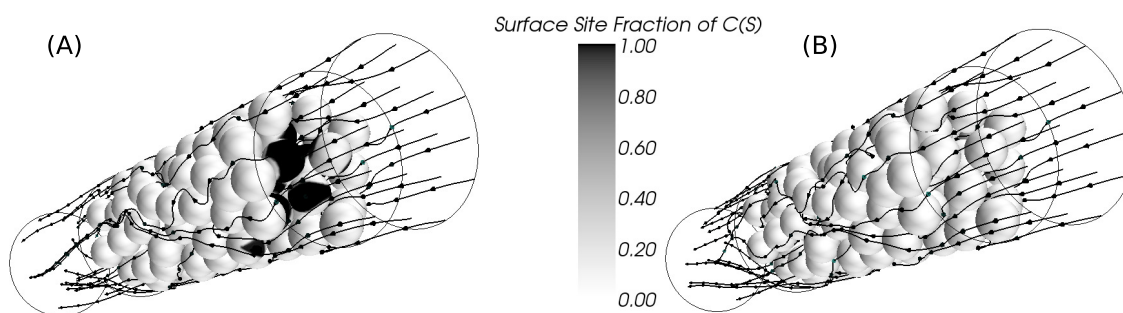


Figure 54: Catalyst deactivation through carbon deposition on the surface. (A) for $Re_p = 35$ mesh M3, (B) for $Re_p = 700$ mesh M5.

circumferentially averaged surface site fractions of the adsorbed species C*, CO*, H* and RH*. For the laminar case (A), surface adsorbed carbon monoxide (CO*) becomes the most abundant reaction intermediate (MARI) after approx. 10 mm in the fixed-bed. Adsorbed carbon is only dominant in the entrance of the reactor, whereby H* occurs on less than 1% of the surface sites. For the turbulent case (B), CO* is again the MARI. Due to the lower residence time, its surface fraction is lower, too. C* and H* are found on less 2% on the surface. These two figures illustrate

that DRM is kinetically limited. However, it has to be kept in mind that the two cases are not under iso-conversion. Therefore, a true comparison of location and quantity of surface adsorbed species cannot be undertaken.



(a) Surface site fractions                (b) Mole fractions
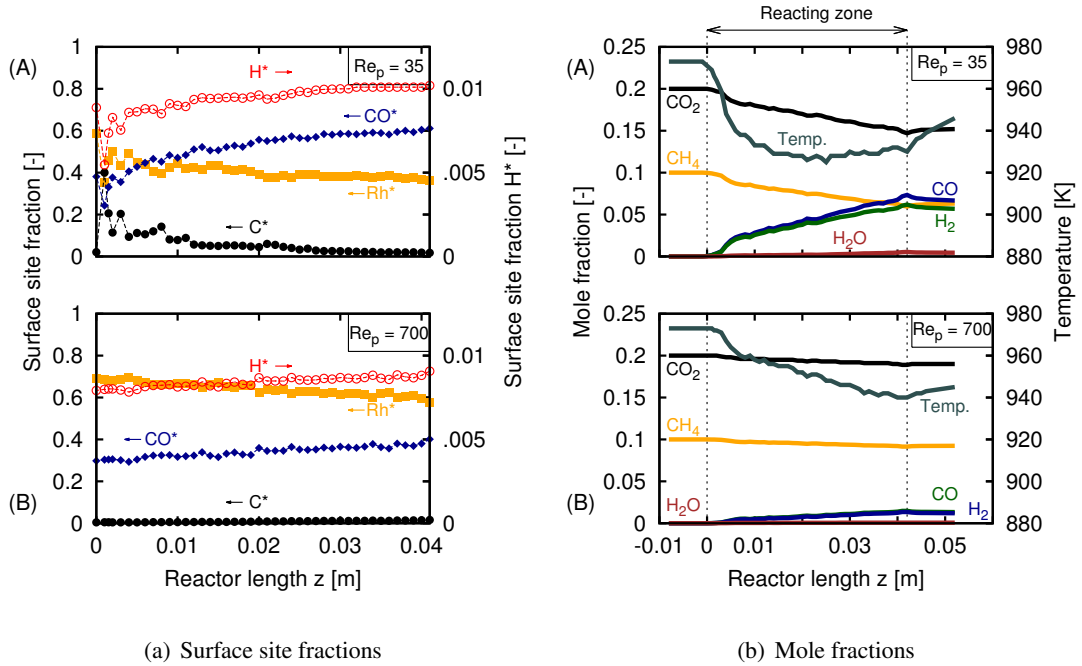
Figure 55: (a) Mean surface site fractions, and (b) mean mole fractions over reactor length. (A) for $Re_p = 35$ mesh M3, (B) for $Re_p = 700$ mesh M5.

### 6.2.2.6   Gas phase species distribution

Radially and circumferentially averaged mole fractions of reactants and products as well as temperature are shown in Fig. 55 (b) over the reactor length for different particle Reynolds numbers. Catalytic conversion can be noticed and besides the main products $H_2$ and CO also water is formed. Water is the result of the reverse water-gas shift (WGS) reaction, $CO_2 + H_2 \rightleftharpoons CO + H_2O$. Under common DRM reforming conditions WGS is extremely fast (Rostrup-Nielsen and Hansen, 1993). For larger residence times more hydrogen and carbon monoxide is produced. It becomes clear that both reactors are economically not feasible, because only few syngas is formed.

However, DRM kinetics is highly influenced by the reactor temperature and vice versa. This strongly demonstrates Fig. 56, where the mole fraction of $H_2$ and surface site fraction of carbon on a plane cut are shown. The strong interplay between velocity and temperature distribution and the resulting reactions can be seen. The low temperature and blockage of the catalyst leads to a weak hydrogen production in the bed center in Fig. 56 (A). In stagnation zones, e.g., between spheres, the production is high due to high residence time and low convection.

Row three and four in Fig. 105 and 106 show mole fractions of $CO_2$, $CH_4$ and CO in the gas phase
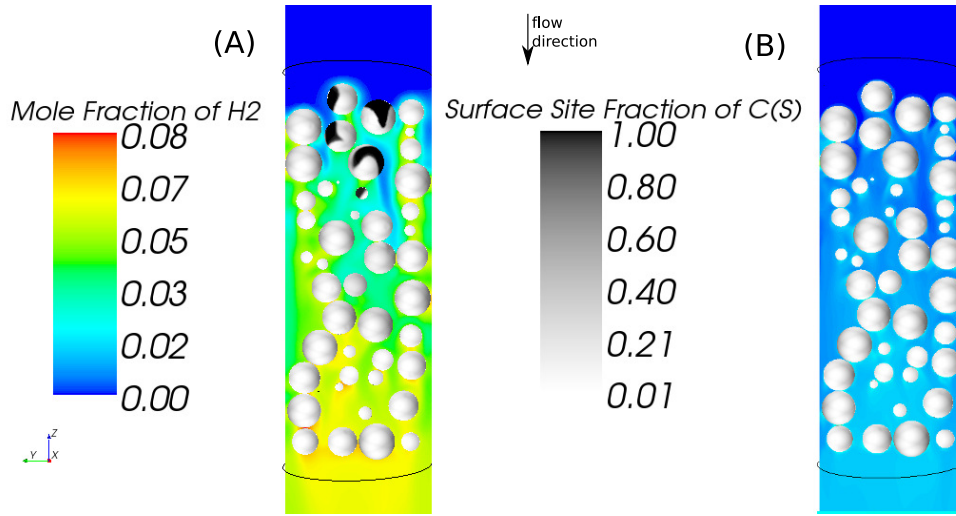
Figure 56: Hydrogen production and surface adsorbed carbon on a plane cut through the fixed bed. (A) for $Re_p = 35$ mesh M3, (B) for $Re_p = 700$ mesh M5.

and at surfaces. For the laminar case, at position 1 no syngas is produced due to complete catalyst blockage by C*. On the contrary, for higher Reynolds numbers, CO is produced and a boundary layer larger than the temperature BL can be recognized, cf. Fig 106 (D). At position 2 and 3 the mole fractions of methane and carbon dioxide decrease at the catalytic surfaces, while syngas is produced. In the laminar case, mesh M1 shows lower conversion than M2 and M3. This could be due to the lower discretization of the surface. Consequently, the velocity field as well as the temperature field is affected. The meshes for the turbulent case show in general similar species profiles.

Comparing Fig. 55, 56, 105, and Fig. 106 it becomes clear that averaged profiles can be illusive, due to the fact that they neglect the radial and circumferential differences, e.g., boundary layers, of species concentrations.

## 6.3   Heat transfer

Conventional reactor experiments are conducted by measuring the inlet and outlet conditions, i.e., temperature, velocity, and species concentrations. The reactor itself remains a "black box". Thus, no idea can be gained of what is happening inside the reactor, e.g., which intermediates are formed, what is the condition of the catalyst at different positions. To get insights into the reactor several researchers have developed in-situ, operando measurement devices.

Horn et al. improved their initial reactor concept to measure at higher pressure conditions and elaborated a more sophisticated capillary system (Horn et al., 2010). With this reactor setup it is possible to measure temperature and concentration profiles in the center line of a catalytic foam, or fixed-bed at different axial position. With such detailed experiments it is possible to validate particle-resolved CFD simulations. In this section heat transfer experiments without chemical reactions are conducted which are reproduced with particle-resolved CFD simulations.

### 6.3.1   Experimental setup

The experiments were realized in the reactor capable to measure spatial temperature and species concentration profiles described in detailed in Horn et al. (2010). A drawing of the reactor setup is shown in Fig. 57.
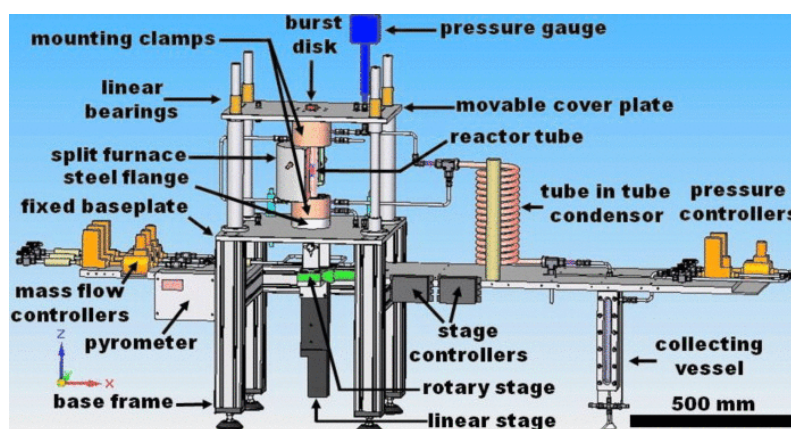


Figure 57: 3D drawing of the reactor setup. Reprinted from Horn et al. (2010) with permission from AIP Publishing LLC.

Summarized the reactor consists of a fused silica tube of an outer diameter of 38 mm and an inner diameter of 18 mm. A scheme of the reactor setup with dimensions can be seen in Fig. 58. Around the tube a split furnace is placed, which is controlled by the temperature of the outer tube wall. The catalytic particles are placed on a non-catalytic $\alpha$-alumina foam of approx. 10 mm in height. The foam has a porosity of approx. 80%. Its purpose is to fix the catalytic particles, and also to shield the heat in the counter-flow direction. Furthermore, the flow passing the heat shield is more uniform than in an open tube. Between the heat shield and the tube wall a ceramic mat (Interam 3 M) is placed to fix the foam. The bed, consisting of alumina spheres of 1 mm, is 25 mm high. In the axis of the bed a capillary is placed which has an outer diameter of 0.7 mm, and an inner

diameter of 0.52 mm. In the center line of the heat shield a hole is drilled to fix the capillary in radial position. In the axial position the capillary can be moved in $\mu$m resolution with the help of a stepper motor. Furthermore, the capillary can be rotated to guarantee for averaged temperature and concentration measurements at each axial position. In the capillary wall a small sampling orifice of 25 $\mu$m in diameter is drilled, see detail in Fig. 58. Through this hole a constant gas flow is guided to the mass spectrometer or gas chromatograph. In addition, inside the capillary a small thermocouple with an outer diameter of 0.35 mm is placed which measures the temperature of the gas flow. As a result, a temperature and concentration profile as a function of axial position inside the packed bed is recorded.
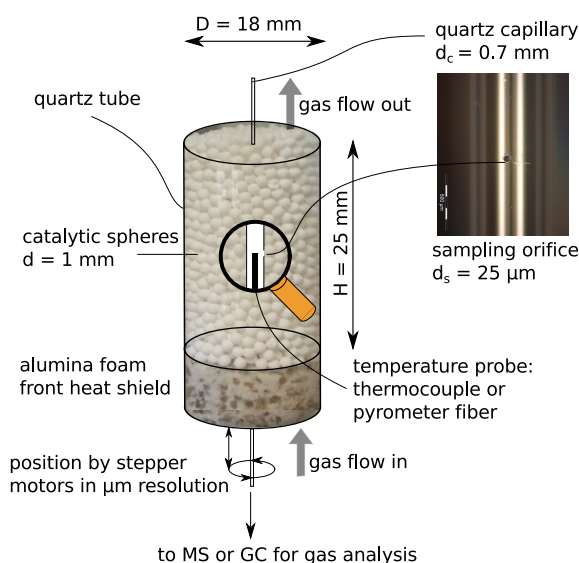


Figure 58: Reactor tube with spherical packing with scheme of the measurement setup and zoom on sampling orifice.

Heat transfer experiments without chemical reactions were carried out. Oven temperature and volume flow rates were varied. The temperature in the axis of the bed was measured. Argon was used as a test gas. Temperatures between $635-850\,°$C, and volume flows of $500-2500$ ml/min were varied.

### 6.3.2    CFD setup

The randomly packed bed of spheres was generated with the procedure based on DEM simulations, described in section 4.1. Fig. 59 illustrates the main steps. A cylinder with the diameter equal to that of the reactor tube ($D = 18$ mm) and the capillary ($d_c = 0.7$ mm) placed in the center was filled from the top constantly with DEM spherical particles of 1 mm in diameter. After the bed reached the desired bed height, i.e., 25 mm, and all particles were settled the data of their positions were extracted. With this information a CAD model of the packed-bed was built and meshed following the recommendations described in section 6.2. Due to the high number of particles, only a $45\,°$ slice was considered for the CFD simulations, see Fig. 59 (top). As can be seen qualitatively, the two confining walls, i.e., capillary wall and reactor wall, determine the bed structure. The front

Table 9: Reactor dimensions, material properties and boundary conditions

| | |
|---|---|
| Tube diameter $D$ | 18 mm |
| Bed height $H$ | 25 mm |
| Capillary diameter $d_\mathrm{c}$ | 0.7 mm |
| Particle diameter $d_\mathrm{p}$ | 1 mm |
| $H/d_\mathrm{p}$ ratio | 25 |
| $N = D/d_\mathrm{p}$ ratio | 18 |
| Porosity | 42% |
| Specific area $a$ | $\approx 3380$ m$^2$/m$^3$ |
| Particle density $\rho_\mathrm{cat}$ | 3,200 kg/m$^3$ |
| Specific heat $c_{p,\mathrm{cat}}$ | 1.066 kJ/(kg K) |
| Thermal conductivity | 4.36 W/(m K) |
| Volume flow | 1500 & 2500 mL/min |
| Wall Temperature | 635 & 735 °C |

heat shield (FHS) was not modeled. Both, the solid particles and the gas phase were meshed with a polyhedral grid in STAR-CCM+ to account for heat transfer inside the solid spheres, see detail in Fig. 59 (bottom). Prism layers were applied at the interface between fluid and solid phase. The particle-particle and particle-wall contact points were flattened in the meshing process (caps method). The total amount of cells for solid and fluid phase accounts for approx. 9 million.

In Fig. 59 (bottom) the CFD setup with boundary conditions can be seen. For further visualization the velocity magnitude is shown on a cut through the packed-bed. The reactor dimensions, material properties and boundary conditions are listed in Tab. 9. Heat transfer without chemical reactions was simulated. The spheres were treated as solid particles with conjugate heat transfer, which means energy exchange between the gas phase and solid particles was modeled. Moreover, a constant inlet temperature $T_\mathrm{in}$ and wall temperature $T_\mathrm{w}$ was set. The capillary wall was defined as an adiabatic wall, which neglects the heat loss by thermal conduction through the capillary. The material properties for the solid particles were taken from VDI (2013), chapter D6.3, where the values for alumina 99% are listed. The reactor was under steady-state operation at ambient pressure, which is indicated by the pressure outlet $p_\mathrm{out} = 1$ bar, as well as neglecting transient terms.

### 6.3.3   Results and discussion

In Fig. 60 the local porosity averaged over height and azimuth of the computer-generated bed is given, as well as a correlation by de Klerk (2003) for annulus reactors. As can be seen, both walls, i.e., the capillary and the outer wall, are defining the local porosity. The local minima and maxima close to both of the walls can be reproduced by the equation. It has to be mentioned that the correlation was developed for tubular packed beds. The influence of the inner wall was later added by van Antwerpen et al. (2010) by simply mirroring the equation at the start of the inner wall. This fact can be seen by the peak at the radial coordinate of approx. 4.7 mm. Another disadvantage of this mirroring is the oscillating nature of the local porosity at the capillary wall. The shape of
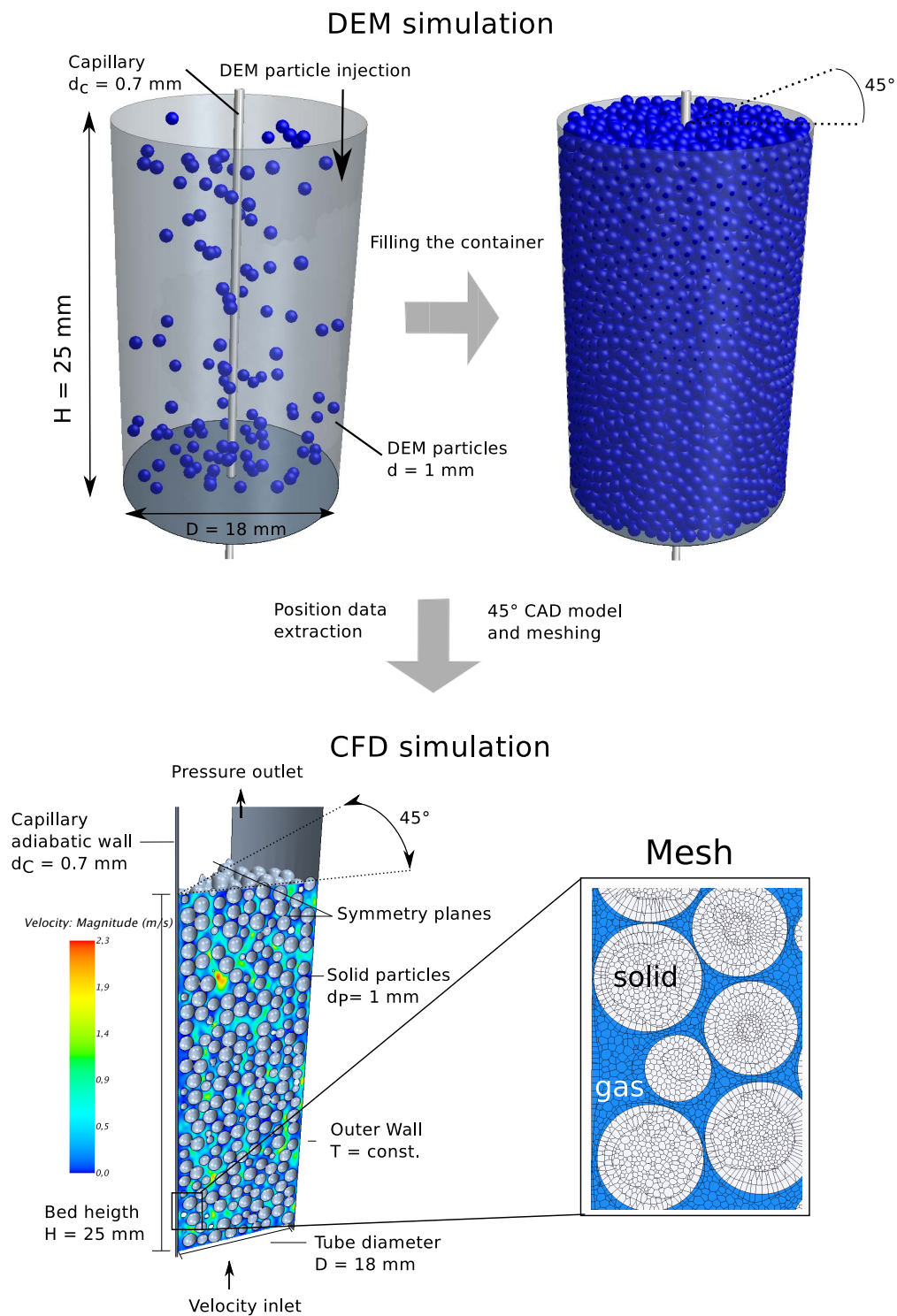
Figure 59: Random bed generation (top), and CFD setup with dimensions and boundary conditions (bottom). Velocity distribution in [m/s] on a cut through the packed-bed.

the profile close to the inner wall differs from that of the outer wall. This is due to the fact that the outer wall is concave, whereas the inner wall is convex. Still, the trend of the equation and the trend of the CFD simulation are close.
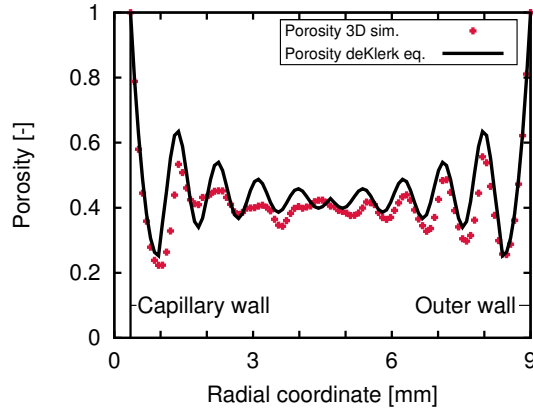


Figure 60: Local porosity of computer-generated bed and correlation by de Klerk (2003) for annulus reactors

In Fig. 61 measured and simulated temperature profiles as function of axial position in the bed center are illustrated for two sets of different wall temperatures and gas flows. Since the front heat shield was not modeled the simulations start with the first row of spheres. The inlet temperatures for the simulations were taken from the experiments at that position. 3D detailed simulations and experiments are in excellent agreement for both cases. One can even recognize the individual particles closest to the capillary wall in the experiment as well as in the detailed CFD simulations. For the 2D simulations the radial porosity profile from Fig. 60 was implemented into the model. For the case of $\dot{V}_{in} = 1500$ mL/min, see Fig. 61 (a), the 2D simulation is close to the experimental profile. In the center of the bed an overestimation of approx. 10 K occurs. On the contrary, the deviation between experiments and 2D simulation for $\dot{V}_{in} = 2500$ mL/min is dramatically higher, with an overestimation of up to 60 K. In this situation, the higher flow rate results in larger wall effects (channeling) which can be reproduced only by the 3D model. Hence, the advantages of the particle-resolved simulation over the 2D pseudo-homogeneous simulation becomes clear, although the 2D model incorporates the radially oscillating porosity of the bed.
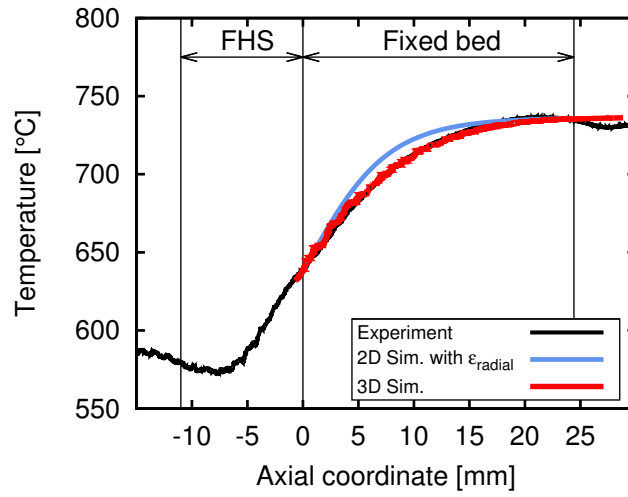
(a) $T_{wall} = 735\,°C$ and $\dot{V}_{in} = 1500$ mL/min
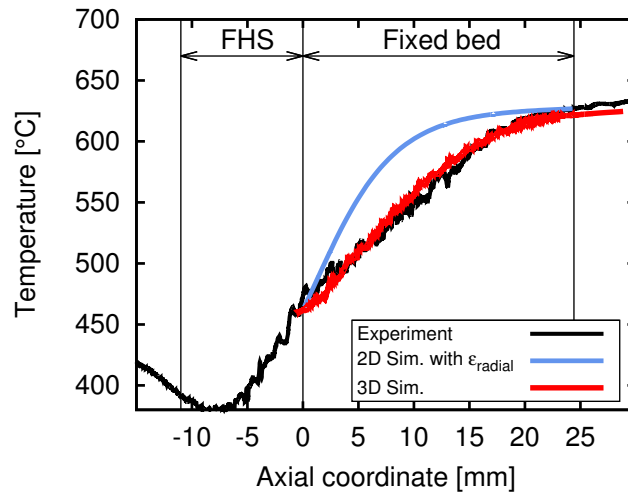


(b) $T_{wall} = 635\,°C$ and $\dot{V}_{in} = 2500$ mL/min

Figure 61: Measured and simulated temperature profile as function of axial position in the bed center without chemical reactions. Front heat shield (FHS).

## 6.4   Dry reforming on nickel

In this chapter DRM over a nickel catalyst performed in a fixed-bed reactor is studied in detail by spatially-resolved experimental data and particle-resolved CFD simulations. Heat transfer inside the packed bed was validated with great accuracy in the last section. Here, the modeling of heterogeneous catalysis is focused with a recent microkinetics of DRM implemented on the particle surface.

### 6.4.1   Experimental setup

The DRM experiments were conducted in the spatial-profile reactor already described in chapter 6.3. The inner diameter of the reactor tube was 18 mm and the bed height was 25 mm. The capillary with an outer diameter of 0.7 mm was moved in axial direction in the center of the bed. With the capillary temperature and species mole-fraction profiles were measured as function of axial coordinate. For this study spherical particles of 1 mm in diameter were coated with a washcoat in which the catalyst was deposited. The catalyst preparation was carried out at Fritz-Haber-Institute (FHI) in Berlin. The preparation is described in detail in Mette et al. (2014) and Düdder et al. (2014). The catalyst was synthesized from a hydrotalcite-like precursor of the nominal composition of $Ni_{0.5}Mg_{0.17}Al_{0.33}(OH)_2(CO_3)_{0.17} \cdot mH_2O$. It was obtained by the constant pH co-precipitation method at 50 °C using aqueous 0.6 M NaOH, 0.09 M $Na_2CO_3$, and 0.4 M metal nitrate solutions at pH 8.5. The precipitate staid for 30 min in the mother liquor. It was filtered, washed with water, and dried at 100 °C. Finally, the precursor was calcined in air at 600 °C for 3 hours (Düdder et al., 2014). Fig. 62 (A-C) show scanning electron microscope (SEM) images of the precursor material before and after reduction at 800 °C.
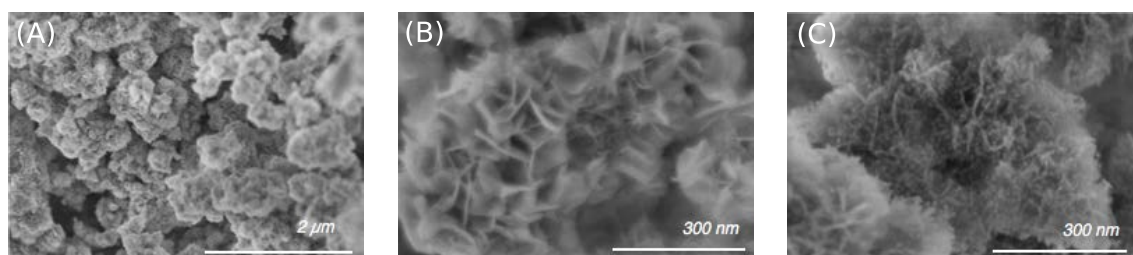


Figure 62: (A) and (B) SEM images of the precursor material. (C) Catalyst after reduction at 800 °C.[4]

This highly stable powder catalyst was deposited on $\alpha$-alumina spheres in form of a washcoat. Due to the washcoat the resulting catalyst exhibits a macroporous enlarged surface. In Fig. 63 (A) a SEM image of a catalytic sphere is shown. In (B) and (C) SEM images of the washcoat and precursor material can be seen. The catalyst characteristics are listed in Tab. 10. The total mass of $Al_2O_3$ pellets accounted for 21.233 g. With an averaged $\alpha$-$Al_2O_3$ density of 3.97 g/cm$^3$ (VDI,

---

[4]SEM images were taken by Giesela Weinberg with a Hitachi S-4800 at the Department of Inorganic Chemistry at Fritz-Haber Institute Berlin.

2013) and a pellet diameter of 1 mm, this results in approx. 10,215 spherical pellets inside the reactor.
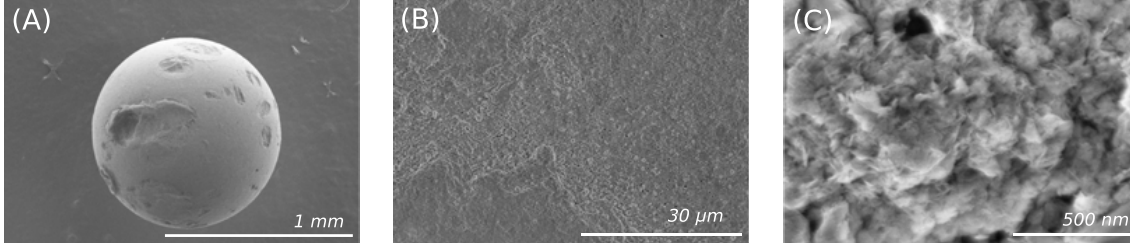


Figure 63: (A) SEM image of a catalytic sphere. (B) and (C) SEM images of the washcoat and precursor material

Table 10: DRM catalyst characteristics. As reported in Mette (2015).

| Ni content [%] | Particle size [nm] | Ni surface area [m$^2$/g$_W$] | Dispersion [%] | Washcoat loading [g$_W$/g$_{Al_2O_3}$] |
|---|---|---|---|---|
| 55.4 | 19.4±7.1 | 6.0 | 1.6 | 0.031 |

The fixed-bed reactor was operated at temperatures up to 850 °C. A split furnace supplied the reactor with the necessary heat. On several locations at the outer quartz tube temperature was measured with thermocouples. With the averaged value the power of the split furnace was controlled. Flow rates between 500-2500 ml/min (at room temperature and ambient pressure) were set. The feed consisted of the following composition: $x_{CH_4}/x_{CO_2}/x_{N_2}$=0.32/0.40/0.28.

### 6.4.2   CFD setup

The reactor, capillary and particle dimensions are equal to the previous chapter, see Tab. 9. For the particle-resolved CFD simulations the same mesh was used as for the heat-transfer validation in chapter 6.3. However, in this study a recently-published detailed reaction mechanism modeling DRM on Ni by Delgado et al. (2015) was implemented on the surface of the particles. In the Appendix in Tab. 23 the microkinetics is listed. It distinguishes between adsorption steps, surface reactions, and desorption steps. It consists of 26 reversible elementary-step like reactions with 14 surface species including carboxyl (COOH) and six gas phase species. The reaction steps are formulated via modified Arrhenius equations, see Eq. (3.46) in chapter 3.2.3. Coverage-dependent activation energies and temperature-dependent pre-exponential factors are taken into account for certain steps. The microkinetics was validated against isothermal experiments in a flow reactor over powdered nickel-based catalyst, see Delgado et al. (2015) for more information.

Since the washcoat deposited on the spheres was relatively thin ($< 10\,\mu$m) instantaneous diffusion was assumed. As a consequence, no additional pore model was applied in the CFD simulation. The chemical source term at the reacting surface is calculated by $R_i^{het} = F_{cat/geo}M_i\dot{s}_i$ in [kg/m$^2\cdot$s], see chapter 3.2.3. The ratio of catalytic active area to geometric area $F_{cat/geo}$ was determined experimentally. The geometric area is the surface area of the spheres which is used in the CFD

simulations. Monodisperse spheres of 1 mm in diameter are assumed. The surface of one sphere results in $A_{\mathrm{geo}} = \pi \cdot d_{\mathrm{p}}^2 = 3.14159 \cdot 10^{-6}$ m$^2$. The catalyst characterization was conducted at FHI, see Tab. 10. $F_{\mathrm{cat/geo}}$ can be calculated with the following equation (Boll et al., 2010):

$$F_{\mathrm{cat/geo}} = \frac{A_{\mathrm{cat}}}{A_{\mathrm{geo}}} = D \cdot \frac{m_{\mathrm{Ni}}}{M_{\mathrm{Ni}}} \cdot \frac{1}{\Gamma} \cdot \frac{1}{A_{\mathrm{geo}}} \tag{6.3}$$

where $D$ is the Ni dispersion, $m_{\mathrm{Ni}}$ is the net weight of nickel on a single pellet, $M_{\mathrm{Ni}}$ is the molecular weight of Ni, and the surface site density of Ni $\Gamma$ equals $2.66 \cdot 10^{-5}$ mol/cm$^2$ (Maier et al., 2011). The net weight of Ni on a single sphere can be calculated by:

$$m_{\mathrm{Ni}} = \text{Ni content} \cdot \text{washcoat loading/numbers of pellets} \tag{6.4}$$

where the number of pellets can be calculated by the density of Al$_2$O$_3$, the weight of all pellets, and the volume of a single pellet. As a consequence, $F_{\mathrm{cat/geo}}$ equals 5.6. It has to be mentioned that nickel was not dispersed uniformly. Furthermore, the pellet shape and weight differed to some extent. Hence, $F_{\mathrm{cat/geo}}$ was tuned in such way that the predicted conversion of reactants was similar to the experiment. This results in a $F_{\mathrm{cat/geo}}$ of 12. Although the values are not totally consistent, they are in the same order of magnitude. In addition, if the Ni particle size distribution is low ($< 10$ nm) structure sensitivity becomes more important (Boll et al., 2010). For further work more detailed catalyst characterization should be carried out, especially in terms of distribution of the different types of surface patches.

Two different sets of thermal boundary conditions were applied in the steady-state CFD simulations:

1. The surface temperature of the catalyst particles was set to the experimental value at the corresponding axial position $\left(T_{\mathrm{cat, surf}}(z) = T_{\mathrm{exp}}(z) \neq f(r)\right)$. The particles were considered to be isothermal. For this set of simulation only gas phase and catalytic surface composition was computed.

2. Conjugate heat transfer was taken into account modeling the energy exchange between gas phase and solid particles. The endothermic reaction leads to a decrease of the particle temperature depending on the location inside the bed $\left(T_{\mathrm{cat, surf}} = f(r, \phi, z)\right)$. This means the inlet temperature and the wall temperature are the only fixed thermal boundary conditions.

For both cases, the capillary surface was treated as an adiabatic and impermeable wall. The boundary conditions and solid material properties are listed in Tab. 11. Gas phase properties were calculated according to section 3.3. Surface to surface radiation was taken into account as an additional heat transport-mechanism. The emissivity of the particle surface was set constant to $\varepsilon_{\mathrm{p}} = 0.85$. This assumption simplifies the fact that emissivity varies with temperature surface and condition of surface, e.g., surface coverage by coke and/or carbonaceous structures. A constant emissivity value was recently taken into account by Hettel et al. (2015) to simulate CPOX in a honeycomb reactor. The authors achieved reasonable agreement between CFD and experiments at temperatures up to 800 °C. The operation temperature of the DRM reactor (up to 850 °C) implies the intensifying effect of radiation on heat transfer inside the fixed bed. As a consequence, it seems

Table 11: Material properties and boundary conditions

| | |
|---|---|
| Mean bed porosity $\bar{\varepsilon}$ | 0.42 |
| Specific surface area $S_V$ | 3,380 m$^2$/m$^3$ |
| Hydraulic diameter $d_h$ | 0.497 mm |
| Specific heat of particle $c_{p,p}$ | 1.1244 kJ/(kg K) |
| Thermal conductivity of particle $k_p$ | 3.93 W/(m K) |
| $F_{cat/geo}$ (Eq. (3.42)) | 12 |
| Emissivity of particle $\varepsilon_p$ | 0.85 |
| Volume flow | 500 mL/min |
| Feed molar composition $CH_4/CO_2/Ar$ | 0.32/0.40/0.28 |
| Wall temperature $T_w$ | 850 °C |

to be more important to include radiation into the model than neglect it due to unknown radiation parameters.

Besides the particle-resolved 3D CFD simulation, a less sophisticated CFD model was used, i.e., the representative channel shown in Fig. 64. The 2D axis symmetric channel has a length similar to the bed height, and a hydraulic diameter according to $d_h = 4 \cdot \bar{\varepsilon}/S_V = 0.497$ mm. On the channel wall the detailed DRM reaction mechanism was implemented, as well as the temperature from the experiments. Close to the wall the rectangular mesh is finer resolving the boundary layer. With this simplified model only the first case of thermal boundary condition was calculated, i.e., with a fixed wall temperature from the experiments $\left(T_{cat,\,surf}(z) = T_{exp}(z)\right)$.

**2D CFD with representative channel**
$d_h = 4\,\varepsilon/S_V = 0.497$ mm
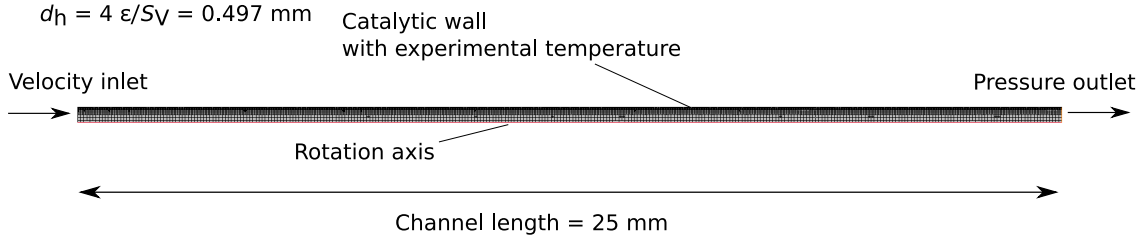


Figure 64: 2D representative channel model with dimensions and boundary conditions for DRM simulation.

### 6.4.3   Results and discussion

The measured temperature and concentration profiles of DRM at 850 °C and 500 ml/min in the fixed-bed reactor are illustrated in Fig. 65. The bed of spheres was placed on an alumina foam which also served as a front heat shield (FHS). The flow direction is from left to right. The reactants, i.e., $CO_2$ and $CH_4$, are consumed almost linearly, whereas the slope of $CO_2$ is steeper. Their profiles begin to decrease before the catalytic zone is reached. This is due to mass diffusion in counterflow direction. Syngas, i.e., CO and $H_2$, is produced with an almost linear slope, whereby CO shows a steeper gradient. Water is found only in a very small extent. Inside the FHS the

temperature increases due to radial heat transfer from the heated wall. The maximum is reached before the entrance of the catalytic bed. Due to endothermic reactions the temperature inside the bed decreases. The minimum is reached after approx. one third of the entire bed length ($z \approx 8$ mm). Temperature increases only slightly for the next 10 mm. After that there is a steep rise until the end of the bed is reached.
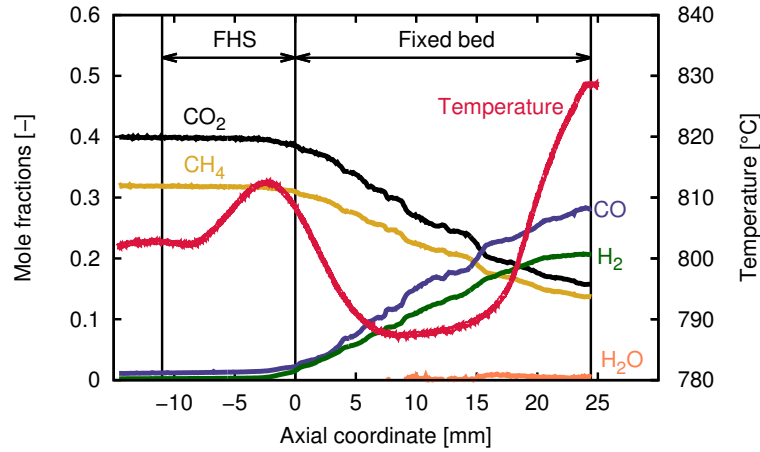


Figure 65: Measured temperature and concentration profiles of DRM at 850 °C and 500 ml/min in fixed-bed reactor.

#### 6.4.3.1 Set 1.1 Experimental temperature on surface and original kinetics

The first set of simulations is executed with the axial experimental temperature set as thermal boundary condition at the particle surface. Hence, over the radius there is no difference in surface temperature. It should be kept in mind that the temperature is measured in the center line of the bed. The measured concentration profile and the simulation results using the 2D representative channel is given in Fig. 66. The microkinetics are used without modifications from Delgado et al. (2015). As can be seen, the experiments are reproduced satisfactorily for $CO_2$, $CH_4$, and CO. However, $H_2$ is underestimated by approximately 50%, while water is highly overestimated. Furthermore, there is a steep gradient in the concentration profiles at the entrance of the bed followed by a nearly linear increase/decrease.

The simulated most abundant surface-adsorbed species for DRM at 850 °C and 500 ml/min are shown in Fig. 67 over axial position. These are CO*, O*, and H*. The other surface species are not shown. After one third of the reactor the catalyst is covered by approx. 40% with CO*, in which all the other surface adsorbed species drop below 1% coverage. Note that vacancies (Ni*) are not considered as surface species.

#### 6.4.3.2 Analysis of DRM kinetics and tuning

The unsatisfactory results of the simulated DRM fixed-bed with the original kinetics from Delgado et al. (2015) calls for an analysis of the kinetics and the CFD model. Firstly, the kinetics
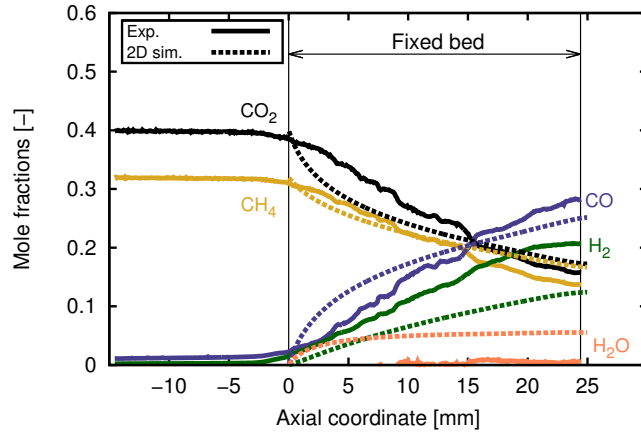
Figure 66: Concentration profiles of DRM at 850 °C and 500 ml/min. Measured profiles and 2D simulated profiles with original kinetics and experimental temperature.
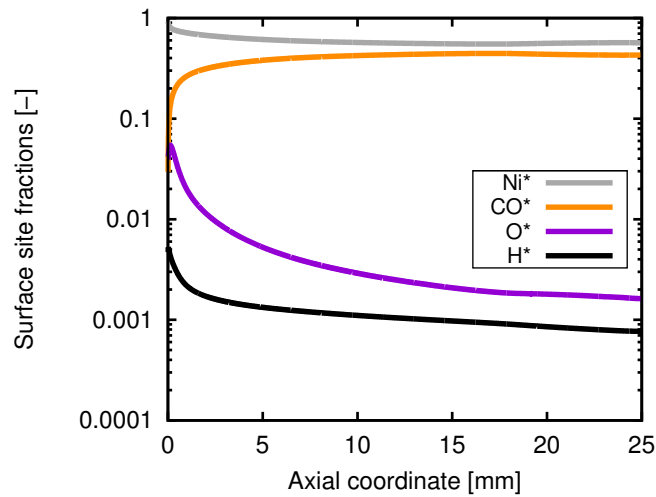


Figure 67: Simulated surface adsorbed species for DRM at 850 °C and 500 ml/min with experimental temperature profile.

in its original way was tested against CPOX and DRM experiments described by Delgado et al. (2015) (not shown). For both reactions experiments were reproduced with good accuracy for gas phase concentrations. However, the feed compositions are interesting to mention. For CPOX inert $N_2$ accounted for 97.86%. For DRM it was 96.0%. Hence, the partial pressure of reactants and products is very low. In comparison, the inert gas fraction in the DRM experiment in this work is 28%. Under the conditions of Delgado et al. (2015) activation energies are unlikely to be dependent on neighboring adsorbed species, like CO*, since the overall surface coverage is low. Coverage dependencies play a significant role under certain circumstances. Blaylock et al. (2011) investigated steam methane reforming over Ni computationally with plane-wave, periodic boundary-condition DFT. Three different facets of Ni were studied. The authors found out that especially CH* and C* show highly coverage dependent binding energies for Ni(100). They adjusted the heat of reaction for all reactions involving CH* and/or C*. However, no additional adsorbate-adsorbate interactions were taken into account (Blaylock et al., 2011). In the microkinetic model of Delgado et al. (2015) several heats of reaction are formulated being dependent on CO* coverage, i.e., reaction step 10, 38, 39, 40, 42, 47, and 49. Note that CO* is the most abundant adsorbed species in the DRM experiment above. Interestingly, not all of the activation energies of reaction steps including CO* are modified, i.e, reaction step 9, 35, 36, 37, 41, 43, 44, and 48. For reaction step 49 and 50 the activation energy depends on CO* although CO* is not participating.
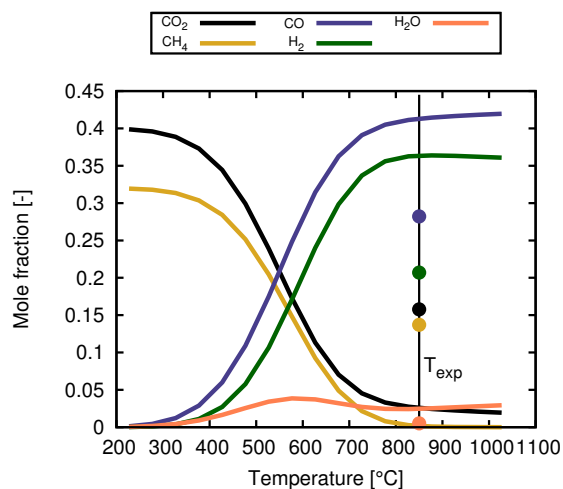


Figure 68: Calculated mole fractions in thermodynamic equilibrium of 32% $CH_4$ and 40% $CO_2$ in Ar as a function of temperature. Calculations based on a Gibbs free energy minimization implemented in DETCHEM$^{EQUIL}$ (Deutschmann et al., 2014). Dots show exit mole fractions of experiment in this work.

Another important aspect of microkinetics is thermodynamic consistency (Cortright and Dumesic, 2001; Mhadeshwar et al., 2003). If there is a violation of thermodynamic consistency, the equilibrium composition cannot be reproduced by the microkinetics. In Fig. 68 mole fractions in thermodynamic equilibrium are shown calculated based on a Gibbs free energy minimization implemented in DETCHEM$^{EQUIL}$ (Deutschmann et al., 2014). The gas composition was equal to the inlet composition of the DRM experiment. The outlet concentration of the fixed bed was not in equilibrium. Still, it becomes apparent that the water production with the original kinetics seems

to be overestimated. A reaction path analysis supports this finding, see Appendix 107 (A) and Fig. 108 (A).
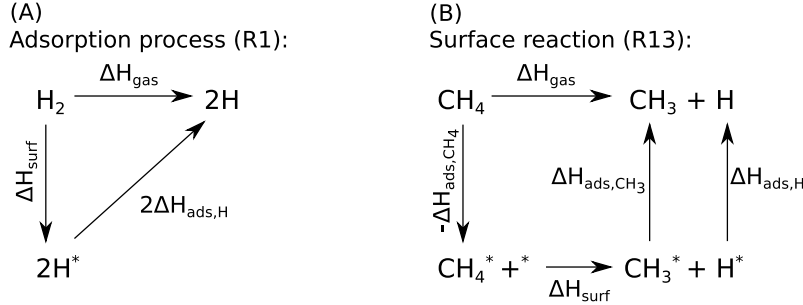


Figure 69: Thermodynamic constraints of adsorption process (A), and surface reaction (B).

Thermodynamic consistency can be analyzed by either evaluating the net reaction equilibrium constant (Eq. (3.39)) or by each individual reversible step (Eq. (3.37) and Eq. (3.38) in chapter 3.2.2). In Fig. 69 the thermodynamic constraints are visualized of an adsorption step and a surface reaction step from the DRM kinetics, reaction step 1 and 13 in Tab. 23 in the Appendix. In the figure only enthalpy is shown. Heat of desorption has a positive sign, whereas heat of adsorption shows a negative sign. A similar path can be drawn with entropy. Each surface step has its analogous gas phase reaction. A thermodynamic path analysis for both reactions reads:

$$\text{For step 1:} \quad \begin{aligned} \Delta H_1^{\text{gas}} &= \Delta H_1^{\text{surf}} + 2 \cdot \Delta H_{\text{H}}^{\text{ads}} \\ &= E_{1,\,\text{f}}^{\text{surf}} - E_{1,\,\text{b}}^{\text{surf}} + 2 \cdot \Delta H_{\text{H}}^{\text{ads}} \end{aligned} \tag{6.5}$$

$$\text{For step 13:} \quad \begin{aligned} \Delta H_{13}^{\text{gas}} &= \Delta H_{13}^{\text{surf}} - \Delta H_{\text{CH}_4}^{\text{ads}} + \Delta H_{\text{CH}_3}^{\text{ads}} + \Delta H_{\text{H}}^{\text{ads}} \\ &= E_{13,\,\text{f}}^{\text{surf}} - E_{13,\,\text{b}}^{\text{surf}} - \Delta H_{\text{CH}_4}^{\text{ads}} + \Delta H_{\text{CH}_3}^{\text{ads}} + \Delta H_{\text{H}}^{\text{ads}} \end{aligned} \tag{6.6}$$

Note that vacancies (*) are not considered in the analysis. Entropy analysis yields in a similar formulation. Some of the reactions are a linear combination of linearly independent reactions. That means that only some parameters in the microkinetics can be chosen independently. The reaction network can be written in form of a reaction matrix $\mathbf{P}$, where reactants have negative stoichiometric coefficients and products have positive stoichiometric coefficients. The columns of this matrix correspond to the species in the mechanism. The rows correspond to the reactions in the mechanism. Matrix $\mathbf{P}$ has a certain rank, which represents the amount of linearly independent reactions. This helps to determine the number of linearly independent adsorption enthalpies or entropies. For the given microkinetics the rank of matrix $\mathbf{P}$ is 15, whereby there are 26 reversible reaction steps. The system is overdetermined. The reduced row Echeleon from the inverse of matrix $\mathbf{P}$ can be computed conveniently with Matlab for example. This delivers the linearly independent reactions, which are R23-24, R25-26, R27-28, R29-30, R31-32, R33-R34, and R37-38, R39-40, R41-42, as well as R49-50, and R51-52. These reaction steps are in bold font in Tab. 12. For the linearly independent reaction steps an absolute error in thermodynamic consistency $\vec{\zeta}^{\text{error}}$ can be written

as:

$$\vec{\zeta}^{\,\text{error}} = \Delta\vec{\zeta}^{\,\text{surf}} - \Delta\vec{\zeta}^{\,\text{gas}} - \mathbf{P}\Delta\vec{\zeta}^{\,\text{ads}} \qquad (6.7)$$

where $\vec{\zeta}^{\,\text{error}}$ is given in [kJ/mol] for enthalpy or [J/mol K] for entropy, $\mathbf{P}$ is the reaction matrix, and $\vec{\zeta}$ is the vector containing $H$ or $S$ of each reaction step. For the DRM microkinetics the absolute error for enthalpy, i.e., heat of adsorption, and entropy of adsorption are shown in Tab 12.

Table 12: Thermodynamic consistency of DRM microkinetics from Delgado et al. (2015).

| Reaction step | Absolute error in enthalpy [kJ/mol] | | Absolute error in entropy [J/mol K] |
|---|---|---|---|
| | at 300 K | at 300 K with $\theta_{CO*} = 0.4$ | at 300 K |
| **R1-2** | 0.00 | 0.00 | $2.64 \cdot 10^{-7}$ |
| **R3-4** | 0.00 | 0.00 | $-8.00 \cdot 10^{-7}$ |
| **R5-6** | 0.00 | 0.00 | 0.00 |
| **R7-8** | 0.00 | 0.00 | 0.00 |
| **R9-10** | 0.00 | 20.00 | 0.00 |
| **R11-12** | 0.00 | 0.00 | 0.00 |
| **R13-14** | 0.00 | 0.00 | $-2.60 \cdot 10^{-8}$ |
| **R15-16** | 0.00 | 0.00 | $-8.10 \cdot 10^{-8}$ |
| **R17-18** | 0.00 | 0.00 | $1.12 \cdot 10^{-7}$ |
| **R19-20** | 0.00 | 0.00 | $6.39 \cdot 10^{-7}$ |
| **R21-22** | 0.00 | 0.00 | $2.18 \cdot 10^{-7}$ |
| R23-24[†] | $2.00 \cdot 10^{-1}$ | $2.00 \cdot 10^{-1}$ | $-9.84 \cdot 10^{-6}$ |
| R25-26[†] | $2.00 \cdot 10^{-1}$ | $2.00 \cdot 10^{-1}$ | $-7.30 \cdot 10^{-3}$ |
| R27-28[†] | $3.00 \cdot 10^{-1}$ | $3.00 \cdot 10^{-1}$ | $-4.04 \cdot 10^{-2}$ |
| R29-30[†] | -4.29 | 35.72 | $-8.25 \cdot 10^{-2}$ |
| R31-32[†] | $2.00 \cdot 10^{-1}$ | $2.00 \cdot 10^{-1}$ | $-2.98 \cdot 10^{-5}$ |
| R33-34[†] | 4.09 | -35.91 | $8.26 \cdot 10^{-2}$ |
| **R35-36** | 0.00 | 0.00 | $-1.42 \cdot 10^{-7}$ |
| R37-38[†] | $3.00 \cdot 10^{-1}$ | 20.30 | $-9.61 \cdot 10^{-6}$ |
| R39-40[†] | $2.00 \cdot 10^{-1}$ | 20.20 | $-1.91 \cdot 10^{-2}$ |
| R41-42[†] | $1.00 \cdot 10^{-1}$ | 20.10 | $-1.92 \cdot 10^{-2}$ |
| **R43-44** | 0.00 | 0.00 | $-2.11 \cdot 10^{-7}$ |
| **R45-46** | 0.00 | 0.00 | $-1.43 \cdot 10^{-7}$ |
| **R47-48** | 0.00 | -20.00 | $-2.26 \cdot 10^{-7}$ |
| R49-50[†] | $1.00 \cdot 10^{-1}$ | $1.00 \cdot 10^{-1}$ | $-1.60 \cdot 10^{-4}$ |
| R51-52[†] | 0.00 | 20.00 | $1.92 \cdot 10^{-2}$ |

**Bold face** reaction numbers are linearly independent.
[†] Linearly dependent reaction steps

As can be seen, the error for the linearly independent steps at 300 K are very low for both enthalpy and entropy. Especially, the linearly dependent reaction steps 29-30 and 33-34 violate thermodynamic consistency. But also the other dependent steps are not free of error. The dependency of activation energies on surface coverage is not thermodynamic consistent for R9-10 and R51-52, and for R29-30, R33-34, R37-38, R39-40, R41-42, and R51-52. Entropy is not violated by surface coverage since pre-exponential factors are not modified by $\Theta_i$. It has to be mentioned that the calculated adsorption enthalpy for R1-2 has a positive sign and the adsorption entropy for R1-2 and R3-4 show a positive sign which indicates violations. All calculated adsorption enthalpies and entropies are given in Tab. 13. In the publication of Delgado et al. (2015) these values are

not listed. As a conclusion, the modification of activation energies by surface site fractions is not thermodynamic consistent. This violation is amplified for high partial pressures of reactants since in those cases the surface site fraction of CO* is high.

Table 13: Calculated adsorption enthalpies and entropies of DRM microkinetics from Delgado et al. (2015).

| Species | Adsorption enthalpy [kJ/mol] | Adsorption entropy [J/mol K] |
|---|---|---|
| $H_2$ | 1.04 | 0.108923 |
| $O_2$ | -245.54 | 0.108244 |
| H | -262.74 | -0.095705 |
| O | -481.08 | -0.151225 |
| $H_2O$ | -60.70 | -0.1957 |
| $CO_2$ | -25.90 | -0.1878 |
| CO | -111.20 | -0.1646 |
| $CH_4$ | -37.50 | -0.2807 |
| $CH_3$ | -221.90 | -0.317825 |
| $CH_2$ | -381.72 | -0.315745 |
| CH | -527.81 | -0.323289 |
| C | -738.43 | -0.331963 |
| OH | -241.47 | -0.110503 |
| COOH | -196.52 | -0.170828 |
| HCO | -176.24 | -0.238111 |

It is difficult to ensure thermodynamic consistency over a wide range of temperatures, since forward and backward reaction steps are both formulated. Errors are amplified due to the exponential relationship of Gibbs free energy and the equilibrium constant. Violation of thermodynamic consistency can lead to erroneous predictions of heat and mass. Enthalpic inconsistency leads to incorrect solution of the energy balance. Thus, in a non-isothermal simulation wrong temperatures are predicted and likewise wrong conversion. In an isothermal simulation, the temperatures are fixed, however, the enthalpic inconsistency leads to errors in the mass balance. On the other hand, inconsistency in terms of entropy is characteristic for a fundamental inconsistency of pre-exponential factors. By defining both the forward and reverse reaction steps an incorrect equilibrium constant can be the result of thermodynamic inconsistency. This leads to an incorrect prediction of the equilibrium state (Mhadeshwar et al., 2003). An alternative to defining forward and backward reaction rates is by defining only the forward (or the backward) reaction and calculate the equilibrium constant from the given thermochemistry. Then the calculated backward (or the forward) reaction is by definition in thermodynamic equilibrium. The obstacle is the calculation of thermochemistry of surface species. Goldsmith (2012) presented an approach for estimating enthalpy, entropy, and specific heat for adsorbates on metals. As input parameters only binding energies of adsorbates and the geometric properties of the gas-phase precursor are needed. With this approach thermodynamic consistency would be maintained even if kinetically significant parameters are tuned to fit experimental data.

It is assumed that the high surface coverage by CO* is the reason for the discrepancy between experiments and simulation. With this original kinetics it is not possible to reproduce the experi-

ments with good accuracy. However, tuning single parameters of the kinetics is difficult and often leads to thermodynamic inconsistencies. Therefore, only a single parameter is tuned so that the model retains its main features but is able to reproduce the experiments.

It was found that the DRM microkinetics is very sensitive toward hydrogen adsorption/desorption (reaction step 1 and 2): $2* + H_2 \rightleftharpoons 2H*$. Consequently, the backward reaction is tuned by modifying the pre-exponential factor in dependency of surface coverage of CO*. With parameters for reaction step 2 from Tab. 23 the modified reaction rate coefficient results in:

$$k_2 = 2.54 \cdot 10^{(20+\eta_2 \cdot \Theta_{CO*})} \exp\left(\frac{-95.2\text{kJ/mol}}{RT}\right) \text{cm}^2/\text{mol}\cdot\text{s} \qquad (6.8)$$

where the tuning factor $\eta_2$ was set to 5, which results in a higher pre-exponential factor of step 2 for high CO* surface coverages. In the following, the tuned microkinetics is used in the CFD simulations.

### 6.4.3.3  Set 1.2 Experimental temperature on surface and tuned kinetics

Concentration profiles of DRM at 850 °C and 500 ml/min simulated with the experimental tem-
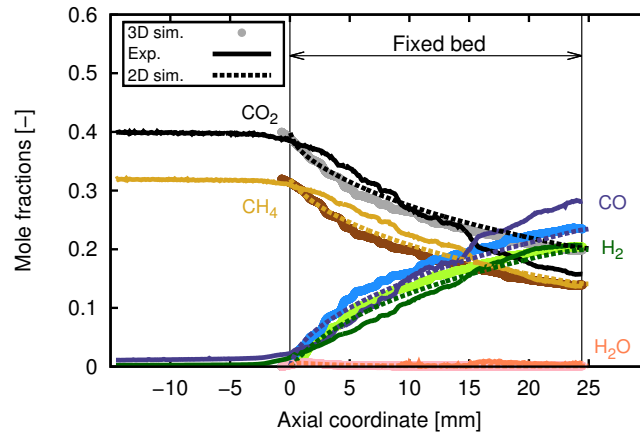


Figure 70: Concentration profiles of DRM at 850 °C and 500 ml/min. Measured and 2D, and 3D simulations with fitted kinetics and experimental temperature profile.

perature and tuned kinetics are shown in Fig. 70. The experimental concentration profiles are reproduced satisfactorily. Yet, the simulations predict a steeper gradient at the inlet of the reactor. The measured concentration profiles show a more linear increase/decrease. There are no large differences present between 2D and 3D simulations. Visualizing the concentration inside the 3D bed clearly indicates that there are almost no radial gradients found, see Fig. 71. Since the particle Reynolds number is very low ($Re_p < 10$), mass transfer limitations in the gas phase are expected to be negligible.

Fig. 72 (A) shows the Damköhler number and Fig. 72 (B) shows the production rates of DRM at 850 °C and 500 ml/min. The Damköhler number determines the dominant regime in terms of mass transport. In general, for $Da \gg 1$ the diffusion is dominant (diffusive regime), whereby for
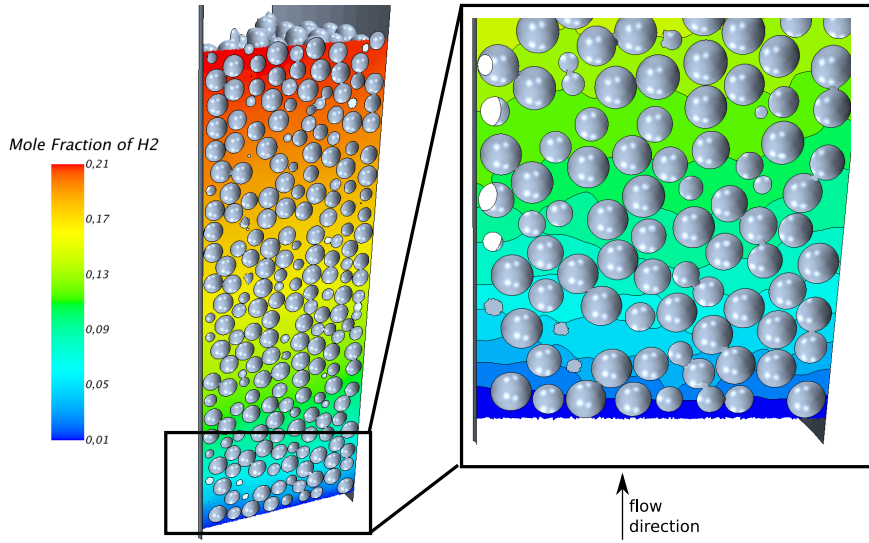
Figure 71: Simulated mole fraction of $H_2$ on a plane cut through the fixed-bed with detail on the inlet of the bed.

$Da \ll 1$ the kinetics controls mass transport (kinetic regime). Since the DRM microkinetics is formulated with multiple steps, the Damköhler number $Da_i$ is written with the pseudo first-order kinetic constant $k^*_i$ [m/s] of reactant $i$:

$$Da_i = \frac{k^*_i \cdot L}{D^i_M} = \frac{\dot{s}_{i,s} \cdot L}{c_{i,g} \cdot D^i_M} \qquad \text{for} \quad i = CO_2, CH_4 \tag{6.9}$$

with $L$ as the characteristic length, $\dot{s}_{i,s}$ is the molar net production rate on the surface [kmol/m$^2\cdot$s], the gas phase concentrations $c_{i,g}$ [kmol/m$^3$], and $D^i_M$ is the effective diffusivity [m$^2$/s] between species $i$ and the remaining mixture. The characteristic length represents the distance which a species has to pass from the bulk gas phase to the catalytic surface. In this case $L$ is approximated with the hydraulic radius of a representative channel, i.e., $L = d_h/2 = 0.497$ mm. The Damköhler number clearly indicates the kinetic regime, since mass transport by diffusion is faster than kinetics by a factor 200-1000. After the entrance zone of the reactor $Da$ drops below 0.002. As a consequence, an advanced transport model is not advantageous over a simplified mass transport model. Fig. 70 supports this finding. The production rates are shown in Fig. 72 (B) only for CO, $H_2$, and $H_2O$. Water is produced only at the very beginning of the reactor. After 2 mm the production rate tends to zero. The production rates of CO and $H_2$ decrease steadily.

Local kinetics is not only dependent on local mass transport but also on temperature. Since radial temperature profiles were not measured in the fixed-bed reactor, ex-situ observations were carried out to give insights into radial differences. Fig. 73 (A) shows the bed of catalytic particles after DRM from a side view. Fig. 73 (B) displays the top view of the third layer of particles. Different shades of grey can be noticed on the particle surfaces. This indicates a different state of surface composition and hence different axial, as well as radial temperatures. Interestingly, in Fig. 73 (B) the brightest particles are found in the core of the bed. This might be due to the low temperature in the center, as well as channeling caused by the capillary. This is a clear evidence that radial temperature differences are present in the bed and significant for DRM process.
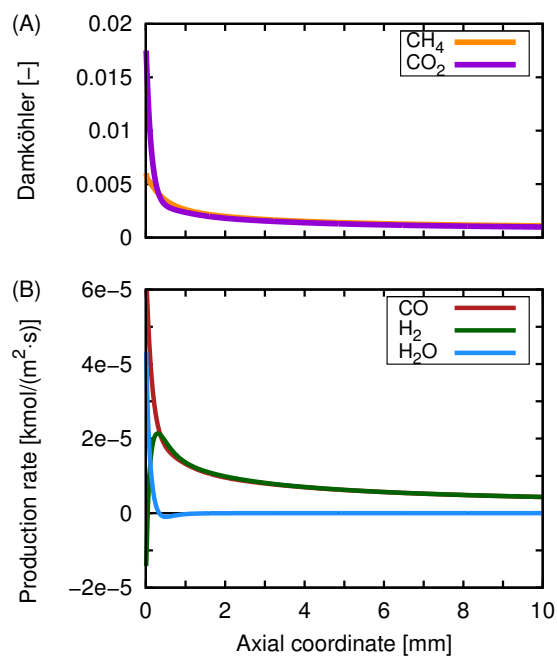
Figure 72: (A) Damköhler number and (B) production rate of DRM at 850 °C and 500 ml/min.
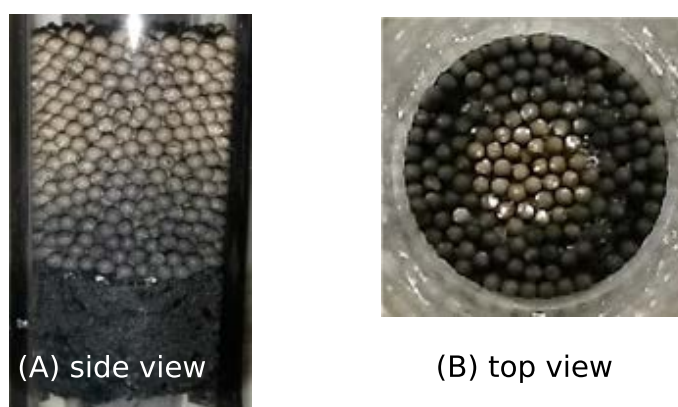


Figure 73: (A) Side view of the packed bed after DRM, and (B) top view of the third layer of catalytic spheres.

### 6.4.3.4    Set 2: Conjugate heat transfer and tuned kinetics

In the second set of simulation thermal conduction through the particles is considered, which the simplified representative channel is not capable to model. Hence, only 3D simulations are performed. Constant inlet temperature and constant wall temperature are set. The temperature of each particle is determined by the local rate of reaction and the local flow field. The steady-state simulation was stopped when convergence was reached for local temperatures and outlet composition. Concentration profiles of DRM at 850 °C and 500 ml/min for measured and 3D simulations with tuned kinetics and conjugate heat transfer is shown in Fig. 74. Now, the simulated $H_2$ and CO profiles coincide in the center line of the bed. Whereas the $H_2$ profile fits well with the experiment, the CO profile is underestimated. In addition, the $CO_2$ conversion is lower than for the fixed temperature case.
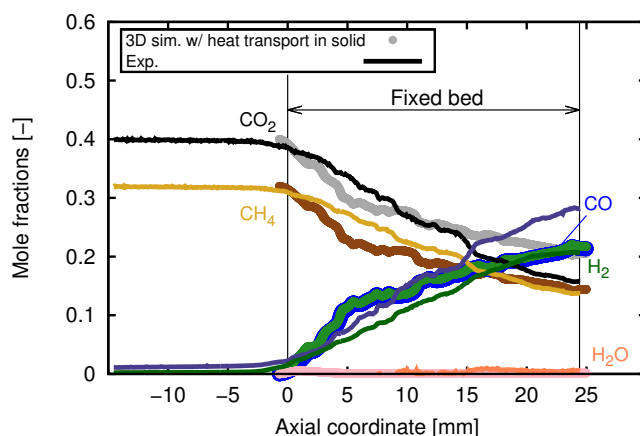


Figure 74: Concentration profiles of DRM at 850 °C and 500 ml/min. Measured and 3D simulations with fitted kinetics and heat transport through the solid particles.

The simulated temperature in the center line of the bed and the experimental temperature profile are shown in Fig. 75. A temperature drop of 70 K is predicted. In the experiment the temperature decreases by only 25 K and a plateau occurs. In the CFD simulation after the minimum is passed the temperature increases steadily until the end of the bed is reached. On the one hand, the discrepancy between experimental and predicted temperature can be attributed to the kinetics, since heat transfer without chemical reactions was validated positively. This might indicate a violation of thermodynamic consistency in the microkinetics. On the other hand, heat fluxes might be modeled incorrectly. For example no heat loss is taken into account for the capillary, although there exists thermal conduction in the capillary. This effect was neglected since the volume of the capillary is very small in comparison to the reactor. Also, in the simulation the FHS was not modeled, although there exists heat transfer by thermal conduction between the bed and the FHS. Moreover, there is a difference in experimentally determined and applied $F_{cat/geo}$ value. This might be the indication that the structure of the Ni particles on the washcoat differs from the experiments of Delgado et al. (2015) in terms of surface-patch distribution.

The interactions between local energy, momentum and species transport can be seen in Fig. 76. On
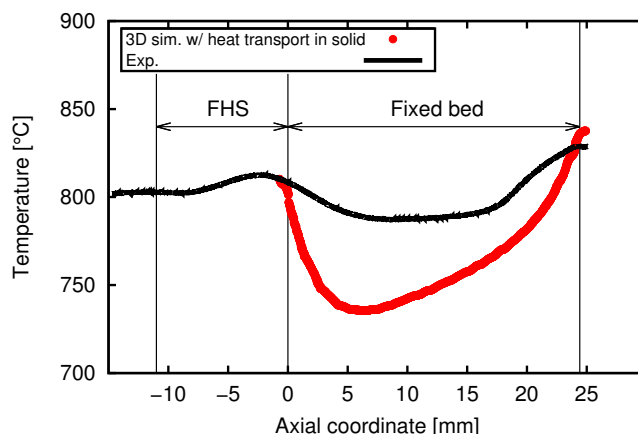
Figure 75: Experimental and simulated temperature with heat transport through the solid particles in axis of bed for DRM at 850 °C and 500 ml/min.

a plane cut through the catalytic fixed-bed the temperature is shown (A), as well as mole fraction of $CH_4$ (B) and $H_2$ (C). On the surface of the spheres the surface site fraction of CO* is visualized in Fig. 76 (D). The temperature shows the lowest values in the central axis with radial gradients. Since the velocity is very low the gas phase temperature is almost similar to the temperature of the spheres. Temperature channeling is not present. Contrarily, the mole fraction profiles show channeling close the reactor wall, which is indicated by contour lines in Fig. 76 (B) and (C). This is mainly due to higher porosity in the near-wall region, cf. local porosity profile in Fig. 60. The local temperature influences the local rate of conversion and vice versa. However, the radial gradients are not very large. The distribution of surface site fraction of CO* is dominated by the axial direction. A correlation between the photograph in Fig. 73 (A) and (B) and the surface site fraction of CO* is not apparent. This indicates that the visible change of surface color is not related to CO*. However, the predicted radial temperature gradients and the radial color distribution in the photograph show a certain correlation.
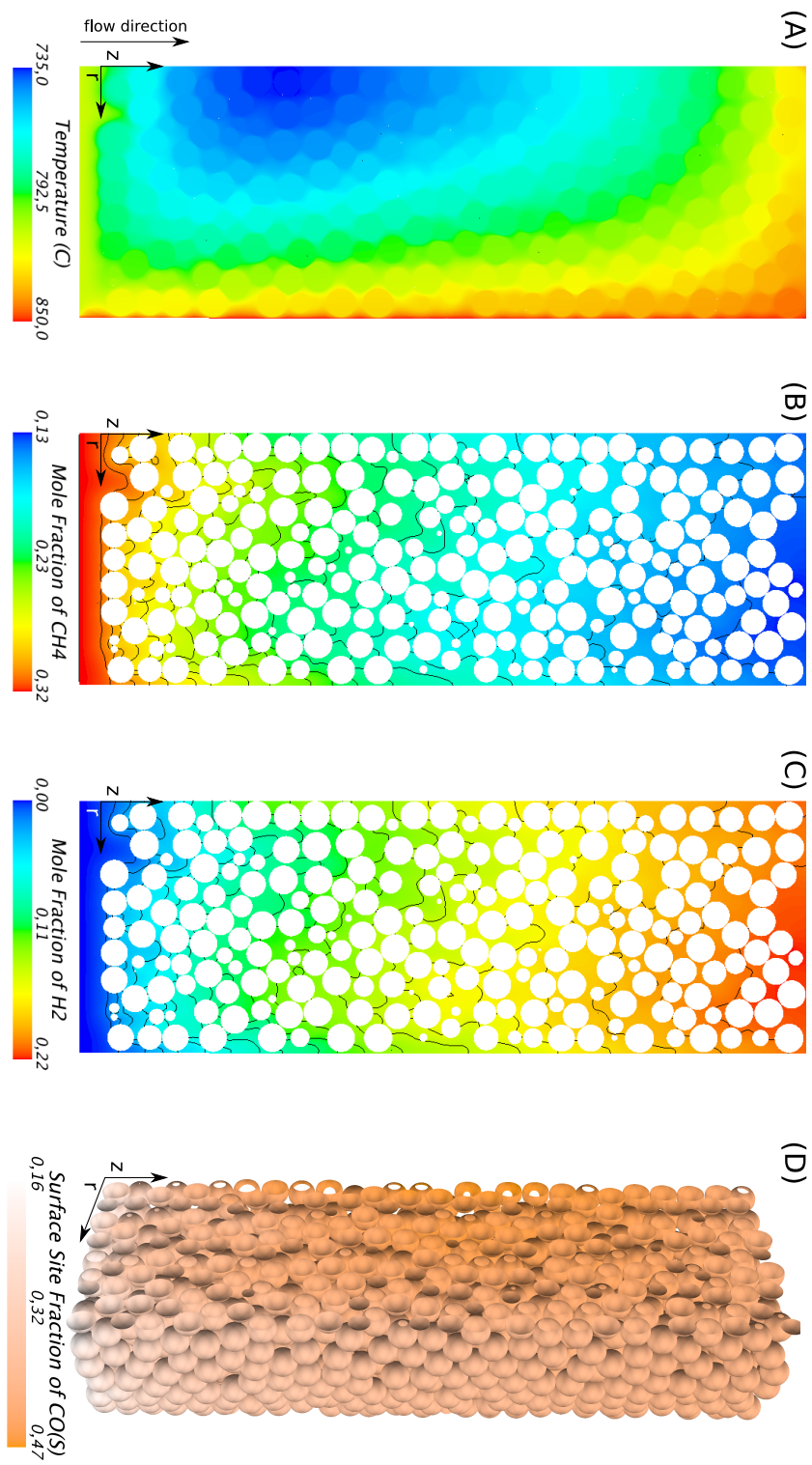
Figure 76: (A) temperature, (B) CH$_4$ concentration, (C) H$_2$ concentration, and (D) CO* on a plane cut through the bed. DRM at 850 °C and 500 ml/min.

## 6.5 Influence of contact-area modification in fixed beds of cylindrical particles

In this study modification approaches of contact areas are explored in a fixed bed of cylindrical particles. Contact-point modifications in fixed beds of spheres have been studied by several authors in the past. The effect of these modifications toward the surrounding flow field and temperature field were analyzed by Dixon et al. (2013b); Eppinger et al. (2014), and Bu et al. (2014). The authors come to the mutual conclusion that local methods are less influencing than global methods. Among the local modification approaches Dixon et al. and Bu et al. recommend the bridges method over the caps method. Especially for higher Reynolds numbers fluid gaps reduce the heat transfer too much (Dixon et al., 2013b).

In contrast to spheres, non-spherical particles can have contact points, contact lines and contact areas with each other and with confining walls, see Fig. 9 for visualization. The different contact areas can occur in varying extent in a packed bed. Moreover, their effect toward the local transport phenomena can be variable depending among others on the individual position, flow regime, and thermal properties. In this study, three different kinds of contact-area modifications are investigated critically, i.e., the *caps* method, the *united* method and the *bridges* method. The influence of the geometrical modifications is evaluated with respect to pressure drop, and local velocity fields, heat transfer, as well as local temperature fields. Finally, recommendations are given which contact modification approach should be chosen to model adequately packed beds of non-spherical particles.

### 6.5.1 Experimental setup

In the experiments from Bey and Eigenberger (1997) velocity profiles were measured below fixed beds of different particle shapes, i.e., spheres, cylinders, and one-hole cylinders. The packed beds were characterized by their low tube-to particle-diameter ratio, which varied from $3.3 \leq N \leq 11$ by using different particle sizes. The working fluid was air at ambient pressure with superficial velocities covering $0.5 \leq v_{in} \leq 1.5$ m/s. The tube had an inner diameter of 25 mm. The bed height is not mentioned in the manuscript. The particles were placed on a monolith of 3.5 mm in length with a channel width of 1 mm and a total porosity of 85%. An anemometer was placed 5 mm below this monolith to measure the local fluid velocity. The position of the sensor was varied in terms of radial and annular position, see Fig. 77. Velocity measurements were averaged after repacking the bed to obtain a statistical representative flow profile. For more information on the experimental setup see Bey and Eigenberger (1997). The authors assume that the monolith has no influence on the velocity profile. However, strong recirculation zones can be noticed below a packing, which was observed already in section 6.2.2.3. Still, the setup itself is interesting since low $N$ beds are investigated experimentally with particle dimensions relevant for industrial applications.

### 6.5.2 CFD setup

A packed bed of cylinders with $d_p = l_p = 12$ mm was studied in line with the experiments from Bey and Eigenberger (1997). The resulting tube-to-particle-diameter-ratio is $N = 0.05/0.012 = 4.17$.
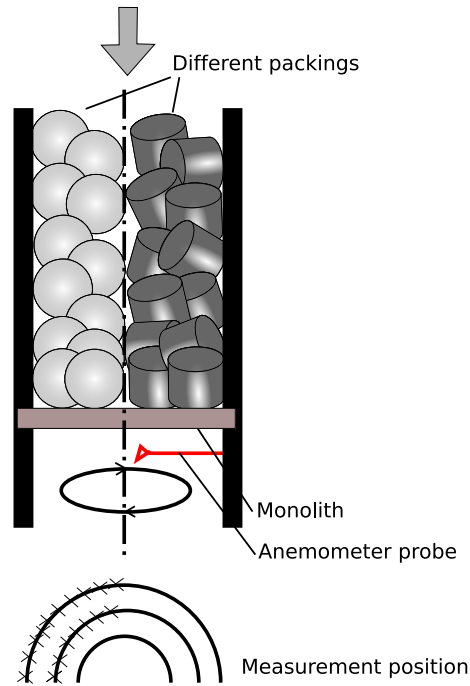
Figure 77: Experimental setup of velocity field measurement. Redrawn from Bey and Eigenberger (1997).
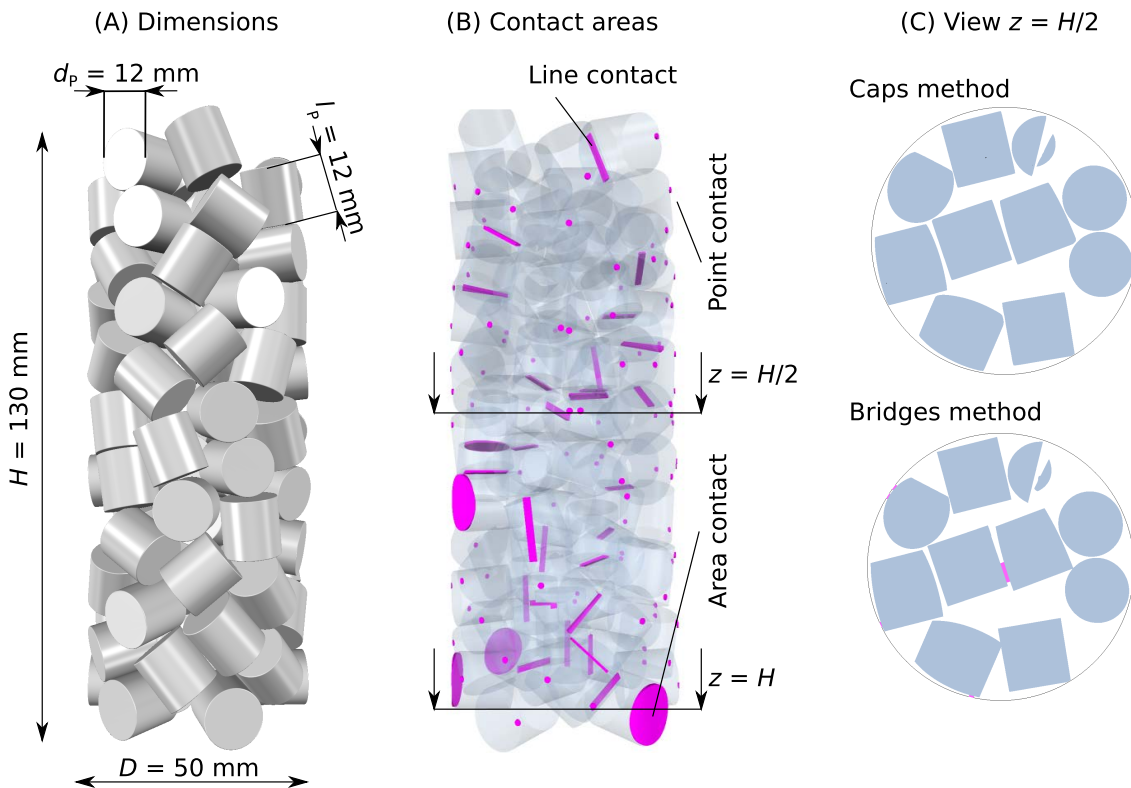


Figure 78: Automatically generated packed bed of cylinders (A), and contact areas highlighted in magenta (B). View at $z = H/2$ (C).

The automatically generated fixed bed with all dimensions is illustrated in Fig. 78 (A). There is no bed height given in Bey and Eigenberger (1997). Since the axial porosity profile is uniform after approx. 3 particle diameters (Giese et al., 1998) a bed height of $\approx 10 \cdot d_\mathrm{p}$ was chosen.

The generation of the randomly packed bed was realized with the work flow described in section 4.1. The amount of particles in this bed was approximated with the overall porosity of bed of cylinders described by the equation of Dixon (1988):
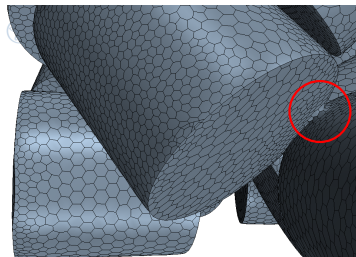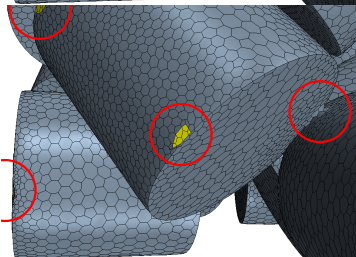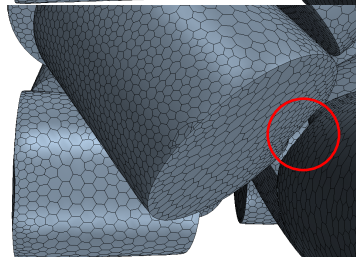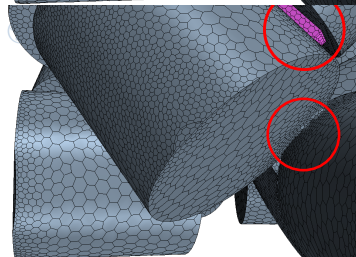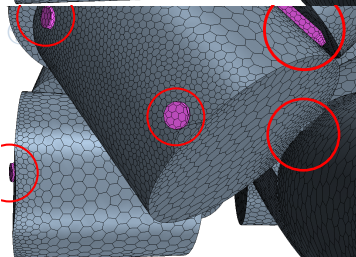
$$\bar{\varepsilon} = 0.36 + 0.1/N + 0.7/N^2 \qquad (6.10)$$

where $N$ is the tube-to-diameter ratio $D/d_\mathrm{p}$. To match the predicted porosity the packing generation was tuned by adjusting the static friction coefficient of the DEM particles. This method was suggested earlied by Ookawara et al. (2007). It turned out that a value of 0.015 results in a porosity that is close to the value predicted by the equation above. It has to be mentioned that this value is unrealistic low. Sliney and DellaCorte (1993) studied friction and wear of ceramic/ceramic and ceramic/metal combinations over a wide range of temperature. The authors found typical friction coefficients for monolithic alumina in the range of $0.5 - 0.7$. However, composite ceramics are characterized by lower values, e.g., mullite showed values between $0.35 - 0.5$.

Three different superficial velocities were chosen in line with the experiments, i.e., 0.25 m/s, 0.5 m/s, and 1 m/s. For the evaluation of pressure drop and heat transfer the properties of air were set constant to $\rho_\mathrm{f} = 1.18$ kg/m$^3$, $\mu_\mathrm{f} = 1.855 \cdot 10^{-5}$ Pa$\cdot$s, $c_{p,\mathrm{f}} = 1003.62$ J/kg$\cdot$K, $k_\mathrm{f} = 2.603 \cdot 10^{-2}$ W/m$\cdot$K. This results in particle Reynolds numbers of 191, 382, and 763, respectively. Conjugate heat transfer inside the packed bed was investigated numerically although there is no corresponding experiment. The wall temperature was set constant at 373.15 K, and the inlet temperature was set to 300 K. The particles were modeled with the following constant properties: $\rho_\mathrm{p} = 1300$ kg/m$^3$, $c_{p,\mathrm{p}} = 1000$ Pa$\cdot$s, $k_\mathrm{p} = 5$ W/m$\cdot$K.

The contact areas were modified with different approaches described already in chapter 4.2, i.e., the caps method, the united method, and the bridges method. Thermal conductivity of bridges was kept constant, since varying values, as described by Dixon et al. (2012b), are complex to calculate for non-spherical particles. However, the value was chosen to be smaller than the solid thermal conductivity. Two different values were tested, i.e., $k_\mathrm{bridge} = 0.07$ and 0.5 W/m$\cdot$K. The composite DEM method results in certain overlaps, which can also occur between particles and the confining wall. Hence, in all cases of contact-area modification a tube with $0.99 \cdot D$ was subtracted from all of the particles touching the tube wall. This ensures a well defined gap between particles and confining wall. In Tab. 14 a detail is given of touching cylinders and a wall contact visualizing the different modifications of contact areas. As can be seen, the local modified regions are small in comparison to an overall modification of the particles. Bridges are highlighted in magenta. These bridges are treated as an additional region type in the CFD simulation, which enables the specification of thermal properties of the bridges. The location of contact areas in a packed bed of cylinders is shown in magenta in Fig. 78 (B). Only four cylinders touch the wall with their plane face. In these cases, area contacts were inserted applying the bridges method. More often, line contacts between the confining wall and the shell surface of cylinders can be found. In addition, inside the bed there exists a number of point contacts and line contacts, respectively.

Table 14: Detail of touching cylinders and wall contact for different contact-area modifications.

| Method | Detail | Comment |
|---|---|---|
| United w/o wall contact |  | Overlaps between particles. Gaps between particles and wall. |
| United w/ wall contact |  | Overlaps between particles. Direct contact between particles and wall. |
| Caps |  | Gaps between particles. Gaps between particles and wall. |
| Bridges w/o wall contact |  | Overlaps at contact points. Bridges at contact lines and areas. Gaps between particles and wall. |
| Bridges w/ wall contact |  | Overlaps at contact points. Bridges at contact lines and areas. Bridges between particles and wall. |

Polyhedral meshes were used with 2-3 prism layers, whose thicknesses depend on the particle Reynolds number. The thickness of the prism layers was approximated with the thickness of the boundary layer in the stagnation point of a sphere depending on $Re_\mathrm{p}$, see Eq. (6.1). In Fig. 79 (A) a detail is given of the mesh close to two connecting cylinders treated with the bridges method. On the left hand side a line contact can be seen. On the right hand side the cylinder and the wall are connected with an area contact bridge. In Fig. 79 (B) the same location is shown for the caps method. At contact areas the particles are slightly flattened. The different colors represent the different calculation regions, i.e., fluid region in blue, particle region in grey, and bridge region in magenta. The total amount of computational cells varies with contact-area modification, see Tab. 15. Much finer meshes are needed applying the bridges method, since more complex geometries and and thinner regions occur.
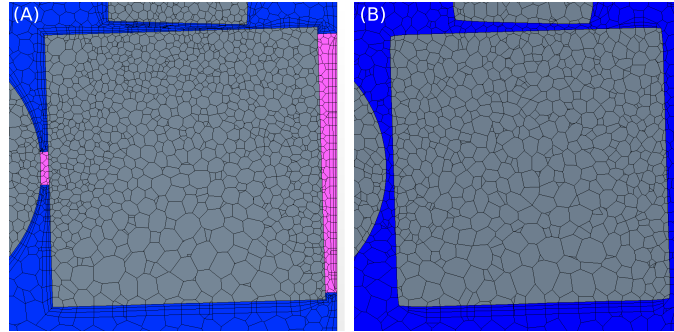


Figure 79: Detail of mesh with bridges method (A). Same location with caps method (B).

### 6.5.3   Results and discussion

#### 6.5.3.1   Pressure drop and velocity profiles

Table 15: Porosity and pressure drop for packed beds of different particle shapes and different contact-area modifications.

| Particle shape | No. of cells | $\bar{\varepsilon}$ | Dev. to Eq. (6.10) | $\Delta p / \Delta H$ for $Re_\mathrm{p} =$ | | |
|---|---|---|---|---|---|---|
| | | | | 191 | 382 | 763 |
| | $[\cdot 10^6]$ | [-] | [%] | [Pa/m] | [Pa/m] | [Pa/m] |
| United w/o wall contact | 1.65 | 0.415 | -1.9 | 103 | 331 | 1110 |
| United w/ wall contact | 1.64 | 0.415 | -1.9 | 103 | 332 | 1112 |
| Caps | 1.66 | 0.416 | -1.7 | 102 | 328 | 1075 |
| Bridges w/o wall contact | 3.66 | 0.413 | -2.4 | 108 | 383 | 1309 |
| Bridges w/ wall contact | 3.67 | 0.413 | -2.4 | 117 | 405 | 1317 |

The global porosity of the bed is a first indication of the influence of geometrical modifications. As can be seen in Tab. 15, the low static friction coefficient leads to a porosity which is close to the predicted value by Eq. (6.10) ($\approx -2\%$). Furthermore, the difference between the individual contact point modification toward global porosity is low, i.e., $< 1\%$. In Fig. 80 (A) the radial porosity of cylinders are compared between different contact-area modifications. The values are obtained by averaging the void fraction, and the velocity component in $z$ direction over height, and over circumference. Differences occur only in the near-wall region, where the bridges method with wall contact shows the lowest porosity. It becomes clear that this local modification approach has a low influence on the averaged porosity profile, and hence on the averaged local velocity, see Fig. 80 (b). Deviations occur only at the first maximum in the near-wall region.
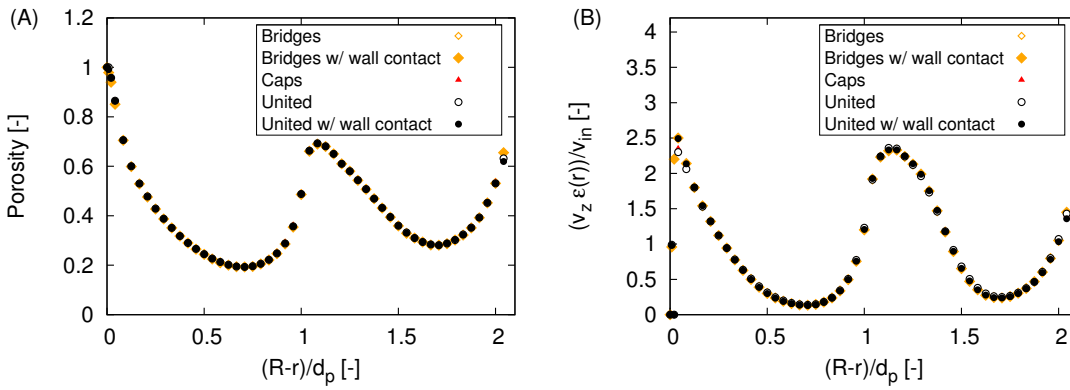


Figure 80: (A) Radial porosity profile and (B) velocity of packed-bed of cylinders averaged over height and circumference. $Re_\mathrm{p} = 382$.

A first impression of the flow field inside the fixed bed gives Fig. 81 (A). Velocity vectors are animated on a plane cut through the bed to get a better idea of changing directions of the flow. The gas enters the bed from the top. Stagnation zones can be identified, as well as channeling close to the wall. Moreover, regions with accelerated flow and recirculation zones occur inside the bed. The largest velocity on this section through the bed is 8-9 times larger than the superficial velocity. In Fig. 81 (C) streamlines indicate the flow direction inside the bed, which is from left to right. Below the bed recirculation zones are visible.

A comparison of the velocity below the bed between CFD and experiments from Bey and Eigenberger (1997) is shown in Fig. 82 (A). The CFD results are shown only for the caps method, since the difference between the methods is very small at this distance below the bed. They are in fair agreement over the radius in the range of $0 \leq (R-r)/d_\mathrm{p} \leq 1.3$. Close to the center of the tube the velocities from CFD simulation differ from the experimental values. The CFD simulation predicts a recirculation zone indicated by negative velocity components in the $z$ direction. These zones inside and below fixed-beds have been shown previously, see chapter 6.2. In the experiments the particles are placed on a monolith, which firstly influences the flow direction below the bed, and secondly prevents recirculation zones. In addition, the anemometer cannot distinguish the direction of the flow. Moreover, the velocity below the bed is dominated by the position of the last row
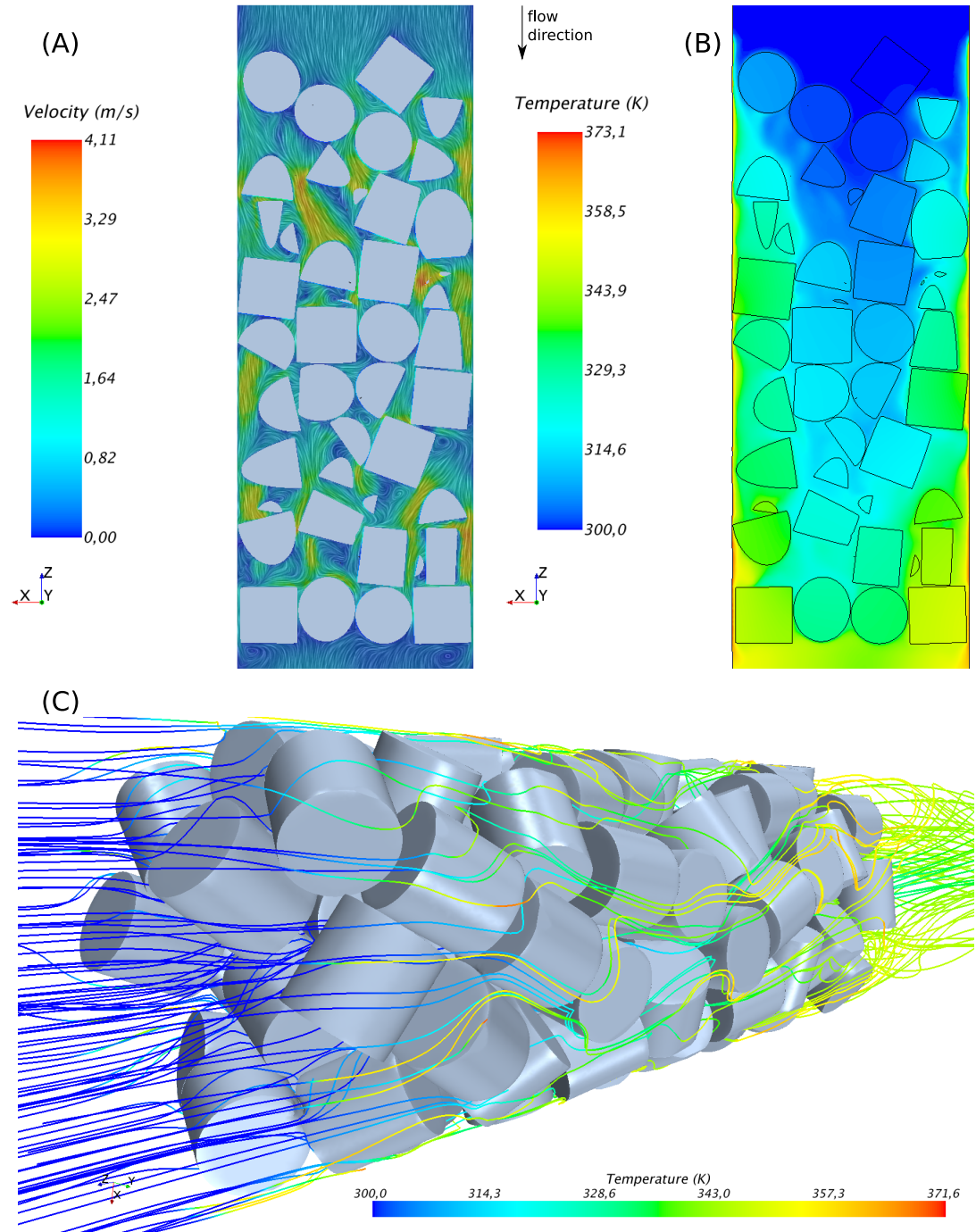
Figure 81: (A) Velocity contour, and (B) temperature on a plane cut through the bed of cylinders. (C) Streamlines inside the bed. $Re_\mathrm{p} = 382$

of particles. Bey and Eigenberger repacked the bed and repeated the measurement a certain number of times. The CFD simulation was carried out only for one bed geometry. Still, the agreement between CFD and experiments is satisfactory.
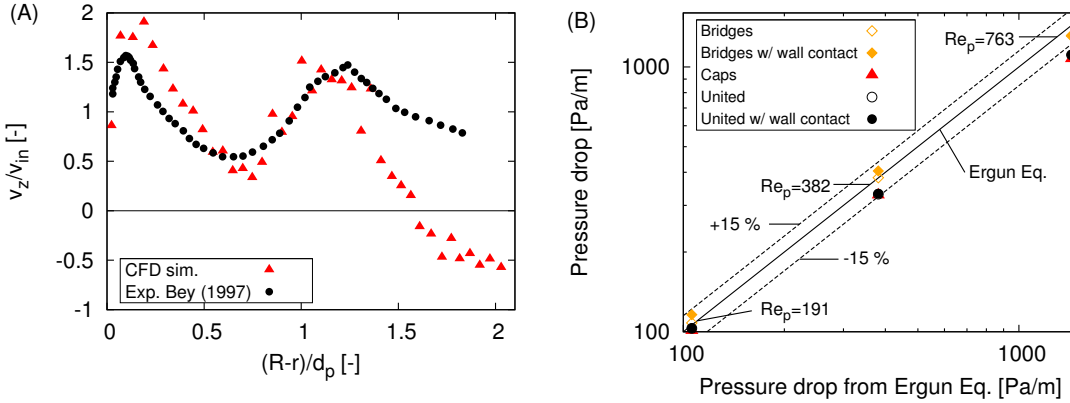


Figure 82: (A) Comparison between experiments and CFD simulations of local velocity below fixed bed of cylinders ($Re_\mathrm{p} = 382$). (B) Parity plot of pressure drop of CFD simulations and prediction from the Ergun equation.

The averaged velocity profiles for the different modifications do not show large deviations. However, the pressure drop differs by approx. 15% between the lowest value, i.e., the caps method, and the highest value, i.e., the bridges method with cylinders inserted at particle-wall contact areas. As can be seen in Tab. 15, wall cylinders have only little influence on the entire pressure drop. It is more influenced by the type of contact modification. Two groups can be identified in Fig. 82 (B). A parity plot is shown for pressure drop of CFD simulations against predictions from the Ergun equation for three different Reynolds numbers. The bridges method with and without wall contacts shows high pressure drops. The caps method and the united method with and without wall contacts show similar lower pressure drops. Over the investigated velocity range the two groups differ by approx. 10%. For the lowest and moderate flow rate CFD pressure drop is in a range of $\pm15\%$ in comparison to the Ergun equation. For the high Reynolds number the CFD values are lower than the values from the equation. It has to be kept in mind that the Ergun equation does not account for the influence of confining walls, which are dominant for low $N$ beds. Moreover, Bai et al. (2009) showed large deviations between experimental pressure drop of low $N$ beds and predictions from the Ergun equation. Particle orientation and void fraction played a significant role.

Integral values like pressure drop, etc. are a first indication for validating the different modification strategies. However, in certain regions the local flow field can show large deviations between the different approaches. Hence a detailed analysis of local velocity and temperature is presented for two different positions ($z = H/2$ and $z = H$) and two different Reynolds numbers ($Re_\mathrm{p} = 191$ and 763), respectively. A view of the bed at $z = H/2$ is given in Fig. 78 (C). The position $z = H$ is just below the packed bed. Consequently, there is no solid phase. In Fig. 83 (a) and Fig. 84 (a) the velocity in axial direction is shown. The figure on top shows values after half of the bed height.

The figure at the bottom shows values below the bed. All values are averaged in circumferential direction. In addition, radial porosity is given only for two modification approaches, i.e., caps and bridges method with wall contacts. As can be seen in this figure and also in Fig. 78 (C) the modified region is very small. Only in the center of the bed radial porosity differs significantly. The local velocities vary by up to a factor of four for the different modifications at the position $z = H/2$. In the figure the velocity in $z$ direction is shown. The deviation is due to the change in geometry at individual positions, which results in a change of velocity direction. A different picture shows the section below the bed, i.e., at $z = H$. The flow field is dominated by the position of the last layer of particles, which is identical for all of the investigated cases. For the low flow situation there exists a stagnation zone at the center of the bed. The axial velocity is close to zero for $(R - r)/d_\mathrm{p} > 1.6$. On the contrary, for the high $Re$ situation a back-flow region occurs in the center. This is indicated by negative axial velocities. Except for the near wall region, there are no large deviations between the different contact-area modifications below the bed. This is also due to the low number of particles at the bottom of the bed. Hence, the influence of contact-area modifications is low.

### 6.5.3.2   Heat transfer

An impression of the temperature field inside the fixed bed gives Fig. 81 (B) for $Re_\mathrm{p} = 382$. The interactions between local flow and local heat transfer can be recognized. Channeling occurs close to the wall, which has a strong effect on the transferred heat from the wall into the bed.

The wall Nusselt number $Nu_\mathrm{w}$ is suitable for comparing near-wall heat-transfer characteristics. In Fig. 85 the wall Nusselt numbers of the CFD simulations are plotted against $Nu_\mathrm{w}$ from the correlation of Martin and Nilles (1993), see Eq. (2.17). Three different Reynolds numbers are evaluated. In the figure intervals of $\pm 10\%$ of the predicted values are represented by dotted lines. Five out of seven contact-area modifications are located in this interval. Contrarily, the united method with wall contacts and the bridges method with wall contacts and $k_\mathrm{bridge} = 0.5$ W/mK overestimate the wall Nusselt number by approx. 50% and 30%, respectively. The heat transferred in the bed with bridges depends significantly on the effective thermal conductivity of the bridges. Using a very low thermal conductivity of the bridges, i.e., $k_\mathrm{bridge} = 0.07$, $Nu_\mathrm{w}$ is even lower than with the caps method. This is due to convective heat transfer inside the gaps by applying the caps method. This mechanism is getting more dominant with higher $Re$. Inside the bridges, only conduction is assumed. However, the largest effect toward transferred heat in the near-wall region is connected with wall contacts. By applying wall contacts with the united method $Nu_\mathrm{w}$ is increased by approx. 50%, in comparison with gaps between the wall and particles. The heat transfer is that high because a large portion of the particles are connected directly with the wall. That means there is no thermal resistance between wall and neighboring particles. However, this fact is contrary to the idea fo $Nu_\mathrm{w}$, which is formulated only with gas phase properties. In addition, a negligible thermal resistance at a wall-particle contact is only imaginable for e.g., sintered particles. Thus, the united model in combination with direct wall contacts is not suited for modeling heat transfer in fixed-bed reactors. The bridges method can be extended by cylinders connecting the particles and the wall. As a convenient fact the effective thermal conductivity

(a) Velocity

(b) Temperature

Figure 83: Circumferentially averaged velocity (a) and temperature (b) over radius for different contact region modifications. (A) at $z = H/2$, and (B) at $z = H$ for $Re = 191$.

(a) Velocity
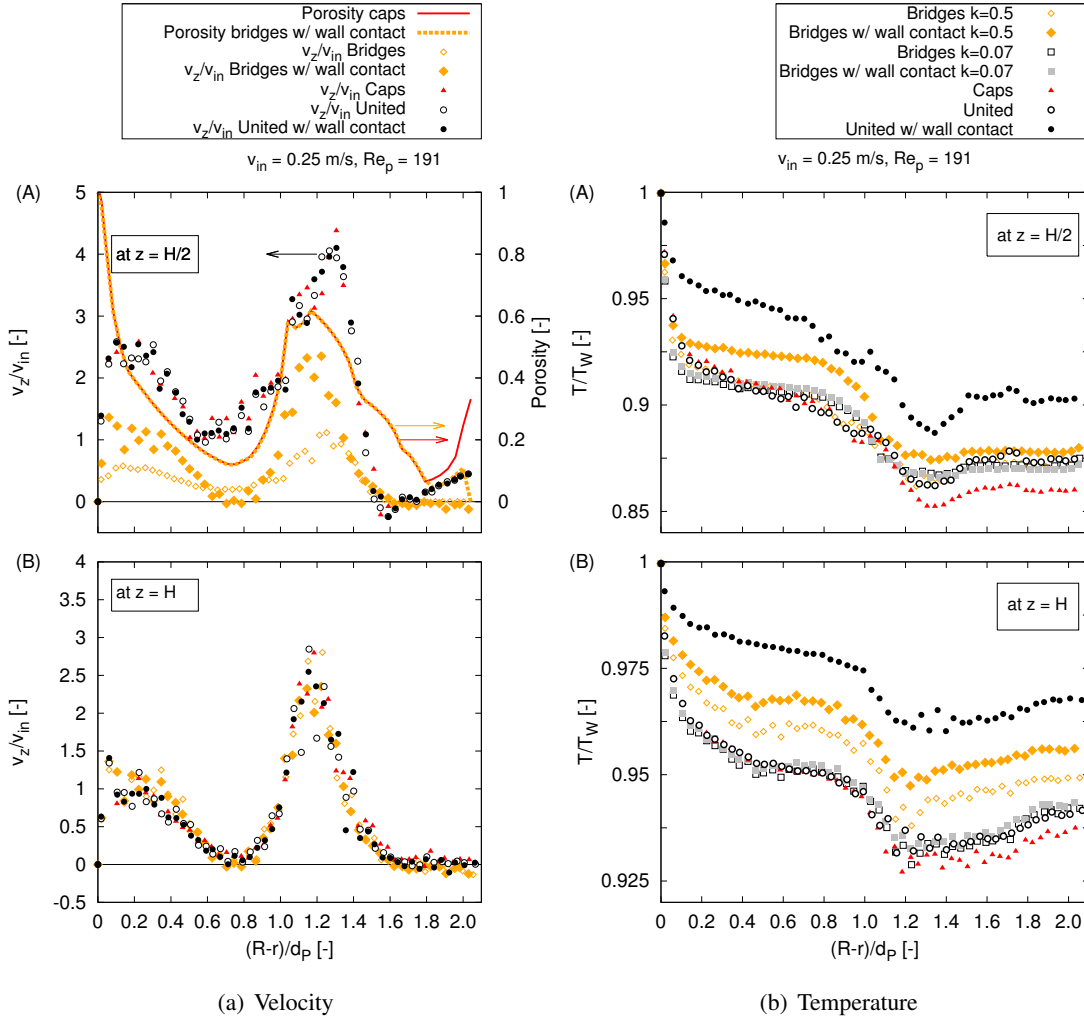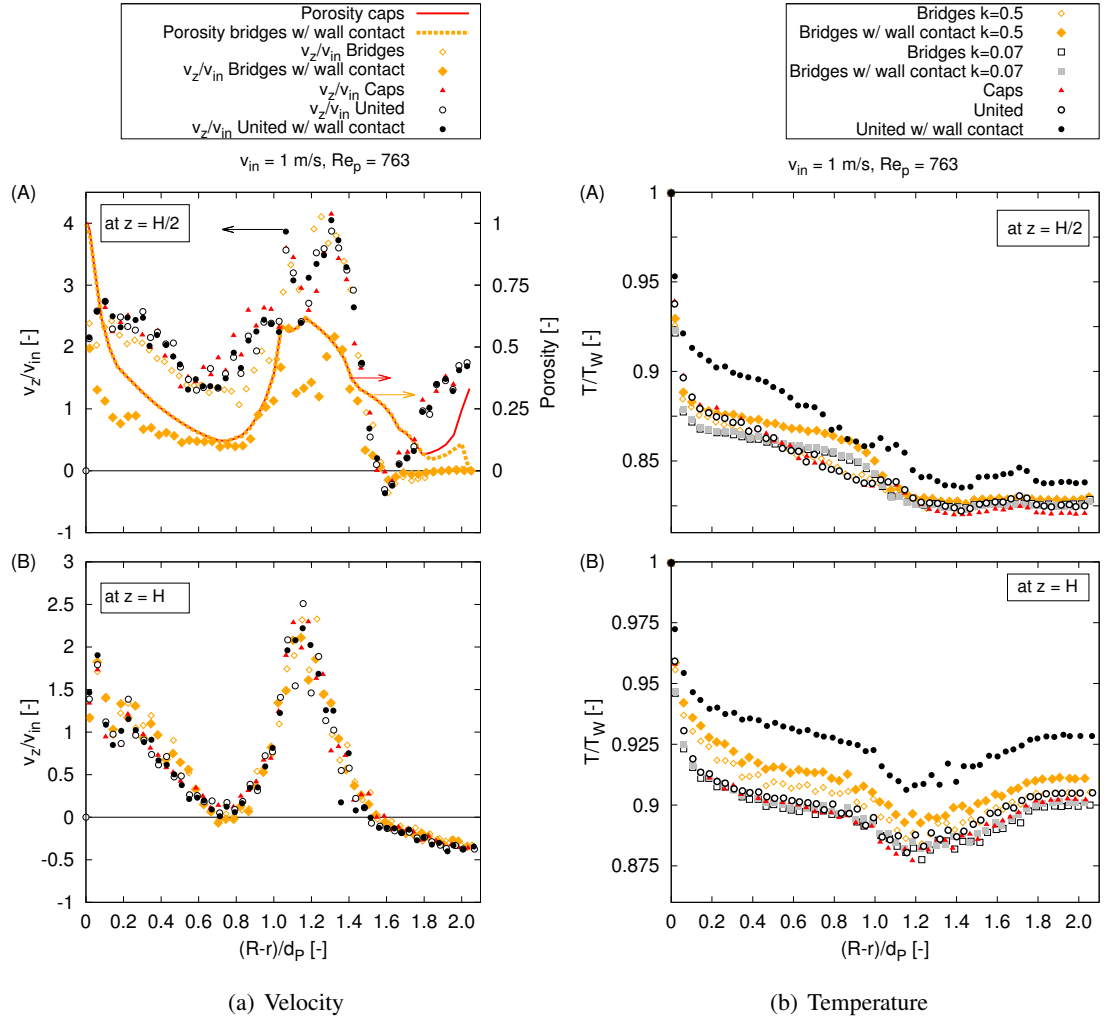
(b) Temperature

Figure 84: Circumferentially averaged velocity (a) and temperature (b) over radius for different contact region modifications. (A) at $z = H/2$, and (B) at $z = H$ for $Re = 763$.

in the bridges $k_{bridge}$ can be used as a *tuning parameter*. It could also be formulated similar to bridges between spherical particles. Dixon et al. (2013b) presented a formula for effective thermal conductivity when a bridge is used to replace particle and fluid near a contact point. The conductivity depends on the height and width of the bridge and on the conductivity of the particle and on the modified fluid thermal conductivity. The Smoluchowski effect takes into account that the thermal conductivity must tend to zero as the gap width tends to zero. One could also think of a dependency on the location of the bridge emphasizing the near-wall resistance.
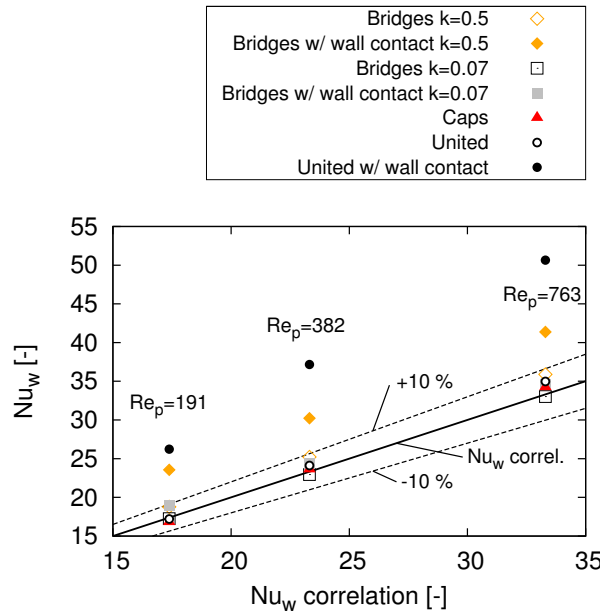


Figure 85: Parity plot of wall Nusselt number from CFD simulations of different contact-area modifications over $Nu_w$ from correlation of Martin and Nilles (1993).

The $Nu_w$ model, as it is described by Martin and Nilles (1993), shows some weakness for low flow rates and cylindrical particles, cf. the discussion in Dixon (2012). The predicted heat transfer is underestimated by a certain extent, especially for low and moderate flow rates. Furthermore, the model is disadvantageous for low $N$ beds in general. As a consequence, the absolute values of the deviation between $Nu_w$ from CFD and from the Martin and Nilles model for cylinders can be misleading. Still, comparing the different contact modifications with each other gives insights into the modeling of low $N$ fixed-bed reactors.

Besides heat transfer in the near-wall region radial heat transfer is also affected by the different contact-area modifications. In Fig. 83 (b) and Fig. 84 (b) normalized temperatures averaged circumferentially are shown for $Re_p = 191$ and $763$. For both flow rates the united method with wall contacts shows the highest radial temperatures. The bridges method with the lower $k_{bridge}$ and the caps method exhibit similar radial temperatures. As it is expected, the higher the flow rate, the lower the influence of heat transfer of conduction in the gas phase. Consequently, for high Reynolds numbers the influence of contact-area modification is getting less important for radial heat transfer. Convective heat transfer is dominant.

## 6.6   Influence of particle shape toward reactor performance[5]

In this numerical study, the influence of the particle shape toward DRM reactor performance is analyzed by particle-resolved CFD simulations. Beside a bed of spheres, two other kinds of particles are simulated, i.e., cylinders and one-hole cylinders with dimensions typical for industrial applications of DRM. The hydraulic residence time and the specific catalytic surface area were kept constant to be able to compare the three packed beds.

### 6.6.1   CFD setup

The investigated reactor consists of a 18 mm diameter tube in which the different particles are placed, see Fig. 86. The height of the packing depends on the particle type, i.e., 33 mm for spheres and 44 mm for cylinders and one-hole cylinders. The procedure of the random packed-bed generation is explained in greater detail in section 4.1.2. In the first step (1) the tube was filled with DEM particles, i.e., spheres or cylinders. When the particles were settled, the local position of each particle was extracted. With this information a CAD model of the packed-bed was built (2) where the cylinders can be replaced by one-hole cylinders. Afterward, the surfaces were assigned and the geometry was meshed (3). Finally, CFD simulations were performed with desired physical models and boundary conditions (4).
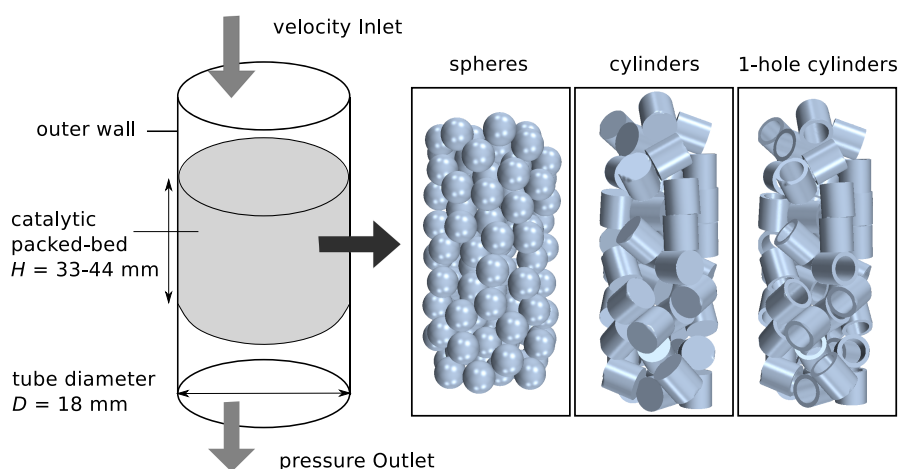


Figure 86: Scheme of the fixed-bed reactor with the three different particle shapes.

For all simulations polyhedral meshes were used with the recommended mesh sizes for gas phase and solid region. The total cell count was approx. 3 million, see Tab. 2. A finer mesh was applied close to the catalytic surfaces. Additionally, the calculation domain was enlarged at the inlet and outlet to minimize the influence of the boundary conditions. The particle-particle contacts and particle-wall contacts were modified with the caps method. That means the particle geometry is flattened locally by a certain amount to avoid bad quality cells. Consequently, in the gap between

---

[5]This section is based on the publication: Wehinger, G. D., Eppinger, T., Kraume, M. (2015). Evaluating catalytic fixed-bed reactors for dry reforming of methane with detailed CFD, *Chemie Ingenieur Technik*, 87(6), 734-745

the particles fluid cells were created. In this study a detailed reaction mechanism by McGuire et al. (2011) was applied for the DRM over rhodium supported strontium-substituted hexaaluminate, see Tab. 22 in the Appendix.

The geometric data and boundary conditions are summarized in Tab. 16. The inlet velocity was adjusted to match a similar hydraulic residence time in the reactor bed $\bar{t}_{\text{hyd}}$ for each packing:.

$$\bar{t}_{\text{hyd}} = \frac{V_{\text{reactor}}\bar{\varepsilon}}{A \cdot v_{\text{in}}} = 1/GHSV = const. \tag{6.11}$$

Table 16: Boundary conditions for the fixed-bed simulations.

|  | Spheres | Cylinders | One-hole cylinders |
|---|---|---|---|
| Tube diameter $D$ [mm] | 18 | 18 | 18 |
| Bed height $H$ [mm] | 33 | 46 | 46 |
| Particle diameter $d_{\text{p}}$ [mm] | 4 | 5 | 5 |
| Particle height $h_{\text{p}}$ [mm] | - | 5 | 5 |
| Inner diameter $d_{\text{i}}$ [mm] | - | - | 3.7 |
| $H/d_{\text{p}} = N$ ratio [-] | 4.5 | 3.6 | 3.6 |
| Specific surface area $S_V$ [m$^2$/m$^3$] | 718 | 556 | 754 |
| $F_{\text{cat/geo}}$ [-] | 90 | 116 | 85 |
| Specific catalytic area $S_{\text{cat}}$ [m$^2$/m$^3$] | $6.4 \cdot 10^4$ | $6.4 \cdot 10^4$ | $6.4 \cdot 10^4$ |
| Mean porosity $\bar{\varepsilon}$ sim. [-] | 0.51 | 0.45 | 0.73 |
| Mean porosity $\bar{\varepsilon}$, Eq. (Dixon (1988)) [-] | 0.52 | 0.44 | 0.72 |
| Cell count [$\cdot 10^6$] | 3.1 | 3.3 | 3.6 |
| Hydraulic residence time $\bar{t}_{\text{hyd}}$ [s] | 0.012 | 0.012 | 0.012 |
| Superficial velocity $v_{\text{in}}$ [m/s] | 1.42 | 1.66 | 2.66 |
| Reynolds number $Re_{\text{p}}$ [-] | 50 | 62 | 62 |
| Inlet temperature $T_{\text{in}}$ [K] | 1123 | 1123 | 1123 |
| Wall temperature $T_{\text{w}}$ [K] | 1123 | 1123 | 1123 |
| Feed [-] | $x_{CH4}/x_{CO2}/x_{N2} = 0.475/0.475/0.05$ | | |

As can be seen from the low particle Reynolds numbers ($Re_{\text{p}} \approx 60 < 150$), the flow can be considered laminar. Consequently, no turbulence model was applied. $F_{\text{cat/geo}}$ was manipulated in such way that all three packings have the equal specific catalytic surface area, i.e., $F_{\text{cat/geo}} \cdot S_V = const.$ (see Tab. 16).

The computational time was high due to the large meshes and the extensive number of chemical species and reaction steps. For the simulation of the bed with spherical particles convergence was reached after approx. 19,000 iterations. This case with a 3.1 million cell mesh yielded in a total CPU time of $7.98 \cdot 10^6$ s or 92 days on an Intel Xeon 3.07 GHz CPU. However, the simulations were performed on a cluster with several parallel CPUs reducing dramatically the computational time.

### 6.6.2   Results and discussion

#### 6.6.2.1   Bed structure

The volume averaged mean porosities for the three different packed beds are given in Tab. 16. Additionally, calculated values are listed based on an equation from Dixon (1988). As can be seen, the deviation between the computer generated packing and the equation is very small ($< 2\%$). The cylinder packing exhibits the lowest void fraction, i.e., 0.45, among which the one-hole cylinders obviously have the highest with approx. 0.7. In Fig. 87 (A) the axially and circumferentially averaged local porosity over the radial coordinate is shown for the three fixed beds. The local porosity is unity at the wall for all three beds. Toward the center of the reactor the porosity decreases in different patterns. Whereas an oscillating manner can be noticed for the spherical particles, the cylinder packing shows a maximum where the distance to the wall corresponds to approx. one particle diameter. However, the local porosity of the one-hole cylinder packing has plateaus at approx. $1/2 \cdot d_\mathrm{p}$ and $3/2 \cdot d_\mathrm{p}$.
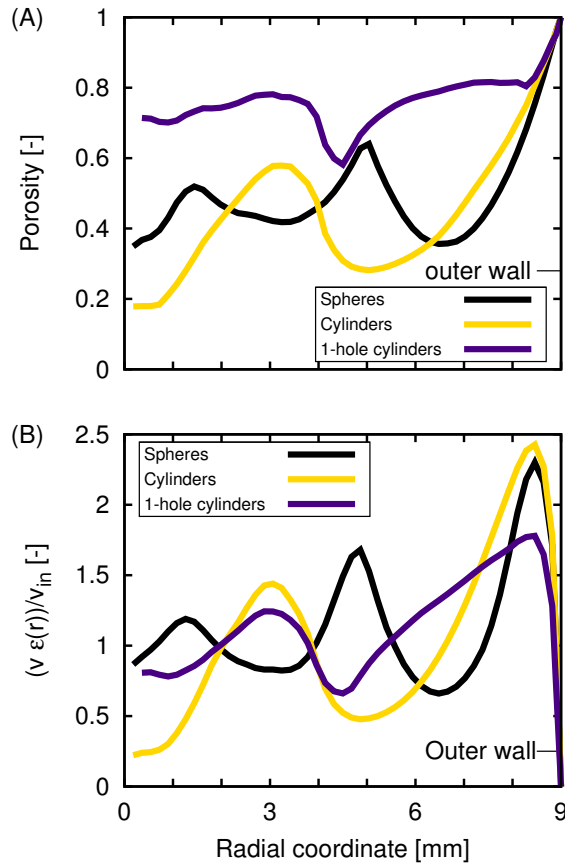


Figure 87: (A) Porosity and (B) interstitial axial velocity as a function of radial coordinate. Outer wall at $r = 9$ mm.

### 6.6.2.2   Velocity and residence time distribution

The local interstitial axial specific velocity $v \cdot \varepsilon(r)/v_{\text{in}}$ as a function of radial coordinate is presented in Fig. 87 (B). It follows the local porosity except for the near wall region, where the velocity decreases to zero due to the no-slip condition at the wall. The sphere and cylinder packings have a similar maximum interstitial velocity of approx. 2.5 close to the wall indicating channeling. On the contrary, the maximum interstitial velocity of the one-hole cylinder packing is approx. 1.7. This can be explained by the lesser pronounced suppression of flow due to the higher porosity. Similar experimental results were found by Giese et al. (1998). However, it has to be mentioned that back-flow regions, e.g., represented by wakes, are neglected by averaging of the velocity. A closer look gives Fig. 88, which shows the velocity distribution $|v|/v_{\text{in}}$ on a longitudinal cut through the different fixed beds. The flow direction is from top to bottom. Different kinds of characteristic regions can be noticed: stagnation zones in front of particles, acceleration and deceleration in regions between particles, channeling close to the reactor wall, as well as wake behind particles. The maximum normalized velocity is approx. 11 and can be found in the cylindrical packing. Due to the higher porosity of the one-hole cylinder packing the velocity in that passage is lower. The flow field in all three packings is characterized by backflow zones and non-axial velocity components highlighting the necessity of three-dimensional resolution.
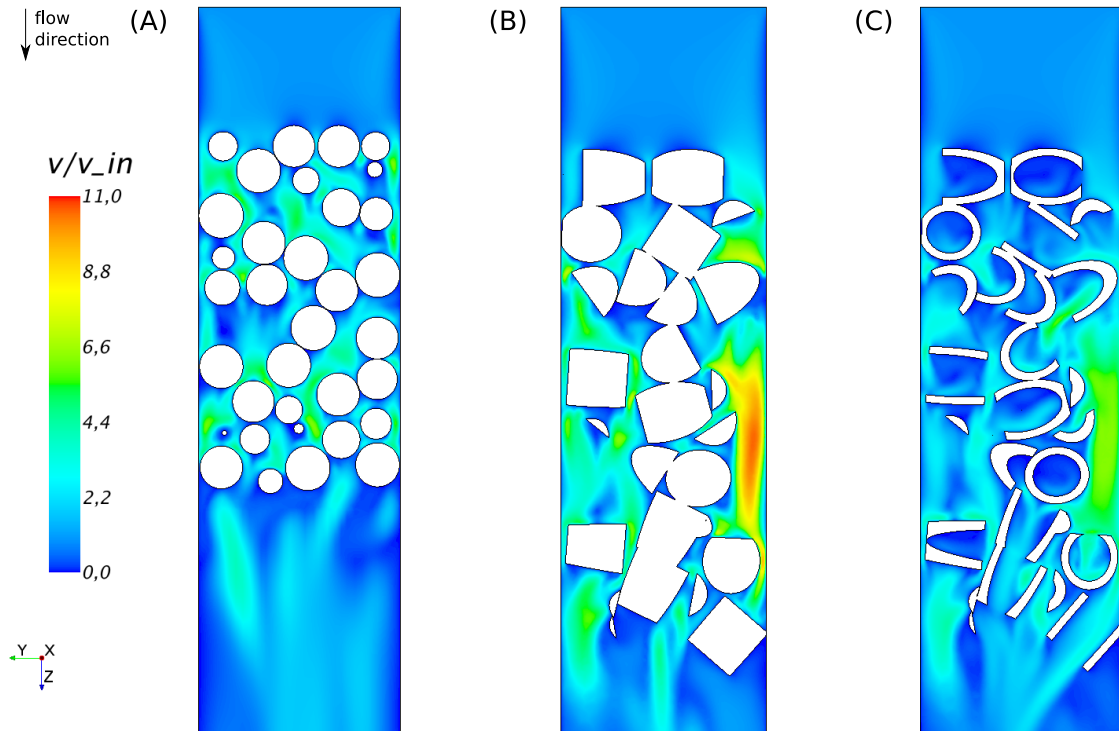


Figure 88: Specific velocity distribution $|\vec{v}|/v_{\text{in}}$ on a plane cut through the fixed bed. (A) spheres, (B) cylinders, (C) 1-hole cylinders.

Residence time distributions are compared to quantify the above mentioned effects of flow. They are governed by evaluating massless particles (approx. 50,000 per packing) using the Lagrangian

Table 17: Results of investigated fixed-beds for similar arithmetical residence time.

| Fixed-bed type | $\tilde{t}/\bar{t}$ [-] | $\sigma_\theta$ [-] | $X_{CH_4}$ [%] | $X_{CO_2}$ [%] | $Y_{CO}$ [%] | $Y_{H_2}$ [%] | $Y_{H_2O}$ [%] | $\bar{\Theta}_{CO^*}$ [-] | $\bar{\Theta}_{C^*}$ [-] | $\bar{\Theta}_{Rh^*}$ [-] |
|---|---|---|---|---|---|---|---|---|---|---|
| Spheres | 0.58 | 0.9153 | 28.2 | 28.4 | 14.6 | 14.3 | 0.1 | 0.238 | 0.516 | 0.236 |
| Cylinders | 0.62 | 0.7809 | 30.2 | 30.5 | 15.6 | 15.3 | 0.1 | 0.287 | 0.447 | 0.254 |
| 1-hole cylinders | 0.70 | 0.5423 | 21.8 | 22.0 | 11.3 | 11.0 | 0.1 | 0.221 | 0.539 | 0.234 |

Multiphase model (CD-adapco, 2014). Massless particles represent a virtual phase, which moves with the continuous phase, without influencing other particles or the surrounding phase. Since large backflow regions exist below the bed, the residence time is evaluated at the outlet of the calculation domain. The mean residence time $\bar{t}$ can be calculated by (Levenspiel, 1998):

$$\bar{t} = \frac{\int_0^\infty tC\,dt}{\int_0^\infty C\,dt} = \frac{\sum t_i C_i \Delta t_i}{\sum C_i \Delta t_i} \tag{6.12}$$

where $t_i$ and $C_i$ are the discrete data for time and massless particle concentration, respectively. Time can be normalized with the mean residence time: $\theta = t/\bar{t}$. The variance $\sigma^2$ can be expressed by:

$$\sigma^2 = \frac{\int_0^\infty t^2 C\,dt}{\int_0^\infty C\,dt} - \bar{t}^2 \cong \frac{\sum t_i^2 C_i \Delta t_i}{\sum C_i \Delta t_i} - \bar{t}^2 \tag{6.13}$$

or in normalized form:

$$\sigma_\theta^2 = \frac{\sigma^2}{\bar{t}^2} \tag{6.14}$$

Since massless particle injection is equal to a pulse experiment, the $E$ curve can be governed by the particle concentration. This curve can be given in normalized form by: $E_\theta = \bar{t} \cdot E$. The cumulative sum of residence time $F$ can be expressed by $E$ in the following way:

$$F = \int_0^\theta E_\theta \, d\theta = \int_0^t E \, dt \tag{6.15}$$

Fig. 89 (A) shows $E_\theta$ and (B) the cumulative sum of residence time for the three different packings. Furthermore, the modes of these residence time distributions $\tilde{t}$ and standard deviations $\sigma_\theta$ are listed in Tab. 17. The mode of a distribution is the value that appears most often. All of the governed normalized modes of residence times $\tilde{t}/\bar{t}$ are significantly lower than one. A long tail can be noticed in Fig. 89 (A) and (B) for all three packings. This is a sign of stagnant backwaters. Furthermore, decaying peaks occur, which represent strong internal recirculation and channeling (Levenspiel, 1998). The large variances and spread sum curves reflect the large deviation from plug flow behavior. The one-hole cylinder packing shows the largest mode, as well as a narrow distribution resulting in the lowest standard deviation $\sigma_\theta$. The packed bed with spherical particles shows the largest standard deviation. It has to be kept in mind that the superficial velocity of the one-hole cylinder packing is larger than for the other packings. Nonetheless, the narrower spread curve indicates a larger radial mixing than for spheres and cylinders. The bed heights and $N$ are really small compared to experimental setups governing typical dispersion coefficients for fixed beds.
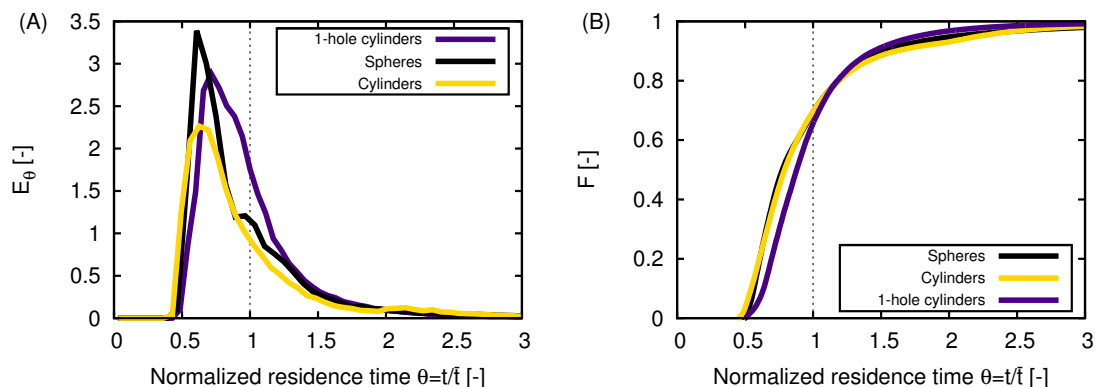
Figure 89: (A) $E_\theta$ curve and (B) cumulative curve of normalized residence time $\theta = t/\bar{t}$ of different packings.

### 6.6.2.3    Temperature

The temperature distribution on a longitudinal view can be seen in Fig. 90. Due to endothermic DRM reactions the temperature decreases inside the bed up to more than 100 K. Strong gradients in axial and non-axial directions can be noticed.

Fig. 91 (A) shows the cross-section averaged temperature over reactor length for the different fixed beds as a function of the normalized reactor length. The temperature decreases rapidly in the first 20% of the bed by approx. 100 K. In the bed with spherical particles the temperature inclines faster than in the other packings. On the contrary, the temperature of the one-hole cylinder packing reaches the lowest temperature at approx. half of the bed.

### 6.6.2.4    Gas phase species

In Tab. 17 conversions, yields and several surface site fractions are listed. The cylinder packing shows the highest conversions with more than 30%. Hydrogen and carbon monoxide yields are the highest, too. On the opposite, the one-hole cylinder packing has conversion rates less than 22% and yields of approx. 11%. In all cases, water yield is very low, being the result of the reverse water-gas shift reaction ($CO_2 + H_2 \rightleftharpoons CO + H_2O$). With larger residence times higher conversion rates and yields are possible. However, it can be noticed that the cylinder packing is advantageous over the spherical packing under these reaction conditions.

In Fig. 92 mole fractions of methane (A-C) and hydrogen (D-E) in a longitudinal view of the fixed beds are presented. This figure demonstrates the strong interplay between reactor temperature, flow field and reaction kinetics. Strong gradients can be noticed with large hydrogen production in stagnation and wake zones, respectively. The one-hole cylinder packing shows large regions with very low hydrogen production. Averaged mole fractions over reactor length for methane and hydrogen are visualized in Fig. 91 (B). In all cases, methane is consumed whereas hydrogen is produced almost linearly. However, the averaging of mole fraction fields neglects boundary layers
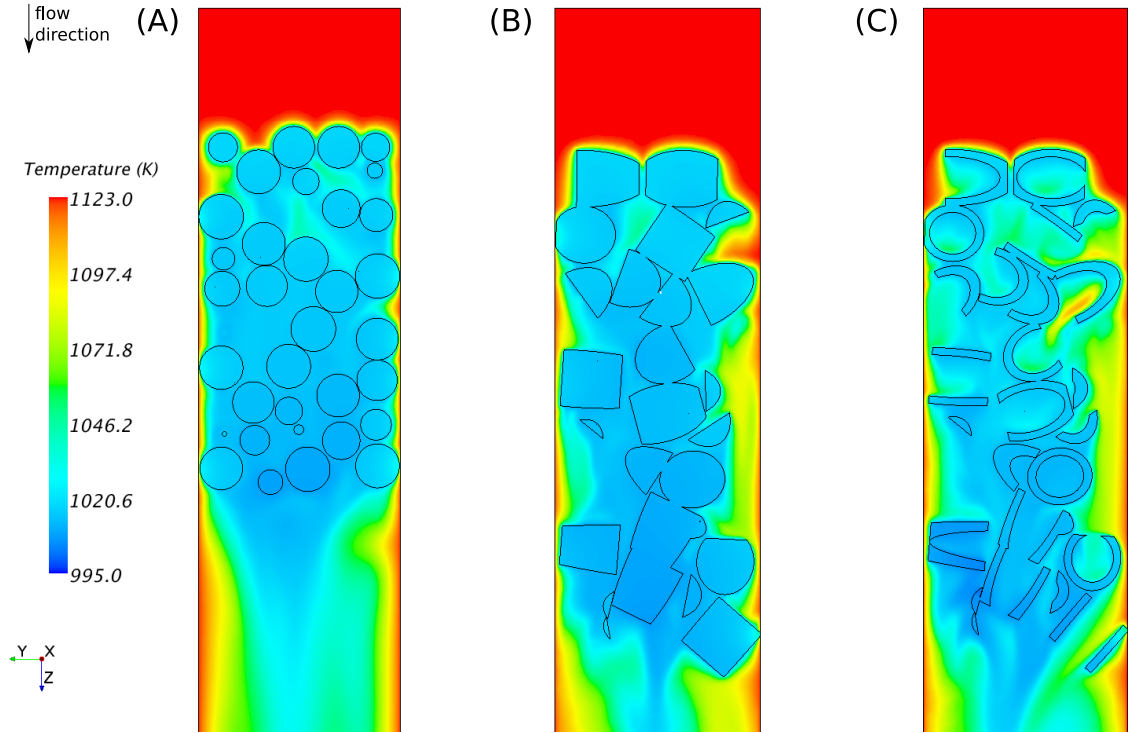
Figure 90: Temperature distribution on a plane cut through the fixed bed. (A) spheres, (B) cylinders, (C) 1-hole cylinders.

and gradients. Hence, such profiles can be illusive.

### 6.6.2.5   Surface adsorbed species

Catalyst deactivation is mainly caused by carbon deposition. The reaction mechanism does not take carbon growth into account explicitly. However, high surface site fractions of surface adsorbed carbon C* represent regions where carbon deposition is likely to occur, as was shown by Kahle et al. (2013) by comparing experimental and simulated results.

Fig. 93 visualizes surface site fractions of C*. The temperature highly influences the adsorbed species. It can be seen, that C* can be found mainly in the interior of the bed and in stagnation zones, respectively. There, convective heat transfer is minimized while the endothermic reaction lowers the temperature. As a result, the surface is covered by C* which leads to catalyst deactivation.

Averaged surface adsorbed species over reactor length are shown in Fig. 94. The most abundant reaction intermediate (MARI) is in all cases surface adsorbed carbon C*. The second most abundant species is CO*. This high amount of carbon leads to a blockage of the surface and finally to an inclined syngas production. Averaged surface site fractions are listed in Tab. 17. The one-hole cylinder packing shows the highest carbon surface site fraction with 0.54. On the contrary, the cylinder packing exhibits the lowest C* fraction (0.45). Although the mean temperatures show similar behaviors in all cases, the synthesis gas yield is the lowest for the one-hole cylinder
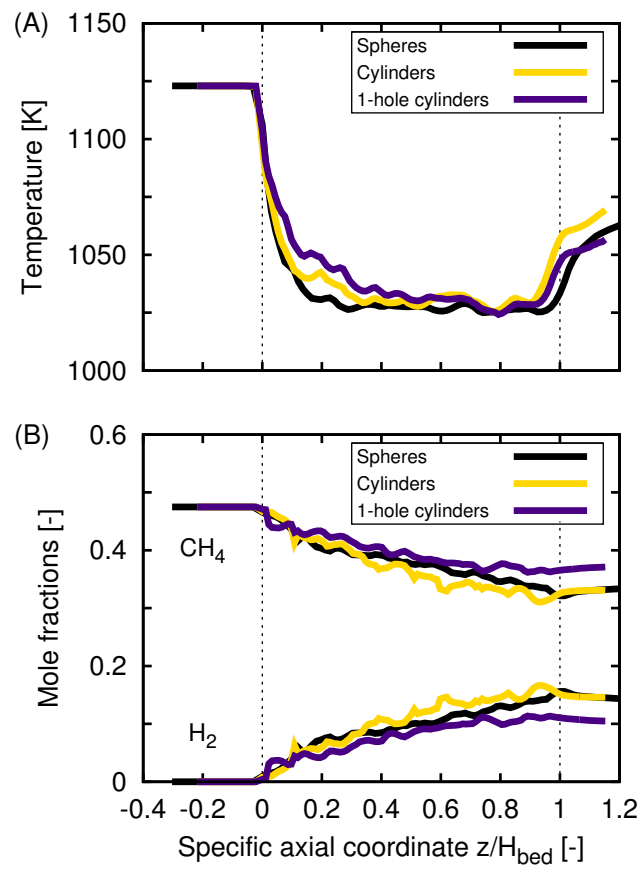
Figure 91: (A) Mean temperature and (B) mean mole fractions of methane and hydrogen over reactor length for different packings.

packing. The reason is probably the narrow residence time distribution and the higher velocities, respectively. It seems that the recirculation zones in the bed are advantageous for the conversion.
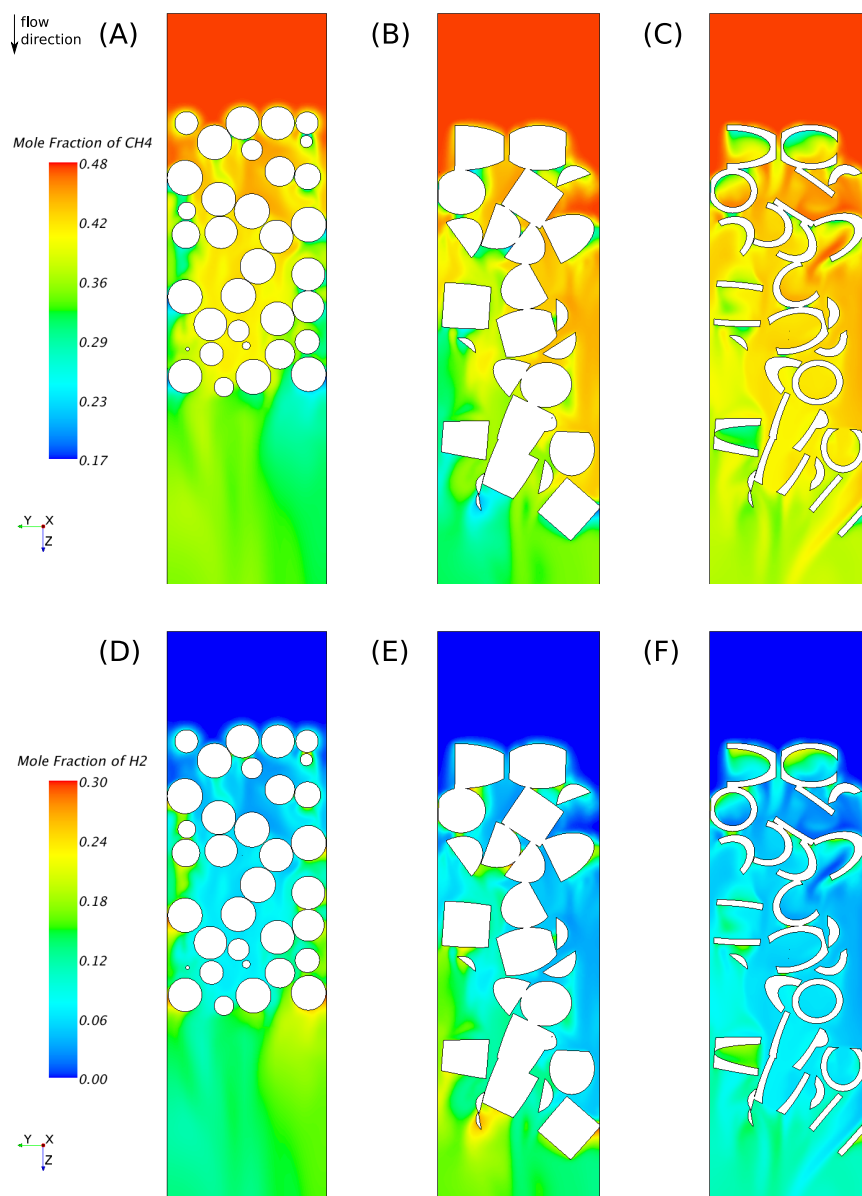


Figure 92: Mole fraction of methane (A-C) and hydrogen (D-E) on a plane cut through the fixed bed for spheres, cylinders and 1-hole cylinders.
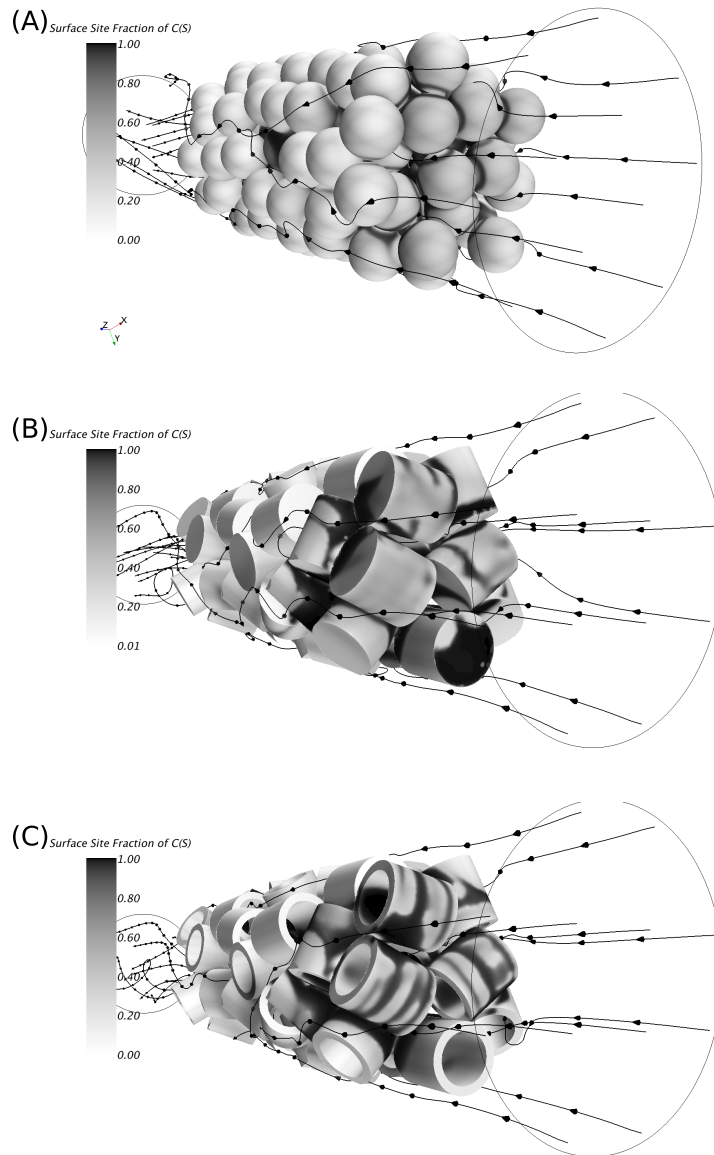
Figure 93: Surface site fraction of adsorbed carbon C* and streamlines for (A) spheres, (B) cylinders, and (C) one-hole cylinders.
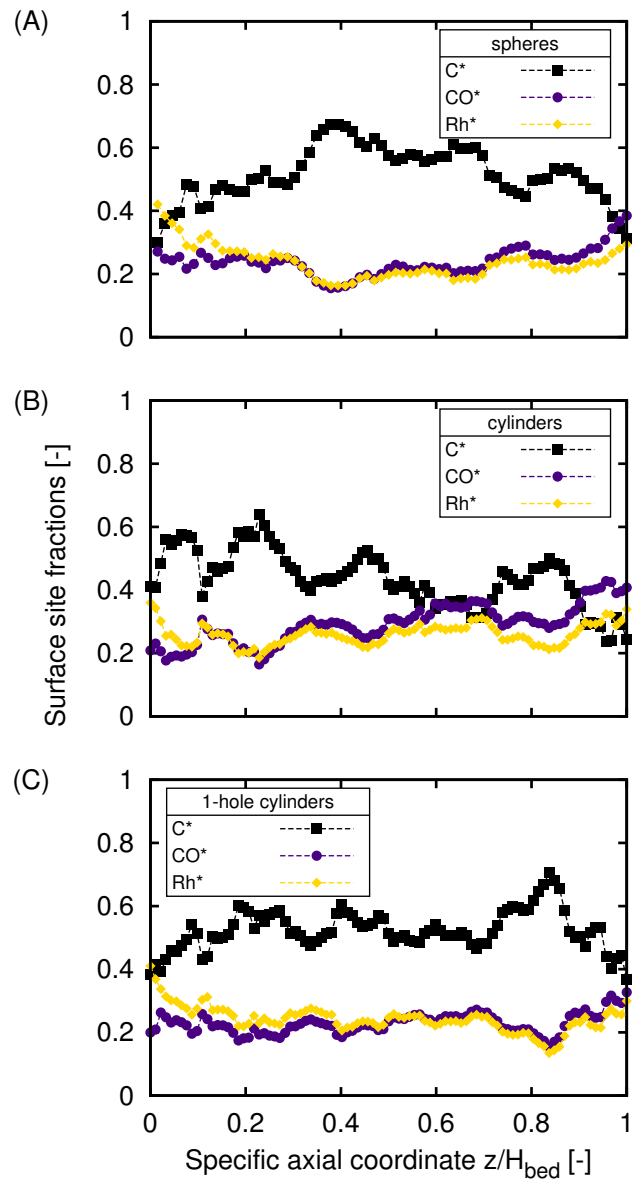
Figure 94: Cross-section averaged surface site fraction of C*, CO* and Rh* for (A) spheres, (B) cylinders, and (C) one-hole cylinders over reactor length.

## 6.7   Conclusions

In a first study, two packed beds were generated automatically consisting of spheres and cylinders in line with experiments from Bey and Eigenberger (1997). Both show a small tube-to-particle-diameter ratio, i.e., $N = 9.3$ and $N = 10$, respectively. The morphology of the beds was analyzed by radial porosity profiles and by radial velocity profiles in the interstitial regions inside the beds. There is a high agreement for radial porosity between CFD simulations and experiments. It can be concluded that the bed-generation workflow using DEM can reproduce real packed beds, at least validated for spherical and cylindrical particles. Furthermore, with the particle-resolved CFD simulation it is possible to simulate the interstitial flow through packed beds, which was also validated by experiments. Since the focus of this thesis are catalytic fixed-bed reactors, more complex particle shapes are not investigated. However, in industrial applications multi-hole cylinders or particles with uneven shaped surfaces are found predominantly.

In the second study, an entire fixed-bed lab-scale reactor for the catalytic dry reforming of methane was simulated. There is no equivalent experiment available. The DEM approach was applied to generate a randomly packed bed of 113 spheres. The meshing method takes into account boundary layers and particle-particle contact-points. The detailed DRM reaction mechanism distinguishes between adsorption, surface reaction and desorption. Two different Reynolds numbers were investigated, i.e., $Re_p = 35$ and 700. The DRM fixed-bed reactor demonstrates the strong interactions between chemical kinetics and transport of momentum, heat and mass. The observed velocity, temperature and species fields are characterized by their three-dimensional behavior and interactions highlighting their complexity and discrepancy from lumped model predictions. Additionally, the reaction mechanism can detect regions where coking takes place with the help of surface adsorbed carbon. Polyhedral meshes are recommended with most of the near wall cells being small enough that $y^+ < 1.5$. This can be achieved by using two or three prism layers with a total height approximated in dependency on $Re_p$ and $d_p$ (Eq. (6.1)). Meshes with approx. 3 million total cells show grid independent results for laminar flows. However, turbulent flows need finer meshes. This study shows that local mesh refinement is necessary depending on flow rates and complexity of physical models.

A heat transfer experiment in a profile reactor consisting of spherical particles was reproduced with particle-resolved CFD simulations and by a 2D porous media model. This study shows that in certain situations conventional 2D CFD simulations cannot predict accurately axial temperature profiles. Although inlet and outlet conditions are in good agreement, large deviations occur between 2D model and experiments in the center of the bed, where steeper gradients occur. On the contrary, particle-resolved CFD simulations addressing the actual shape of the bed are in excellent agreement with experimental data. Reduced mixing characteristics due to the bed geometry are mainly the cause for the discrepancy between 2D and 3D CFD.

DRM experiments on nickel were carried out in the same reactor setup with catalytic spheres of 1 mm in diameter. Constant wall temperature of 850 °C and a flow rate of 500 ml/min were set. High reactant mole fractions were tested, i.e. $x_{CH_4}/x_{CO_2}/x_{N_2}$=0.32/0.40/0.28. For the simulation a recently published DRM microkinetics from Delgado et al. (2015) was implemented on the particle surface. The DRM experiments could not be reproduced with the original microkin-

etics even with the experimentally measured temperature profile applied. The discrepancy can be attributed to possible catalyst dynamics, divergent catalyst and support composition, as well as to parameters of the microkinetics. CO*, which is the most abundant surface species, is predicted to cover approx. 40% of the catalyst surface. A thermodynamic analysis supposes thermodynamic violations in terms of enthalpy and entropy, which are amplified with high surface coverage of CO*. Nonetheless, the original kinetics was tuned by modifying the rate of $H_2$ desorption. The introduced tuning factor is dependent on the surface coverage of CO*. With this modification the experiments were reproduced well. An analysis of the dominant regime shows that DRM is limited by the kinetics under the studied reaction conditions. That is a reason why the simple 2D channel shows similar results than the particle-resolved 3D simulation with the experimental temperature applied. However, the assumption of no radial gradients seems to be invalid by considering the photographs of the bed after DRM experiments. Hence, 3D simulations with conjugate heat transfer are necessary to predict also radial gradients. The 2D channel is not capable to compute such radial gradients. The predicted temperature drop is approx. 70 K lower than experimentally measured. This is assumed to be due to the thermodynamics of the microkinetics and by some extent due to neglected heat losses. Still, the particle-resolved approach is very promising though very time consuming.

Three different contact-area modifications were applied and analyzed for a packed bed of cylinders, i.e., the *caps* method, the *united* method and the *bridges* method. Furthermore, particle-wall contacts have been considered separately. The bed is characterized by a low tube-to-particle-diameter ratio ($N = 4.17$). Averaged porosity and velocity profiles show low dependencies of the different contact modifications. However, pressure drop gives some idea of the influence of a changing flow pattern. Whereas the caps method shows the lowest pressure drop, the bridges method in combination with cylinders at the wall-particle contacts shows the highest values. This trend can be explained in more detail with local velocity fields. Especially the bridges method provokes flow separation, which results in higher pressure drop. The results for the heat transfer study show that the higher $Re_p$, the more important the modeling of particle-wall contact areas. Contact-area modifications inside the bed are becoming less important, since convective heat transfer is dominant. Over the entire investigated range of $Re_p$ the caps method shows encouraging results in comparison with predictions from heat-transfer correlations. This model is in most cases the easiest method to implement and most stable to calculate. However, all CFD simulations are compared with the $Nu_w$ model from Martin and Nilles (1993), which itself shows disadvantages for cylindrical particles. Still, the differences between the different contact modifications are apparent. As a consequence, more detailed and more precisely designed experiments are needed with which it is possible to validate the different contact modifications in CFD simulations of low $N$ fixed-bed reactors, especially for more complex particle shapes. A recommendation can be given for modeling transport of momentum and heat in particle-resolved fixed-bed reactors of non-spherical particles. On the one hand, the bridges method with cylinders between wall-particle contacts shows good results for pressure drop and heat transfer prediction. Moreover, the thermal conductivity of the bridges can be used as a tuning parameter. On the other hand, the easy to implement caps method should be considered for preliminary calculations due to its low time consumption, numerical stability, and straightforward parameter selection.

In the last study, three fixed beds of different particle shapes were compared toward DRM performance using particle-resolved CFD simulations. For the investigated conditions, the cylindrical packing shows the highest conversions and yields, respectively. Furthermore, it exhibits the lowest fractions of surface adsorbed carbon which is an indicator for catalyst deactivation. It has to be kept in mind that the one-hole cylinder packing shows the smallest smallest standard deviation. With such detailed simulations the effect of particle shapes toward reactor performance can be quantified with minimized dependencies on empirical correlations.

# 7   Simulating catalytic foam reactors[6]

In the following chapter open-cell foam structures are generated artificially by the algorithm **cat**alytic **F**oam **M**odeler (*catFM*) described in section 4.3. They are studied in terms of morphology, pressure drop, and residence-time distribution. Additionally, the performance of catFM is tested by reproducing catalytic partial oxidation of methane in a rhodium catalyst foam. Conjugate heat transfer between the solid foam structure and the gas phase, as well as surface-to-surface radiation was taken into account.

## 7.1   Morphological parameters

The geometrical similarity between real foams and model foams generated by catFM is essential for an accurate prediction of transport phenomena in CFD simulations. One of these model foams is shown in Fig. 30 in chapter 4.3. In Tab. 18 the foam topology of an experimentally investigated foam (values taken from Kumar and Kurtz (1994)) is compared with foams (20, 30 and 45 PPI) generated with catFM. As can be seen, the topological parameters, i.e., number of struts per window, number of windows per cell, and number of vertices per cell, are in accurate agreement with experimental data.

Table 18: Comparison of foam topology between model foams and literature data (Kumar and Kurtz, 1994).

| Foam structure | No. of struts per window | No. of windows per cell | No. of vertices per cell |
|---|---|---|---|
| 20 PPI catFM model | 5.12 | 14.18 | 24.56 |
| 30 PPI catFM model | 5.11 | 14.93 | 23.86 |
| 45 PPI catFM model | 5.07 | 13.61 | 23.23 |
| Exp. from Kumar and Kurtz (1994) | $\approx 5.1$ | $\approx 14$ | $\approx 23$ |

The specific surface area $S_V$ is a crucial factor for all kinds of applications in ceramic foams. In Tab. 19 specific surface areas between model-generated foams and experiments (values are taken from Garrido et al. (2008); Richardson et al. (2000) and Habisreuther et al. (2009)) are compared. Additionally, an empirical equation for $S_V$ from Buciuman and Kraushaar-Czarnetzki (2003) is given:

$$S_V = C_1 \cdot \frac{1}{d_s + d_w} \cdot (1 - \varepsilon)^{C_2}$$

$$\text{with} \quad C_1 = 2.87 \quad \text{and} \quad C_2 = 0.25$$

(7.1)

where $d_s$ is the strut diameter, $d_w$ is the window diameter, $d_c$ is the cell diameter, and $\varepsilon$ is the mean porosity of the foam. Three different foam structures are studied, i.e., PPI = 20, 30 and 45. As can be seen, the deviations of the specific surface area are predominantly below 5%. However,

---

[6]This section is based on the publication: Wehinger, G. D., Heitmann, H., Kraume, M. (2016). An artificial structure modeler for 3D CFD simulations of catalytic foams, *Chemical Engineering Journal*, 284, 543-556

Table 19: Comparison of specific surface area between catFM foams and literature

| PPI | $\varepsilon$ [-] | $d_\text{w}$ [mm] | $d_\text{s}$ [mm] | $d_\text{c}$ [mm] | $S_{V,\text{catFM}}$ [m$^2$/m$^3$] | $S_{V,\text{Eq. (7.1)}}$ [m$^2$/m$^3$] | Deviation [%] | $S_{V,\text{exp}}$ [m$^2$/m$^3$] | Deviation [%] |
|---|---|---|---|---|---|---|---|---|---|
| 10 | 0.82 | 1.53 | 1.08 | 4.80 | 699 | 720 | 2.9 | - | - |
| 20[a] | 0.81 | 0.89 | 0.65 | 2.77 | 1245 | 1239 | 0.5 | 1187[b] | 4.9 |
| 20 | 0.80 | 0.81 | 0.73 | 2.86 | 1250 | 1239 | 0.9 | - | - |
| 20 | 0.80 | 0.73 | 0.94 | 3.14 | 1221 | 1141 | 7.0 | - | - |
| 20 | 0.80 | 0.85 | 0.65 | 2.76 | 1252 | 1272 | 0.1 | - | - |
| 20 | 0.81 | 0.89 | 0.65 | 2.77 | 1241 | 1239 | 0.8 | - | - |
| 45 | 0.74 | 0.53 | 0.59 | 1.96 | 1749 | 1823 | 4.0 | - | - |
| 45[a] | 0.79 | 0.62 | 0.51 | 2.07 | 1694 | 1719 | 1.4 | 1610[c] | 5.2 |

[a] Foam structure for CFD simulations of pressure drop without chemical reactions.
[b] Experiments from Garrido et al. (2008)
[c] Experiments from Richardson et al. (2000)

it has to be noticed that such equations are mostly limited to foam structures investigated in the underlying experiments. Extrapolation to for example different PPI values can lead to erroneous predictions. Thus, the reproduction and following comparison with experimentally investigated foams is more revealing. These deviations account for approx. 5%. Summing up, catFM is able to generate foam structures with a similar parameter set (PPI, specific surface area, and porosity) as real foams.

## 7.2   Pressure drop without chemical reactions and residence-time distribution

Besides morphological parameters, pressure drop can provide interesting insights into the automatically generated foam structures. For that purpose, CFD simulations were carried out reproducing two sets of experiments.

### 7.2.1   Experimental setup

For the reproduction of pressure drop, CFD simulations were carried out for two separate experiments. The first set was conducted by Garrido et al. (2008) using a 20 PPI foam with a porosity of 0.804 and a specific surface area of 1187 m$^2$/m$^3$, see Tab. 19 row two. The second foam structure can be found in the last row in Tab. 19. It is a 45 PPI foam with 0.79 porosity and 1610 m$^2$/m$^3$. The experimental pressure drop was measured by Richardson et al. (2000). Although many pressure drop data are available in literature, only few report, besides PPI values, the specific surface area and the porosity, as well as struts dimensions.
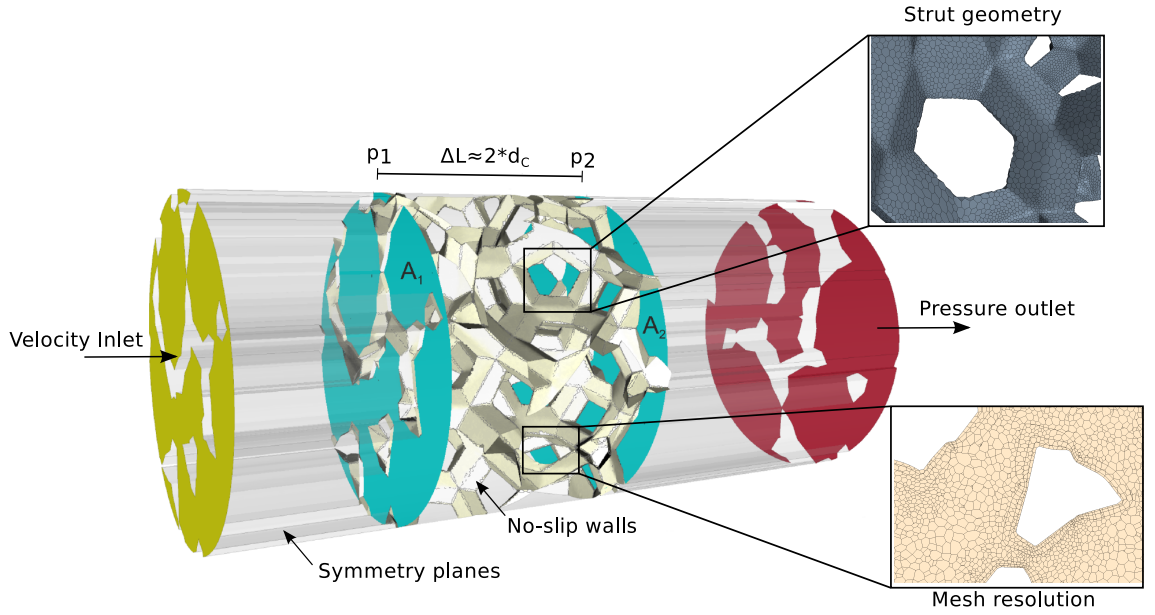
Figure 95: CFD setup for pressure drop simulations in foam with details of strut geometry and mesh resolution close to surface.

### 7.2.2   CFD setup

Fig. 95 shows the calculation domain of the foam structure with details on the strut geometry and the meshing. The calculation domain was approximately 2 times the cell diameter in length and width. The confined walls were set to symmetry planes. In addition to the foam structure an upstream and downstream region was generated to minimize the influence of the entrance zone. The calculation domain was meshed with polyhedral cells including two prism layers close to the foam surface (see Fig. 95 lower detail on the right hand side). As an orientation, previous findings for mesh development for fixed-bed reactors were used, see chapter 6.2. Especially, the cell windows were resolved with a finer mesh, since the flow is accelerated due to cross-sectional tapering. Prism layers are used at the walls. Theses special cells are oriented normally toward the wall, since the main velocity component is parallel to the wall. For turbulent flow simulations the near-wall cells were chosen in such way, that the majority of the $y^+$ values are smaller than 1. An iterative mesh study guaranteed mesh independent results (not shown here). The total mesh size accounts for approx. one million cells. Several superficial velocities (0.5-10 m/s) were applied at the inlet assuming isothermal conditions. The fluid properties are calculated at 300 K. For the interstitial flow regime a Reynolds number can be defined based on the averaged cell diameter: $Re_c = v_{in} d_c \rho / (\mu \cdot \varepsilon)$ The literature distinguishes four flow regimes in porous media based on $Re_c$: (a) creeping or Darcy flow regime ($Re_c < 1$), (b) Forchheimer flow regime ($1 \sim 10 < Re_c < 150$), (c) post-Forchheimer flow regime (unsteady laminar flow, $150 < Re_c < 300$), (d) fully turbulent flow ($Re_c > 300$) (Pedras and de Lemos, 2001). Interestingly, Della Torre et al. (2014) investigated open cell foams by CFD simulations over a wide range of flow regimes. The authors highlight that at high Reynolds numbers, the wall shear stress becomes a less important factor, while the form drag gives the most significant contribution to the pressure. As a consequence, even in the

turbulent regime, also a laminar model is capable to sufficiently predict the pressure drop (Della Torre et al., 2014). Since laminar model simulations became unstable at $Re_c > 500$ in preliminary simulations, Reynolds-Averaged Navier-Stokes (RANS) based turbulent models were applied. In a former study the Realizable $k - \varepsilon$ turbulence model developed by Shih et al. (1995) with a Two-Layer all-$y^+$ Wall Treatment driven by shear (Wolfshtein, 1969) showed good results, both for pressure drop and stability, in packed-beds of spheres, cf. 6.2. Therefore, this turbulence model was applied in the simulations for $Re_c > 300$.

### 7.2.3    Results and discussion
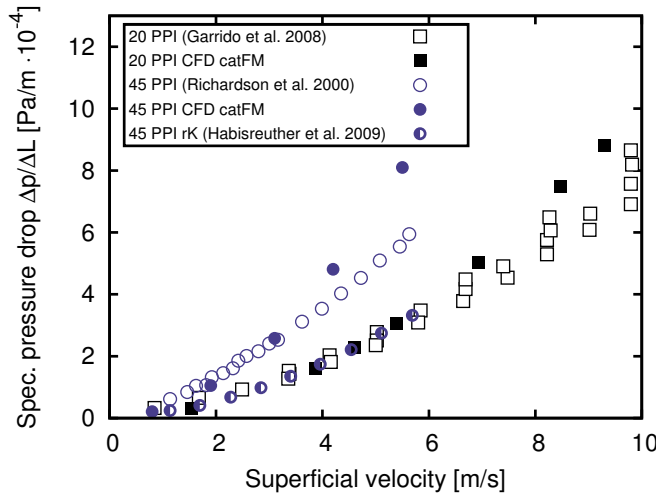


Figure 96: Comparison of pressure drop as a function of superficial velocity obtained from the CFD simulations from catFM (solid symbols) with measured data from Ref. Garrido et al. (2008) and Richardson et al. (2000) (empty symbols) and simulated data from randomized Kelvin (rK) cells from Ref. Habisreuther et al. (2009).

Fig. 96 shows the comparison of pressure drop as a function of superficial velocity $v_{in}$ obtained from the CFD simulations from catFM with measured data from Garrido et al. (2008) and Richardson et al. (2000). The predicted values show great accuracy for superficial velocities below 4 m/s and 8 m/s, respectively. For higher velocities the pressure drop of the simulations is higher than in the experiments. Especially for the 45 PPI foam, velocities higher than 4 m/s , i.e. $Re_c > 650$, result in an overestimation of the pressure drop by factor 1.3. Additionally to the experimental values, pressure drop obtained by flow simulations with a randomized Kelvin cell model from Ref. Habisreuther et al. (2009) is shown. This model, however, underestimation the pressure drop by a factor 2. The higher pressure drops at high velocities lead to the speculation that the strut profiles are responsible. As it can be seen in Fig. 26 the struts are more angular than in reality. Consequently, flow separation is provoked leading to higher pressure drop. Furthermore, real struts narrow its diameters away from the vertex. This changing in strut diameters was not accounted for. The residence-time distribution (RTD) in a foam gives additional information about its randomness and real foam behavior. In the following the RTD of a real foam and catFM are compared.

Table 20: residence-time distribution parameter for the 45 PPI foam with $v_{in} = 4.2$ m/s, i.e. $Re_c = 715$.

| Structure | $\bar{t}/\bar{t}_{bulk}$ | $\sigma/\bar{t}_{bulk}$ |
|---|---|---|
| MRI simulation, from Habisreuther et al. (2009) | 0.720 | 0.307 |
| rK simulation, from Habisreuther et al. (2009) | 0.714 | 0.164 |
| catFM simulation | 0.793 | 0.335 |

Habisreuther et al. (2009) examined a 45 PPI foam in detail. It was scanned via MRI, its structure was extracted and CFD simulations were carried out. In addition, they compared the RTD of this MRI based simulation with their randomized Kelvin cell approach. The results of catFM for RTD and its standard deviation $\sigma_{RTD}$ are listed in Table 20. The RTD was obtained by evaluating massless particles (approx. 25,000) using Lagrangian multiphase model CD-adapco (2014). Massless particles represent a virtual phase, which moves with the continuous phase, without influencing other particles or the surrounding phase. For normalization of the RTD, the volumetric averaged residence time of the flow without the porous structure was used, as applied by Habisreuther et al. (2009):

$$\bar{t}_{bulk} = \frac{V_{bulk}}{\dot{V}} = \frac{l_{probe}}{v_{in}} \tag{7.2}$$

As a consequence of the normalization, the mean value of the normalized RTD $\bar{t}/\bar{t}_{bulk}$ should echo the mean porosity of the structure, i.e. $\varepsilon = 0.791$. catFM reproduces that value correctly, see Table 20. However, the standard deviation $\sigma$ of the catFM structure is by 10% higher than the simulation of the scanned foam structure, indicated as MRI simulation. The randomized Kelvin (rK) structure has a narrow distribution, i.e. small standard deviation. This indicates the shortcut behavior of this model, although the overall porosity is similar to the real foam. As it can be seen from Fig. 97 the distribution of the normalized residence time has a positive skew, which is reflected by the high $\sigma_{RTD}$. This means that in the catFM structure more recirculation zones and wake situations exist than in the MRI or rK structure. The longer tail of the RTD is mainly due to the primitive strut shape, cf. Fig. 30 and Fig. 26. The strong edges of the struts, especially for higher PPI, leads to flow separation, stagnation zones and acceleration zones. Similar trends can be seen in the pressure drop discussion, where only higher flow rates lead to a significant deviation between simulation and experimental results. Since the flow rates for the CPOX experiments are quite low ($v_{in} < 2$ m/s, i.e. $Re_c < 250$), the pressure drop results are satisfactory. The above results encouraged us to simulate catalytic foams with catFM, where the strong interplay between chemical kinetics and transport phenomena can be investigated.

## 7.3   Catalytic partial oxidation of methane on rhodium

The CFD studies on catalytic foams is related to the work of Dalle Nogare et al. (2008) in which they investigated the catalytic partial oxidation of methane (CPOX). With this study the performance of catFM is tested in terms of including catalytic reactions on the foam surface. Furthermore,
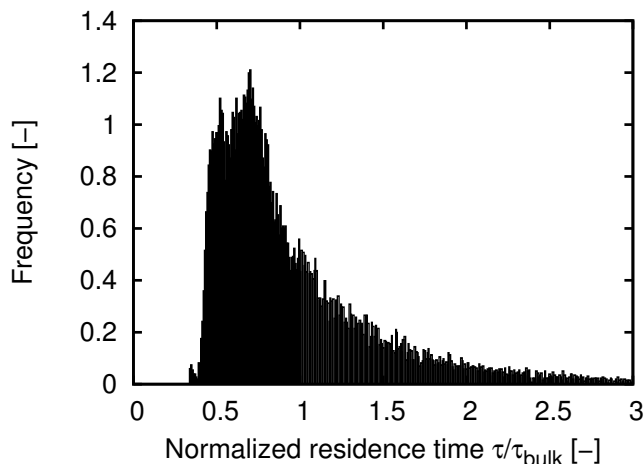
Figure 97: Frequency density of the normalized residence-time distribution in the examined 45 PPI foam.

different boundary conditions of the energy equation at the catalytic surface are tested.

### 7.3.1   Experimental setup

The experiments were realized in an $\alpha$-Al$_2$O$_3$ foam monolith (10 mm in length and 16.5 mm in diameter), which was loaded with 6 wt% Rh Dalle Nogare et al. (2008). Axial temperature, as well as axial species concentration profiles were measured with the capillary technique introduced by Horn et al. (2006a,b). The reaction was carried out in a quartz tube. Besides the reactants, CH$_4$ and O$_2$, argon was fed through calibrated mass flow controllers. The $\alpha$-Al$_2$O$_3$ foam monolith was Rh loaded using incipient wetness method. A washcoat was not applied. In front and in back of the Rh coated foam uncoated foams were used to avoid axial radiative heat losses. The capillary can be moved axially through the foam, in which a channel of 0.8 mm in diameter was diamond drilled through its centerline. The dimensions of the capillary are: outer diameter of 0.65 mm, inner diameter of 0.53 mm. Inside the capillary a thermocouple was placed to measure axial temperature profiles. The axial concentration profiles were measured through a mass spectrometer (UTI model 100C) at the bottom of the capillary. Experimentally H$_2$O signal was not used for the profiles, since water adsorption in the transfer lines could not be fully avoided. Hence, it was calculated by closing the oxygen balance. The C and H atom balances closed better than $\pm 5\%$, whereas in regions of steep gradients the H atom balance reached $+20\%$ at some points. A spatial resolution of 0.3175 mm was applied. For more information on the reactor setup and the Rh foam, see Horn et al. (2006a,b).

### 7.3.2   CFD setup

Due to the fact that the characterization of the 80 PPI foam surface was inconsistent, data was used from Korup et al. (2013), who investigated a similar foam more recently. The pore density

accounted for 80 PPI with a porosity of 70%, and a geometric surface area of 4650 $m^2/m^3$. CPOX is considered as a promising alternative to methane steam reforming, since it is slightly exothermic and can be carried out in very small short contact-time reactors. Furthermore, autothermal operation is possible. Many authors observed a two-zone structure in the catalyst on stream: the fast exothermic oxidation chemistry at the entrance is followed by the slow endothermic reforming chemistry York et al. (2007); Korup et al. (2013); Hettel et al. (2013).

Since the computational time for the entire reactor would be very high, the applicability of catFM for catalytic foam systems is shown for a cylindrical section of a much smaller diameter, see Fig. 98 (A). Again, the inlet and outlet areas have been extruded. A simplified model for fixed-bed reactors is the representative channel, which can be easily adopted for foam reactors. It is illustrated in Fig. 98 (B) with the hydraulic diameter obtained by: $d_h = 4 \cdot \varepsilon / S_V$. This model considers only the gas phase of the foam and neglects the tortuous pore network found in foam structures. The Navier-Stokes equations are now formulated in a rotationally symmetric way neglecting the azimuth. The mesh for the 2D model is finer closer to the surface and accounts for a total of 90000 cells.

**(A) 3D CFD with *catFM* (80 PPI) - Case 1**
gas phase only
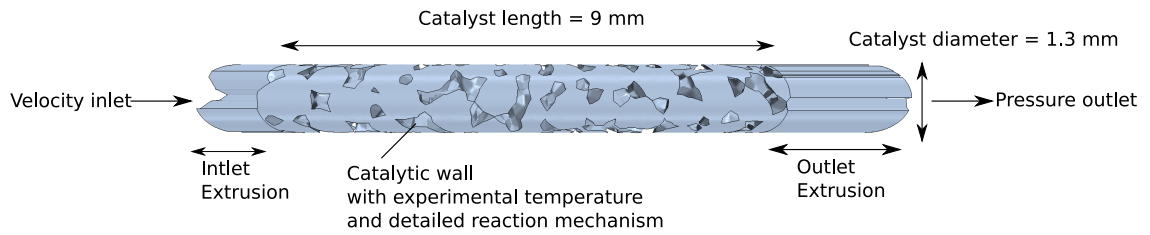


**(B) 2D CFD with representative channel - Case 1**
$d_h = 4 \, \varepsilon / S_V = 0.3$ mm
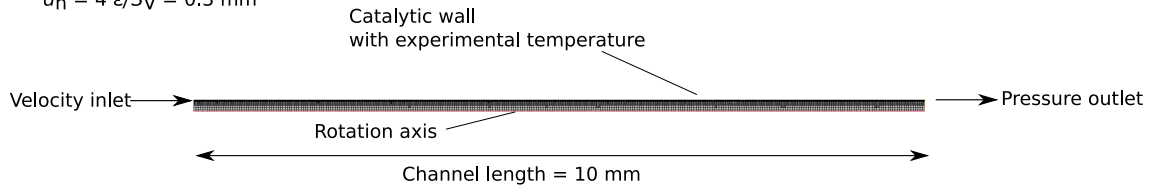


**(C) 3D CFD with catFM (80 PPI) - Case 2**
gas phase and solid gas
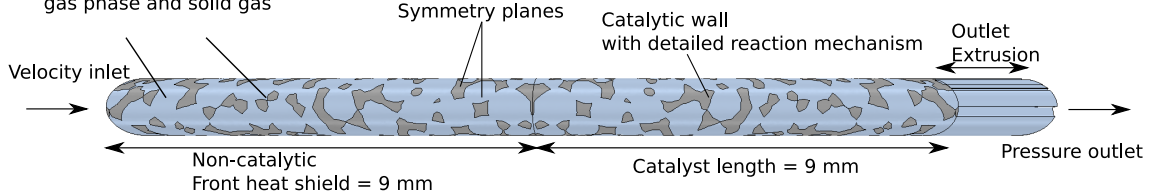


Figure 98: CFD setup for CPOX simulations. (A) 3D foam from catFM gas phase only, (B) 2D representative channel, and (C) 3D gas phase and solid phase.

On the surfaces a detailed reaction mechanism for CPOX on Rh from Schwiedernoch et al. (2003)

is implemented. The detailed mechanism consists of 38 irreversible elementary-like reactions including adsorption-desorption reactions, and surface reactions. 6 gas phase species and 11 surface adsorbed species participate in the kinetics, see Appendix Tab. 24 (the asterisk (*) represents a surface site of rhodium or a surface adsorbed species). No further pore model was applied (instantaneous diffusion).

### 7.3.3    Results and discussion

#### 7.3.3.1    CPOX with measured temperature profile

For the first set of simulations for CPOX foams the measured axial temperature profile, see Fig. 99 indicated as Exp. from Dalle Nogare et al. (2008), was applied on the strut surface (case 1). This means that heat transfer inside the struts is neglected and that each strut face is assumed to be isothermal.
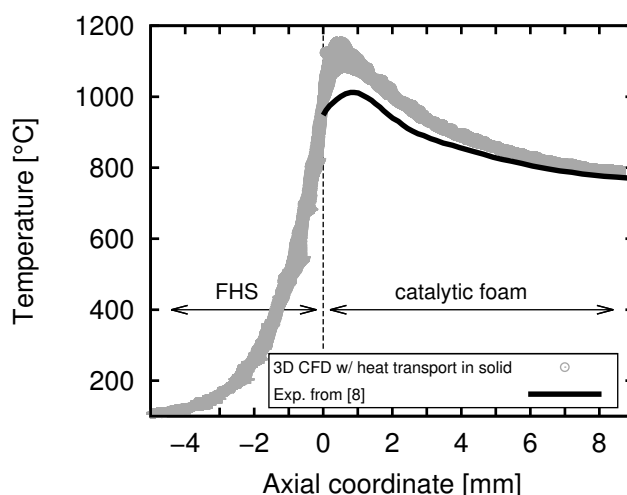


Figure 99: Axial temperature profile in CPOX foam on surface. Experimental values from Dalle Nogare et al. (2008) applied in case 1 and calculated values at the surface using catFM with heat transport inside struts, i.e., case 2. Catalytic foam starts at $z = 0$ mm. Front heat shield (FHS).

In Fig. 100 the velocity magnitude distribution with streamlines, temperature and hydrogen mole fractions on a plane cut through the catalytic foam and adsorbed CO* on the foam surface for case 1 are shown. It can be noticed that the flow field is characterized by steep gradients, stagnation and acceleration zones, as well as back flow regions. Especially due to a decrease of the cross-sectional area in cell windows, the velocity is accelerated by a factor 8. Streamlines visualize flow deviation indicating enhanced radial mixing. Temperature and consequently mole fraction gradients between catalytic wall and gas phase are higher at the beginning of the reactor than at the end. Adsorbed carbon monoxide (CO*) fractions are shown on the foam surface, which gradually increase with axial position.
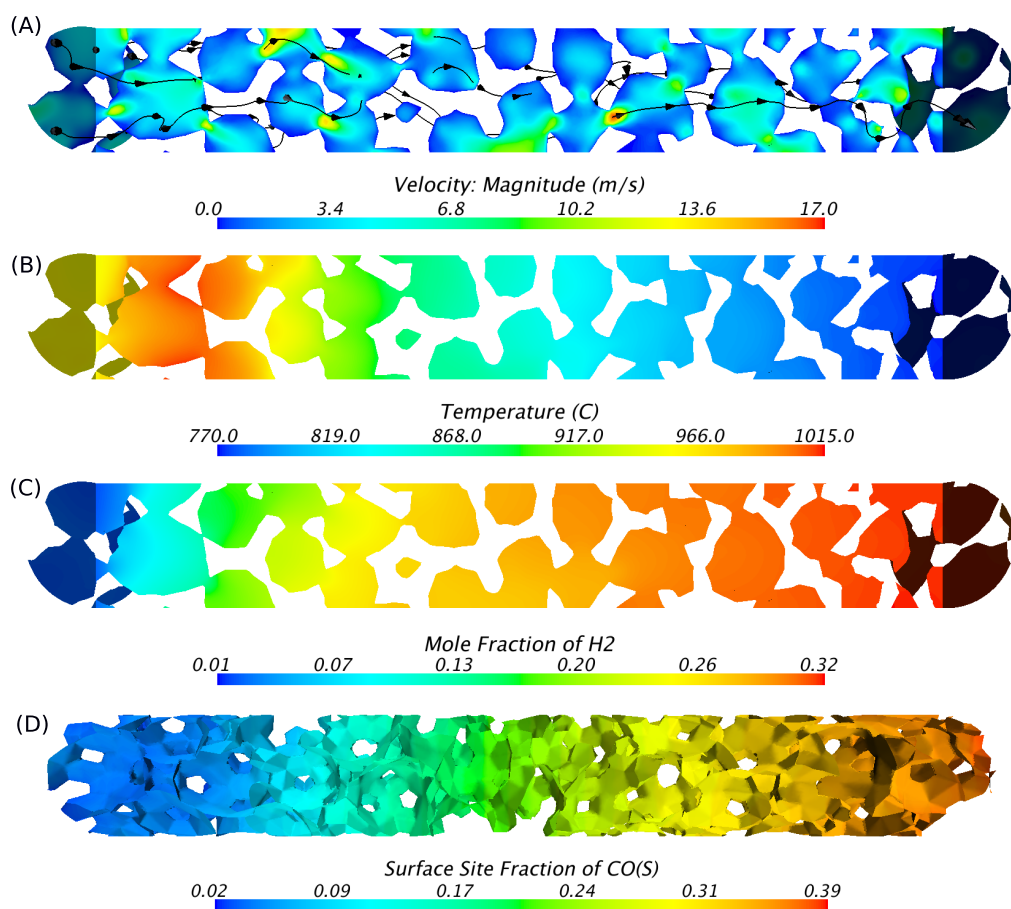
Figure 100: (A) velocity magnitude with streamlines, (B) temperature, and (C) hydrogen mole fractions on a plane cut through the CPOX foam. (D) adsorbed CO* on the foam surface (case 1).

(a) With experimental surface temperature

(b) With conjugate heat transfer
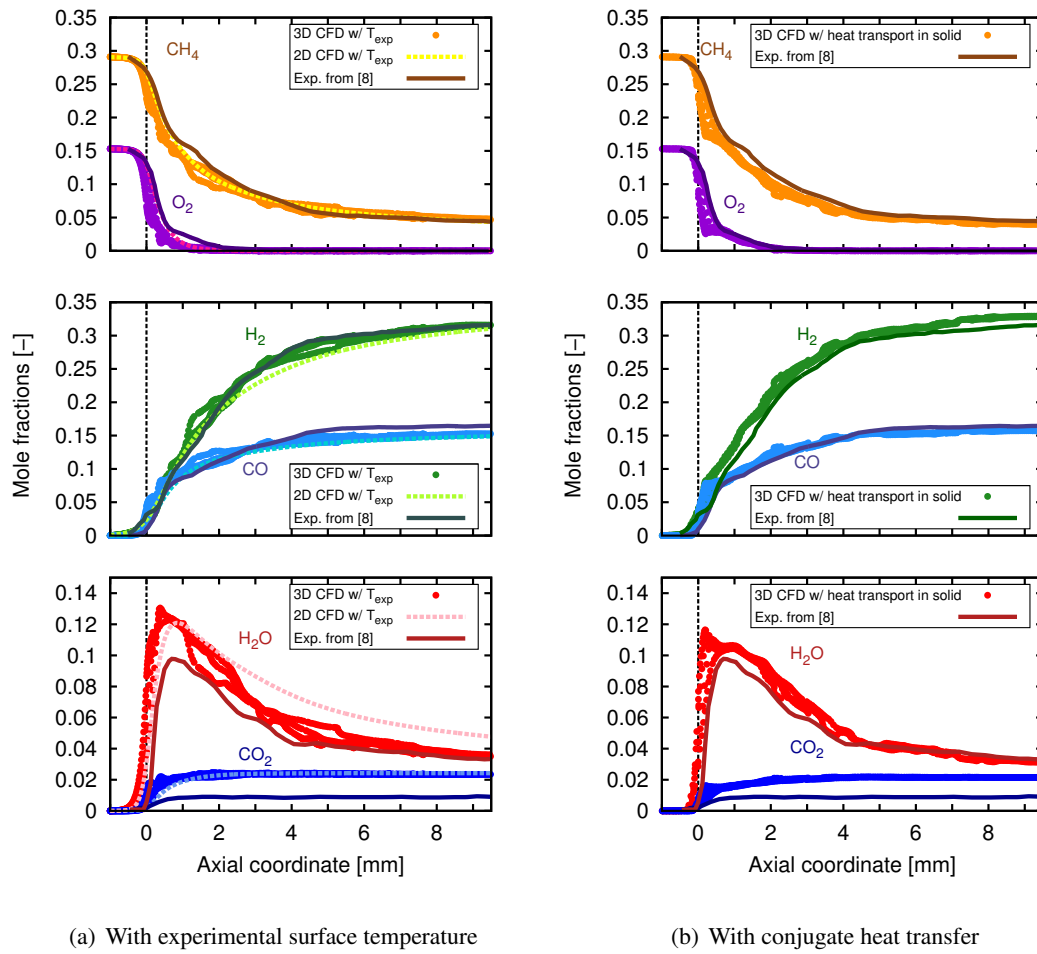
Figure 101: Comparison between measured and simulated axial mole fraction profiles. (a) case 1 with experimental temperature. (b) case 2 with heat transport inside struts.

In Fig. 101 (a) mole fractions of reactants and products over reactor length of the experiment Dalle Nogare et al. (2008), as well as simulated values with experimental temperature are shown. It has to be mentioned that in the experiments blocked pores delayed the conversion of reactants. By comparing other measured CPOX Rh foams by the group Horn et al. (2006a,b), this unique delay becomes apparent. Consequently, the axial experimental species profiles were shifted by 0.5 mm to the left, as was suggested by the authors Dalle Nogare et al. (2008). The 3D values are gathered on the velocity streamlines shown in Fig. 100 (A). Due to gradients in the gas phase these values differ to some extent, especially in the first 3 mm of the reactor. The 2D values are gathered in the rotation axis of the calculation domain. Due to diffusion fluxes the concentration of the reactants already decreases before the catalyst entrance. This behavior is typically found on flame fronts (Turns, 2012). The experimental values show a steep decrease of $O_2$, which is totally consumed after approx. 2 mm, i.e., the oxidation zone. All products ($H_2$, CO, $H_2O$, and $CO_2$) are produced in that first zone. Water is switched from being a product to a reactant indicated by a maximum at approx. 0.5 mm. It reacts with methane in the steam reforming reaction ($CH_4 + H_2O \rightleftharpoons 3H_2 + CO$) and in the water gas shift reaction ($H_2O + CO \rightleftharpoons H_2 + CO_2$). The oxidation zone is followed by the reforming zone, where $H_2$ is largely produced. Here, methane reacts with CO, $H_2O$ and $H_2$ in a ratio that is typical for steam reforming. As it can be seen both models, i.e., the 2D representative channel and the 3D foam structure, can predict the experimental profiles with a high accuracy for oxygen, methane, hydrogen and CO. However, $CO_2$ is overestimated while CO is underestimated in both cases, which seems to be due to irregularities in the foam structure, or due to deficiencies of the kinetic mechanism. This lower CO selectivity was also found numerically elsewhere (Dalle Nogare et al., 2008, 2011). Interestingly, the exit concentrations of water differ the most for 2D and 3D simulations. For both cases water production in its maximum is overestimated. That means in the simulations methane is earlier transformed into water, whereas in the experiment a certain limitation can be noticed. This might be due to pore diffusion limitations, which were not taken into account in the simulations, or the influence of blocked pores in the experiments. Still, it can be concluded that the 3D model is slightly advantageous over the 2D model applying a measured temperature profile on the catalytic surface. However, the computational time is dramatically higher for the 3D simulation, i.e. by a factor of approx. 15.

With the help of numerical simulations a deeper discussion of the CPOX mechanism can be carried out. The dominant regime, i.e. kinetics vs. diffusive regime, of reaction can change with the reactor coordinate, which will be analyzed in the following for the 2D CFD simulation. In Fig. 102 (A) the Damköhler numbers for $O_2$ and $CH_4$ over the reactor length are illustrated. Due to the fact that reactants participate in a multi-step reaction mechanism rather than in a single first-order reaction, the Damköhler number $Da$ is formulated with the pseudo-first-order kinetic constant $k^*_i$ [m/s] and the gas phase concentrations $c_{i,s}$ [kmol/m$^3$]:

$$Da_i = \frac{k^*_i \cdot d_h}{2 \cdot D_M^i} = \frac{\dot{s}_{i,s} \cdot d_h}{2 \cdot c_{i,g} \cdot D_M^i} \qquad \text{for} \quad i = O_2, CH_4 \qquad (7.3)$$

where $d_h/2$ is the hydraulic radius of the representative channel, $\dot{s}_{i,s}$ is the molar net production rate on the surface [kmol/m$^2 \cdot$s] and $D_M^i$ is the effective diffusivity [m$^2$/s] between species $i$ and the remaining mixture. $Da$ describes the ratio of the reaction rate to the diffusive mass transfer rate. As
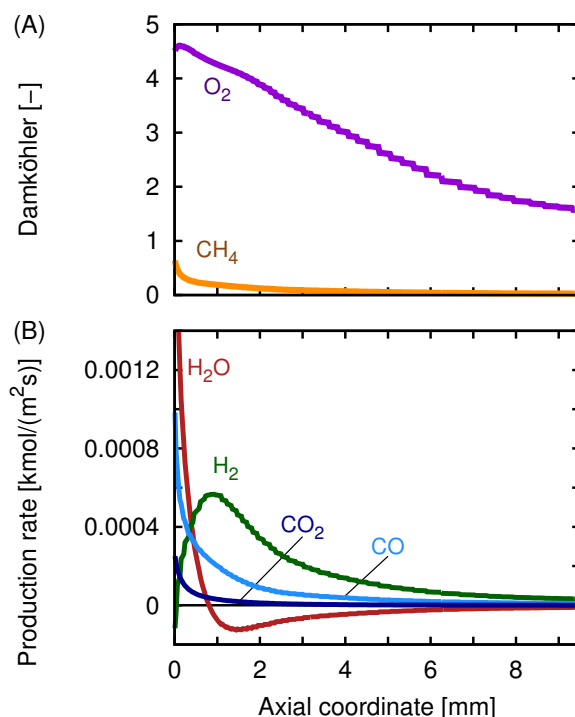
Figure 102: (A) Damköhler number [-] over reactor length for $O_2$ and $CH_4$, and (B) production rate [kmol/m$^2 \cdot$s] of $H_2$, CO, $H_2O$, and $CO_2$

it can be seen in the figure, for oxygen the kinetics is by factor 4 faster than the transport. Hence, $O_2$ reacts in the diffusive regime over the whole reactor length. Although $O_2$ is only relevant in the oxidation zone, i.e. $z < 2$ mm. On the contrary, methane reacts in the kinetic controlled regime, since its ratio is below unity over the whole reactor length. This indicates that the description of the fluid flow in the reforming zone can be abstracted by a simplified model, since it is the kinetic controlled regime. In the oxidation zone the fluid flow has to be described in more detail, since it is the diffusive controlled regime. This is an explanation for the differences, especially in the first millimeters, between the 2D and 3D simulations. In Fig. 102 (B) the production rates [kmol/m$^2 \cdot$s] of $H_2$, CO, $H_2O$, and $CO_2$ are illustrated as a function of reactor length. Water is produced mainly in the entrance region of the catalyst, through the total oxidation of methane ($CH_4 + 2O_2 \rightleftharpoons 2H_2O + CO_2$). However, its production rate decreases rapidly and falls below zero at approx. $z = 1$ mm, which is the beginning of the reforming zone. This location is also the maximum of the mole fraction of water in Fig. 101. Interestingly, the production rate of $H_2$ is negative at the entrance of the catalyst, increases rapidly and decreases after passing a maximum at $z = 1$ mm. That means that the small amount of $H_2$ produced by the reforming reactions is immediately consumed by the reverse water gas shift reaction ($H_2 + CO_2 \rightleftharpoons H_2O + CO$) at least in the very beginning of the catalyst. As it can be seen in the figures $CO_2$ is produced only in the oxidation zone. The overestimated $CO_2$ and $H_2O$ concentrations in that zone are probably due to a favoritism of the total oxidation of methane in the microkinetics. The mechanism was developed for the light-off of catalytic partial oxidation of methane (Schwiedernoch et al., 2003). In their experiments at ignition, only total oxidation of methane to carbon dioxide and water occurs.

In Fig. 103 the surface fractions of the main surface species are illustrated, which cannot be measured experimentally. CO* is the most abundant surface intermediate. The stepwise profiles of the 2D simulations are caused by the non-continuous input temperature profile rather than transport phenomena. The deviation between both models is small. However, the 3D model shows a certain fluctuation of species fractions. This is mainly due to local interactions between velocity and gas phase concentrations influencing the species composition close to the catalytic wall. Catalyst deactivation is mainly caused by carbon deposition, which was recently observed experimentally (Korup et al., 2012). The reaction mechanism does not take carbon growth into account explicitly. However, high surface site fractions of surface adsorbed carbon C* or CO* represent regions where carbon deposition is likely to occur, as was shown by comparing experimental and simulated results (Chen et al., 2001; Kahle et al., 2013).
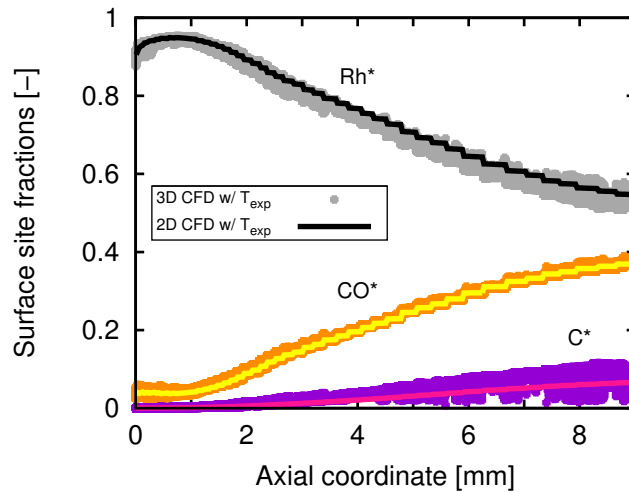


Figure 103: Surface site fractions of the main surface species. Case 1 with experimental temperature.

### 7.3.3.2   CPOX with heat transport inside solid foam

In only few cases a measured temperature profile is available for simulations. Consequently, case 2 accounts for heat transport in the solid material. Constant temperatures are only given at the entrance of the front heat shield. In Fig. 99 the experimental and calculated temperature profile over the reactor length is shown on the surface. Consequently, for each calculation face a value is plotted. A certain range of variation occurs in the simulation mainly due to geometric randomness of the foam structure leading to differences in local transport of momentum, heat and mass. As it can be seen in Fig. 99, the calculated temperatures on the surface are higher than the measured ones in the catalytic foam. Especially, the maximum value (at $z \approx 0.5$ mm) is overestimated by approx. 150 K, which represents the oxidation zone of CPOX. However, with increasing axial coordinate the simulation predicts the measured values fairly, i.e., in the reforming zone. It has to be kept in mind that the simulation involves only a small part of the actual CPOX foam, hence

the solid structure has an important influence on the temperature profile. Furthermore, although the reactor in the experiments was under autothermal operation it can be doubted that no radial heat loss occurred. Hettel et al. (2015) simulated a part of a CPOX honeycomb monolith where they implemented a radiation heat loss as a radial thermal boundary condition. They observed radial temperature differences in the solid monolith in the range of 150 K and could reproduce the axial temperature profile with a high accuracy except for the maximum values. However, it has to be kept in mind that the flow and measurement inside honeycomb channels can be described more precisely. In addition, the capillary and drilling hole might have a significant influence on the temperature and species concentration. For a honeycomb monolith CFD simulations showed the significance of the probing technique's impact on the measured data for heterogeneous CPOX (Hettel et al., 2013). Several positions of the probe influenced the flow field, residence time and reaction progress to a different extent. However, in this study the drilling hole and capillary have not been resolved. Another point of influence are material properties of the foam structure. Especially, the values of thermal conductivity and emissivity of the solid were approximated from literature but not measured. The thermal conductivity of foams is highly linked to local porosity distributions, in some cases the struts are hollow, and furthermore it is dependent on temperature (Dietrich et al., 2010). Emissivity of the solid material, in this case $\varepsilon_{\text{foam}}$ was set to 0.8, depends obviously on several factors, e.g., material, wavelength, and might vary with surface adsorbed species. One might imagine a foam with coke and a fresh foam made of ceramic. However, the results indicate that the principal effects can be captured with this kind of model.

In Fig. 101 (b) mole fractions of reactants and products are shown for the experiment and the 3D simulation on three different stream lines for case 2 including heat transfer inside the solid material. Although the calculated temperature was overestimated in the oxidation zone the model can predict the slopes of species profiles with high accuracy. The higher temperatures at the entrance of the catalytic foam lead to a higher production of water. The maximum can be noticed right after the entrance. In the experiments the maximum values are found 1 mm downstream. This might be either due to processes inside the porous struts or due to the position of the capillary. Remember the first pores in the experiments were blocked and the orifice has some distance from the catalytic surface. However, after 1 mm the profiles of the simulation and the experiments are in good agreement. Again, carbon dioxide is overestimated as discussed before. It has to be mentioned that the model assumes instantaneous diffusion, that means transport processes inside the pores of the struts are neglected. Nonetheless, the influence of pore processes toward conversion in catalytic reactors can be significant, as was shown for honeycomb monoliths (Mladenov et al., 2010) and for stagnation-flow reactors (Karadeniz et al., 2015). Still, the simulated species profiles demonstrate the feasibility of catFM to predict heterogeneous catalytic reactions inside complex foam structures taking into account heat transport inside the solid struts.

## 7.4   Conclusions

In this chapter a fully automatic workflow (catFM) is presented with which it is possible to model a realistic foam structure ready for CFD simulations. The model uses common foam characteristics, i.e., porosity, specific surface area and strut dimensions, as input parameters to generate artificially

the foam structure. Typical morphological parameters, i.e., number of struts per window, windows per cell and vertices per cell, as well as specific surface area are reproduced with a high accuracy. The comparison between experimental pressure drop and simulated values in foams of 20 and 45 PPI are in very good agreement for laminar flow regimes. However, for high Reynolds numbers and high PPI foams the pressure drop is overestimated by a factor of 1.3. As a residence-time distribution analysis shows this is mainly due to the primitive strut shapes.

The performance of catFM is illustrated by modeling a catalytic partial oxidation reformer of methane in a Rh catalyst 80 PPI foam. The first set of simulations takes the experimental temperature on the surface as thermal boundary condition. The experimental species profiles are reproduced with good accuracy. Nonetheless, a representative channel with hydraulic diameter predicts similar results with a much smaller computational effort. This is mainly due to the fact that in the reforming zone the kinetics is slow. That means mass transfer is limited by the kinetics. As a consequence, the description of the mass transport due to diffusion is less important. However, in the oxidation zone, $O_2$ reacts in the diffusive regime. This is indicated by differences between the 2D model and catFM in the entrance of the reactor. All of the products ($H_2$, CO, $H_2O$, and $CO_2$) are produced in the oxidation zone. The microkinetics model underestimates the final CO concentration, whereas it overestimates the final $CO_2$ concentration. As stated already by other authors the microkinetics should be revised in terms of critical steps to overcome this deficiency (Dalle Nogare et al., 2011).

In the second set of simulations heat transfer inside the solid material is taken into account, whereas only the entrance temperature is set as boundary conditions. Furthermore, radiation between surfaces is considered. Although the simulated temperature profile predicts higher values, especially in the oxidation zone, the simulated species profiles show almost no deviation from the experiment. Heat losses from the reactor into the environment are neglected, although they might have a certain influence on the reactor temperature profile. Furthermore, no additional pore model was assumed, since the Rh loaded foam in the experiment was not washcoated. However, in industrial applications washcoats are widely used and their effects can be dramatic toward conversion caused by internal mass transfer limitations. Nonetheless, catFM gives the opportunity to include washcoat models implemented either as boundary conditions on the catalytic surface or by assuming computationally costly 3D reaction-diffusion inside the struts.

# 8 Summary and outlook

Syngas is used as an intermediate to produce synthetic fuels, ammonia or methanol. Commonly, syngas is produced by steam methane reforming. An alternative represents dry reforming of methane which combines methane and carbon dioxide, both are highly abundant greenhouse gases. DRM is commonly carried out in fixed-bed reactors which are characterized by a low tube-to-particle-diameter ratio ($N$). In such fixed-bed arrangements strong interactions occur between local transport phenomena and local kinetics. Thus, conventional plug-flow models and pseudo-homogeneous kinetics lead to erroneous predictions. In this thesis low $N$ catalytic fixed-bed reactors were modeled rigorously with CFD simulations on the particle-resolved scale. Each individual particle of the bed is represented by its actual geometry. Hence, the interstitial flow field is determined by the arrangement and shape of the particles. With this approach it is possible to model these complex reactors on a first-principles basis without relying on transport correlations. The particle-resolved modeling approach consists of several different aspects, i.e., generation of representative bed morphology, meshing strategies including modification of particle-particle and particle-wall contact areas, implementation of reliable microkinetics, approximation of pore processes, and inclusion of heat transfer mechanisms. In this thesis theses aspects were analyzed critically by reproducing detailed experiments from literature or from project partners.

Stagnation-flow reactors represent an interesting tool for identifying intrinsic kinetics for heterogeneous catalysis. The experimental setup is well defined. As a consequence, fluidic effects can be suppressed. Fully three-dimensional CFD simulations of SFR were carried out for DRM over Rh and oxidation of carbon monoxide on Rh with detailed reaction mechanisms. The first example shows that the three-dimensional formulation gives no more information than the stagnation-flow boundary-layer problem, which is one-dimensional. No time-consuming three-dimensional CFD simulations have to be carried out. In a SFR a boundary layer is formed toward the heated catalytic surface. Consequently, surface as well as gas-phase concentration profiles can be measured promptly to estimate kinetic data. In a future task the influence of the measurement probe on the species and temperature field should be quantified with full 3D CFD. Pore processes can have a significant influence on reactor performance since they limit mass transport. Therefore, in the second example, three different pore models were implemented into CFD simulations. Instantaneous diffusion ($\infty$-approach), effectiveness-factor ($\eta$-approach), as well as three-dimensional reaction-diffusion model are compared with experimental data and 1D simulations from Karadeniz et al. (2013). The 3D approach predicts the experiments with high accuracy over the entire temperature range. However, it is much more time consuming than the less sophisticated models. Therefore, it is recommended to use the "cheap" $\infty$-approach to carry out preliminary CFD simulations. After analyzing the washcoat in detail a more "expansive" model can be applied in certain interesting regions.

A packed bed of spheres ($N = 9.3$) and cylinders ($N = 10$) was generated artificially. Measured radial porosity and velocity profiles inside the bed from Giese et al. (1998) were reproduced with high accuracy. The applied workflow of Eppinger et al. (2011) is capable to generate realistic bed structures with spherical and non-spherical particles. The static friction coefficient was utilized to tune global porosity, as it was recommended by Ookawara et al. (2007). However, this procedure

is not meaningful in a physical sense. In the future, more insights have to be gained reproducing catalyst-bed filling with DEM simulations. Especially, complex particle shapes should be in the focus since they are predominantly found in industry.

Polyhedral meshes are recommended to discretize the complex bed geometry. Boundary layers should be resolved by 2-4 prism layers close to walls. The boundary layer thickness can be approximated with $\delta_{BL} = 1.13 \cdot d_p \cdot Re_p^{-0.5}$ (Dhole et al., 2006), which is a function of the particle Reynolds number and particle diameter. However, local mesh refinement should be carried out based on $y^+$ values of the near-wall cells and physical values in the core region. Industrial relevant flow rates are in the order of $Re_p > 5000$, i.e., highly turbulent flow regimes. Hence, more detailed CFD simulations accompanied by detailed experiments have to be carried out modeling turbulence in packed beds.

Contact regions in packed beds of non-spherical particles can be either points, lines or areas. Thus the modifications are much more complex than for spherical particles, where only contact points occur. A study was carried out of a bed of cylinders with different local contact-area modifications, i.e., caps method, united method, and bridges method. The effect of local modifications was analyzed in terms of pressure drop, local velocity, and local heat transfer. Radial velocity profiles were compared with experimental data from Bey and Eigenberger (1997). Results show that modeling particle-wall contact area is becoming more important with increasing $Re_p$. Contact-area modifications inside the bed are becoming less important, since convective heat transfer is dominant. Over the entire studied range of $Re_p$ the stable caps method shows promising results in comparison with predictions from correlations of $Nu_w$ from Martin and Nilles (1993). However, the caps method overestimates convective heat transfer in the contact regions. The bridges method with cylinders between wall-particle contacts shows good results for pressure drop and heat transfer prediction. A convenient feature of this method is the thermal conductivity of the bridges which can be utilized as a tuning factor. Still, there is a lack of detailed experiments of heat and mass transfer in low $N$ packed beds with which CFD can be validated in an adequate way. Especially, more complex particle shapes, i.e., multi-hole cylinders, and shaped surfaces, are of interest. Furthermore, the influence of contact-area modifications toward local kinetics should be studied.

A detailed approach to investigate catalytic fixed-bed reactors was presented in the thesis. The approach combines the in-situ, operando measurement technique (Horn et al., 2010) with particle-resolved CFD simulations. With this combination heat transfer in a fixed bed of spheres was studied. It is shown that the local transport of momentum and heat cannot be predicted by pseudo-homogeneous 2D models inside the packed bed. On the contrary, the particle-resolved approach can reproduce with high accuracy the measured temperature profile in the reactor axis. Interestingly, the 2D model overestimates the temperature inside the bed but predicts the outlet temperature correctly. This highlights the need for in-situ, operando measurement techniques for analyzing heat and mass transport inside catalytic fixed-bed reactors.

In the same reactor setup DRM on nickel was carried out experimentally and by CFD simulations implementing a recently published DRM microkinetics from Delgado et al. (2015). The measured concentration profiles were reproduced satisfactorily for $CH_4$, $CO_2$ and CO. However,

H$_2$ and water predictions were inaccurate even with the given experimental temperature profile. The discrepancy can be attributed to possible catalyst dynamics, divergent catalyst and support composition, different surface patch distribution, as well as to parameters of the microkinetics. For future work more detailed catalyst characterization should be carried out, specifically regarding distribution of the different types of surface patches. With this information kinetics of theses different patches can be derived, which was demonstrated by Blaylock et al. (2011) for SRM. A thermodynamic analysis of the microkinetics identified inconsistencies in enthalpy and entropy. Since activation energies are modified dependent on surface coverage inconsistencies in enthalpy are amplified with increasing surface coverage. Nonetheless, the microkinetics was tuned to reproduce the experiments. Conjugate heat transfer simulations including surface-to-surface radiation of the catalytic fixed-bed predicts the catalyst temperature. As it was assumed by the thermodynamic analysis the inconsistency led to an erroneous prognosis of the temperature profile. The predicted minimum temperature was underestimated by approx. 70 K. With detailed CFD simulations and microkinetics the dominant regime was detected. Over the entire bed mass transfer is limited by the kinetics. Hence, a less sophisticated mass transport model in the bed retains the main features. However, heat transfer in the bed is complex which interacts with mass transport and vice versa. This study quantifies the interplay between local kinetics and local transport phenomena and underscores the importance of consistent microkinetics. In the future, thermodynamic consistency of microkinetics could be maintained by defining only the forward reaction rate and the equilibrium constant by thermochemistry of the surface species. The crucial aspect of this microkinetic description is the thermochemistry. However, Goldsmith (2012) presented an encouraging method which allows the "cheap" estimation of thermochemistry for adsorbates.

Finally, the particle-resolved CFD-simulation approach was applied for exploring the effect of different particle shapes toward DRM reactor performance. Three different particle shapes were compared, i.e., spheres, cylinders, and one-hole cylinders. It was found that the fixed bed consisting of cylindrical particles shows the highest conversions and yields. On the contrary, the one-hole cylinder packing exhibits a low performance. Residence-time distribution helped to understand the complex interplay between local kinetics and local transport. Lastly, a substantial quantitative comparison between different particle shapes and bed structures is possible based on particle-resolved CFD simulations.

An alternative to catalytic fixed-bed reactors are catalytic open-cell foam reactors. Among other aspects, they are characterized by an intensified radial heat and mass transport. Conventional modeling of foam reactors is based on transport correlations which can show significant deviations between experiment and prediction (Reitzmann et al., 2006; Edouard et al., 2008). In this thesis an algorithm (*catFM*) is presented which generates artificially open-cell foam structures. With such structure 3D CFD simulations can be carried out on a particle-resolved scale. The generated foams were studied in terms of morphology, pressure drop, and residence time distribution. Good agreement was found between experimental data and catFM for low to medium flow rates. For higher flow rates the primitive strut shapes lead to a higher pressure drop. Additionally, the performance of catFM was tested by reproducing catalytic partial oxidation of methane in a rhodium catalyst foam (Dalle Nogare et al., 2011). Conjugate heat transfer between the solid foam structure and the gas phase, as well as surface-to-surface radiation was taken into account. The

experimental species profiles were well reproduced. In the future, the primitive strut shape should be replaced by a more realistic one taking into account round and thinning struts.

With particle-resolved CFD simulations it is possible to explore catalytic flow reactors fundamentally. Gas phase, solid temperature, and species concentrations are predicted without relying on transport correlations. Still, there are several fundamental assumptions or modifications needed. Hence, under certain circumstances CFD can be a valuable design tool for catalytic flow reactors.

# Appendix

## A   CO-oxidation microkinetics on rhodium

Table 21: Detailed surface reaction mechanism for the oxidation of CO on rhodium from Karakaya and Deutschmann (2013).

|   | Reaction | A [$^a$] | $\beta$ [-] | E$^c$ [kJ/mol] |
|---|----------|----------|-------------|----------------|
| Adsorption-desorption reactions | | | | |
| 1 | $O_2 + 2* \rightarrow 2O*$ | $1.000 \cdot 10^{-2,b}$ | 0.0 | 0.0 |
| 2 | $2O* \rightarrow 2* + O_2$ | $5.329 \cdot 10^{22}$ | -0.137 | 387 |
| 3 | $CO_2 + * \rightarrow CO_2*$ | $4.800 \cdot 10^{-2,b}$ | 0.0 | 0.0 |
| 4 | $CO_2* \rightarrow CO_2 + *$ | $3.920 \cdot 10^{11}$ | 0.315 | 20.51 |
| 5 | $CO + * \rightarrow CO*$ | $4.971 \cdot 10^{-1,b}$ | 0.0 | 0.0 |
| 6 | $CO* \rightarrow CO + *$ | $1.300 \cdot 10^{13}$ | 0.295 | $134.07 - 47\Theta_{CO*}$ |
| Surface reactions | | | | |
| 7 | $CO_2* + * \rightarrow CO* + O*$ | $5.752 \cdot 10^{22}$ | -0.175 | 106.49 |
| 8 | $CO* + O* \rightarrow CO_2* + *$ | $6.183 \cdot 10^{22}$ | 0.043 | $129.89 - 47\Theta_{CO*}$ |
| 9 | $CO* + * \rightarrow C* + O*$ | $6.390 \cdot 10^{21}$ | 0.0 | $174.76 - 47\Theta_{CO*}$ |
| 10 | $C* + O* \rightarrow CO* + *$ | $1.173 \cdot 10^{22}$ | 0.0 | 92.14 |

$^a$ Arrhenius parameters for rate constants. Units: pre-exponential factor $A$ for unimolecular reactions [s$^{-1}$], for bimolecular reactions [cm$^2$ mol$^{-1}$ s$^{-1}$]
$^b$ Initial Sticking coefficient $S_i^0$ [-]
$^c$ Coverage dependent activation energy in 3.46.
Surface site density $\Gamma = 2.72 \cdot 10^{-9}$ mol/cm$^2$

## B   DRM microkinetics on rhodium

Table 22: Detailed surface reaction mechanism for the dry reforming of methane on rhodium from McGuire et al. (2011).

|   | Reaction | A [$^a$] | E$^c$ [kJ/mol] |
|---|----------|----------|----------------|
| Adsorption-desorption reactions | | | |
| 1 | $H_2 + * + * \rightarrow H* + H*$ | $1.0 \cdot 10^{-2,b}$ | 0.0 |
| 2 | $O_2 + * + * \rightarrow O* + O*$ | $1.0 \cdot 10^{-2,b}$ | 0.0 |
| 3 | $CH_4 + * \rightarrow CH_4*$ | $8.0 \cdot 10^{-3,b}$ | 0.0 |
| 4 | $H_2O + * \rightarrow H_2O*$ | $1.0 \cdot 10^{-3,b}$ | 0.0 |
| 5 | $CO_2 + * \rightarrow CO_2*$ | $4.8 \cdot 10^{-2,b}$ | 0.0 |
| 6 | $CO + * \rightarrow CO*$ | $5.0 \cdot 10^{-1,b}$ | 0.0 |
| 7 | $H* + H* \rightarrow H_2 + * + *$ | $3.0 \cdot 10^{21}$ | 77.8 |
| 8 | $O* + O* \rightarrow O_2 + * + *$ | $1.3 \cdot 10^{22}$ | $355.2 - 280\Theta_{O*}$ |

| | | | |
|---|---|---|---|
| 9 | $H_2O* \rightarrow H_2O + *$ | $3.0 \cdot 10^{13}$ | 45.0 |
| 10 | $CO* \rightarrow CO + *$ | $3.5 \cdot 10^{13}$ | $133.4 - 15\Theta_{CO*}$ |
| 11 | $CO_2* \rightarrow CO_2 + *$ | $4.1 \cdot 10^{11}$ | 18.0 |
| 12 | $CH_4* \rightarrow CH_4 + *$ | $1.9 \cdot 10^{14}$ | 25.1 |
| Surface reactions | | | |
| 13 | $H* + O* \rightarrow OH* + *$ | $5.0 \cdot 10^{22}$ | 83.7 |
| 14 | $OH* + * \rightarrow H* + O*$ | $3.0 \cdot 10^{20}$ | 37.7 |
| 15 | $H* + OH* \rightarrow H_2O* + *$ | $3.0 \cdot 10^{20}$ | 33.5 |
| 16 | $H_2O* + * \rightarrow H* + OH*$ | $5.0 \cdot 10^{22}$ | 106.4 |
| 17 | $OH* + OH* \rightarrow H_2O* + O*$ | $3.0 \cdot 10^{21}$ | 100.8 |
| 18 | $H_2O* + O* \rightarrow OH* + OH*$ | $3.0 \cdot 10^{21}$ | 171.8 |
| 19 | $C* + O \rightarrow CO* + *$ | $5.2 \cdot 10^{23}$ | 97.9 |
| 20 | $CO* + * \rightarrow C* + O*$ | $2.5 \cdot 10^{21}$ | 169.0 |
| 21 | $CO* + O* \rightarrow CO_2* + *$ | $5.5 \cdot 10^{18}$ | 121.6 |
| 22 | $CO_2* + * \rightarrow CO* + O*$ | $3.0 \cdot 10^{21}$ | 171.8 |
| 23 | $CO* + H* \rightarrow HCO* + *$ | $5.0 \cdot 10^{19}$ | 108.9 |
| 24 | $HCO* + * \rightarrow CO* + H*$ | $3.7 \cdot 10^{21}$ | $0.0 + 50\Theta_{CO*}$ |
| 25 | $HCO* + * \rightarrow CH* + O*$ | $3.7 \cdot 10^{24}$ | 59.5 |
| 26 | $CH* + O* \rightarrow HCO* + *$ | $3.7 \cdot 10^{21}$ | 167.5 |
| 27 | $CH_4* + * \rightarrow CH_3* + H*$ | $3.7 \cdot 10^{21}$ | 61.0 |
| 28 | $CH_3* + H* \rightarrow CH_4* + *$ | $3.7 \cdot 10^{21}$ | 51.0 |
| 29 | $CH_3* + * \rightarrow CH_2* + H*$ | $3.7 \cdot 10^{24}$ | 103.0 |
| 30 | $CH_2* + H* \rightarrow CH_3* + *$ | $3.7 \cdot 10^{23}$ | 44.1 |
| 31 | $CH_2* + * \rightarrow CH* + H*$ | $3.7 \cdot 10^{24}$ | 100.0 |
| 32 | $CH* + H* \rightarrow CH_2* + *$ | $3.7 \cdot 10^{21}$ | 68.0 |
| 33 | $CH* + * \rightarrow C* + H*$ | $3.7 \cdot 10^{21}$ | 21.0 |
| 34 | $C* + H* \rightarrow CH* + *$ | $3.7 \cdot 10^{21}$ | 172.8 |
| 35 | $CH_4* + O* \rightarrow CH_3* + OH*$ | $1.7 \cdot 10^{24}$ | 80.34 |
| 36 | $CH_3* + OH* \rightarrow CH_4* + O*$ | $3.7 \cdot 10^{21}$ | 24.27 |
| 37 | $CH_3* + O* \rightarrow CH_2* + OH*$ | $3.7 \cdot 10^{24}$ | 120.31 |
| 38 | $CH_2* + OH* \rightarrow CH_3* + O*$ | $3.7 \cdot 10^{21}$ | 15.06 |
| 39 | $CH_2* + O* \rightarrow CH* + OH*$ | $3.7 \cdot 10^{24}$ | 114.5 |
| 40 | $CH* + OH* \rightarrow CH_2* + O*$ | $3.7 \cdot 10^{21}$ | 36.82 |
| 41 | $CH* + O* \rightarrow C* + OH*$ | $3.7 \cdot 10^{21}$ | 30.13 |
| 42 | $C* + OH* \rightarrow CH* + O*$ | $3.7 \cdot 10^{21}$ | 136.0 |

[a] Arrhenius parameters for rate constants. Units: pre-exponential factor $A$ for unimolecular reactions [$s^{-1}$], for bimolecular reactions [$cm^2$ $mol^{-1}$ $s^{-1}$]

[b] Initial Sticking coefficient $S_i^0$ [-]

[c] Coverage dependent activation energy in Eq. (3.46). For more information see e.g., (Kee et al., 2003)

Surface site density $\Gamma = 2.72 \cdot 10^{-9}$ mol/cm$^2$

# C   DRM microkinetics on nickel

Table 23: Detailed surface reaction mechanism for the dry reforming of methane on nickel from Delgado et al. (2015).

| | Reaction | A [$^a$] | $\beta$ [-] | E$^c$ [kJ/mol] |
|---|---|---|---|---|
| Adsorption-desorption reactions | | | | |
| 1 | $* + * + H_2 \rightarrow H* + H*$ | $3.000 \cdot 10^{-2,b}$ | 0.0 | 5.00 |
| 2 | $H* + H* \rightarrow * + * + H_2$ | $2.544 \cdot 10^{20}$ | 0.0 | 95.209 |
| 3 | $O_2 + * + * \rightarrow O* + O*$ | $4.358 \cdot 10^{-2,b}$ | -0.206 | 1.511 |
| 4 | $O* + O* \rightarrow * + * + O_2$ | $1.188 \cdot 10^{21}$ | 0.823 | 468.91 |
| 5 | $* + CH_4 \rightarrow CH_4*$ | $8.000 \cdot 10^{-3,b}$ | 0.0 | 0.0 |
| 6 | $CH_4* \rightarrow * + CH_4$ | $8.705 \cdot 10^{15}$ | 0.0 | 37.550 |
| 7 | $* + H_2O \rightarrow H_2O*$ | $9.999 \cdot 10^{-2,b}$ | 0.0 | 0.0 |
| 8 | $H_2O* \rightarrow * + H_2O$ | $3.732 \cdot 10^{12}$ | 0.0 | 60.791 |
| 9 | $* + CO_2 \rightarrow CO_2*$ | $7.001 \cdot 10^{-6,b}$ | 0.0 | 0.0 |
| 10 | $CO_2* \rightarrow * + CO_2$ | $6.442 \cdot 10^{07}$ | 0.0 | 25.979 |
| 11 | $* + CO \rightarrow CO*$ | $4.999 \cdot 10^{-1,b}$ | 0.0 | 0.0 |
| 12 | $CO* \rightarrow CO + *$ | $3.566 \cdot 10^{11}$ | 0.0 | $111.271 - 50 \cdot \Theta_{CO*}$ |
| Surface reactions | | | | |
| 13 | $* + CH_4* \rightarrow H* + CH_3*$ | $1.548 \cdot 10^{21}$ | 0.087 | 55.825 |
| 14 | $H* + CH_3* \rightarrow * + CH_4*$ | $1.443 \cdot 10^{22}$ | -0.087 | 63.455 |
| 15 | $CH_3* + * \rightarrow H* + CH_2*$ | $1.548 \cdot 10^{24}$ | 0.087 | 98.125 |
| 16 | $H* + CH_2* \rightarrow CH_3* + *$ | $3.091 \cdot 10^{23}$ | -0.087 | 57.205 |
| 17 | $* + CH_2* \rightarrow CH* + H*$ | $3.700 \cdot 10^{24}$ | 0.087 | 95.225 |
| 18 | $CH* + H* \rightarrow * + CH_2*$ | $9.774 \cdot 10^{24}$ | -0.087 | 81.055 |
| 19 | $CH* + * \rightarrow H* + C*$ | $9.888 \cdot 10^{20}$ | 0.500 | 21.991 |
| 20 | $H* + C* \rightarrow CH* + *$ | $1.707 \cdot 10^{24}$ | -0.500 | 157.919 |
| 21 | $CH_4* + O* \rightarrow CH_3* + OH*$ | $5.621 \cdot 10^{24}$ | -0.101 | 92.72 |
| 22 | $CH_3* + OH* \rightarrow CH_4* + O*$ | $2.987 \cdot 10^{22}$ | 0.101 | 25.798 |
| 23 | $CH_3* + O* \rightarrow CH_2* + OH*$ | $1.223 \cdot 10^{25}$ | -0.101 | 134.672 |
| 24 | $CH_2* + OH* \rightarrow CH_3* + O*$ | $1.393 \cdot 10^{21}$ | 0.101 | 19.048 |
| 25 | $CH_2* + O* \rightarrow CH* + OH*$ | $1.223 \cdot 10^{25}$ | -0.101 | 131.372 |
| 26 | $CH* + OH* \rightarrow CH_2* + O*$ | $4.407 \cdot 10^{22}$ | 0.101 | 42.498 |
| 27 | $CH* + O* \rightarrow C* + OH*$ | $2.471 \cdot 10^{21}$ | 0.312 | 57.742 |
| 28 | $C* + OH* \rightarrow CH* + O*$ | $2.433 \cdot 10^{21}$ | -0.312 | 118.968 |
| 29 | $H* + O* \rightarrow * + OH*$ | $3.951 \cdot 10^{23}$ | -0.188 | 104.346 |
| 30 | $* + OH* \rightarrow H* + O*$ | $2.254 \cdot 10^{20}$ | 0.188 | 29.644 |
| 31 | $H* + OH* \rightarrow * + H_2O*$ | $1.854 \cdot 10^{20}$ | 0.086 | 41.517 |
| 32 | $* + H_2O* \rightarrow H* + OH*$ | $3.674 \cdot 10^{21}$ | -0.086 | 92.943 |
| 33 | $OH* + OH* \rightarrow H_2O* + O*$ | $2.346 \cdot 10^{20}$ | 0.274 | 92.366 |
| 34 | $H_2O* + O* \rightarrow OH* + OH*$ | $8.148 \cdot 10^{24}$ | -0.274 | 218.494 |
| 35 | $C* + O* \rightarrow * + CO*$ | $3.402 \cdot 10^{23}$ | 0.0 | 148.001 |
| 36 | $* + CO* \rightarrow C* + O*$ | $1.758 \cdot 10^{13}$ | 0.0 | $116.239 - 50 \cdot \Theta_{CO*}$ |
| 37 | $CO* + CO* \rightarrow CO_2* + C*$ | $1.624 \cdot 10^{14}$ | 0.500 | $241.761 - 100 \cdot \Theta_{CO*}$ |

| 38 | $CO_2* + C* \rightarrow CO* + CO*$ | $7.294 \cdot 10^{28}$ | -0.500 | 239.239 |
| 39 | $CO* + O* \rightarrow * + CO_2*$ | $2.002 \cdot 10^{19}$ | 0.0 | $123.601 - 50 \cdot \Theta_{CO*}$ |
| 40 | $* + CO_2* \rightarrow CO* + O*$ | $4.648 \cdot 10^{23}$ | -1.000 | 89.319 |
| 41 | $CO* + H* \rightarrow C* + OH*$ | $3.522 \cdot 10^{18}$ | -0.188 | $10.45 - 50 \cdot \Theta_{CO*}$ |
| 42 | $C* + OH* \rightarrow H* + CO*$ | $3.888 \cdot 10^{25}$ | 0.188 | 62.555 |
| 43 | $H* + CO_2* \rightarrow * + COOH*$ | $6.250 \cdot 10^{24}$ | -0.475 | 117.344 |
| 44 | $* + COOH* \rightarrow H* + CO_2*$ | $3.737 \cdot 10^{20}$ | 0.475 | 33.656 |
| 45 | $* + COOH* \rightarrow CO* + OH*$ | $1.461 \cdot 10^{24}$ | -0.213 | 54.366 |
| 46 | $CO* + OH* \rightarrow * + COOH*$ | $6.003 \cdot 10^{20}$ | 0.213 | $97.634 - 50 \cdot \Theta_{CO*}$ |
| 47 | $H* + CO* \rightarrow * + HCO*$ | $4.009 \cdot 10^{20}$ | -1.000 | 132.227 |
| 48 | $* + HCO* \rightarrow H* + CO*$ | $3.710 \cdot 10^{21}$ | 0.0 | $0.00 + 50 \cdot \Theta_{CO*}$ |
| 49 | $* + HCO* \rightarrow CH* + O*$ | $3.796 \cdot 10^{14}$ | 0.0 | 81.911 |
| 50 | $CH* + O* \rightarrow * + HCO*$ | $4.599 \cdot 10^{20}$ | 0.0 | 109.969 |
| 51 | $H* + COOH* \rightarrow HCO* + OH*$ | $6.000 \cdot 10^{22}$ | -1.163 | 104.878 |
| 52 | $HCO* + OH* \rightarrow H* + COOH*$ | $2.282 \cdot 10^{20}$ | 0.263 | 15.922 |

[a] Arrhenius parameters for rate constants. Units: pre-exponential factor $A$ for unimolecular reactions [$s^{-1}$], for bimolecular reactions [$cm^2\ mol^{-1}\ s^{-1}$]
[b] Initial Sticking coefficient $S_i^0$ [-]
[c] Coverage dependent activation energy in Eq. (3.46). For more information see e.g., (Kee et al., 2003)
Surface site density $\Gamma = 2.66 \cdot 10^{-9}$ mol/cm$^2$

# D  CPOX microkinetics on rhodium

Table 24: Detailed surface reaction mechanism for the catalytic partial oxidation of methane on rhodium from Schwiedernoch et al. (2003).

| | Reaction | A [$^a$] | E$^c$ [kJ/mol] |
|---|---|---|---|
| Adsorption-desorption reactions | | | |
| 1 | $CH_4 + * \rightarrow CH_4*$ | $8.0 \cdot 10^{-3,b}$ | 0.0 |
| 2 | $CH_4* \rightarrow CH_4 + *$ | $1.0 \cdot 10^{13}$ | 25.1 |
| 3 | $O_2 + 2* \rightarrow 2O*$ | $0.01 \cdot b$ | 0.0 |
| 4 | $2O* \rightarrow 2* + O_2$ | $1.3 \cdot 10^{22}$ | $355.2 - 280\Theta_{O*}$ |
| 5 | $H_2 + 2* \rightarrow 2H*$ | $0.01 \cdot b$ | 0.0 |
| 6 | $2H* \rightarrow 2* + H_2$ | $3.0 \cdot 10^{21}$ | 77.8 |
| 7 | $H_2O + * \rightarrow H_2O*$ | $0.1 \cdot b$ | 0.0 |
| 8 | $H_2O* \rightarrow H_2O + *$ | $3.0 \cdot 10^{13}$ | 45.0 |
| 9 | $CO + * \rightarrow CO*$ | $0.5 \cdot b$ | 0.0 |
| 10 | $CO* \rightarrow CO + *$ | $3.5 \cdot 10^{13}$ | $133.4 - 15\Theta_{CO*}$ |
| 11 | $CO_2 + * \rightarrow CO_2*$ | $1.0 \cdot 10^{-5,b}$ | 0.0 |
| 12 | $CO_2* \rightarrow CO_2 + *$ | $1.0 \cdot 10^{13}$ | 21.7 |

Surface reactions

| 13 | $H* + O* \rightarrow OH* + *$ | $5.0 \cdot 10^{22}$ | 83.7 |
|---|---|---|---|
| 14 | $OH* + * \rightarrow H* + O*$ | $3.0 \cdot 10^{20}$ | 37.7 |
| 15 | $H* + OH* \rightarrow H_2O* + *$ | $3.0 \cdot 10^{20}$ | 33.5 |
| 16 | $H_2O* + * \rightarrow H* + OH*$ | $5.0 \cdot 10^{22}$ | 104.7 |
| 17 | $OH* + OH* \rightarrow H_2O* + O*$ | $3.0 \cdot 10^{21}$ | 100.8 |
| 18 | $H_2O* + O* \rightarrow OH* + OH*$ | $3.0 \cdot 10^{21}$ | 171.8 |
| 19 | $C* + O* \rightarrow CO* + *$ | $3.0 \cdot 10^{22}$ | 97.9 |
| 20 | $CO* + * \rightarrow C* + O*$ | $2.5 \cdot 10^{21}$ | 169.0 |
| 21 | $CO* + O* \rightarrow CO_2* + *$ | $1.4 \cdot 10^{20}$ | 121.6 |
| 22 | $CO_2* + * \rightarrow CO* + O*$ | $3.0 \cdot 10^{21}$ | 115.3 |
| 23 | $CH_4* + * \rightarrow CH_3* + H*$ | $3.7 \cdot 10^{21}$ | 61.0 |
| 24 | $CH_3* + H* \rightarrow CH_4* + *$ | $3.7 \cdot 10^{21}$ | 51.0 |
| 25 | $CH_3* + * \rightarrow CH_2* + H*$ | $3.7 \cdot 10^{24}$ | 103.0 |
| 26 | $CH_2* + H* \rightarrow CH_3* + *$ | $3.7 \cdot 10^{21}$ | 44.0 |
| 27 | $CH_2* + * \rightarrow CH* + H*$ | $3.7 \cdot 10^{24}$ | 100.0 |
| 28 | $CH* + H* \rightarrow CH_2* + *$ | $3.7 \cdot 10^{21}$ | 68.0 |
| 29 | $CH* + * \rightarrow C* + H*$ | $3.7 \cdot 10^{21}$ | 21.0 |
| 30 | $C* + H* \rightarrow CH* + *$ | $3.7 \cdot 10^{21}$ | 172.8 |
| 31 | $CH_4* + O* \rightarrow OH* + CH_3*$ | $1.7 \cdot 10^{24}$ | 80.3 |
| 32 | $CH_3* + OH* \rightarrow O* + CH_4*$ | $3.7 \cdot 10^{21}$ | 24.3 |
| 33 | $CH_3* + O* \rightarrow OH* + CH_2*$ | $3.7 \cdot 10^{24}$ | 120.3 |
| 34 | $CH_2* + OH* \rightarrow O* + CH_3*$ | $3.7 \cdot 10^{21}$ | 15.1 |
| 35 | $CH_2* + O* \rightarrow OH* + CH*$ | $1.7 \cdot 10^{24}$ | 158.4 |
| 36 | $CH* + OH* \rightarrow O* + CH_2*$ | $3.7 \cdot 10^{21}$ | 36.8 |
| 37 | $CH* + O* \rightarrow OH* + C*$ | $3.7 \cdot 10^{21}$ | 30.1 |
| 38 | $C* + OH* \rightarrow O* + CH*$ | $3.7 \cdot 10^{21}$ | 145.5 |

[a] Arrhenius parameters for rate constants. Units: pre-exponential factor $A$ for unimolecular reactions [$s^{-1}$], for bimolecular reactions [$cm^2$ $mol^{-1}$ $s^{-1}$]

[b] Initial Sticking coefficient $S_i^0$ [-]

[c] Coverage dependent activation energy in 3.46.

Surface site density $\Gamma = 2.72 \cdot 10^{-9}$ mol/cm$^2$

# E  List of publications of particle-resolved CFD of fixed-bed reactors

Table 25: Publications of particle-resolved CFD of fixed-bed reactors

| Author | particle shape | No. of particles | $N$ | $Re_p$ | bed generation | treatment of contact points |
|---|---|---|---|---|---|---|
| Derkx and Dixon (1996) | spheres | 3 | 2.14 | 25–101 | structured | not touching |
| Logtenberg and Dixon (1998) | spheres | 8 | 2.86 | 9–1450 | structured | not touching |
| Logtenberg et al. (1999) | spheres | 10 | 2.43 | 42–3344 | structured | local refinement |
| Nijemeisland and Dixon (2001) | spheres | 44 | 2 | 373–1922 | structured | gaps (1%) |
| Dixon and Nijemeisland (2001) | spheres | 44 | 2, 4 | 373–1922 | structured | gaps (1%) |
| Calis et al. (2001) | spheres | 8-16 | 1-2 | 0.01–50000 | structured | gaps (1%) |
| Zeiser et al. (2001) | spheres | – | 5, 6 | 4.32, 5.2 | Monte Carlo | none[†] |
| Romkes et al. (2003) | spheres | – | 1–2 | $0.1$–$10^5$ | structured | gaps |
| Freund et al. (2003) | spheres | – | 3–5.6 | 0.3–100 | Monte Carlo | none[†] |
| Magnico (2003) | spheres | 80-620 | 5–8 | 7–200 | deposition algorithm | none[‡] |
| Guardo et al. (2004) | spheres | 44 | 3.9 | 84–912 | structured | overlaps (1%) |
| Nijemeisland and Dixon (2004) | spheres | 72 (120°) | 4 | 1000 | structured | gaps (1%) |
| Nijemeisland et al. (2004) | cylinders | 10 (120°) | 4 | 8000 | adopted from experiments | gaps (1%) |
| Klöker et al. (2004) | spheres | <10 | periodic | 13.1 | structured | gaps ($< 0.5\%$) |
| Dixon et al. (2005) | spheres, cylinders | 10 (120°) | 4 | 9000 | structured | gaps (1%) |
| Gunjal et al. (2005) | spheres | unit cell | FCC, BCC[§] | 12–2000 | structured | none[‡] |
| Freund et al. (2005) | spheres | >100 | 5, 15 | 4–227 | Monte Carlo | none[†] |
| Guardo et al. (2005) | spheres | 44 | 3.9 | 84–912 | structured | overlaps (1%) |

| Reference | particle | number | aspect ratio | Re | packing | contact treatment |
|---|---|---|---|---|---|---|
| Ookawara et al. (2007) | spheres | <880 | 4–8 | <1000 | random with DEM | bridges |
| Lee et al. (2007) | spheres | 32 | periodic | 24000 | structured | gaps (1%) |
| Dixon et al. (2007) | cylinders | 10 (120°) | 4 | 8000 | structured | gaps (.5%) |
| Reddy and Joshi (2008) | cylinders | 151 | 5 | 0.1–10000 | structured | gaps (1%) |
| Hassan (2008) | spheres | 44 | periodic | 30000 | structured | local refinement |
| Magnico (2009) | spheres | 236, 620 | 5–8 | 80–160 | deposition algorithm | none‡ |
| Atmakidis and Kenig (2009) | spheres | <400 | 1–7 | <100 | Monte Carlo | gaps (2%) |
| Bai et al. (2009) | spheres, cylinders | ≈150 | 1.8–3.2 | 2000–20000 | random with DEM | gaps (0.5, 1%) |
| Augier et al. (2010) | spheres | 440, 620 (40°) | 25 | 1–100 | random with DEM | gaps (2%) |
| Reddy and Joshi (2010) | spheres | <1120 | 3.5, 10 | 0.1–10000 | structured | gaps (1%) |
| Baker and Tabor (2010) | spheres | 160 | 7, 14 | 700–5000 | Monte Carlo | local refinement |
| Yang et al. (2010) | spheres | <30 | periodic | 1–5000 | structured | gaps (1%) |
| Guo and Dai (2010) | spheres | 120 | 7 | 4–56 | random with sequential packing scheme | not mentioned |
| Cheng et al. (2010) | spheres | <10 (120°) | 4 | 9000–30000 | structured | caps |
| Eppinger et al. (2011) | spheres | | 3–10 | 1–1000 | random with DEM | caps |
| Baker et al. (2011) | cylinders | 1000, 1250 | 4.4 | 1431–5000 | from MRI | wrapping |
| Dixon et al. (2012b) | spheres | | 5.5, 7.4 | 1600–5600 | random with sequential packing scheme | gaps, caps, bridges |
| Mirhashemi and Hashemabadi (2012) | cylinders | 24 | 2.7 | 2500–6800 | structures | gaps (1%) |
| Shams et al. (2012) | spheres | unit cell | FCC | 21000 | structured | not touching |
| Dixon et al. (2013a) | spheres | 72 | 4 | 0 | structured | gaps |

| Reference | Particles | | | | Method | Notes |
|---|---|---|---|---|---|---|
| Zobel et al. (2012) | spheres | <1000 | 3–8 | 186 | random with DEM | caps |
| Behnam et al. (2013) | spheres | <1000 | 3.9–8 | 80–1900 | soft-sphere algorithm$ | gaps (1%) |
| Maestri and Cuoci (2013) | spheres, Raschig rings | 2, 8 | 50 | structured | wrapping | |
| Yang et al. (2013) | spheres | 6800 | 17.6 | 0.6 | from MRI | local refinement |
| Bu et al. (2014) | spheres | unit cell | FCC | <3000 | structured | gaps, overlap, caps, bridges |
| Shams et al. (2014) | spheres | <30 | periodic | 9700 | overlap removal methods†† | not touching |
| Boccardo et al. (2015) | spheres, cylinders, trilobes | <2000 | periodic | 0.001–100 | random with Blender‡‡ | overlap |

† due to Lattice Boltzmann method
‡ due to structured mesh
§ BCC: body centered cubical, FCC: face centered cubical
$ algorithm developed by Salvat et al. (2005)
†† algorithm by Pavlidis and Lathouwers (2013)
‡‡ software for 3D computer graphics Blender-Foundation (2015)

# F    Mesh study of fixed-bed reactor of spheres
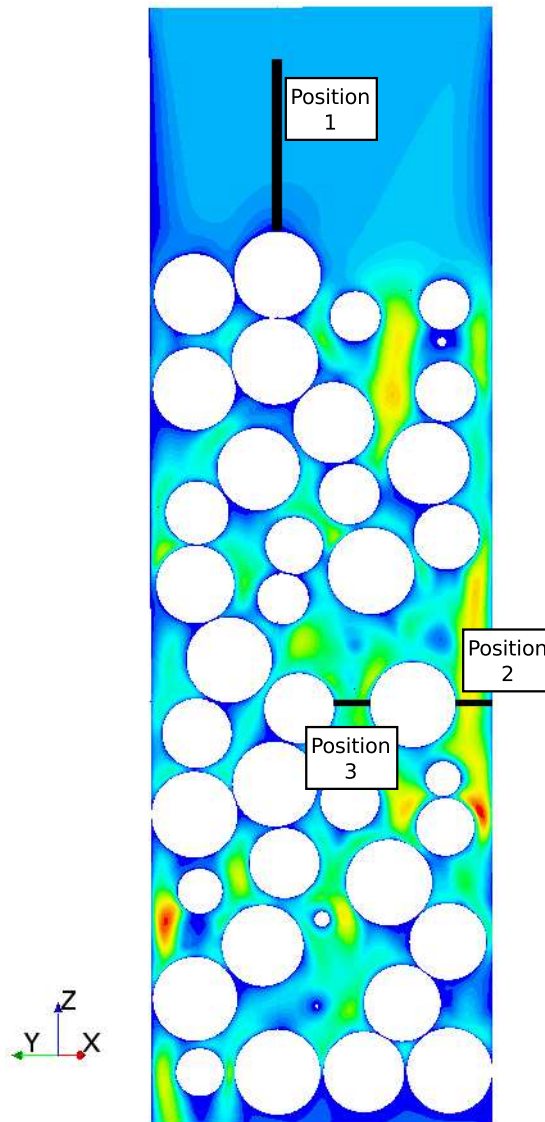


Figure 104: Velocity magnitude contours for $Re_p = 35$ and positions for the mesh validation
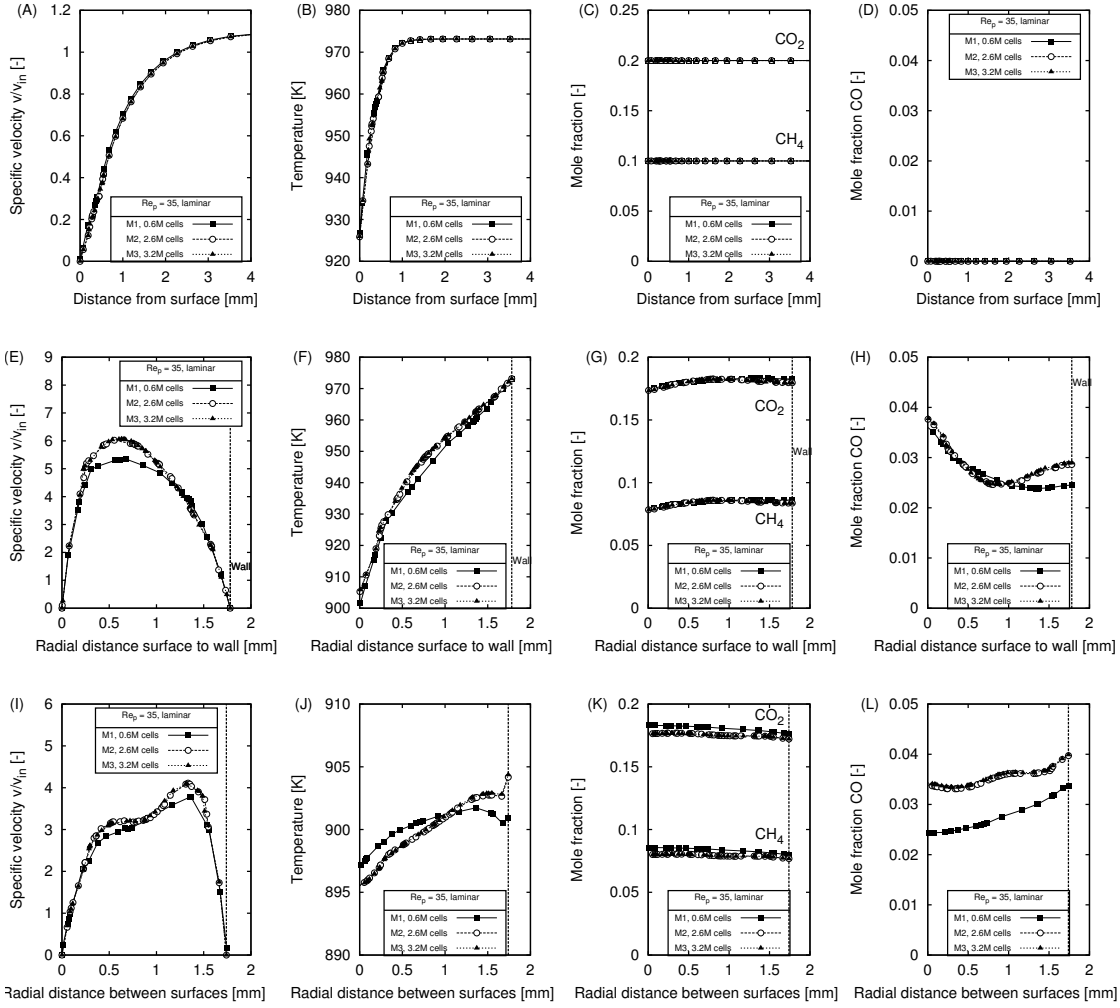
Figure 105: Results of mesh refinement for laminar case $Re_p = 35$. Specific velocity for (a) position 1, (E) position 2, (I) position 3. Temperature for (B) position 1, (F) position 2, (J) position 3. Mole fractions $CO_2$ and $CH_4$ for (C) position 1, (G) position 2, (K) position 3. Mole fractions CO for (D) position 1, (H) position 2, (L) position 3.
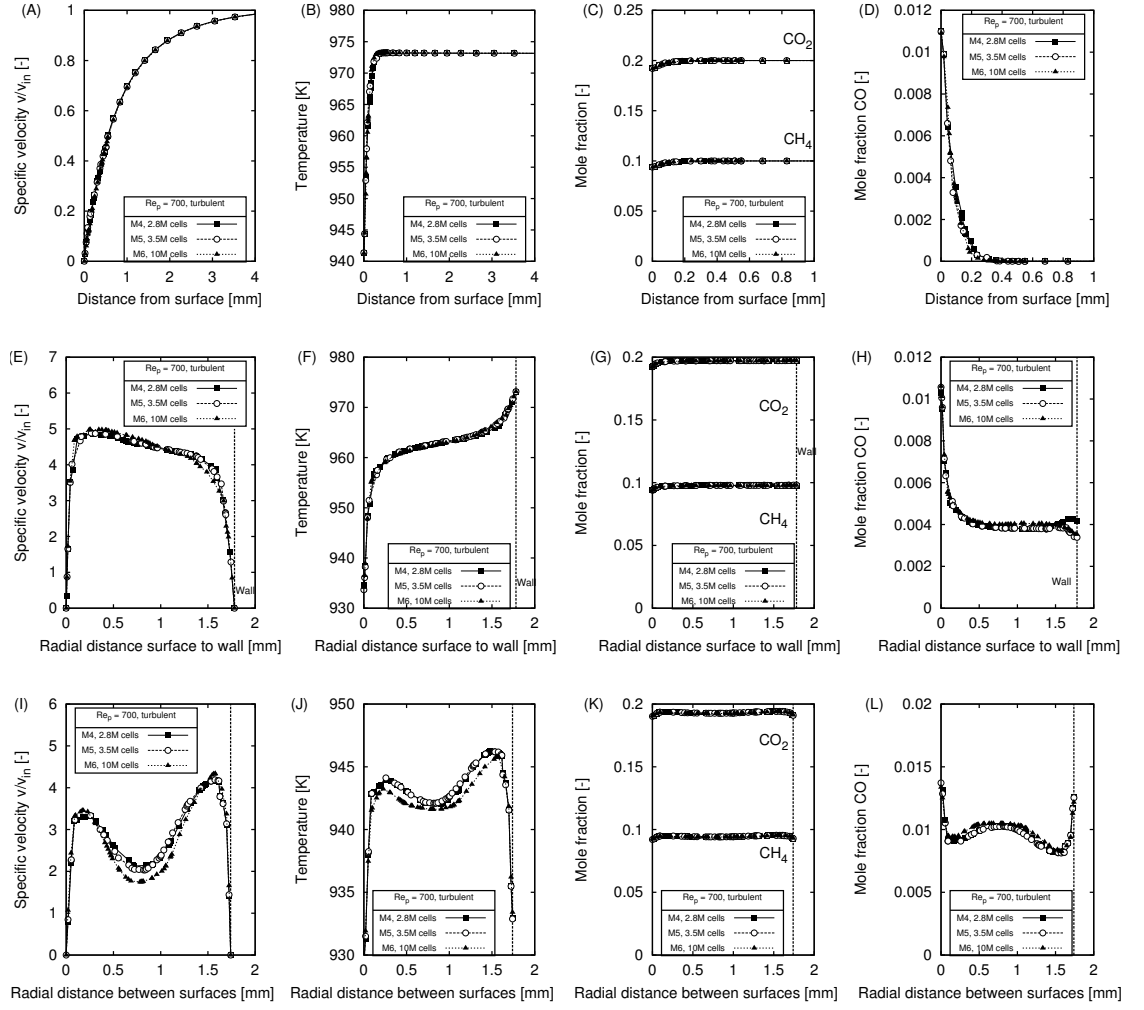
Figure 106: Results of mesh refinement for turbulent case $Re_p = 700$. Specific velocity for (A) position 1, (E) position 2, (I) position 3. Temperature for (B) position 1, (F) position 2, (J) position 3. Mole fractions $CO_2$ and $CH_4$ for (C) position 1, (G) position 2, (K) position 3. Mole fractions CO for (D) position 1, (H) position 2, (L) position 3.

# G  Reaction-path analysis of DRM microkinetics



Figure 107: Reaction-path analysis of DRM microkinetics of (A) original kinetics and (B) fitted kinetics. Analyzing C atoms.

(A) Original kinetics
Delgado et al. (2015)
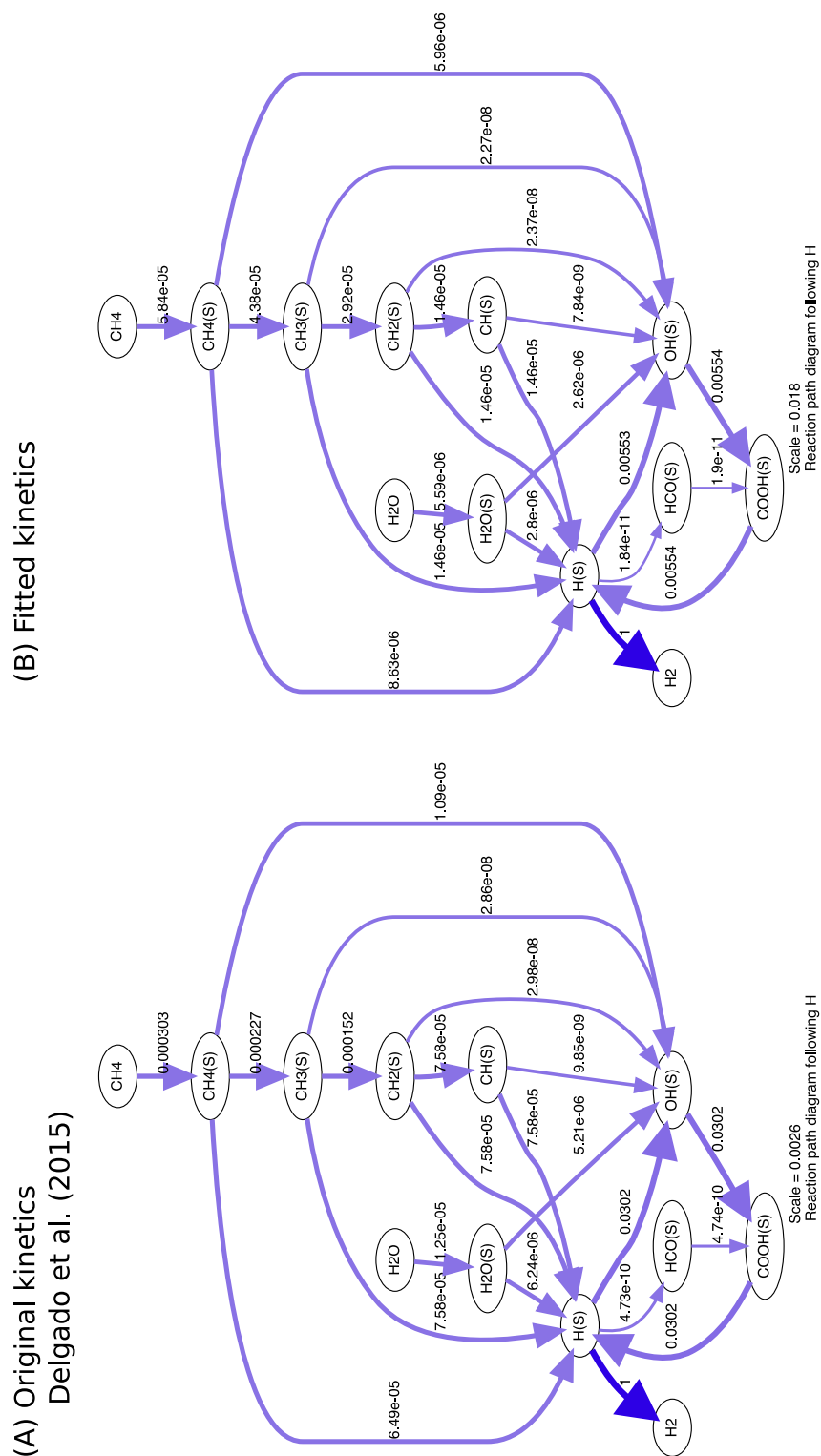
(B) Fitted kinetics

Figure 108: Reaction-path analysis of DRM microkinetics of (A) original kinetics and (B) fitted kinetics. Analyzing H atoms.

# References

Atmakidis, T., Kenig, E. Y., 2009. CFD-based analysis of the wall effect on the pressure drop in packed beds with moderate tube/particle diameter ratios in the laminar flow regime. Chemical Engineering Journal 155 (1-2), 404–410.

Augier, F., Idoux, F., Delenne, J., 2010. Numerical simulations of transfer and transport properties inside packed beds of spherical particles. Chemical Engineering Science 65 (3), 1055–1064.

Avila, K., Moxey, D., de Lozar, A., Avila, M., Barkley, D., Hof, B., 2011. The onset of turbulence in pipe flow. Science 333 (6039), 192–196.

Baerns, M., Behr, A., Brehm, A., Gmehling, J., Hofmann, H., Onken, U., Renken, A., 2006. Technische Chemie. Wiley-VCH-Verlag.

Bai, H., Theuerkauf, J., Gillis, P. A., Witt, P. M., 2009. A coupled DEM and CFD simulation of flow field and pressure drop in fixed bed reactor with randomly packed catalyst particles. Industrial & Engineering Chemistry Research 48 (8), 4060–4074.

Baker, M., Tabor, G., 2010. Computational analysis of transitional air flow through packed columns of spheres using the finite volume technique. Computers & Chemical Engineering 34 (6), 878–885.

Baker, M., Young, P., Tabor, G., 2011. Image based meshing of packed beds of cylinders at low aspect ratios using 3d MRI coupled with computational fluid dynamics. Computers & Chemical Engineering 35 (10), 1969–1977.

Bartholomew, C. H., 1982. Carbon deposition in steam reforming and methanation. Catalysis Reviews 24 (1), 67–112.

Behnam, M., Dixon, A. G., Nijemeisland, M., Stitt, E. H., 2013. A new approach to fixed bed radial heat transfer modeling using velocity fields from computational fluid dynamics simulations. Industrial & Engineering Chemistry Research NASCRE 3.

Beretta, A., Donazzi, A., Livio, D., Maestri, M., Groppi, G., Tronconi, E., Forzatti, P., 2011. Optimal design of a $CH_4$ CPO-reformer with honeycomb catalyst: Combined effect of catalyst load and channel size on the surface temperature profile. Catalysis Today 171 (1), 79–83.

Bey, O., Eigenberger, G., 1997. Fluid flow through catalyst filled tubes. Chemical Engineering Science 52 (8), 1365–1376.

Bianchi, E., Groppi, G., Schwieger, W., Tronconi, E., Freund, H., 2015. Numerical simulation of heat transfer in the near-wall region of tubular reactors packed with metal open-cell foams. Chemical Engineering Journal 264, 268–279.

Bianchi, E., Heidig, T., Visconti, C. G., Groppi, G., Freund, H., Tronconi, E., 2013. Heat transfer properties of metal foam supports for structured catalysts: Wall heat transfer coefficient. Catalysis Today 216, 121–134.

Bitsch-Larsen, A., Horn, R., Schmidt, L., 2008. Catalytic partial oxidation of methane on rhodium and platinum: Spatial profiles at elevated pressure. Applied Catalysis A: General 348 (2), 165–172.

Blaylock, D., Zhu, Y.-A., Green, W., 2011. Computational investigation of the thermochemistry and kinetics of steam methane reforming over a multi-faceted nickel catalyst. Topics in Catalysis 54 (13-15), 828–844.

Blaylock, D. W., Ogura, T., Green, W. H., Beran, G. J. O., 2009. Computational investigation of thermochemistry and kinetics of steam methane reforming on Ni(111) under realistic conditions. The Journal of Physical Chemistry C 113 (12), 4898–4908.

Blender-Foundation, 2015. Blender. www.blender.org.

Boccardo, G., Augier, F., Haroun, Y., Ferré, D., Marchisio, D. L., 2015. Validation of a novel open-source work-flow for the simulation of packed-bed reactors. Chemical Engineering Journal 279, 809–820.

Boll, W., Tischer, S., Deutschmann, O., 2010. Loading and aging effects in exhaust gas after-treatment catalysts with Pt as active component. Industrial & Engineering Chemistry Research 49 (21), 10303–10310.

Boomsma, K., Poulikakos, D., Ventikos, Y., 2003. Simulations of flow through open cell metal foams using an idealized periodic cell structure. International Journal of Heat and Fluid Flow 24 (6), 825–834.

Bradford, M. C. J., Vannice, M. A., 1999. $CO_2$ reforming of $CH_4$. Catalysis Reviews 41 (1), 1–42.

Brinkmeier, C., Eigenberger, G., Bernnat, J., Tuttlies, U., Schmeißer, V., Opferkuch, F., 2005. Autoabgasreinigung – eine Herausforderung für die Verfahrenstechnik. Chemie Ingenieur Technik 77 (9), 1333–1355.

Bu, S., Yang, J., Zhou, M., Li, S., Wang, Q., Guo, Z., 2014. On contact point modifications for forced convective heat transfer analysis in a structured packed bed of spheres. Nuclear Engineering and Design 270, 21–33.

Buciuman, F. C., Kraushaar-Czarnetzki, B., 2003. Ceramic foam monoliths as catalyst carriers. 1. Adjustment and description of the morphology. Industrial & Engineering Chemistry Research 42 (9), 1863–1869.

Buyevskaya, O., Walter, K., Wolf, D., Baerns, M., 1996. Primary reaction steps and active surface sites in the rhodium-catalyzed partial oxidation of methane to CO and $H_2$. Catalysis Letters 38 (1-2), 81–88.

Calis, H., Nijenhuis, J., Paikert, B., Dautzenberg, F., van den Bleek, C., 2001. CFD modelling and experimental validation of pressure drop and flow profile in a novel structured catalytic reactor packing. Chemical Engineering Science 56 (4), 1713–1720.

Caulkin, R., Ahmad, A., Fairweather, M., Jia, X., Williams, R., 2009. Digital predictions of complex cylinder packed columns. Computers & Chemical Engineering 33 (1), 10–21.

Caulkin, R., Tian, W., Pasha, M., Hassanpour, A., Jia, X., 2015. Impact of shape representation schemes used in discrete element modelling of particle packing. Computers & Chemical Engineering 76, 160–169.

CD-adapco, 2014. STAR-CCM+ 9.06. www.cd-adapco.com.

Chan, D., Tischer, S., Heck, J., Diehm, C., Deutschmann, O., 2014. Correlation between catalytic activity and catalytic surface area of a $Pt/Al_2O_3$ DOC: An experimental and microkinetic modeling study. Applied Catalysis B: Environmental 156-157, 153–165.

Chen, D., Lødeng, R., Anundskås, A., Olsvik, O., Holmen, A., 2001. Deactivation during carbon dioxide reforming of methane over Ni catalyst: microkinetic analysis. Chemical Engineering Science 56 (4), 1371–1379.

## References

Cheng, S.-H., Chang, H., Chen, Y.-H., Chen, H.-J., Chao, Y.-K., Liao, Y.-H., 2010. Computational fluid dynamics-based multiobjective optimization for catalyst design. Industrial & Engineering Chemistry Research 49 (21), 11079–11086.

Chiu, S. N., Stoyan, D., Kendall, W. S., Mecke, J., 2013. Stochastic Geometry and its Applications, 3rd Edition. John Wiley & Sons.

Choi, J.-S., Partridge, W. P., Daw, C. S., 2005. Spatially resolved in situ measurements of transient species breakthrough during cyclic, low-temperature regeneration of a monolithic $Pt/K/Al_2O_3$ $NO_x$ storage-reduction catalyst. Applied Catalysis A: General 293, 24–40.

Choi, J.-S., Partridge, W. P., Daw, C. S., 2007. Sulfur impact on $NO_x$ storage, oxygen storage, and ammonia breakthrough during cyclic lean/rich operation of a commercial lean $NO_x$ trap. Applied Catalysis B: Environmental 77 (1–2), 145–156.

Colombo, P., Hellmann, J., 2002. Ceramic foams from preceramic polymers. Materials Research Innovations 6 (5-6), 260–272.

Cortright, R., Dumesic, J., 2001. Kinetics of heterogeneous catalytic reactions: Analysis of reaction schemes. Vol. 46 of Advances in Catalysis. Academic Press, pp. 161–264.

Cui, Y., Zhang, H., Xu, H., Li, W., 2007. Kinetic study of the catalytic reforming of $CH_4$ with $CO_2$ to syngas over $Ni/\alpha$-$Al_2O_3$ catalyst: The effect of temperature on the reforming mechanism. Applied Catalysis A: General 318, 79–88.

Cundall, P., Strack, O., 1979. A discrete numerical model for granular assemblies. Géotechnique 29, 47–65.

Dalle Nogare, D., Degenstein, N., Horn, R., Canu, P., Schmidt, L., 2008. Modeling spatially resolved profiles of methane partial oxidation on a Rh foam catalyst with detailed chemistry. Journal of Catalysis 258 (1), 131–142.

Dalle Nogare, D., Degenstein, N., Horn, R., Canu, P., Schmidt, L., 2011. Modeling spatially resolved data of methane catalytic partial oxidation on Rh foam catalyst at different inlet compositions and flowrates. Journal of Catalysis 277 (2), 134–148.

de Berg, M., Cheong, O., van Kreveld, M., Overmars, M., 2008. Computational Geometry –Algorithms and Applications. Springer.

de Klerk, A., 2003. Voidage variation in packed beds at small column to particle diameter ratio. AIChE Journal 49 (8), 2022–2029.

de Smet, C., de Croon, M., Berger, R., Marin, G., Schouten, J., 2001. Design of adiabatic fixed-bed reactors for the partial oxidation of methane to synthesis gas. application to production of methanol and hydrogen-for-fuel-cells. Chemical Engineering Science 56 (16), 4849–4861.

Delgado, K. H., Maier, L., Tischer, S., Zellner, A., Stotz, H., Deutschmann, O., 2015. Surface reaction kinetics of steam- and $CO_2$-reforming as well as oxidation of methane over nickel-based catalysts. Catalysts 5 (2), 871–904.

Della Torre, A., Montenegro, G., Tabor, G., Wears, M., 2014. CFD characterization of flow regimes inside open cell foam substrates. International Journal of Heat and Fluid Flow 50, 72–82.

Derkx, O. R., Dixon, A. G., 1996. Determination of the fixed-bed wall heat transfer coefficient using computational fluid dynamics. Numerical Heat Transfer, Part A: Applications 29 (8), 777–794.

Deutschmann, O., 2008. Computational Fluid Dynamics Simulation of Catalytic Reactors. Handbook of Heterogeneous Catalysis. Wiley-VCH Verlag GmbH & Co. KGaA, Weinheim, Ch. 6.6, pp. 1811–1828.

Deutschmann, O., Grunwaldt, J.-D., 2013. Abgasnachbehandlung in mobilen Systemen: Stand der Technik, Herausforderungen und Perspektiven. Chemie Ingenieur Technik 85 (5), 595–617.

Deutschmann, O., Schmidt, R., Behrendt, F. Warnatz, J., 1996. Numerical modeling of catalytic ignition. Twenty-Sixth Symposium (International) on Combustion/The Combustion Institute, Pittsburgh, 1747–1754.

Deutschmann, O., Tischer, S., Correa, C., Chatterjee, D., Kleditzsch, S., Janardhanan, V., Mladenov, N., Minh, H. D., Karadeniz, H., Hettel, M., 2014. DETCHEM Software package. Karlsruhe, 2nd Edition.

Dhole, S., Chhabra, R., Eswaran, V., 2006. A numerical study on the forced convection heat transfer from an isothermal and isoflux sphere in the steady symmetric flow regime. International Journal of Heat and Mass Transfer 49 (5-6), 984–994.

Di Renzo, A., Di Maio, F. P., 2000. Comparison of contact-force models for the simulation of collisions in dem-based granular flow codes. Chemical Engineering Science 59 (3), 525–541.

Diehm, C., Deutschmann, O., 2014. Hydrogen production by catalytic partial oxidation of methane over staged Pd/Rh coated monoliths: Spatially resolved concentration and temperature profiles. International Journal of Hydrogen Energy 39 (31), 17998–18004.

Diehm, C., Karadeniz, H., Karakaya, C., Hettel, M., Deutschmann, O., 2014. Chapter two - spatial resolution of species and temperature profiles in catalytic reactors: In situ sampling techniques and CFD modeling. In: Dixon, A. G. (Ed.), Modeling and Simulation of Heterogeneous Catalytic Processes. Vol. 45 of Advances in Chemical Engineering. Academic Press, pp. 41–95.

Dietrich, B., Schell, G., Bucharsky, E., Oberacker, R., Hoffmann, M., Schabel, W., Kind, M., Martin, H., 2010. Determination of the thermal properties of ceramic sponges. International Journal of Heat and Mass Transfer 53 (1-3), 198–205.

Dixon, A. G., 1988. Wall and particle-shape effects on heat transfer in packed beds. Chemical Engineering Communications 71 (1), 217–237.

Dixon, A. G., 1997. Heat transfer in fixed beds at very low (<4) tube-to-particle diameter ratio. Industrial & Engineering Chemistry Research 36 (8), 3053–3064.

Dixon, A. G., 2012. Fixed bed catalytic reactor modelling - the radial heat transfer problem. The Canadian Journal of Chemical Engineering 90 (3), 507–527.

Dixon, A. G., Boudreau, J., Rocheleau, A., Troupel, A., Taskin, M. E., Nijemeisland, M., Stitt, E. H., 2012a. Flow, transport, and reaction interactions in shaped cylindrical particles for steam methane reforming. Industrial & Engineering Chemistry Research 51 (49), 15839–15854.

Dixon, A. G., Gurnon, A. K., Nijemeisland, M., Stitt, E. H., 2013a. CFD testing of the pointwise use of the Zehner-Schlünder formulas for fixed-bed stagnant thermal conductivity. International Communications in Heat and Mass Transfer 42, 1–4.

Dixon, A. G., Nijemeisland, M., 2001. CFD as a design tool for fixed-bed reactors. Industrial & Engineering Chemistry Research 40 (23), 5246–5254.

## References

Dixon, A. G., Nijemeisland, M., Stitt, E. H., 2005. CFD study of heat transfer near and at the wall of a fixed bed reactor tube: Effect of wall conduction. Industrial & Engineering Chemistry Research 44 (16), 6342–6353.

Dixon, A. G., Nijemeisland, M., Stitt, E. H., 2006. Packed tubular reactor modeling and catalyst design using computational fluid dynamics. In: Marin, G. B. (Ed.), Computational Fluid Dynamics. Vol. 31 of Advances in Chemical Engineering. Academic Press, pp. 307–389.

Dixon, A. G., Nijemeisland, M., Stitt, E. H., 2013b. Systematic mesh development for 3D CFD simulation of fixed beds: Contact points study. Computers & Chemical Engineering 48, 135–153.

Dixon, A. G., Taskin, M. E., Nijemeisland, M., Stitt, E. H., 2011. Systematic mesh development for 3D CFD simulation of fixed beds: Single sphere study. Computers & Chemical Engineering 35 (7), 1171–1185.

Dixon, A. G., Taskin, M. E., Stitt, E. H., Nijemeisland, M., 2007. 3d CFD simulations of steam reforming with resolved intraparticle reaction and gradients. Chemical Engineering Science 62 (18-20), 4963–4966.

Dixon, A. G., Walls, G., Stanness, H., Nijemeisland, M., Stitt, E. H., 2012b. Experimental validation of high reynolds number CFD simulations of heat transfer in a pilot-scale fixed bed tube. Chemical Engineering Journal 200-02, 344–356.

Donazzi, A., Livio, D., Beretta, A., Groppi, G., Forzatti, P., 2011a. Surface temperature profiles in $CH_4$ CPO over honeycomb supported Rh catalyst probed with in situ optical pyrometer. Applied Catalysis A: General 402 (1–2), 41–49.

Donazzi, A., Livio, D., Maestri, M., Beretta, A., Groppi, G., Tronconi, E., Forzatti, P., 2011b. Synergy of homogeneous and heterogeneous chemistry probed by in-situ spatially resolved measurements of temperature and composition. Angewandte Chemie International Edition 50 (17), 3943–3946.

Donazzi, A., Maestri, M., Beretta, A., Groppi, G., Tronconi, E., Forzatti, P., 2011c. Microkinetic analysis of $CH_4$ CPO tests with $CO_2$-diluted feed streams. Applied Catalysis A: General 391 (1-2), 350–359.

Donazzi, A., Maestri, M., Michael, B., Beretta, A., Forzatti, P., Groppi, G., Tronconi, E., Schmidt, L., Vlachos, D., 2010. Microkinetic modeling of spatially resolved autothermal $CH_4$ catalytic partial oxidation experiments over Rh-coated foams. Journal of Catalysis 275 (2), 270–279.

Düdder, H., Kähler, K., Krause, B., Mette, K., Kühl, S., Behrens, M., Scherer, V., Muhler, M., 2014. The role of carbonaceous deposits in the activity and stability of Ni-based catalysts applied in the dry reforming of methane. Catalysis Science & Technology 4, 3317–3328.

Dudukovic, M. P., 2009. Frontiers in Reactor Engineering. Science 325 (5941), 698–701.

Dybbs, A., Edwards, R., 1984. A new look at porous media fluid mechanics – darcy to turbulent. In: Bear, J., Corapcioglu, M. (Eds.), Fundamentals of Transport Phenomena in Porous Media. Vol. 82 of NATO ASI Series. Springer Netherlands, pp. 199–256.

EASAC, 2013. Carbon capture and storage in Europe. EASAC - European Academies Science Advisory Council, EASAC Brussels Office, Brussels, Belgium.

Eckhardt, B., 2009. Introduction. turbulence transition in pipe flow: 125th anniversary of the publication of Reynold's paper. Philosophical Transactions of the Royal Society of London A: Mathematical, Physical and Engineering Sciences 367 (1888), 449–455.

Edouard, D., Lacroix, M., Huu, C. P., Luck, F., 2008. Pressure drop modeling on SOLID foam: State-of-the art correlation. Chemical Engineering Journal 144 (2), 299 – 311.

EIA, 2015. International Energy Statistics. U.S. Energy Information Administration, http://www.eia.gov.

Eigenberger, G., 2008. Handbook of Heterogeneous Catalysis. Wiley-VCH Verlag GmbH & Co. KGaA, Ch. 10.1 Catalytic Fixed-Bed Reactors, pp. 2075–2106.

Eisfeld, B., Schnitzlein, K., 2001. The influence of confining walls on the pressure drop in packed beds. Chemical Engineering Science 56, 4321–4329.

Elmoutaouakkil, A., Salvo, L., Maire, E., Peix, G., 2002. 2D and 3D characterization of metal foams using X-ray tomography. Advanced Engineering Materials 4 (10), 803–807.

Enger, B. C., Lodeng, R., Holmen, A., 2008. A review of catalytic partial oxidation of methane to synthesis gas with emphasis on reaction mechanisms over transition metal catalysts. Applied Catalysis A: General 346 (1-2), 1–27.

Eppinger, T., Jurtz, N., Aglave, R., 2014. Automated workflow for spatially resolved packed bed reactors with spherical and non-spherical particles. In: $10^{th}$ International Conference on CFD in Oil & Gas, Metallurgical and Process Industries. SINTEF, Trondheim, Norway, pp. 1–10.

Eppinger, T., Seidler, K., Kraume, M., 2011. DEM-CFD simulations of fixed bed reactors with small tube to particle diameter ratios. Chemical Engineering Journal 166 (1), 324–331.

Ergun, S., 1952. Fluid flow through packed columns. Chemical Engineering Progress 48, 89–94.

Ertl, G., 2000. Dynamics of reactions at surfaces. In: Impact of Surface Science on Catalysis. Vol. 45 of Advances in Catalysis. Academic Press, pp. 1–69.

Fan, C., Zhu, Y.-A., Yang, M.-L., Sui, Z.-J., Zhou, X.-G., Chen, D., 2015. Density functional theory-assisted microkinetic analysis of methane dry reforming on Ni catalyst. Industrial & Engineering Chemistry Research 54 (22), 5901–5913.

Fernández-Ramos, A., Miller, J. A., Klippenstein, S. J., Truhlar, D. G., 2006. Modeling the kinetics of bimolecular reactions. Chemical Reviews 106 (11), 4518–4584.

Freund, H., Bauer, J., Zeiser, T., Emig, G., 2005. Detailed simulation of transport processes in fixed-beds. Industrial & Engineering Chemistry Research 44 (16), 6423–6434.

Freund, H., Zeiser, T., Huber, F., Klemm, E., Brenner, G., Durst, F., Emig, G., 2003. Numerical simulations of single phase reacting flows in randomly packed fixed-bed reactors and experimental validation. Chemical Engineering Science 58 (3-6), 903–910.

Garrido, G. I., Patcas, F., Lang, S., Kraushaar-Czarnetzki, B., 2008. Mass transfer and pressure drop in ceramic foams: A description for different pore sizes and porosities. Chemical Engineering Science 63 (21), 5202–5217.

Geske, M., Korup, O., Horn, R., 2013. Resolving kinetics and dynamics of a catalytic reaction inside a fixed bed reactor by combined kinetic and spectroscopic profiling. Catal. Sci. Technol. 3, 169–175.

Giese, M., 1997. Strömung in porösen Medien unter Berücksichtigung effektiver Viskositäten. Ph.D. thesis, Technische Universität München.

References

Giese, M., Rottschafer, K., Vortmeyer, D., 1998. Measured and modeled superficial flow profiles in packed beds with liquid flow. AIChE Journal 44 (2), 484–490.

Ginsburg, J. M., Piña, J., El Solh, T., de Lasa, H. I., 2005. Coke formation over a nickel catalyst under methane dry reforming conditions: Thermodynamic and kinetic models. Industrial & Engineering Chemistry Research 44 (14), 4846–4854.

Goguet, A., Partridge, W. P., Aiouche, F., Hardacre, C., Morgan, K., Stere, C., Sá, J., 2014. Comment on "The critical evaluation of in situ probe techniques for catalytic honeycomb monoliths" by Hettel et al. Catalysis Today 236, Part B, 206–208.

Goldsmith, C., 2012. Estimating the thermochemistry of adsorbates based upon gas-phase properties. Topics in Catalysis 55 (5-6), 366–375.

Goodling, J., Vachon, R., Stelpflug, W., Ying, S., 1983. Radial porosity distribution in cylindrical beds packed with spheres. Powder Technology 35 (1), 23–29.

Goralski, C. J., Schmidt, L., 1996. Lean catalytic combustion of alkanes at short contact times. Catalysis Letters 42 (1-2), 47–55.

Große, J., Dietrich, B., Garrido, G. I., Habisreuther, P., Zarzalis, N., Martin, H., Kind, M., Kraushaar-Czarnetzki, B., 2009. Morphological characterization of ceramic sponges for applications in chemical engineering. Industrial & Engineering Chemistry Research 48 (23), 10395–10401.

Große, J., Dietrich, B., Martin, H., Kind, M., Vicente, J., Hardy, E., 2008. Volume image analysis of ceramic sponges. Chemical Engineering & Technology 31 (2), 307–314.

Grunwaldt, J.-D., Hannemann, S., Schroer, C. G., Baiker, A., 2006. 2D-mapping of the catalyst structure inside a catalytic microreactor at work: Partial oxidation of methane over $Rh/Al_2O_3$. The Journal of Physical Chemistry B 110 (17), 8674–8680.

Guardo, A., Coussirat, M., Larrayoz, M., Recasens, F., Egusquiza, E., 2005. Influence of the turbulence model in CFD modeling of wall-to-fluid heat transfer in packed beds. Chemical Engineering Science 60 (6), 1733–1742.

Guardo, A., Coussirat, M., Larrayoz, M. A., Recasens, F., Egusquiza, E., 2004. CFD flow and heat transfer in nonregular packings for fixed bed equipment design. Industrial & Engineering Chemistry Research 43 (22), 7049–7056.

Gunjal, P. R., Ranade, V. V., Chaudhari, R. V., 2005. Computational study of a single-phase flow in packed beds of spheres. AIChE Journal 51 (2), 365–378.

Guo, J., Lou, H., Zhao, H., Chai, D., Zheng, X., 2004. Dry reforming of methane over nickel catalysts supported on magnesium aluminate spinels. Applied Catalysis A: General 273 (1-2), 75–82.

Guo, J., Lou, H., Zheng, X., 2007. The deposition of coke from methane on a $Ni/MgAl_2O_4$ catalyst. Carbon 45 (6), 1314–1321.

Guo, X., Dai, R., 2010. Numerical simulation of flow and heat transfer in a random packed bed. Particuology 8 (3), 293–299.

Habisreuther, P., Djordjevic, N., Zarzalis, N., 2009. Statistical distribution of residence time and tortuosity of flow through open-cell foams. Chemical Engineering Science 64 (23), 4943–4954.

Hartmann, D., Tank, A. K., Rusticucci, M., Alexander, L., Brönnimann, S., Charabi, Y., Dentener, F., Dlugokencky, E., Easterling, D., Kaplan, A., Soden, B., Thorne, P., Wild, M., Zhai, P., 2013. IPCC Fifth Assessment Report: Climate Change 2013 (AR5): The Physical Science Basis. Contribution of Working Group I to the Fifth Assessment Report of the Intergovernmental Panel on Climate Change. Cambridge University Press, Cambridge, United Kingdom and New York, NY, USA, Ch. Observations: Atmosphere and Surface, pp. 159–254.

Hassan, Y. A., 2008. Large eddy simulation in pebble bed gas cooled core reactors. Nuclear Engineering and Design 238 (3), 530–537.

Hasse, H., 2013. EASAC study on carbon capture and storage in Europe. Chemie Ingenieur Technik 85 (9), 1401–1401.

Hayes, R., Liu, B., Moxom, R., Votsmeier, M., 2004. The effect of washcoat geometry on mass transfer in monolith reactors. Chemical Engineering Science 59 (15), 3169–3181.

Hettel, M., Diehm, C., Bonart, H., Deutschmann, O., 2015. Numerical simulation of a structured catalytic methane reformer by DUO: The new computational interface for OpenFOAM$^{®}$ and DETCHEM$^{TM}$. Catalysis Today 258, Part 2, 230–240.

Hettel, M., Diehm, C., Deutschmann, O., 2014. Answer to the comment from goguet et al. to the paper "The critical evaluation of in situ probe techniques for catalytic honeycomb monoliths" by Hettel et al. [1]. Catalysis Today 236, Part B, 209–213.

Hettel, M., Diehm, C., Torkashvand, B., Deutschmann, O., 2013. Critical evaluation of in situ probe techniques for catalytic honeycomb monoliths. Catalysis Today 216, 2–10.

Hickman, D. A., Schmidt, L. D., 1993a. Production of syngas by direct catalytic oxidation of methane. Science 259 (5093), 343–346.

Hickman, D. A., Schmidt, L. D., 1993b. Steps in $CH_4$ oxidation on Pt and Rh surfaces: High-temperature reactor simulations. AIChE Journal 39 (7), 1164–1177.

Holman, J., 2001. Heat Transfer, 8th Edition. McGraw Hill Higher Education.

Horn, R., Degenstein, N., Williams, K., Schmidt, L., 2006a. Spatial and temporal profiles in millisecond partial oxidation processes. Catalysis Letters 110 (3-4), 169–178.

Horn, R., Korup, O., Geske, M., Zavyalova, U., Oprea, I., Schlögl, R., 2010. Reactor for in situ measurements of spatially resolved kinetic data in heterogeneous catalysis. Review of Scientific Instruments 81 (6), 064102.

Horn, R., Williams, K., Degenstein, N., Bitsch-Larsen, A., Nogare, D. D., Tupy, S., Schmidt, L., 2007a. Methane catalytic partial oxidation on autothermal Rh and Pt foam catalysts: Oxidation and reforming zones, transport effects, and approach to thermodynamic equilibrium. Journal of Catalysis 249 (2), 380–393.

Horn, R., Williams, K., Degenstein, N., Schmidt, L., 2006b. Syngas by catalytic partial oxidation of methane on rhodium: Mechanistic conclusions from spatially resolved measurements and numerical simulations. Journal of Catalysis 242 (1), 92–102.

Horn, R., Williams, K., Degenstein, N., Schmidt, L., 2007b. Mechanism of and CO formation in the catalytic partial oxidation of on Rh probed by steady-state spatial profiles and spatially resolved transients. Chemical Engineering Science 62 (5), 1298–1307.

Inayat, A., Freund, H., Zeiser, T., Schwieger, W., 2011. Determining the specific surface area of ceramic foams: The tetrakaidecahedra model revisited. Chemical Engineering Science 66 (6), 1179–1188.

Kahle, L. C. S., Roussière, T., Maier, L., Herrera Delgado, K., Wasserschaff, G., Schunk, S. A., Deutschmann, O., 2013. Methane dry reforming at high temperature and elevated pressure: Impact of gas-phase reactions. Industrial & Engineering Chemistry Research 52 (34), 11920–11930.

Karadeniz, H., Karakaya, C., Tischer, S., Deutschmann, O., 2013. Numerical modeling of stagnation-flows on porous catalytic surfaces: CO oxidation on $Rh/Al_2O_3$. Chemical Engineering Science 104, 899–907.

Karadeniz, H., Karakaya, C., Tischer, S., Deutschmann, O., 2015. Mass transfer effects in stagnation flows on a porous catalyst: Water-gas-shift reaction over $Rh/Al_2O_3$. Zeitschrift für Physikalische Chemie 229 (5), 709–737.

Karakaya, C., Deutschmann, O., 2013. Kinetics of hydrogen oxidation on $Rh/Al_2O_3$ catalysts studied in a stagnation-flow reactor. Chemical Engineering Science 89, 171–184.

Kee, R., Rupley, F., Miller, J., 1987. The Chemkin thermodynamic data base; Sandia Report. SAND87-8215B, Livermore, CA.

Kee, R. J., Colin, M. E., Glarborg, P., 2003. Chemically Reacting Flow, Theory and Pratice. Wiley, Hoboken, NJ.

Klöker, M., Kenig, E. Y., Piechota, R., Burghoff, S., Egorov, Y., 2004. CFD-gestützte Untersuchungen von Hydrodynamik und Stofftransport in Katalysatorschüttungen. Chemie Ingenieur Technik 76 (3), 236–242.

Kopanidis, A., Theodorakakos, A., Gavaises, E., Bouris, D., 2010. 3D numerical simulation of flow and conjugate heat transfer through a pore scale model of high porosity open cell metal foam. International Journal of Heat and Mass Transfer 53 (11–12), 2539–2550.

Korup, O., Goldsmith, C. F., Weinberg, G., Geske, M., Kandemir, T., Schlögl, R., Horn, R., 2013. Catalytic partial oxidation of methane on platinum investigated by spatial reactor profiles, spatially resolved spectroscopy, and microkinetic modeling. Journal of Catalysis 297, 1–16.

Korup, O., Mavlyankariev, S., Geske, M., Goldsmith, C. F., Horn, R., 2011. Measurement and analysis of spatial reactor profiles in high temperature catalysis research. Chemical Engineering and Processing: Process Intensification 50 (10), 998–1009.

Korup, O., Schlögl, R., Horn, R., 2012. Carbon formation in catalytic partial oxidation of methane on platinum: Model studies on a polycrystalline Pt foil. Catalysis Today 181 (1), 177–183.

Koči, P., Novák, V., Štěpánek, F., Marek, M., Kubiček, M., 2010. Multi-scale modelling of reaction and transport in porous catalysts. Chemical Engineering Science 65 (1), 412–419.

Krishnan, S., Murthy, J. Y., Garimella, S. V., 2006. Direct simulation of transport in open-cell metal foam. Journal of heat transfer 128.8, 793–799.

Kumar, S., Kurtz, S. K., 1994. Simulation of material microstructure using a 3D Voronoi tesselation: Calculation of effective thermal expansion coefficient of polycrystalline materials. Acta Metallurgica et Materialia 42 (12), 3917–3927.

Kuroki, M., Ookawara, S., Ogawa, K., 2009. A high-fidelity CFD model of methane steam reforming in a packed bed reactor. Journal of Chemical Engineering of Japan 42 (Supplement.), s73–s78.

Launder, B. E., Spalding, D. B., 1972. Lectures in mathematical models of turbulence. Academic press.

Lautensack, C., Giertzsch, M., Godehardt, M., Schladitz, K., 2008. Modelling a ceramic foam using locally adaptable morphology. Journal of Microscopy 230 (3), 396–404.

Lee, J.-J., Yoon, S.-J., Park, G.-C., Lee, W.-J., 2007. Turbulence-induced heat transfer in PBMR core using LES and RANS. Journal of Nuclear Science and Technology 44 (7), 985–996.

Levenspiel, O., 1998. Chemical Reaction Engenieering. Vol. 3. John Wiley & Sons.

Livio, D., Diehm, C., Donazzi, A., Beretta, A., Deutschmann, O., 2013. Catalytic partial oxidation of ethanol over $Rh/Al_2O_3$: Spatially resolved temperature and concentration profiles. Applied Catalysis A: General 467, 530–541.

Livio, D., Donazzi, A., Beretta, A., Groppi, G., Forzatti, P., 2012. Experimental and modeling analysis of the thermal behavior of an autothermal $C_3H_8$ catalytic partial oxidation reformer. Industrial & Engineering Chemistry Research 51 (22), 7573–7583.

Logtenberg, S., Nijemeisland, M., Dixon, A., 1999. Computational fluid dynamics simulations of fluid flow and heat transfer at the wall-particle contact points in a fixed-bed reactor. Chemical Engineering Science 54 (13-14), 2433–2439.

Logtenberg, S. A., Dixon, A. G., 1998. Computational fluid dynamics studies of fixed bed heat transfer1. Chemical Engineering and Processing: Process Intensification 37 (1), 7–21.

Lucci, F., Torre, A. D., Montenegro, G., Eggenschwiler, P. D., 2015. On the catalytic performance of open cell structures versus honeycombs. Chemical Engineering Journal 264, 514–521.

Lucci, F., Torre, A. D., von Rickenbach, J., Montenegro, G., Poulikakos, D., Eggenschwiler, P. D., 2014. Performance of randomized Kelvin cell structures as catalytic substrates: Mass-transfer based analysis. Chemical Engineering Science 112, 143–151.

Lyubovsky, M., Roychoudhury, S., LaPierre, R., 2005. Catalytic partial "oxidation of methane to syngas" at elevated pressures. Catalysis Letters 99 (3-4), 113–117.

Maestri, M., Beretta, A., Groppi, G., Tronconi, E., Forzatti, P., 2005. Comparison among structured and packed-bed reactors for the catalytic partial oxidation of $CH_4$ at short contact times. Catalysis Today 105 (3-4), 709–717.

Maestri, M., Cuoci, A., 2013. Coupling CFD with detailed microkinetic modeling in heterogeneous catalysis. Chemical Engineering Science 96, 106–117.

Maestri, M., Vlachos, D. G., Beretta, A., Groppi, G., Tronconi, E., 2009. A $C_1$ microkinetic model for methane conversion to syngas on $Rh/Al_2O_3$. AIChE Journal 55 (4), 993–1008.

Magnico, P., 2003. Hydrodynamic and transport properties of packed beds in small tube-to-sphere diameter ratio: pore scale simulation using an eulerian and a lagrangian approach. Chemical Engineering Science 58 (22), 5005–5024.

Magnico, P., 2009. Pore-scale simulations of unsteady flow and heat transfer in tubular fixed beds. AIChE Journal 55 (4), 849–867.

Maier, L., Schädel, B., Herrera Delgado, K., Tischer, S., Deutschmann, O., 2011. Steam reforming of methane over nickel: Development of a multi-step surface reaction mechanism. Topics in Catalysis 54 (13-15), 845–858.

References

Mallard, W., Westley, F., Herron, J., Hampson, R., Frizzell, D., 1992. NIST chemical kinetics database. Vol. 126. National Institute of Standards and Technology.

Mantzaras, J., 2013. New directions in advanced modeling and in situ measurements near reacting surfaces. Flow, Turbulence and Combustion 90 (4), 681–707.

Martin, H., Nilles, M., 1993. Radiale Wärmeleitung in durchströmten Schüttungsrohren. Chemie Ingenieur Technik 65 (12), 1468–1477.

McBride, B. J., Gordon, S., 1971. Computer Program for Calculation of Complex Chemical Equilibrium Compositions and Applications II. User's Manual and Program Description. National Aeronautics and Space Administration.

McGuire, N. E., Sullivan, N. P., Deutschmann, O., Zhu, H., Kee, R. J., 2011. Dry reforming of methane in a stagnation-flow reactor using Rh supported on strontium-substituted hexaaluminate. Applied Catalysis A: General 394 (1-2), 257–265.

McGuire, N. E., Sullivan, N. P., Kee, R. J., Zhu, H., Nabity, J. A., Engel, J. R., Wickham, D. T., Kaufmande, M. J., 2009. Catalytic steam reforming of methane using Rh supported on Sr-substituted hexaaluminate. Chemical Engineering Science 64 (24), 5231–5239.

Mehta, D., Hawley, M. C., 1969. Wall effect in packed columns. Industrial & Engineering Chemistry Process Design and Development 8 (2), 280–282.

Mette, K., 2015. Development of hydrotalcite-derived ni catalysts for the dry reforming of methane at high temperatures. Ph.D. thesis, Technische Universität Berlin.

Mette, K., Kühl, S., Düdder, H., Kähler, K., Tarasov, A., Muhler, M., Behrens, M., 2014. Stable performance of Ni catalysts in the dry reforming of methane at high temperatures for the efficient conversion of $CO_2$ into syngas. ChemCatChem 6 (1), 100–104.

Mhadeshwar, A. B., Vlachos, D. G., 2007. A catalytic reaction mechanism for methane partial oxidation at short contact times, reforming, and combustion, and for oxygenate decomposition and oxidation on platinum. Industrial & Engineering Chemistry Research 46 (16), 5310–5324.

Mhadeshwar, A. B., Wang, H., Vlachos, D. G., 2003. Thermodynamic consistency in microkinetic development of surface reaction mechanisms. Journal of Phyical Chemistry B 107 (46), 12721–12733.

Michael, B. C., Donazzi, A., Schmidt, L. D., 2009. Effects of $H_2O$ and $CO_2$ addition in catalytic partial oxidation of methane on Rh. Journal of Catalysis 265 (1), 117–129.

Michael, B. C., Nare, D. N., Schmidt, L. D., 2010. Catalytic partial oxidation of ethane to ethylene and syngas over Rh and Pt coated monoliths: Spatial profiles of temperature and composition. Chemical Engineering Science 65 (12), 3893–3902.

Mirhashemi, F., Hashemabadi, S., 2012. Experimental and CFD study of wall effects on orderly stacked cylindrical particles heat transfer in a tube channel. International Communications in Heat and Mass Transfer 39 (3), 449–455.

Mladenov, N., Koop, J., Tischer, S., Deutschmann, O., 2010. Modeling of transport and chemistry in channel flows of automotive catalytic converters. Chemical Engineering Science 65 (2), 812 – 826.

Mueller, G. E., 1992. Radial void fraction distributions in randomly packed fixed beds of uniformly sized spheres in cylindrical containers. Powder Technology 72 (3), 269 – 275.

Najera, M., Solunke, R., Gardner, T., Veser, G., 2011. Carbon capture and utilization via chemical looping dry reforming. Chemical Engineering Research and Design 89 (9), 1533–1543.

Nandini, A., Pant, K., Dhingra, S., 2006. Kinetic study of the catalytic carbon dioxide reforming of methane to synthesis gas over Ni-K/CeO$_2$-Al$_2$O$_3$ catalyst. Applied Catalysis A: General 308, 119–127.

Neufeld, P. D., Janzen, A., Aziz, R., 1972. Empirical equations to calculate 16 of the transport collision integrals $\omega$ (l, s)* for the Lennard-Jones (12–6) potential. The Journal of Chemical Physics 57 (3), 1100–1102.

Nguyen, H., Harold, M. P., Luss, D., 2015a. Spatiotemporal behavior of Pt/Rh/CeO$_2$/BaO catalyst during lean-rich cycling. Chemical Engineering Journal 262, 464–477.

Nguyen, H., Luss, D., Harold, M. P., 2015b. Impact of mass spectrometer capillary probe on the measured concentration in a monolith reactor. In: AICHE Annual Meeting 2015, Salt Lake City, UT, USA. p. 1.

Nijemeisland, M., Dixon, A. G., 2001. Comparison of CFD simulations to experiment for convective heat transfer in a gas-solid fixed bed. Chemical Engineering Journal 82 (1-3), 231–246.

Nijemeisland, M., Dixon, A. G., 2004. CFD study of fluid flow and wall heat transfer in a fixed bed of spheres. AIChE Journal 50 (5), 906–921.

Nijemeisland, M., Dixon, A. G., Stitt, E. H., 2004. Catalyst design by CFD for heat transfer and reaction in steam reforming. Chemical Engineering Science 59 (22-23), 5185–5191.

Olsbye, U., Wurzel, T., Mleczko, L., 1997. Kinetic and reaction engineering studies of dry reforming of methane over a Ni/La/Al$_2$O$_3$ catalyst. Industrial & Engineering Chemistry Research 36 (12), 5180–5188.

Ookawara, S., Kuroki, M., Street, D., Ogawa, K., 2007. High-fidelity DEM-CFD modeling of packed bed reactors for process intensification. Proceedings of European Congress of Chemical Engineering (ECCE-6), Copenhagen.

Pachauri, R. K., Allen, M., Barros, V., Broome, J., Cramer, W., Christ, R., Church, J., Clarke, L., Dahe, Q., Dasgupta, P., et al., 2014. Climate change 2014: Synthesis report. contribution of working groups i, ii and iii to the fifth assessment report of the intergovernmental panel on climate change. IPCC, 1.

Partridge, W., Toops, T., Green, J., Armstrong, T., 2006. Intra-fuel cell stack measurements of transient concentration distributions. Journal of Power Sources 160 (1), 454–461.

Patil, V. A., Liburdy, J. A., 2013. Turbulent flow characteristics in a randomly packed porous bed based on particle image velocimetry measurements. Physics of Fluids 25 (4), 043304–1–043304–23.

Pavlidis, D., Lathouwers, D., 2013. Realistic packed bed generation using small numbers of spheres. Nuclear Engineering and Design 263, 172–178.

Peña, M., Gómez, J., Fierro, J., 1996. New catalytic routes for syngas and hydrogen production. Applied Catalysis A: General 144 (1-2), 7–57.

Pedras, M. H., de Lemos, M. J., 2001. Macroscopic turbulence modeling for incompressible flow through undeformable porous media. International Journal of Heat and Mass Transfer 44 (6), 1081–1093.

Prettre, M., Eichner, C., Perrin, M., 1946. The catalytic oxidation of methane to carbon monoxide and hydrogen. Transactions of the Faraday Society 42, 335–339.

## References

Reddy, R. K., Joshi, J. B., 2008. CFD modeling of pressure drop and drag coefficient in fixed and expanded beds. Chemical Engineering Research and Design 86 (5), 444–453.

Reddy, R. K., Joshi, J. B., 2010. CFD modeling of pressure drop and drag coefficient in fixed beds: Wall effects. Particuology 8 (1), 37–43.

Reichelt, W., 1972. Zur Berechnung des Druckverlustes einphasig durchströmter Kugel- und Zylinderschüttungen. Chemie Ingenieur Technik 44 (18), 1068–1071.

Reinke, M., Mantzaras, J., Schaeren, R., Bombach, R., Kreutner, W., Inauen, A., 2002. Homogeneous ignition in high-pressure combustion of methane/air over platinum: Comparison of measurements and detailed numerical predictions. Proceedings of the Combustion Institute 29 (1), 1021–1029.

Reitzmann, A., Patcas, F., Kraushaar-Czarnetzki, B., 2006. Keramische Schwämme – Anwendungspotenzial monolithischer Netzstrukturen als katalytische Packungen. Chemie Ingenieur Technik 78 (7), 885–898.

Richardson, J., Peng, Y., Remue, D., 2000. Properties of ceramic foam catalyst supports: pressure drop. Applied Catalysis A: General 204 (1), 19–32.

Roberts, A., Garboczi, E., 2002. Elastic properties of model random three-dimensional open-cell solids. Journal of the Mechanics and Physics of Solids 50 (1), 33–55.

Romkes, S., Dautzenberg, F., van den Bleek, C., Calis, H., 2003. CFD modelling and experimental validation of particle-to-fluid mass and heat transfer in a packed bed at very low channel to particle diameter ratio. Chemical Engineering Journal 96 (1-3), 3–13.

Rostrup-Nielsen, J., Hansen, J., 1993. $CO_2$-Reforming of methane over transition metals. Journal of Catalysis 144 (1), 38–49.

Rostrup-Nielsen, J. R., Sehested, J., Nørskov, J. K., 2002. Hydrogen and synthesis gas by steam- and $CO_2$ reforming. Vol. 47 of Advances in Catalysis. Academic Press, pp. 65–139.

Sá, J., Fernandes, D. L. A., Aiouache, F., Goguet, A., Hardacre, C., Lundie, D., Naeem, W., Partridge, W. P., Stere, C., 2010. SpaciMS: spatial and temporal operando resolution of reactions within catalytic monoliths. Analyst 135, 2260–2272.

Sains, M. C., El-Bachir, M. S., Sederman, A. J., Gladden, L. F., 2005. Rapid imaging of fluid flow patterns in a narrow packed bed using MRI. Magnetic Resonance Imaging 23 (2), 391–393.

Salciccioli, M., Stamatakis, M., Caratzoulas, S., Vlachos, D., 2011. A review of multiscale modeling of metal-catalyzed reactions: Mechanism development for complexity and emergent behavior. Chemical Engineering Science 66 (19), 4319–4355.

Salvat, W., Mariani, N., Barreto, G., Martinez, O., 2005. An algorithm to simulate packing structure in cylindrical containers. Catalysis Today 107–108, 513–519.

Schwiedernoch, R., Tischer, S., Correa, C., Deutschmann, O., 2003. Experimental and numerical study on the transient behavior of partial oxidation of methane in a catalytic monolith. Chemical Engineering Science 58 (3-6), 633–642.

Scopus, 2015. Abstract and citation database.
URL `www.scopus.com`

Sederman, A., Alexander, P., Gladden, L., 2001. Structure of packed beds probed by magnetic resonance imaging. Powder Technology 117 (3), 255–269.

Seijger, G., Oudshoorn, O., Boekhorst, A., van Bekkum, H., van den Bleek, C., Calis, H., 2001. Selective catalytic reduction of $NO_X$ over zeolite-coated structured catalyst packings. Chemical Engineering Science 56 (3), 849–857.

Seyed-Reihani, S.-A., Jackson, G. S., 2004. Effectiveness in catalytic washcoats with multi-step mechanisms for catalytic combustion of hydrogen. Chemical Engineering Science 59 (24), 5937–5948.

Shah, Y. T., Gardner, T. H., 2014. Dry reforming of hydrocarbon feedstocks. Catalysis Reviews 56 (4), 476–536.

Shams, A., Roelofs, F., Komen, E., Baglietto, E., 2012. Optimization of a pebble bed configuration for quasi-direct numerical simulation. Nuclear Engineering and Design 242, 331–340.

Shams, A., Roelofs, F., Komen, E., Baglietto, E., 2013a. Large eddy simulation of a nuclear pebble bed configuration. Nuclear Engineering and Design 261, 10–19.

Shams, A., Roelofs, F., Komen, E., Baglietto, E., 2013b. Quasi-direct numerical simulation of a pebble bed configuration. Part I: Flow (velocity) field analysis. Nuclear Engineering and Design 263, 473–489.

Shams, A., Roelofs, F., Komen, E., Baglietto, E., 2014. Large eddy simulation of a randomly stacked nuclear pebble bed. Computers & Fluids 96, 302–321.

Shih, T.-H., Liou, W. W., Shabbir, A., Yang, Z., Zhu, J., 1995. A new k-$\varepsilon$ eddy viscosity model for high reynolds number turbulent flows. Computers & Fluids 24 (3), 227–238.

Sie, S., Krishna, R., 2011. Process development and scale up: II. catalyst design strategy. Reviews in Chemical Engineering 14 (3), 159–202.

Sliney, H. E., DellaCorte, C., 1993. The friction and wear of ceramic/ceramic and ceramic/metal combinations in sliding contact. In: STLE-ASME Tribology Conference; 24-27 Oct. 1993; New Orleans, LA; United States. Vol. NASA-TM-106348. pp. 1–11.

Soppe, W., 1990. Computer simulation of random packings of hard spheres. Powder Technology 62 (2), 189–197.

Stapf, S., Han, S.-I., 2006. NMR Imaging in Chemical Engineering. Wiley-VCH Verlag GmbH & Co. KGaA.

Stitt, E., 2005. Reactor technology for syngas and hydrogen. In: Derouane, E., Parmon, V., Lemos, F., Ramoa Ribeiro, F. (Eds.), Sustainable Strategies for the Upgrading of Natural Gas: Fundamentals, Challenges, and Opportunities. Vol. 191 of NATO Science Series II: Mathematics, Physics and Chemistry. Springer Netherlands, pp. 185–216.

Studart, A. R., Gonzenbach, U. T., Tervoort, E., Gauckler, L. J., 2006. Processing routes to macroporous ceramics: A review. Journal of the American Ceramic Society 89 (6), 1771–1789.

Sun Microsystems, 2008. Java 3D 1.5.1. www.oracle.com.
    URL www.oracle.com

Taskin, M. E., Troupel, A., Dixon, A. G., Nijemeisland, M., Stitt, E. H., 2010. Flow, transport, and reaction interactions for cylindrical particles with strongly endothermic reactions. Industrial & Engineering Chemistry Research 49 (19), 9026–9037.

## References

Taylor, J. D., Allendorf, M. D., McDaniel, A. H., Rice, S. F., 2003. In situ diagnostics and modeling of methane catalytic partial oxidation on Pt in a stagnation-flow reactor. Industrial & Engineering Chemistry Research 42 (25), 6559–6566.

Thomson, W., 1887. On the division of space with minimum partitional area. Acta Mathematica 11 (1-4), 121–134.

Torniainen, P., Chu, X., Schmidt, L., 1994. Comparison of monolith-supported metals for the direct oxidation of methane to syngas. Journal of Catalysis 146 (1), 1–10.

Trimm, D., 2005. The challenges in converting remote natural gas to valuable products. In: Derouane, E., Parmon, V., Lemos, F., Ramoa Ribeiro, F. (Eds.), Sustainable Strategies for the Upgrading of Natural Gas: Fundamentals, Challenges, and Opportunities. Vol. 191 of NATO Science Series II: Mathematics, Physics and Chemistry. Springer Netherlands, pp. 125–136.

Trimm, D. L., 1977. The formation and removal of coke from nickel catalyst. Catalysis Reviews 16 (1), 155–189.

Tsang, S., Claridge, J., Green, M., 1995. Recent advances in the conversion of methane to synthesis gas. Catalysis Today 23 (1), 3–15.

Turns, S. R., 2012. An introduction to combustion: concepts and application, 3rd Edition. McGraw Hill, New York.

Twigg, M. V., Richardson, J. T., 2007. Fundamentals and applications of structured ceramic foam catalysts. Industrial & Engineering Chemistry Research 46 (12), 4166–4177.

Ulpts, J., Dreher, W., Klink, M., Thöming, J., 2015. NMR imaging of gas phase hydrogenation in a packed bed flow reactor. Applied Catalysis A: General 502, 340–349.

van Antwerpen, W., du Toit, C., Rousseau, P., 2010. A review of correlations to model the packing structure and effective thermal conductivity in packed beds of mono-sized spherical particles. Nuclear Engineering and Design 240 (7), 1803–1818.

van der Laan, G. P., Beenackers, A. A. C. M., 1999. Kinetics and selectivity of the Fischer-Tropsch synthesis: A literature review. Catalysis Reviews 41 (3-4), 255–318.

VDI, 2013. VDI Heat Atlas. In: Verein Deutscher Ingenieure. Springer Berlin Heidelberg, pp. 551–614.

Védrine, J. C., 2005. Natural gas as feedstock. In: Derouane, E., Parmon, V., Lemos, F., Rama Ribeiro, F. (Eds.), Sustainable Strategies for the Upgrading of Natural Gas: Fundamentals, Challenges, and Opportunities. Vol. 191 of NATO Science Series II: Mathematics, Physics and Chemistry. Springer Netherlands, pp. 403–412.

Vlachos, D., Caratzoulas, S., 2010. The roles of catalysis and reaction engineering in overcoming the energy and the environment crisis. Chemical Engineering Science 65 (1), 18–29.

von Rickenbach, J., Lucci, F., Narayanan, C., Eggenschwiler, P. D., Poulikakos, D., 2014. Multi-scale modelling of mass transfer limited heterogeneous reactions in open cell foams. International Journal of Heat and Mass Transfer 75, 337–346.

Wang, S., Lu, G. Q. M., Millar, G. J., 1996. Carbon dioxide reforming of methane to produce synthesis gas over metal-supported catalysts: State of the art. Energy & Fuels 10 (4), 896–904.

Warnatz, J., 1982. Influence of transport models and boundary conditions on flame structure. In: Numerical methods in laminar flame propagation. Springer, pp. 87–111.

Warnatz, J., Allendorf, M. D., Kee, R. J., Coltrin, M. E., 1994. A model of elementary chemistry and fluid mechanics in the combustion of hydrogen on platinum surfaces. Combustion and Flame 96 (4), 393–406.

Weaire, D., Phelan, R., 1994. A counter-example to Kelvin's conjecture on minimal surfaces. Philosophical Magazine Letters 69 (2), 107–110.

Wehinger, G. D., Eppinger, T., Kraume, M., 2014. Fluidic effects on kinetic parameter estimation in lab-scale catalysis testing - A critical evaluation based on computational fluid dynamics. Chemical Engineering Science 111, 220–230.

Wehinger, G. D., Eppinger, T., Kraume, M., 2015a. Detailed numerical simulations of catalytic fixed-bed reactors: Heterogeneous dry reforming of methane. Chemical Engineering Science 122, 197–209.

Wehinger, G. D., Eppinger, T., Kraume, M., 2015b. Evaluating catalytic fixed-bed reactors for dry reforming of methane with detailed CFD. Chemie Ingenieur Technik 87 (6), 734–745.

Wehinger, G. D., Heitmann, H., Kraume, M., 2016. An artificial structure modeler for 3D CFD simulations of catalytic foams. Chemical Engineering Journal 284, 543–556.

Wei, J., Iglesia, E., 2004. Isotopic and kinetic assessment of the mechanism of reactions of $CH_4$ with $CO_2$ or $H_2O$ to form synthesis gas and carbon on nickel catalysts. Journal of Catalysis 224 (2), 370–383.

Wolfshtein, M., 1969. The velocity and temperature distribution in one-dimensional flow with turbulence augmentation and pressure gradient. International Journal of Heat and Mass Transfer 12 (3), 301–318.

Yang, J., Wang, Q., Zeng, M., Nakayama, A., 2010. Computational study of forced convective heat transfer in structured packed beds with spherical or ellipsoidal particles. Chemical Engineering Science 65 (2), 726–738.

Yang, X., Scheibe, T. D., Richmond, M. C., Perkins, W. A., Vogt, S. J., Codd, S. L., Seymour, J. D., McKinley, M. I., 2013. Direct numerical simulation of pore-scale flow in a bead pack: Comparison with magnetic resonance imaging observations. Advances in Water Resources 54, 228–241.

York, A. P. E., Xiao, T.-c., Green, M. L. H., Claridge, J. B., 2007. Methane oxyforming for synthesis gas production. Catalysis Reviews 49 (4), 511–560.

Yuan, T., Lai, Y.-H., Chang, C.-K., 2008. Numerical studies of heterogeneous reaction in stagnation flows using one-dimensional and two-dimensional Cartesian models. Combustion and Flame 154 (3), 557–568.

Yuen, E., Sederman, A., Sani, F., Alexander, P., Gladden, L., 2003. Correlations between local conversion and hydrodynamics in a 3-D fixed-bed esterification process: An MRI and lattice-boltzmann study. Chemical Engineering Science 58 (3–6), 613–619.

Zeiser, T., Lammers, P., Klemm, E., Li, Y. W., Bernsdorf, J., Brenner, G., 2001. CFD-calculation of flow, dispersion and reaction in a catalyst filled tube by the lattice boltzmann method. Chemical Engineering Science 56 (4), 1697–1704.

Zellner, A., Suntz, R., Deutschmann, O., 2015. Two-dimensional spatial resolution of concentration profiles in catalytic reactors by planar laser-induced fluorescence: NO reduction over diesel oxidation catalysts. Angewandte Chemie International Edition 54 (9), 2653–2655.

Zhu, H., Hobdell, J., Windle, A., 2000. Effects of cell irregularity on the elastic properties of open-cell foams. Acta Materialia 48 (20), 4893–4900.

Zhu, H., Zhou, Z., Yang, R., Yu, A., 2007. Discrete particle simulation of particulate systems: Theoretical developments. Chemical Engineering Science 62 (13), 3378–3396.

Zhu, Q., Zhao, X., Deng, Y., 2004. Advances in the partial oxidation of methane to synthesis gas. Journal of Natural Gas Chemistry 13, 191–203.

Zhu, Y.-A., Chen, D., Zhou, X.-G., Yuan, W.-K., 2009. DFT studies of dry reforming of methane on Ni catalyst. Catalysis Today 148 (3-4), 260–267.

Ziółkowska, I., Ziółkowski, D., 1988. Fluid flow inside packed beds. Chemical Engineering and Processing: Process Intensification 23 (3), 137–164.

Zobel, N., Eppinger, T., Behrendt, F., Kraume, M., 2012. Influence of the wall structure on the void fraction distribution in packed beds. Chemical Engineering Science 71, 212–219.

# List of Figures

# List of Tables

# Publications

This manuscript involves results, which were (partly) published in the following articles:

1. Wehinger, G. D., Heitmann, H., Kraume, M. (2016). An artificial structure modeler for 3D CFD simulations of catalytic foams, *Chemical Engineering Journal*, 284, 543-556

2. Wehinger, G. D., Eppinger, T., Kraume, M. (2015). Evaluating catalytic fixed-bed reactors for dry reforming of methane with detailed CFD, *Chemie Ingenieur Technik*, 87(6), 734-745

3. Wehinger, G. D., Eppinger, T., Kraume, M. (2015). Detailed numerical simulations of catalytic fixed-bed reactors: Heterogeneous dry reforming of methane, *Chemical Engineering Science*, 122, 197-209

4. Wehinger, G. D., Eppinger, T., Kraume, M. (2014). Fluidic effects on kinetic parameter estimation in lab-scale catalysis testing – A critical evaluation based on computational fluid dynamics, *Chemical Engineering Science*, 111, 220-230

Furthermore, the results of this manuscript have been presented at national and international conferences. Speaker is underlined.

1. Wehinger, G. D., Kraume, M. (2016) Ist die CFD bereit als Design-Tool für Festbettreaktoren eingesetzt zu werden?, *ProcessNet-Jahrestreffen Reaktionstechnik 2016*, Würzburg, Germany

2. Wehinger, G. D., Kraume, M., Berg, V., Mette, K., Behrens M., Schlögl, R., Korup, O., Horn, R. (2015) Dry Reforming of Methane on Ni in a Fixed-Bed Reactor: Spatial Reactor Profiles and Detailed CFD Simulations, *AIChE Annual Meeting*, Salt Lake City, USA honored as "Best Presentation"

3. Wehinger, G. D., Kraume, M. (2015) Interstitial-Scale Modeling of Catalytic Foam Reactors: Partial Oxidation of Methane, *AIChE Annual Meeting*, Salt Lake City, USA

4. Eppinger, T., Jurtz, N., Wehinger, G. D., Kraume, M., Aglave, R. (2015) A Numerical Optimization Study on the Catalytic Dry Reforming of Methane in a Spatially Resolved Fixed-Bed Reactor, *AIChE Annual Meeting*, Salt Lake City, USA

5. Wehinger, G. D., Eppinger, T., Aglave, R. (2015) Effect of Catalyst Shape on Yield and Performance of Packed Beds, *7th AIChE Southwest Process Technology Conference*, Galveston, TX, USA

6. Wehinger, G. D. (2015). Particle-resolved CFD simulations of heterogeneous catalytic reactors: dry reforming of methane, invited talk at *Air Products*, Allentown, PA, USA

7. Wehinger, G. D., Eppinger, T., Kraume, M. (2015). Is CFD Ready for Being a Design Tool for Fixed-Bed Reactors? *AIChE Spring Meeting & 10th Global Congress on Process Safety*, Austin, USA

8. Wehinger, G. D., Heitmann, H., Kraume, M. (2015). Detaillierte Modellierung katalytischer Schwämme für CFD-Simulationen, *ProcessNet-Jahrestagung der Fachgruppen Computational Fluid Dynamics und Mehrphasenströmungen 2014*, Lüneburg, Germany

9. Wehinger, G. D., Kraume, M. (2014). New insights into catalytic fixed-bed reactors through detailed CFD, invited talk at *Clariant – Department Oxidation Catalysis*, Heufeld, Germany

10. Wehinger, G. D. (2014). Detaillierte Simulation von katalytischen Festbettreaktoren, *VDI-Workshop Simulation*, Chemiepark DOW, Schkopau, Germany

11. Wehinger, G. D., Eppinger, T., Kraume, M. (2014). Detailed Catalytic Fixed-Bed Reactor Simulations: The Dry Reforming of Methane, *AIChE Annual Meeting*, Atlanta, USA

12. Wehinger, G. D. (2014). Detailed numerical simulations of fixed-bed reactors: the heterogeneous dry reforming of methane, invited talk at *KIT, Prof. Deutschmann group, ITCP*, Karlsruhe, Germany

13. Wehinger, G. D., Kraume, M. (2014). Ortsaufgelöste Simulationen des heterogenen Dry-Reforming von Methan in Festbettreaktoren, *ProcessNet-Jahrestreffen Reaktionstechnik 2014*, Würzburg, Germany

14. Wehinger, G. D., Eppinger, T., Kraume, M. (2014). Spatially Resolved Simulations of Heterogeneous Dry Reforming of Methane in Fixed-bed Reactors, *AIChE Spring Meeting & 10th Global Congress on Process Safety*, New Orleans, USA honored with Best Presentation Award

15. Wehinger, G. D., Eppinger, T., Kraume, M. (2014). Spatially resolved simulations of heterogeneous dry reforming of methane in fixed-bed reactors, *STAR Global Conference 2014*, Vienna, Austria

16. Wehinger, G. D., Peeters, J., Muzaferija, S., Kraume, M. (2014). Numerische Simulation des Stofftransports von vertikalen Flüssigfilmen, *ProcessNet-Jahrestagung der Fachgruppe CFD, Mischvorgänge und Rheologie 2014*, Würzburg, Germany

17. Wehinger, G. D., Eppinger, T., Muzaferija, S., Kraume, M. (2013). Numerische Simulation der Dynamik von vertikalen Flüssigfilmen, *ProcessNet-Jahrestagung der Fachgemeinschaft Fluiddynamik und Trenntechnik 2013*, Würzburg, Germany

Additionally, posters with the results were presented at several conferences:

1. Wehinger, G. D., Heitmann, H., Kraume, M. (2016). catFM: ein Algorithmus zur automatischen Erzeugung von detaillierten Schwammstrukturen für CFD-Simulationen, *ProcessNet Jahrestreffen der Fachgruppen Agglomerations- und Schüttguttechnik, Computational Fluid Dynamics und Mehrphasenströmungen*, Bingen, Germany

2. Wehinger, G. D., Kraume, M., Berg, V., Mette, K., Behrens, M., Schlögl, R., Korup, O., Horn, R. (2015) Methane dry reforming on nickel in a fixed-bed reactor: Spatial reactor

profiles and particle resolved numerical simulations, *European Symposium of Chemical Reaction Engineering (ESCRE) 2015*, Fürstenfeldbruck, Germany

3. Berg, V., Wehinger, G. D., Kraume, M., Mette, K., Behrens, M., Schlögl, R., Korup, O., Horn, R. (2015). Dry reforming of methane on nickel in a fixed-bed reactor: A study by spatially resolved reactor profiles and numerical simulation, *48. Jahrestreffen Deutscher Katalytiker 2015*, Weimar, Germany

4. Wehinger, G. D., Kraume, M. (2014). Numerische Simulation komplexer Geometrien mit detaillierten heterogenen Reaktionsmechanismen, *ProcessNet-Jahrestagung 2014*, Aachen, Germany

5. Wehinger, G. D., Eppinger, T., Kraume, M. (2013). Combining CFD and Statistical Methods to Optimize the Oxidative Coupling of Methane in a Fixed Bed Reactor, *AIChE Annual Meeting 2013*, San Francisco, USA

6. Wehinger, G. D., Eppinger, T., Kraume, M. (2013). Anforderungen an eine OCM-Kinetik aus ingenieurstechnischer Sicht, *ProcessNet-Jahrestagung der Fachgemeinschaft Fluiddynamik und Trenntechnik 2013*, Würzburg, Germany